The University Of Sheffield.

Cleaner Coal Combustion Technologies – The Impact on NO_x Emissions and Fireside Corrosion

Thomas Sam Yelland

A thesis submitted in partial fulfilment of the requirements for the degree of Engineering Doctorate

The University of Sheffield

Faculty of Engineering

Department of Mechanical Engineering

June 2020

ACKNOWLEDGEMENTS

Firstly I'd like to thank Prof. Bill Nimmo for his calm guidance, support and expert knowledge; I have been very lucky to have him as my primary supervisor. I am also thankful to Dr. Sheraz Daood for his kindness, mentorship and training in using pilot-scale facilities. Thanks go to Dmitry Govorukhin, it is a shame our work together was always beset by delays and issues but I am thankful for your time, help and your friendship. Thanks go to Janos Szuhanszki for training on the PACT oxy-combustion test facility.

I would, also, like to thank the CDT for Carbon Capture and Storage and Cleaner Fossil Energy, the University of Sheffield and the EPSRC for the funding and administration of my EngD and the training that took place during my EngD, with particular thanks to Diane Vincent and Prof. Colin Snape.

To my Mum and Dad, thank you for being interested when I prattle on about energy and CCS and just being the most supportive and wonderful parents that I could ask for. To my brother Matt, thank you for helping me feel confident, being my role model and inviting me to United games. To my sister Sophs, thank you for being a best friend and making me laugh at a moment's notice.

To Ala, thank you for your love, support and always believing in me. Most of all, thank you for helping me leave work at the office, so I can come home and relax; I would not have been able to do this without you.

ABSTRACT

Despite efforts to curb global warming, the use of coal for power generation is projected to increase. The impact of this on global warming could be negated by the proliferation of carbon capture technologies, but their adoption is slow and inhibited by techno-economic challenges. In the meantime, coal combustion is associated with NO_x emissions, which cause a plethora of environmental problems, and economic uncertainties caused by ash-related issues. The aim of this thesis is to minimise the negative impacts of coal's continued consumption, through aiding the development of clean coal power generation. This aim was achieved by investigating two technologies.

The first was the use of low-NO_x burners during oxy-coal combustion in order to minimise NO formation and maximise destruction of recycled NO via reburning, using a 250 kW_{th} combustion test facility that can be run in air-firing or oxy-firing mode. A range of burner configurations were tested across two oxy-fuel regimes with varying levels of NO recycling. Measurements were taken at the flue, radially in the flame and axially down the centreline of the flame. The profiles showed that burner staging aids in controlling the products of NO reburning.

The second technology, an Fe-based additive, was investigated in two parts. The first route was investigating the impact of this additive on selective non-catalytic reduction, using a 100 kW_{th} combustion test facility able to load the fuel with additive. The presence of the Fe-based additive was shown to increase NO reduction due to SNCR. This interaction was then kinetically modelled and analysed for its sensitivity to process conditions. The second route was investigating the impact of the additive on fireside corrosion, using the equilibrium modelling software, FactSage. The investigated coal ash was not corrosive enough to show any trends in FactSage, so three biomass fuel ashes were investigated and the Fe-based additive was compared with two coal ashes and alumina to analyse the extent of any inhibition witnessed. The metrics used for analysis were the formation of various corrosive compounds and by-products. The Fe-based additive could inhibit corrosion but not as well as either of the coal ashes, as it was key to increase the Al and Si content of the deposits. The Fe-based additive should not be used solely to inhibit corrosion but it is a positive side effect if used for other applications.

DECLARATION

I, the author, confirm that the Thesis is my own work. I am aware of the University's Guidance on the Use of Unfair Means (www.sheffield.ac.uk/ssid/unfair-means). This work has not been previously been presented for an award at this, or any other, university.

Journal Publications

Chapter 4 contains the following publication:

- Daood, S.S., Yelland, T.S., Szuhánszki, J., Pourkashanian, M., Nimmo, W. (2019). Experimental Investigation of NO Reburning During Oxy-Coal Burner Staging. Energy & Fuels, 33(2), 1590-1602.

The author of this thesis created the experimental plans, conducted the experimental work and was the principle author of the manuscript.

Chapter 5 contains the following publication:

- Daood, S., Yelland, T., Nimmo, W. (2017). Selective non-catalytic reduction – Fe-based additive hybrid technology. Fuel, 208, 353-362.

The author of this thesis created the experimental plans, conducted the experimental work, conducted the economic analysis and was the principle author of the manuscript.

Chapter 6 contains the following publication:

- Yelland, T.S., Daood, S.S., Nimmo, W. (2020-Submitted). Comparing Fuel Additives for Fireside Corrosion Inhibition in Pulverised Fuel Boilers Using Thermodynamic Modelling. Fuel.

The author of this thesis conducted the modelling work, the analysis and was the principle author of the manuscript.

Conference Presentations

- Yelland, T., Daood, S., Nimmo, W. (2018) 'Novel Hybrid NO_x Technology for Pulverised Coal Combustion', UK-PK Joint R-L Workshop on Fuels and Energy Systems, Cambridge, 28th March 2018.

- Yelland, T., Daood, S., Szuhánszki, J., Pourkashanian, M., Nimmo, W. (2018) 'Minimising NO emissions from oxy-coal combustion: The impact of burner staging on NO reburning during oxy-coal combustion', IFRF 2018 Conference, Sheffield, 30-31st May 2018.
- Yelland, T.S., Daood, S.S., Nimmo, W. (2018) 'SNCR-Fuel Additive Based Hybrid Technology for Low NOx Pulverised Coal Combustion', 12th ECCRIA Conference, Cardiff, 5-7th September 2018.
- Yelland, T., Daood, S., Szuhánszki, J., Pourkashanian, M., Nimmo, W. (2018) 'Experimental Investigation into Burner Staging during Oxy-coal Combustion', 12th ECCRIA Conference, Cardiff, 5-7th September 2018.
- Yelland, T., Daood, S., Szuhánszki, J., Pourkashanian, M., Nimmo, W. (2019) 'The Impact of Burner Staging on NO Reburning during Oxy-coal Combustion', 9th International Conference on Clean Coal Technologies, Houston, Texas, USA, 3-7th June 2019.

TABLE OF CONTENTS

LIST OF FIGURES

LIST OF TABLES

ABBREVIATIONS

AFR	ammonia flow rate
ASNCR	Advanced selective non-catalytic reduction
ASU	Air separation unit
BACT	Best available control technology
BECCS	Bio-energy carbon capture and storage
BOOS	Burners out of service
CAPEX	Capital expenditure
CCS	Carbon capture and storage
CMOS	Complementary metal oxide semiconductor
CSTR	Continuously stirred tank reactor
CTF	Combustion test facility
DAC	Direct air capture
DSZ	Downstream zone
ERZ	External recirculation zone
FGR	Flue gas recirculation
FTIR	Fourier transform infra-red spectroscopy
HELE	High efficiency low emission
HMI	Human-machine interface
IDF	Induced draft fan
IGCC	Integrated gasification combined cycle
IRZ	Inner recirculation zone
JEZ	Jet expansion zone
LNB	Low-NO_x burner
MEA	Monoethanolamine
NET	Negative emission technology
NSR	Normalised stoichiometric ratio
OFA	Overfire air
OPEX	Operating expenditure
PACT	Pilot-scale advanced CO_2-capture technology centre

PF	Pulverised fuel
PM	Particulate matter
PV	Photo voltaic
ROFA	Reducing overfire air
SCADA	Supervisory control and data acquisition
SCO	Selective catalytic oxidation
SCR	Selective catalytic reduction
SNCR	Selective non-catalytic reduction
THC	Total hydrocarbons
TOTEX	Total expenditure
TPES	Total primary energy supply
VOC	Volatile organic carbon

CHAPTER 1 INTRODUCTION

1.1 Thesis Overview

This thesis will attempt to present and discuss novel technologies, which aim to improve coal combustion, with respect to reducing NO_x emissions and impeding fireside corrosion, so that it is compatible for use in future power generation portfolios. It is split into seven chapters, starting with the introduction, which aims to set the scene with regards to the use of coal for power generation, the state of carbon capture technologies, the impact of NO_x emissions on the environment and the cost of corrosion in coal boilers. Chapter 2 will survey literature to determine how NO_x is formed, the state of technologies to reduce formation, how NO_x processes differ during oxy-coal combustion, how fireside corrosion occurs and the state of additive technologies that reduce corrosion. This will highlight two technologies with the potential to significantly aid the techno-economic feasibility of clean coal processes but requiring greater industrial confidence.

The first technology to be discussed is the implementation of low-NO_x burner technology during oxy-coal combustion, with particular attention on the impact of different burner staging environments on the reburning of NO from the recirculated flue gas; Chapter 4 will encompass this discussion. The second technology is to be discussed in two separate contexts; the first being the use of an Fe-based additive in conjunction with selective non-catalytic reduction in order to improve the NO reduction potential of the latter technology, and the second being the impact of an Fe-based additive on reducing the rate of fireside corrosion. The first of these investigations will be presented in Chapter 5 with experimental findings, techno-economic analysis and kinetic modelling analysis. The second will be presented in Chapter 6 using equilibrium modelling, comparing the impacts across a variety of fuels with a variety of additives. A description of the facilities, processes and software used will be presented in Chapter 3. Chapter 7 will conclude the thesis with the major findings and recommendations for future work.

1.2 Our Energy Landscape

1.2.1 The State of Power Generation

Since the dawn of the Industrial Revolution, access to electricity has become so increasingly vital to modern society that it is now widely regarded as a human right (Tully, 2006) and key to the socio-economic development of developing nations (Kanagawa and Nakata, 2008). Over the course of the 20th century, the expansion of the global economy and the vast growth of the world's population has led to an incredible demand for electricity, which has in turn, unintentionally, been the root cause of a plethora of environmental crises. Two of the most prominent of these crises are anthropogenic climate change caused by global warming and the decrease of urban air quality caused by photochemical pollution. Both of these issues are at least partly attributable to the use of fossil fuels in power generation.

The world's power generation portfolio principally contains fossil fuel sources (Figure 1.1) and, despite an uptake in renewable and nuclear energy technologies, will continue to do so for the foreseeable future. The share of individual fossil fuels, however, has changed quite dramatically since 1971. The proportion of electricity generation from oil has decreased radically (Figure 1.2) as oil usage has been increasingly earmarked for transport fuel and plastic production, while the use of natural gas has become far more popular due to progress in the shale gas industry in the USA, primarily driven by a desire for energy security.

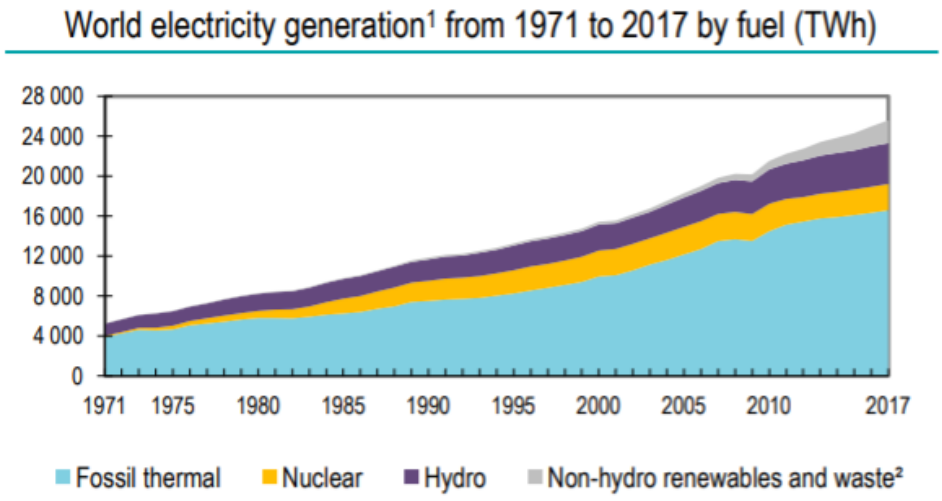

Figure 1.1 – World electricity generation by fuel (TWh) (1971-2017) (IEA, 2019)

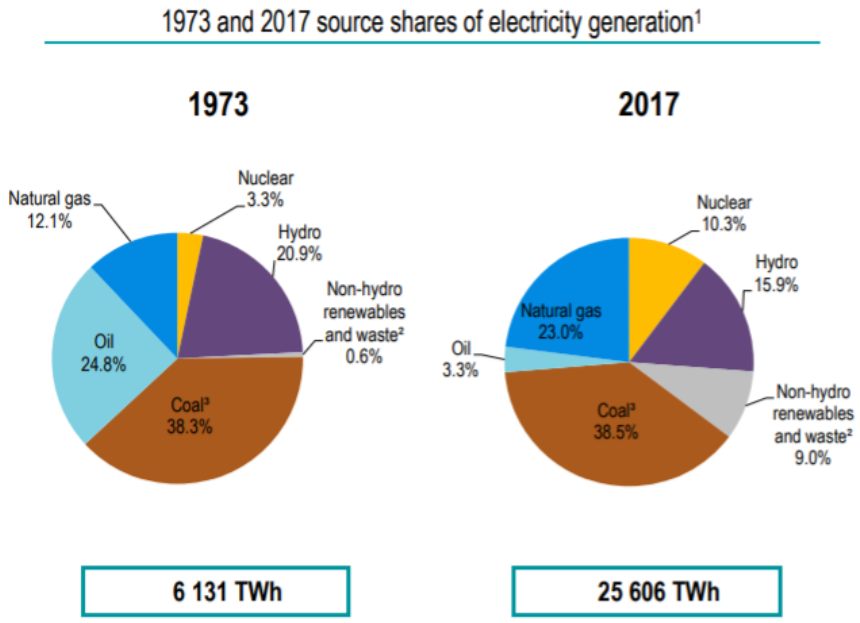

Figure 1.2 – Shares of electricity generation attributed to major sources (1973 and 2017) (IEA, 2019)

The apparent constancy of the proportion of electricity generation from coal over the last 40 years does not accurately represent the actual transformation. In this time period, coal use has remained relatively stable in OECD nations in terms of total primary energy supply (TPES) (IEA, 2019) but the rapid economic development experienced in China and India required a great increase in energy demand (up to ~33% of the world's energy demand (IEA, 2019)), which was largely powered by coal, hence maintaining the status quo. Together, India and China are responsible for over 55% of power generation from coal (IEA, 2019). The proportional decrease in coal use in OECD nations is attributable to, at first, concerns over deteriorating air quality in major cities, which unfortunately culminated in events such as the Great London Smog of 1952 claiming the lives of 8000 people (Stone, 2002), and, later following increased scientific consensus, anthropogenic climate change. In recent years, this process has been helped by the improving economic qualities of renewable energy options and, as mentioned, the falling cost of natural gas (IEA, 2019b).

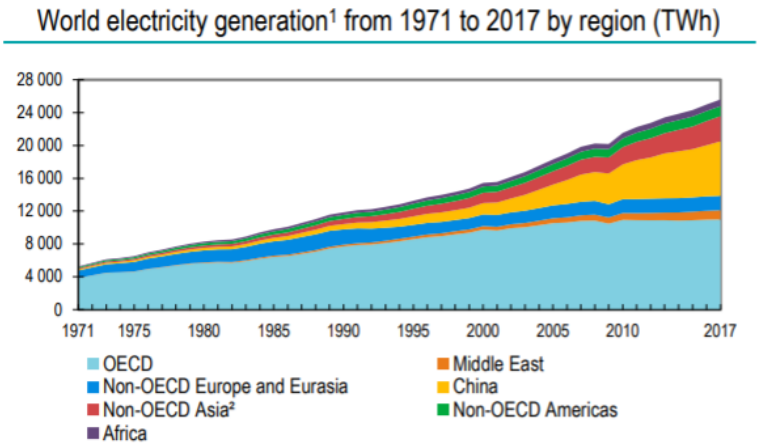

Figure 1.3 – The growth in world energy demand by region (IEA, 2019)

Carbon dioxide is formed from the combustion of any carbon-based fuel, however, due to its significantly greater carbon to hydrogen ratio, coal produces far more CO_2 per unit energy when compared to oil and gas. As highlighted in Figure 1.4, coal combustion is responsible for 44.2% of CO_2 emissions, even though it contributes a meagre 27.1% of global TPES (IEA, 2019). The Kyoto Protocol and Paris Climate Agreement have brought nations together with the aim of decreasing CO_2 emissions in order to minimise climate change to only a 1.5 °C temperature rise. This drive will see the reduction in overall fossil fuel use, in particular the use of coal. However, coal could still be used in an environmentally acceptable way if a carbon capture and storage technology is utilised; this is a desirable outcome given the vast quantities of coal reserves still present (Abas, 2015).

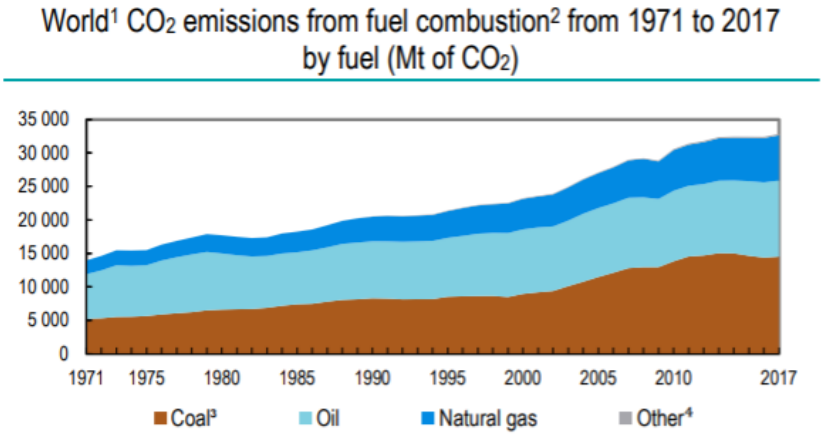

Figure 1.4 – Change in contribution of individual fossil fuels to CO_2 emissions from 1971 to 2017 (IEA, 2019)

This reduction in coal use, however, is not a definite outcome yet. Under the policies that national governments have laid out, coal demand will remain relatively stable through to 2040 as China and India's growth in demand absorbs the effort of European and North American attempts to move away from coal (Figure 1.5). Under a sustainable development scenario, there must be greater effort to decrease coal use by all parties. Even the European and North American nations must bring their coal demand to under 150 Mtce, instead of the 600 Mtce that they are currently forecast to use. The greatest effort must be made by the Asia Pacific group of nations that must agree to decreasing coal demand by over 50%.

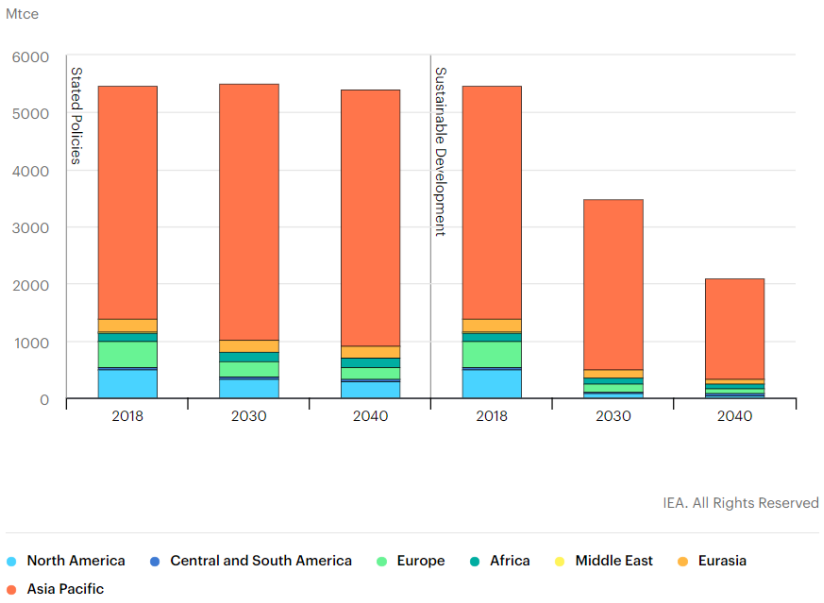

Figure 1.5 – The forecast demand for coal under business as usual and sustainable development scenarios (IEA, 2019b)

In contrast, the progression of renewable technologies must be able to cover the drop in coal demand and to be able to account for an increase in total energy demand that will accompany the aim of continuing global economic growth. These renewable technologies will mainly be solar PV, wind turbines (on-shore and off-shore), hydropower and biomass/biogas, and different nations will have limited capacity to install each of these based on their geographical characteristics. Nevertheless, as seen in Figure 1.6, great changes will need to be made to existing plans in order to meet sustainable development goals by 2040. In particular, greater uptake of renewable technologies in the Asia Pacific region is required between 2030 and 2040. This is something that is becoming more and

more feasible as technologies mature and innovations are made, leading to changing associated economic landscapes, as seen with Europe's collective success with off-shore wind in the recent past (IEA, 2019b).

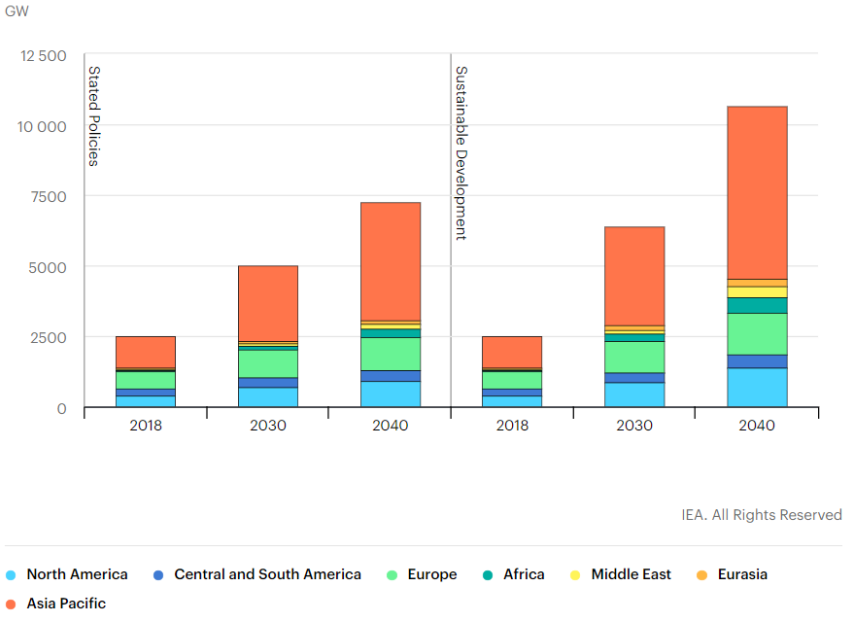

Figure 1.6 – The forecast renewable electricity capacity under business as usual and sustainable development scenarios (IEA, 2019b)

1.2.2 Solid Fuel Combustion

Coal combustion for power generation can occur in a number of different technologies, namely: fixed bed, fluidised bed or pulverised fuel systems, with the most common technology being the last. In pulverised fuel boilers/furnaces (Figure 1.7), the coal, which has been pulverised in a mill, is entrained in a portion of the overall excess air known as the primary air and is carried to a burner; this mixture is then enveloped by a preheated secondary portion of the oxidant to enable combustion. There are two common classifications of burner: swirl burners and jet burners. Basic swirl burners introduce both streams with significant angular momentum; this affects the mixing of the primary and secondary oxidant and, hence, burnout of the fuel. Jet burners inject the fuel and portions of oxidant with no angular momentum and are mainly utilised for high-moisture fuels (Toporov, 2014). The resulting combustion forms a flame, whose shape and length are dictated by the fluid dynamics of the air. In an industrial furnace, there will be a series of flames arranged either in the wall-fired pattern, where burners appear only on one wall or

two opposing walls, or the tangentially-fired pattern, where the burners are placed in the corners of the furnace (Tillman, et al., 2012).

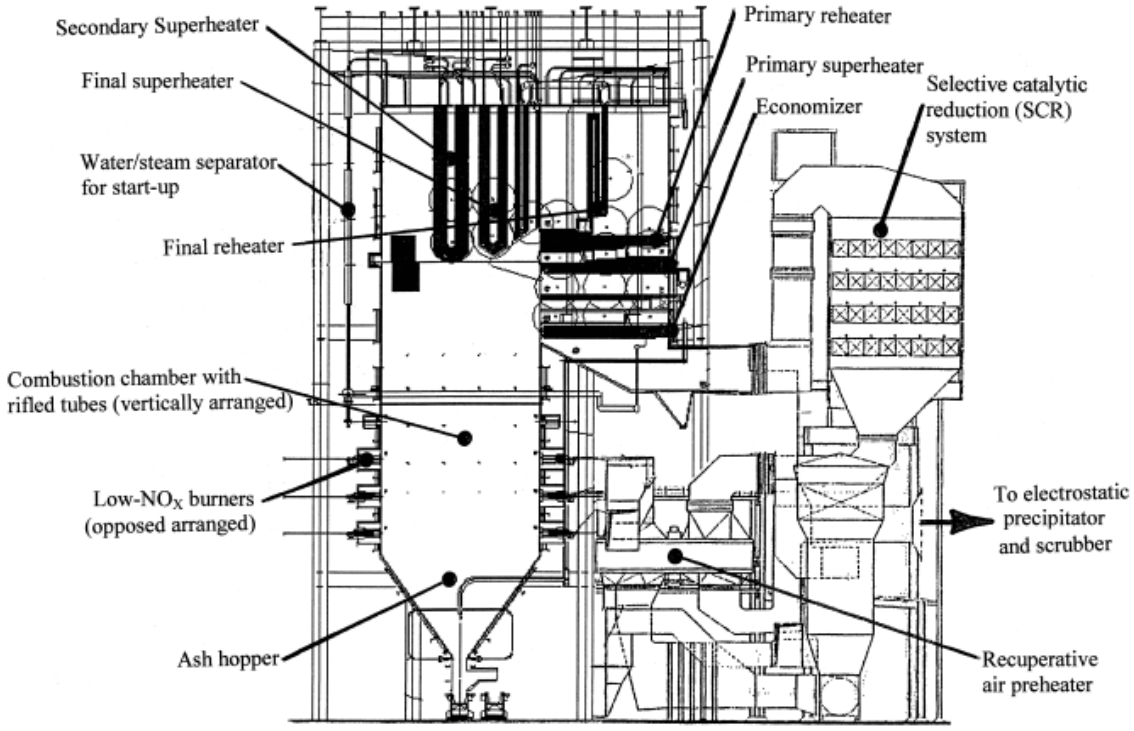

Figure 1.7 – Two-Pass Benson-Type 750 MW Pulverised Coal Boiler for Supercritical Steam Generation (with SCR) (Termuehlen and Emsperger, 2003)

When coal particles enter the flame, water is driven off and the coal undergoes devolatilization, where the small chain hydrocarbons known as volatiles are released from the coal particle and combusted. The heat from the combusted volatiles is then great enough to commence combustion and breakdown of the char, the remaining heterogenous hydrocarbon-based matrix forming the majority of the coal particle. The heat from this combustion is radiated from the flames to the waterwall tubes and from the flue gas into the superheater and reheater tubes. The steam is heated to the designed temperature and is used to generate electricity via turbines.

One method to reduce CO_2 emissions from coal combustion is to increase the designed temperature of the steam by improving efficiencies in the heat transfer surfaces and combustion process, so less coal is needed to generate a unit of electricity. Most existing coal power plants are designated as subcritical and have efficiencies of ~33%, but this method to reduce CO_2 emissions can improve efficiencies to ~40% and ~46% by installing

supercritical and ultra-supercritical technologies (Kumar and Kumar, 2018). These high efficiencies were made attainable due to significant progress in the research of steel alloys that are able to withstand higher temperatures and pressures than previous steels. This research has primarily been in increasing the high temperature strength of ferritic steels, which, unlike austenitic steels, do not present thermal fatigue issues. Ferritic steels allow for upper operating conditions of 620-630 °C; while, above this temperature, nickel-based superalloys have been found to be promising (Holcomb, et al., 2005). Together, these techniques, along with others, are known as high efficiency low emission (HELE) technologies, as improvements in efficiency not only lead to a decrease in CO_2 emissions but also a decrease in NO_x, SO_x and PM emissions.

Once the flue gas has passed the boiler arch, it is treated to minimise the content of SO_2, NO and PM, before being released from a stack. Technologies to reduce NO emissions may already be in service within the flame or post-flame regions of the boiler, but some of these technologies can have the effect of decreasing the flame temperature, thus leading to an increased carbon content in the ash, which can make the fly ash unsuitable for use as a precursor in concrete production, leading to issues regarding disposability of the fly ash.

In an effort to meet Paris Climate Agreement targets, some power plant operators have switched to co-firing coal with biomass or even burning pure biomass; this will lead to a reduction in life-cycle CO_2 emissions in the former and a carbon neutral lifecycle in the latter, due to the CO_2 sequestered by the biomass when growing. Biomass is a catch-all term, but, generally, currently utilised biomass fuels tend to have some major differences to the previously used coals. Biomass fuels will have a higher water content and a greater oxygen and hydrogen content, therefore producing greater amounts of volatiles. This will result in low heating values and some flame stability issues when utilising existing industrial burners, which, together with increased corrosion from greater chlorine and alkali metal contents, can lead to economic problems (Werther, et al., 2000). Typically, the sustainability of harvesting biomass fuels with low chlorine/alkali metal contents is disputed (European Commission, 2017). However, biomass fuels also commonly have low nitrogen and sulphur contents, often low enough to eliminate the need for costly abatement processes.

1.2.3 Carbon Capture and Storage

Carbon capture and storage technologies are processes that aim to reduce or eliminate carbon dioxide emissions from fossil fuel combustion through the chemical/physical capture of CO_2. This CO_2 is then to be transported to a storage site, most likely a retired oil reservoir or saline aquifer, where it is sequestered using the geological formations present. There are three major carbon capture technologies: pre-combustion capture (utilising integrated gasification combined cycle (IGCC)), post-combustion capture and oxy-fuel combustion.

Pre-combustion capture involves gasifying coal in order to create a syngas stream constituted of CO, CO_2 and H_2, which can then be utilised as a fuel in a combined cycle gas turbine. Alternatively, the syngas can be treated using the water-gas shift reaction so that the CO is converted to CO_2 , which can be separated ready for transportation and storage, while the remaining pure H_2 stream is combusted in a turbine to produce only water as a by-product. This process is shown in Figure 1.8. This process has favourable process economics but is associated with disparaging capital costs and complex design features (Toftegaard, et al., 2010). However, this may be a more desirable option in East Asian countries, which typically have large coal stockpiles and little access to natural gas (Tillman, 2018).

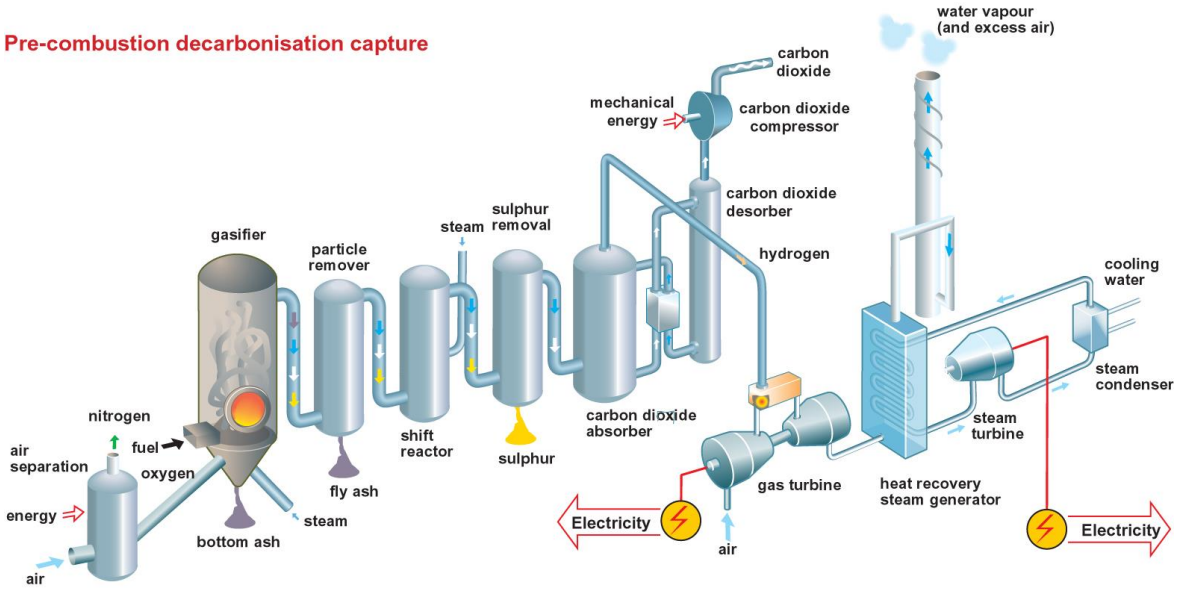

Figure 1.8 – Pre-combustion capture process (Vattenfall, 2008)

Post-combustion capture involves the conventional combustion of the coal in air, but, rather than emitting the flue gas after some pollutant control, the CO_2 is scrubbed out of the exhaust using, most commonly, monoethanolamine (MEA). This creates a rich CO_2-laden sorbent that is then pumped to a stripper, where the absorbent is regenerated and the CO_2 is driven off, collected, and prepared for transportation and storage (Abu-Zahra, et al., 2016). This process is shown in Figure 1.9. However, this technology currently carries a significant efficiency penalty for the plant and requires a flue gas stream effectively free from SO_2 and NO_2 as these can permanently degrade the absorbent (Toftegaard, et al., 2010). Currently, there are two major post-combustion capture plants being operated at Petra Nova in Texas, USA and Boundary Dam in Saskatchewan, Canada.

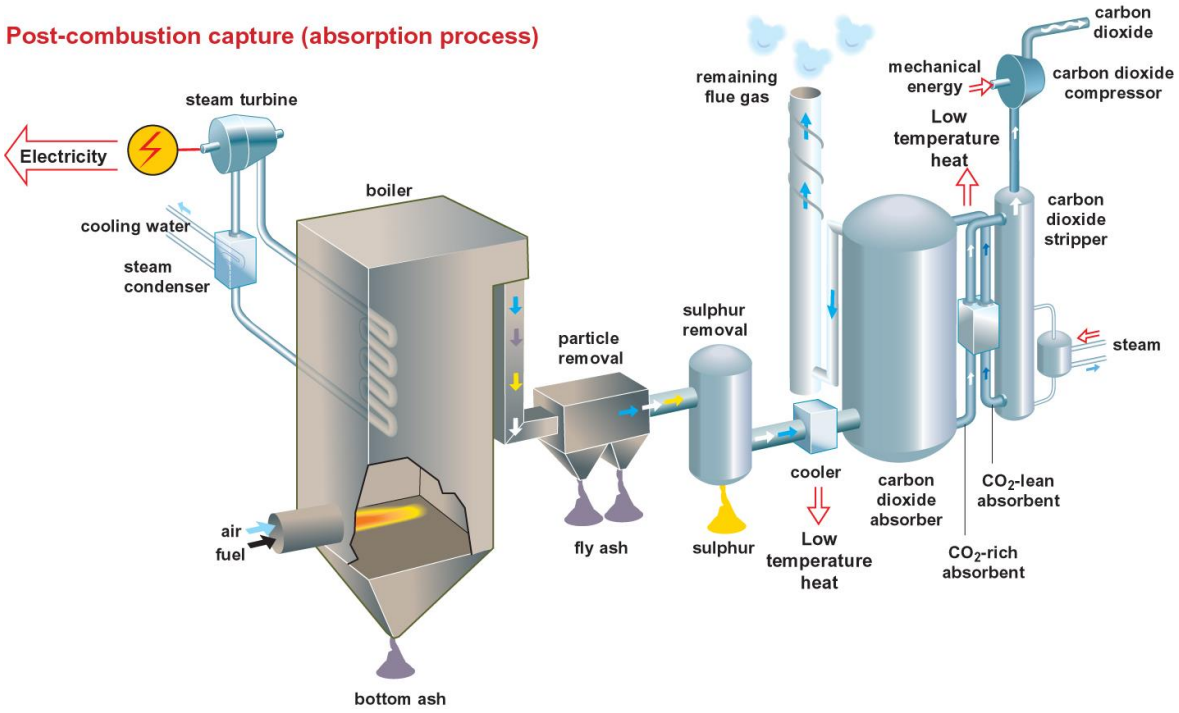

Figure 1.9 – Post-combustion capture process (Vattenfall, 2008)

Oxy-fuel combustion of fuel in an O_2/CO_2 mixture, as opposed to air, is used in order to produce a flue gas with a far greater CO_2 concentration, hence simplifying CO_2 purification processes to simply dehydration and the usual pollutant abatement units (desulphurisation and SCR or acid gas compression). The O_2/CO_2 mixture is formed by recirculating a portion of the flue gas back to the burner and mixing with O_2 purified from air using an air separation unit (ASU). This process is shown in Figure 1.10. This technology can provide

some technical challenges and an energy penalty due to the ASU but is said to be 'the most energy and cost efficient of the carbon capture technologies' (Toftegaard, et al., 2010).

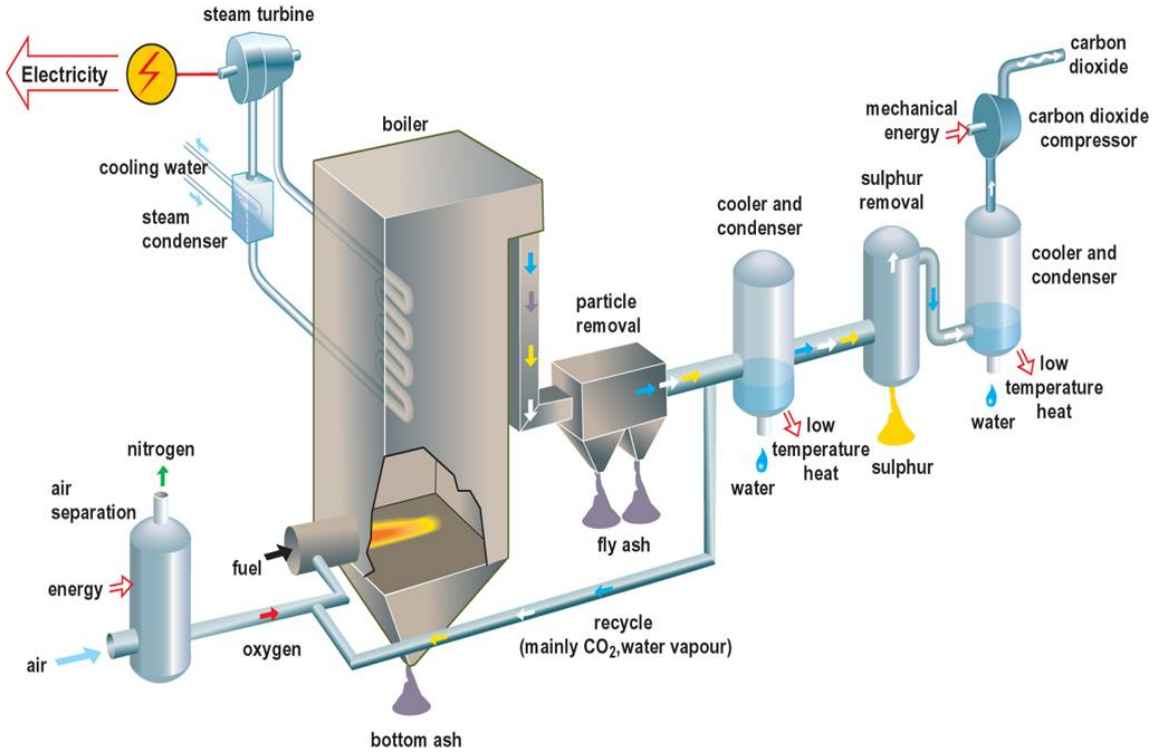

Figure 1.10 – Oxy-fuel combustion process (Vattenfall, 2008)

Further novel technologies are continuously being developed, an example being chemical looping combustion. This involves solid fuel being fed into a fuel reactor, where it comes into contact with a metal oxide known as an oxygen carrier. The fuel reactor is heated and the fuel/oxygen carrier mixture is fluidised with steam or recirculated flue gas; this causes the fuel to devolatilise, the char to be gasified and the subsequent gaseous mixture of H_2, CO and volatiles are oxidised by the oxygen carrier. Following this, the reduced oxygen carrier passes into the air reactor, where it is re-oxidised by air (Adanez, et al., 2018).

Carbon capture and storage technologies can also be used to capture CO_2 emissions from biomass combustion in order to create a negative emission technology (NET). These technologies are known by the umbrella term 'bio-energy carbon capture and storage' (BECCS) and are believed to be a key part of the effort to meet the Paris Climate Agreement obligations by making up for industries that will not be able to decarbonise without significant innovations, such as shipping and air travel. In addition to BECCS, direct air

capture (DAC) is another collection of carbon negative technologies, where CO_2 is scrubbed out of ambient air at atmospheric pressure. DAC is thought to require a large amount of energy, up to 12% of electric energy and 60% of non-electric energy by 2100, but can potentially be coupled with dedicated renewable power generation technologies to reduce operating costs (Creutzig, et al., 2019).

1.3 Nitrogen Oxides: A Noxious Problem

1.3.1 Origins and Impact

Nitrogen oxides, NO_x, refers to a group of pollutants arising from the oxidation of fuel-bound nitrogen or nitrogen in air during high temperature combustion, and contributing to a number of prominent environmental problems. Nitric oxide (NO) is likely to evolve from any combustion, where nitrogen is present, and will eventually oxidise to nitrogen dioxide (NO_2) when emitted to atmosphere. Nitrous oxide (N_2O) is most relevant in fluidised bed combustion systems due to the lower temperature combustion zones, but can be emitted from any combustion process, as well as chemical processes (Skalska, et al., 2010). In the UK, as of 2016, 34% of the total NO_x emissions came from road transport, while power generation was responsible for 22% and domestic and industrial combustion emitted 19% (DEFRA, 2019). From immediately after emission in the troposphere to migration into the stratosphere, NO_x is involved in complex processes of oxidation, reduction and photolysis that leads to the formation of transitionary highly reactive NO_y compounds (short-lived oxidised NO_x compounds, such as NO_3 and N_2O_5) (Figure 1.11). Subsequently, NO_x compounds play a role in all major air pollution crises, e.g. photochemical pollution (smog), acid rain, ozone depletion and, even, global warming, leading to up to 40000 deaths per year and an economic cost of £20 billion per year in the UK alone (Holgate, 2017).

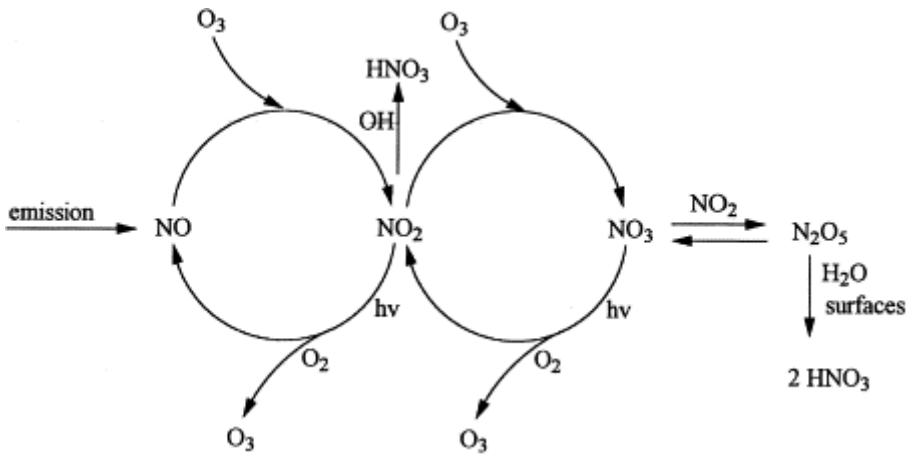

Figure 1.11 – Atmospheric NO_x chemistry (Atkinson, 2000)

The most notable NO_x associated process is that of photochemical pollution/smog. This process involves NO_2 catalysing the production of ozone (O_3), which is highly toxic due to its highly oxidising nature. In reaction (1-1), NO_2 is photolysed by daylight, producing NO and an oxygen radical that, subsequently, attacks an oxygen atom in reaction (1-2). Reaction (1-3) should complete the cycle, remove the O_3 and return the NO_2 and O_2; but the environments in which these processes occur also contains radicals originating from the incomplete combustion of hydrocarbons, such as peroxy and hydroperoxyl radicals, which can react with NO to reform NO_2, thus competing with reaction (1-3).

$$NO_2 + h\nu \rightarrow NO + O \quad (1\text{-}1)$$

$$O + O_2 + M \rightarrow O_3 + M \quad (1\text{-}2)$$

$$NO + O_3 \rightarrow NO_2 + O_2 \quad (1\text{-}3)$$

During the night, reaction (1-1) cannot occur and reaction (1-3) continues rapidly, resulting in virtually all NO_x being NO_2; NO_3 then starts to accumulate through reaction (1-4) and the lack of light to photolyse it after formation.

$$NO_2 + O_3 \rightarrow NO_3 + O_2 \quad (1\text{-}4)$$

The NO_3 can then react with NO_2 to form N_2O_5, which will readily dissolve in water to form nitric acid, hence contributing to acid rain.

$$NO_3 + NO_2 \rightarrow N_2O_5 \quad (1\text{-}5)$$

$$N_2O_5 + H_2O_{(l)} \rightarrow 2HNO_{3(l)} \quad (1\text{-}6)$$

The formation of HNO_3 is a chain termination reaction that leads to the consumption of the majority of the tropospheric NO and NO_2 within four days (Skalska, et al., 2010). However, some NO_x will migrate to the stratosphere, where it will catalyse the decomposition of ozone, as seen with reactions (1-3) and (1-7) with reaction (1-8) combining the two.

$$NO + O_3 \rightarrow NO_2 + O_2 \quad (1\text{-}3)$$

$$NO_2 + O \rightarrow NO + O_2 \quad (1\text{-}7)$$

$$O + O_3 \rightarrow 2O_2 \quad (1\text{-}8)$$

As mentioned, only a small amount of NO and NO_2 will reach the stratosphere; N_2O can act as a source of NO within the stratosphere as it is photolysed (reactions (1-9) and (1-10)) or attacked by an O radical (reactions (1-11) and (1-12)).

$$N_2O + hv \rightarrow NO + N \quad (1\text{-}9)$$

$$N_2O + hv \rightarrow N_2 + O \quad (1\text{-}10)$$

$$N_2O + O \rightarrow N_2 + O_2 \quad (1\text{-}11)$$

$$N_2O + O \rightarrow 2NO \quad (1\text{-}12)$$

In addition to N_2O participating in stratospheric ozone destruction, it is also known to be a greenhouse gas that is 270 times more potent than carbon dioxide (Wright, 2003).

1.3.2 Legislative Limits

The discussed issue caused by NO_x has led to increasingly stringent legislation around the world. The greatest users of coal for power generation are shown in Figure 1.12 to be the People's Republic of China (PRC), United States of America, India, European Union, Japan and Korea (IEA, 2019). The current legislative limits of NO_x emissions for these nations will be discussed.

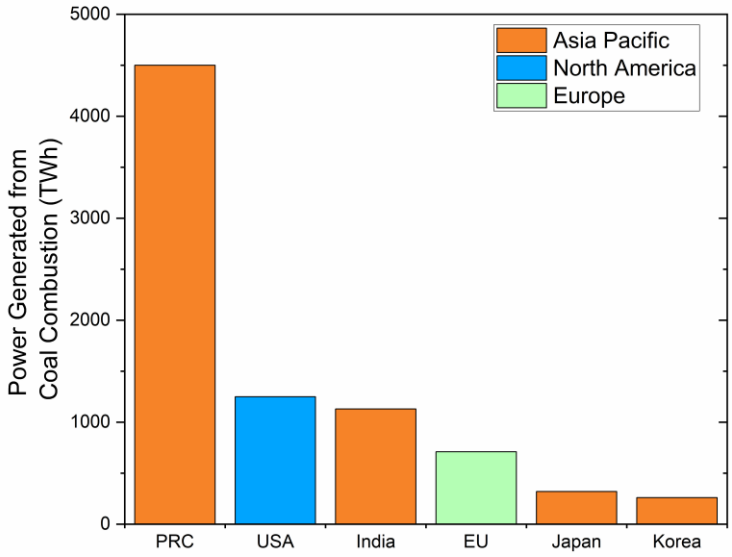

Figure 1.12 – Greatest users of coal for power generation

Starting with China, the NO_x emission limits depend on the capacity of the boiler and the location, with more stringent limits in conurbations. Being the largest user of coal, it is important that China leads the way with significant standards. These limits can be seen in Table 1.1.

Capacity (tonnes/hour)		NO_x limit (mg/m^3)
>65		100
10-65	Existing boilers	400
	New boilers	300
	Boilers located in key regions	200

Table 1.1 – Emission limit values (mg/m^3) for NO_x from utility coal-fired boilers in China (IEA Clean Coal Centre, 2015)

In the US, the emission limits are more complicated and depend heavily on when the plant was constructed or modified rather than the capacity of the plant. Further, the Clean Air Act states that these emission limits are merely a maximum level and that plants will be assessed on a case-by-case basis with the specific limit being decided by the best available control technology (BACT), which is decided from techno-economic analysis.

Period of construction/modification		NO_x Limit (mg/MW)
1971-1978		300
1978-1997		210 (subbituminous), 260 (other coals)
1978-2005		200 (gross output), 65 (heat input)
2005-2011	Construction	130 (gross output)
2005-2011	Reconstruction	130 (gross output), 47 (heat input)
2005-2011	Modified	180 (gross output), 65 (heat input)
Post-2011	Construction/reconstruction	88 (gross output), 98 (net output)
Post-2011	Modified	140 (gross output)

Table 1.2 – Emission limit values (mg/MW) for NO_x from utility coal plants in the USA (IEA Clean Coal Centre, 2019d)

India, a nation with chronic and severe air pollution issues, has adopted stringent emission limits for new coal-fired power plants, while older plants face some of the most lax limits of the major coal using nations.

Period of construction	NO_x Limit (mg/m^3)
Pre-2004	600
2004-2017	300
Post-2017	100

Table 1.3 – Emission limit values (mg/m^3) for NO_x from coal and lignite fired power plants in India (IEA Clean Coal Centre, 2019a)

The European Union's Industrial Emissions Directive (Directive 2010/75/EU) has mandated the following emission limits of NO_x in mg/Nm^3 (6% O_2) for solid fuels:

Total rated thermal input (MW)	NO_x Limit (mg/Nm^3)		
	Coal (except lignite)	Lignite	Biomass
50-100	300	400	250
100-300	200	200	200
> 300	150	200	150

Table 1.4 – Emission limit values (mg/Nm^3) for NO_x from large combustion plants using solid fuels in the EU

These values come with some caveats. Combustion plants of a thermal rating <500 MW built before 2003 are allowed to emit up to 450 mg/Nm^3, as long as they do not operate for more than 1500 hours per year. Similarly, combustion plants of a thermal rating >500 MW built before 1987 are subject to the same conditions. This is most likely to provide flexibility in extreme scenarios. The EU also legislated for medium combustion plants (1-50 MW) (Directive (EU) 2015/2193), with the following emission limits of NO_x in mg/Nm^3 (6% O_2) for solid fuels:

Total rated thermal input (MW)		NO_x Limit (mg/Nm^3)	
		Coal	Biomass
1-50	Existing plants	650	650
1-5	New plants	500	500
5-50	New Plants	300	300

Table 1.5 – Emission limit values (mg/Nm^3) for NO_x from medium combustion plants using solid fuels in the EU

Japan sets limits based on steam generation, rather than thermal rating, and, when converted to mg/m^3 using a simplistic conversion factor of ppm x 2.05, is rather more lax than the EU for the higher capacity units. That being said, individual prefectures in Japan regularly set stricter standards for emissions than the national limits.

Capacity (m^3/hr)	NO_x Limit (ppm)
>700,000	200
400,000-700,000	250
<400,000	300

Table 1.6 – Emission limit values (ppm) for NO_x from coal combustion boilers in Japan (IEA Clean Coal Centre, 2019b)

Korea leads the way with the most stringent NO_x emission limits of this group. The legislation is clear, concise and is likely to promote innovation and eliminate the contribution of power plants to the NO_x related issues raised in section 1.3.1. However, it will likely have been incredibly expensive to achieve these limits, which may have a negative impact on the plant economics, as well as the consumer, and could be used as a political tool to indirectly close coal power plants.

Capacity (MW)	NO_x Limit (ppm)		
	Pre-July 1996	July 1996-2014	Post-2014
<100	90	60	30
>100	70	50	15

Table 1.7 – Emission limit values (ppm) for NO_x from coal power plants in Korea (IEA Clean Coal Centre, 2019c)

The emission limits displayed in this section are likely to be the principal drivers behind innovations leading to the research and development of new and improved NO_x abatement technologies. The result of these innovations may be that the rising consumers of coal, such as South Africa, Indonesia and Poland, will not face the same economic trade-off between air quality and affordable power as their predecessors.

1.4 Fireside Corrosion: Eating Away at Profitability

Solid fuels contain many impurities in addition to nitrogen; in particular, sulphur, chlorine and mineral matter, known as ash, interact around the boiler to degrade components, reduce efficiencies, increase costs and, ultimately, cause outages. The principle ash related

problems are fireside corrosion, slagging and fouling. Fireside corrosion is the process of chemical attack reducing wall thickness of the heat transfer surfaces by acidic gases in the flue. Slagging refers to ash deposition on a heat transfer surface or the refractory, resulting from the sintering of molten ash components (Malmgrem and Riley, 2012). Fouling refers to deposits on a heat transfer surface by condensed volatile salts and fly ash at a temperature below its melting point (Bryers, 1996). Both slagging and fouling reduce the rate of heat transfer through the tube wall, resulting in reduced plant efficiencies and higher CO_2 emissions per unit of power, while also providing a reservoir of corrosive species to accelerate fireside corrosion.

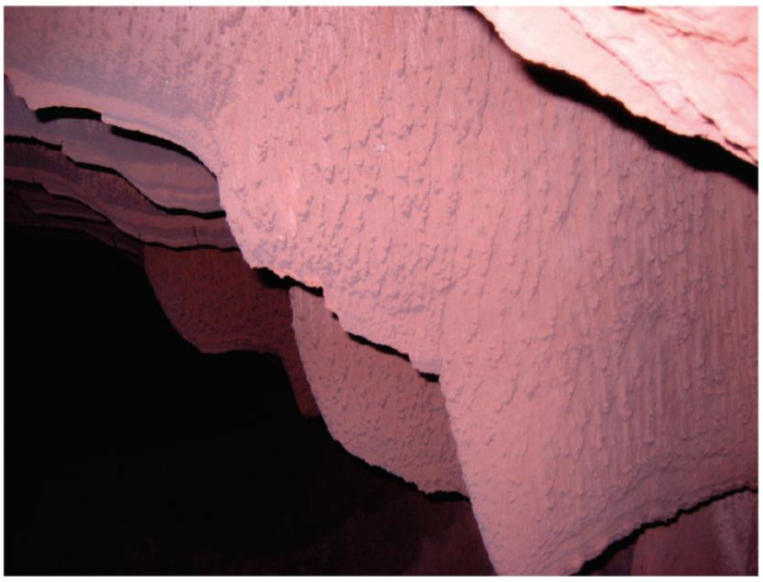

Figure 1.13 – Extreme slagging on superheater tubes (Niu, et al., 2010)

In a 2001 report, the Electric Power Research Institute (EPRI) estimated the cost of corrosion in American power plants during 1998 as $17.3 billion, which represents 7.9% of the cost of electricity to the US and 0.2% of the 1998 GDP (EPRI, 2001). They also estimated that 22% of this cost is avoidable through affordable measures (EPRI, 2001). Subsequently, some power generators have looked towards fuel additives to relieve their ash related problems; this is in conflict to reports suggesting that most commercial additives, other than kaolin and calcium based additives (for SO_2 removal in fluidised bed combustion) are ineffective (Minchener and McMullan, 2007, and European Commission, 1994). Nevertheless, Drax Power Ltd. filed a patent describing the use of a mitigant in order to reduce slagging, fouling and corrosion problems (Drax Power Ltd, 2014). Other additives,

such as one investigated by Daood, et al., (2017), have also been empirically shown to be able to mitigate corrosion, as well as reduce NO emissions and improve combustion.

1.5 Summary, Aims and Objectives

It has been discussed that coal combustion is an integral part of the world's power generation portfolio and, under current strategies, will remain so unless there is a dramatic change. This dramatic change is thought to be necessary in order to meet Paris Climate Agreement obligations, but the progression of carbon capture and storage technologies may open alternative routes to meeting these obligations. Nevertheless, coal combustion is responsible for much of the global NO_x emissions that can cause devastating environmental and health problems. In light of this, the principal users of coal for power generation have enacted stringent legislation, which will require significant uptake of effective NO_x abatement technologies or the closure of coal power plants. Fireside corrosion and other ash-related problems also significantly affect the life and economics of coal power plants and may be aggravated by the adoption of certain NO_x abatement technologies/strategies.

Thus, the aim of this thesis is to improve the confidence of clean coal power generation technologies so that the detrimental effects of the continued use of coal can be as little as possible. The following section will conduct a literature review, outlining the current status of, and gaps in, knowledge of the impact of important parameters for NO_x abatement in a variety of coal combustion configurations and, through this action, will identify the thesis's objectives.

CHAPTER 2 LITERATURE REVIEW

2.1 Introduction

This literature review will first describe the fundamentals of nitrogen chemistry within combustion, then discuss and critique primary NO_x abatement techniques along with a detailed analysis of the state of NO_x abatement within oxy-coal combustion. This will be followed by a review of secondary NO_x abatement techniques, namely SNCR and SCR, and an introduction to Fe-based additives. The impact of Fe-based additives on fireside corrosion will then require an understanding of the fundamentals of fireside corrosion and its precursors. Each of these sections will be concluded with a summary of the identified research gaps.

2.2 NO_x Production in PF Combustion and Primary NO_x Abatement Technologies

2.2.1 NO Production in PF Combustion

NO formation during combustion has been researched extensively, with three major mechanisms taking precedence:

- Thermal NO formation
- Prompt NO formation
- Fuel NO formation

Thermal NO formation, also known as the Zeldovich mechanism (Zeldovich, 1946), involves elemental nitrogen being oxidised by oxygen in the combustion flame. This mechanism occurs primarily through this sequence:

$$O + N_2 \leftrightarrow NO + N \quad (2\text{-}1)$$

$$N + O_2 \leftrightarrow NO + O \quad (2\text{-}2)$$

During fuel-rich conditions, reaction (2-3) becomes dominant and, together with the previous reactions, the entire mechanism is known as the extended Zeldovich mechanism.

$$N + OH \leftrightarrow NO + H \quad (2\text{-}3)$$

Due to the high activation energy of the first reaction (2-1), the mechanism only becomes significant at temperatures above 1800 K (van der Lans, et al., 1997). Low-NO_x burners are now widely used in commercial power plants, greatly reducing NO formation through the Zeldovich mechanism by lowering the flame temperature. However, thermal NO remains the greatest contributor to NO formation from natural gas combustion (Wünning and Wünning, 1997).

Prompt NO formation, also known as the Fenimore mechanism (Fenimore, 1971), was discovered when recorded NO formation rates from a hydrocarbon flame exceeded those predicted from thermal NO formation. This extra NO formation was found to be initiated through rapid attack of elemental nitrogen from CH radicals:

$$CH + N_2 \leftrightarrow HCN + N \qquad (2\text{-}4)$$

The HCN is then oxidised to produce NO. This mechanism can be dominant in fuel-rich hydrocarbon flames (Glarborg, et al., 1986), but is negligible in solid fuel systems; even when the solid fuel contains a large low-N volatile component (Glarborg, et al., 2003).

The most important source of NO from pulverised coal is that produced from fuel nitrogen; roughly 80% of NO produced from solid fuels is produced via conversion of fuel nitrogen to NO (Glarborg, et al, 2003). The dominance of fuel-NO production can lead to a drop in thermal-NO production due to the reversibility of the reaction (2-1) (Glarborg, et al., 2003). On initiation of pulverised coal combustion, devolatilisation of the coal particle occurs and the fuel nitrogen is partitioned into volatile-N and char-N, the distribution of which can be dependent upon the fuel structure, temperature and the rank of the coal (Bassilakis, et al., 1993). The relative conversion of volatile-N and char-N to NO is vastly different.

Char-N, nitrogen bound inside/to the fuel matrix, has been found to exclusively convert to NO during combustion within a temperature range of 1050-1150 °C, while only 65% of char-N converts to NO at 850 °C; this lower net NO formation was found to be due to reduction of NO by reaction with char (Jensen, et al., 2000). However, Pohl and Sarofim (1977) found that at 1500 K, 60-80% of NO is formed from oxidation of volatile-N. Therefore, it is imperative to have an understanding of the complexities of volatile-N oxidation.

Volatile-N consists of tar-N and light gaseous compounds, such as HCN and NH_3. The tar-N, produced during primary devolatilisation, consists of fragments of the coal matrix that have vaporised during initial heating and is defined by Glarborg, et al., (2003) as 'the volatiles released that condense at room temperature'; this contains almost all of the initial nitrogen released (Zhang and Fletcher, 2001). While secondary devolatilisation leads to the release of the light gaseous compounds from decomposing char and tar, the remaining tar-N is incorporated into soot (Chen, et al., 1992), this soot-N is further oxidised to NO (Rigby, et al, 2001).

The most important volatile-N constituents are HCN and NH_3, both of which have been found to undergo complex reaction pathways oxidising selectively towards N_2 or NO depending on oxygen availability and fuel-nitrogen levels (Glarborg, et al., 2003). The reaction pathways have been extensively investigated and overview of the reactions are shown in Figure 2.1 below:

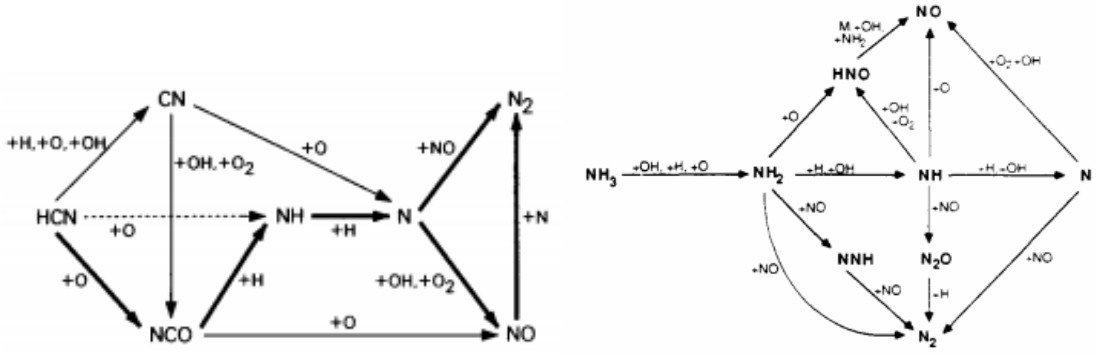

Figure 2.1 – HCN and NH_3 evolution pathways (Miller, et al., 1985)

These pathways give the opportunity for engineers to design modifications to the combustion conditions to favour the pathways leading to N_2 formation.

2.2.2 Low-NO_x Burners and Other Primary NO_x Abatement Technologies

Low-NO_x burners (LNBs) are a combustion modification technique that involves staging of the combustion; LNBs can be either air-staged or fuel-staged. Air-staged LNBs operate to maximise volatile release, provide an initial O_2 deficient zone, maximise char residence time in this zone and then provide a fuel-lean zone to maximise burnout. The lack of oxygen in the fuel-rich zone favours the N_2 formation pathways for volatile-N (Figure 2.1) and goes further to reduce NO formed elsewhere to N_2 (Hill and Smoot, 2000). The control of air-

fuel mixing patterns is achieved by swirling secondary and tertiary air to stabilise the fuel-rich zone and complete combustion in a cooler environment (due to the sub-stoichiometric conditions); this also enables a lower flame temperature and, therefore, limited thermal-NO production (Muzio and Quartucy, 1997). The structure of zones within the low-NO_x burner is shown in Figure 2.2:

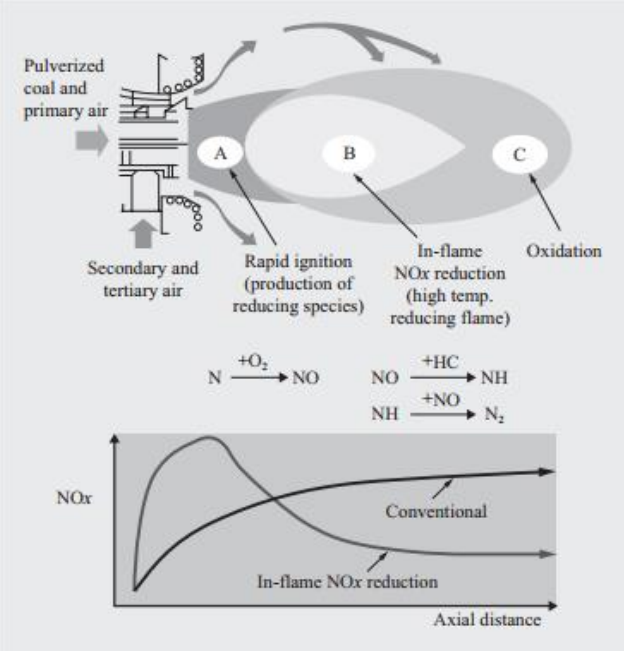

Figure 2.2 – Low-NO_x burner concept (Ochi, et al., 2009)

Doosan Power Systems has had success with the Mk III burner (Doosan Babcock, 2020), which involves staging the oxidant (usually air) input into three streams. The primary stream entrains the fuel and provides the initial oxygen, the secondary stream is heavily swirled in order to create an inner recirculation zone at the centre of the flame and the tertiary zone enters with comparatively less swirl to complete char combustion and create an external recirculation zone at the edge of the flame. The inner recirculation zone (IRZ) has the effect of maintaining the devolatilization process and primary combustion products in an oxygen deficient environment for as long as possible, as well as recirculating these products and heat. This results in maximising devolatilisation and the activity of volatile-N to N_2 formation pathways (Szuhánszki, 2014), while the external recirculation zone (ERZ) helps stabilise the flame by recycling hot combustion gas back into the flame root (Smart and Morgan, 1992). The shear boundary layer between the IRZ and the secondary stream acts to introduce oxygen in the IRZ to initiate the completion of combustion.

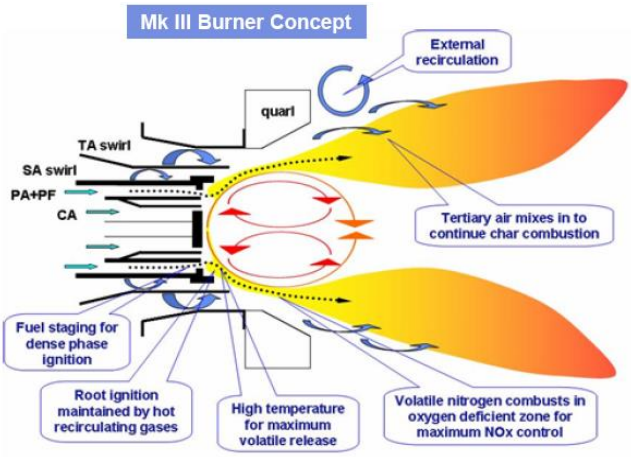

Figure 2.3 – Doosan Mk III Burner (Doosan Babcock, 2015)

The above burner will most likely create a type-2 flame. The IFRF (2006) defined four types of flame. A type-0 flame is essentially a swirled jet flame with just external recirculation zones that is only seen with gaseous and liquid fuels. A type-1 flame contains greater swirl and is accompanied by the formation of internal recirculation zones but it is still penetrated by a jet; this can be achieved with any fuel. A type-2 flame contains an even stronger swirl and the internal recirculation zones are more protected due to the lack of jet penetration. A type-3 flame is considered unusual; it contains the most swirl and has two sets of inner recirculation zones.

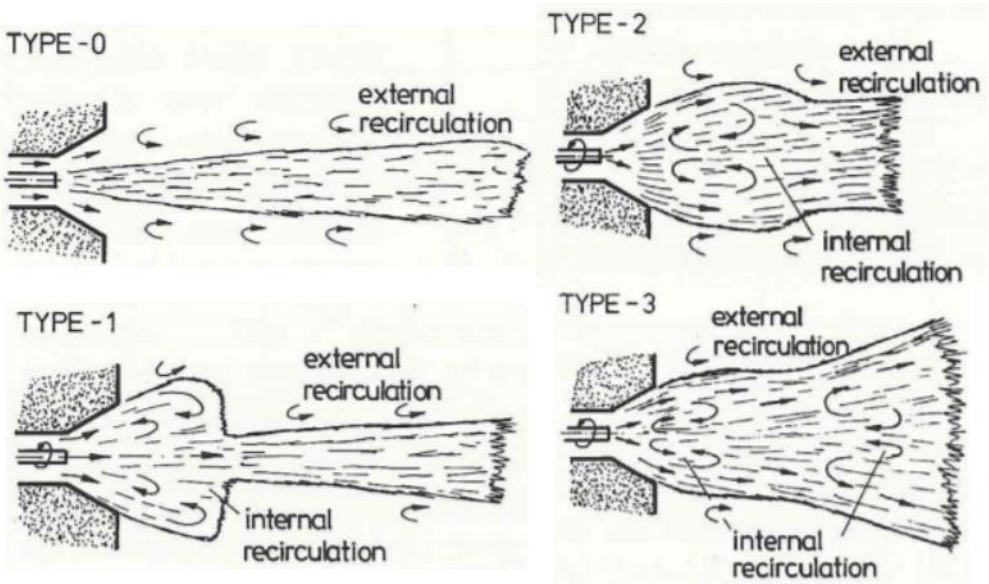

Figure 2.4 – Flame types as defined by the IFRF (IFRF, 2006)

Another popular air staging method is known as overfire air (OFA). Similar to LNBs, OFA involves creating a fuel-rich primary combustion zone and a fuel-lean lower temperature

secondary combustion zone (Javed, et al., 2007); but OFA involves injecting a portion of the combustion air (10-25%) above the upper most burner (Skalska, et al., 2010). This can lead to 10-30% reduction in NO emissions (with an average reduction of 23%) at a cost of 5-15 $/kW (with an average cost of 8.2 $/kW) (Nelson, et al., 1994). Unfortunately, like LNBs, OFA has been found to lead to a diminished combustion efficiency (Smart, et al., 1989) due to the decreased stoichiometry in the primary combustion zone. This can also lead to an extreme reducing atmosphere, which will lead to increased corrosion (USEPA, 1994). Further to this, the primary zone created during air staging is highly reducing and can lead to high temperature corrosion and slagging in the vicinity of the burner (Ma, et al., 2017).

The most studied fuel staging technique is reburning; this involves burning 80-90% of the fuel under fuel-lean conditions in the primary combustion zone and introducing the remaining fuel in a fuel-rich zone known as the reburn zone. This reburn zone is heavily reducing due to incomplete combustion generating hydrocarbon radicals, which reduce NO formed in the primary zone (Nimmo and Liu, 2010).

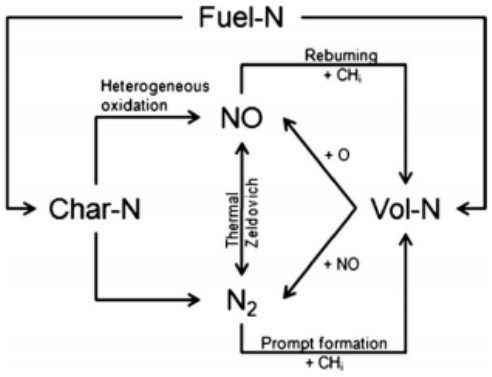

Figure 2.5 – Reburning mechanism (Toftegaard, et al., 2010)

A third zone called the burnout zone then introduces the remaining air to complete burnout of hydrocarbons and char. Liu, et al., (1997) reported that, when testing a variety of coals, up to 60% NO_x reduction could be achieved when there is a high NO concentration in the primary zone, high carbon burnout in the reburn zone and high volatile-N release in the reburn zone. However, it can prove beneficial to NO_x reduction to use a different fuel for reburning, for example, Mereb and Wendt (1994) compared the use of natural gas and bituminous coal as reburn fuels to find that natural gas offered ~80% NO_x reduction compared to ~60% for bituminous coal.

In order to increase NO_x reduction from reburning, research has been undertaken into variation of reburning known as advanced reburning. This hybrid technology combines reburning and selective non-catalytic reduction (SNCR) (discussed further in 2.4.1) so that ammonia/urea is added in the fuel-rich reburning zone or the overfire air (Maly, et al., 1999) to provide up to 80-90% NO_x reduction compared to classic reburning, which can provide 45-65% (Zamansky, et al., 1996). Maly, et al., (1999) achieved a 95% NO_x reduction when the reducing agent was combined with a sodium containing additive; they went on to claim that this technology was in the same category as selective catalytic reduction (SCR) (discussed further in Section 2.4.2) for effectiveness but with a far lower cost. The operating temperature for this technology would not be optimal for conventional SNCR, but, due to the sub-stoichiometric conditions upstream, there is a large concentration of CO, which expands the operating temperature window for reduction (Hampartsoumian, et al., 2003). Major complications due to reburning are avoided with advanced reburning. Hampartsoumian, et al., (2003) found that with advanced reburning, lower reburn fuel fractions can be used. This means that the reburn zone can be operated closer to stoichiometric conditions, and thus practical consequences of a fuel-rich zone can be avoided.

2.2.3 Flue Gas Recirculation and Oxy-coal Combustion

Flue gas recirculation (FGR) involves redirecting a small portion of flue gas into the combustion zone; the high concentration of inerts in the flue gas has the effect of lowering the adiabatic flame temperature, which in turn helps reduce thermal-NO formation but has been said to have little effect on fuel-NO (Muzio and Quartucy, 1997). The lower temperature flue gas leads to a decreased furnace temperature; this can cause less stable combustion and lower combustion efficiency (Zhang, et al., 2015). Muzio and Quartucy (1997) describe tests on boilers using combinations of BOOS (burners out of service), OFA and FGR. These tests found that FGR can provide NO_x reductions of up to 45%; but they comment that this is a technique more applicable to natural gas configurations. Baltasar, et al., (1997) found that FGR is especially good at disrupting the prompt NO formation mechanism; since these mechanisms are insignificant in coal, Muzio and Quartucy's recommendation is appropriate.

However, this process can be considered operationally inherent in oxy-fuel combustion; a process that is cited as being one of the most promising carbon capture techniques. Oxy-fuel combustion involves combusting fuel using an O_2/flue gas mixture instead of air, creating a flue gas in which there is a far larger CO_2 concentration than air-fired combustion (14% vol/vol dry). The flue gas is scrubbed to remove NO_x, SO_2 and particulates and then cooled to remove water vapour (Toftegaard, et al., 2010). Further purification of the flue gas to remove O_2, N_2 and Ar creates a 96-98% pure CO_2 stream that is ready for sequestration (Li, et al., 2009); this amounts to a capture of 90-95% of the carbon dioxide produced from combustion (Pehnt and Henkel, 2009). Oxy-fuel combustion provides a carbon capture process with simpler and cheaper CO_2 purification compared to the other conventional capture processes. It also provides higher boiler efficiency due to smaller flue gas volumes and less required NO_x abatement, due to reduced thermal-NO formation (Varagani, et al., 2005).

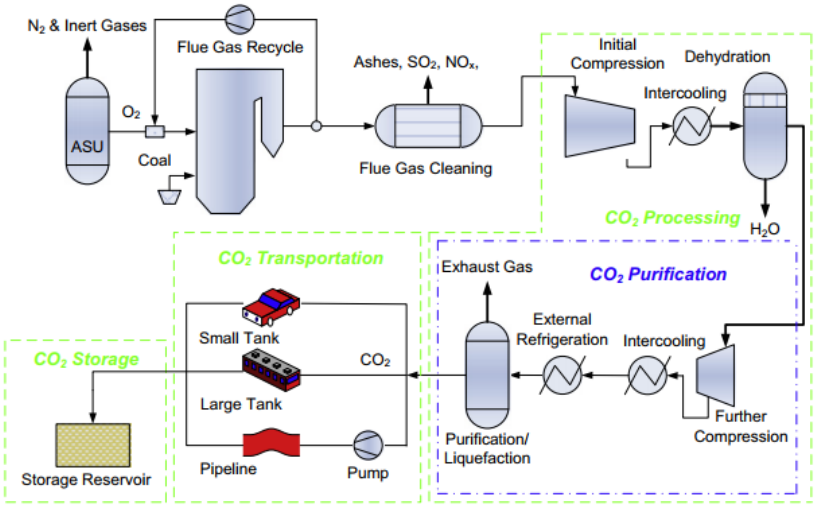

Figure 2.6 – Typical oxy-fuel combustion plant design (Li, et al., 2009)

However, a major complication with oxy-fuel combustion involves the value of the adiabatic flame temperature when compared to air-fired combustion. The O_2/CO_2 mixture has a higher specific heat capacity compared to air; this results in a decreased adiabatic flame temperature and a destabilised flame if the oxygen concentration is 21% (analogous to air) (Liu, et al., 2005a). In order to mimic the flame temperature observed during air-fired combustion and therefore operate using developed burners, the oxygen concentration must be around or above 30% (Liu, et al., 2005a). Although, this high level of oxygen is thought to enhance the fuel NO_x formation mechanisms (Tan, et al., 2006).

One would expect that NO_x emissions from oxy-fuel combustion to be comparable to the air case flue gas recirculation scenario without any thermal-NO or prompt-NO formation, due to the lack of nitrogen, and with the extra fuel-NO, but this is not the case. Andersson, et al., (2008) found that when run with an oxy-fuel configuration, NO emissions (mg/MW) were reduced to less than 30% of emissions from air-firing.

One could expect the impact of recirculating a flue gas with a significant level of NO to initiate processes similar to the reburning mechanisms, processes which reduce NO through the use of fuel fragments as reducing agents. Toftegaard, et al., (2010) defined three types of reaction that contribute to the reduction of NO through reburning:

The reaction with volatile-C, released during devolatilisation of the coal, to form volatile-N.

$$CH_i + NO \rightarrow HCN + products \qquad (2\text{-}5)$$

The reaction with volatile-N, released during devolatilisation of the coal, to form N_2.

$$NH_i + NO \rightarrow N_2 + products \qquad (2\text{-}6)$$

The reaction with coal char, in the presence of CO, to form N_2.

$$CO + C_{(O)} \rightarrow CO_2 + C_{(f)} \qquad (2\text{-}7)$$

$$NO + C_{(f)} \rightarrow C_{(O)} + \frac{1}{2}N_2 \qquad (2\text{-}8)$$

Where $C_{(O)}$ represents oxygen chemisorbed to char and $C_{(f)}$ represents an activated carbon site on the char (Chan, et al, 1983).

Okazaki and Ando (1997) investigated the impact of each of these mechanisms as well as the increased CO_2 concentration on the final NO_x concentration. The effect of the increased CO_2 concentration is used to test NO reduction on char under the assumption that at high CO_2 concentrations, the CO concentration will be increased and this will enhance NO_x reduction on char. They found that the increased CO_2 led char reactions accounted for less than 10% of the NO_x reduction while NO reactions with volatile-C account for 50-80% of NO_x reduction and the remaining 10-50% is caused by NO reactions with volatile-N. Andersson, et al., (2008) show that at high temperatures (>1500 °C) during oxy-fuel combustion it is possible for the Zeldovich mechanism to be reversed due to the lack of

nitrogen. However, Normann, et al., (2008) show that for the reverse Zeldovich mechanism to be dominant, there must be negligible air ingress, high oxygen purity, sub-stoichiometric combustion conditions, long residence time and high temperatures (>1800 °C); although the temperature must also decrease with NO_x concentration through the flame.

Operation of an oxy-fuel burner will present inevitable variations in the flame structure and mixing of the fuel and oxidiser (Toftegaard, et al., 2010). The comparable lack of secondary oxidiser flow leads to limited O_2 availability and a higher adiabatic flame temperature, promoting conversion of volatile-N to N_2 and aiding NO_x reduction (Mackrory, et al., 2007). The lack of secondary oxidiser, however, is an issue and arises from the requirement for an O_2 concentration of ~30% as this leads to a smaller volumetric flow rate through the burner. If future oxy-fuel plants are to be commissioned from old air-fired plants, then the coal feed rate must remain constant; this requires the same primary oxidant velocity in order to keep the coal in suspension (Zanganeh and Shafeen, 2007). Since the density of the O_2/CO_2 mixture is greater than that of air, the mass flow rate of the primary flow for oxy-fuel is higher and the secondary mass flow rate is reduced; this leads to a reduced velocity for the secondary flow (Khare, et al., 2008). In the average burner, the secondary flow is swirled to aid stability of the flame; if there is a slower secondary flow, there is less swirl and therefore the flame is less stable. In order to correct issues regarding stability of oxy-fuel flames in burners designed for air-fired use, NO_x reduction may have to be compromised.

In order to maximise NO reduction without significantly affecting the flow dynamics, Liu, et al., (2005b) studied the impact of staging recycled NO_x in oxy-fuel flames. This study showed that injecting recycled NO in either the primary or the secondary stream will provide high reduction (~90%); however, if the NO is recycled in the tertiary stream then the reduction is severely reduced (~45%). This is due to the lack of fuel-rich zones, to initiate the reburning mechanisms, in the tertiary zone. Staging NO_x introduction into an oxy-fuel flame may not be feasible, since commercial plants will likely not split the recirculated flue gas into its constituent parts due to cost impacts; therefore, attention must be paid instead, to burner configuration. Chui, et al., (2003) showed that increasing the swirl number of the secondary stream in an oxy-fuel burner leads to a reduction in NO_x production (~37% reduction); they said that the swirl has the ability of retaining the fuel-N

within the fuel-rich zone to maximise N_2 formation, therefore preventing fuel-N oxidation in the burnout zone. This study, however, found that more NO_x is produced when their burner was run on an oxy-fuel configuration. An enhanced burner was tested in Chui, et al., (2004) and notable NO_x reductions were achieved; however, the trends and configurations used to achieve these reductions were said to be very explicit to the burners tested and general recommendations are lacking (Toftegaard, et al., 2010).

In Spinti and Pershing's 2003 study on char-N oxidation in air-fired flames, they identify four factors that influence overall NO emissions. These are the volatile-N oxidation, char-N/volatile-N split, char-N oxidation and reduction of volatile-N during char oxidation. A burner designed for low NO_x emissions must manipulate these factors; this can be done by providing a fuel-rich core to minimise volatile-N oxidation, high temperatures during devolatilisation for maximum volatile formation and a low temperature char oxidation zone with a low oxygen concentration (Spinti and Pershing, 2003). These assertions concur with Hesselmann and Marta's (2001) recommendations that included: creating an initial oxygen-lean/fuel-rich zone early in the flame, maximising volatile yield within this zone, optimising the residence time in this zone, maximising char-N residence time in this zone and avoiding high temperature peaks.

In contrast to the established belief that oxy-coal combustion requires an oxygen concentration of 30%, Toporov, et al., (2008) investigated an oxy-fuel burner designed to run at 21% O_2. They found that the flame could be stabilised in both air and oxy-fuel regimes using swirl to recirculate hot combustion products (~1200 °C) back to the burner in order to compensate for higher specific heat capacity of the oxidant. The NO concentration was measured axially across the flame and compared to predictions from a numerical model but no optimisation took place to maximise NO_x reduction. The experimental results also deviated from the predictions indicating issues with the models used. Becher, et al., (2007) also tested a burner working away from the 30% recommendation; this burner was run using 50% O_2 with the aim to reduce the required flue gas recirculation in order to reduce energy and cost intensity. The flame temperature was then controlled by staging fuel input, either using over-stoichiometric and then under-stoichiometric burners or vice versa. This shows promise in NO reduction by creating strong reducing atmospheres; however, NO reduction was not investigated. Tan, et al., (2006)

recommended that in order to maximise NO_x reduction in oxy-fuel processes, the burner should be specifically designed for O_2 and recirculated flue gas. Doosan Power Systems successfully demonstrated an oxy-coal burner achieving low NO_x (250 mg/Nm^3) flue gas concentrations in air and flame stability during oxy-fuel configuration; but unfortunately the NO_x and CO emissions were twice as high (Sturgeon, et al., 2013). However, installing an oxy-coal burner may not be economically feasible for those looking to retrofit to oxy-fuel due to the cost of the burner and costs associated with installing SCR to meet NO_x limits.

In light of this, Fry, et al., (2011) established some principles for retrofitting air-coal burners for use during oxy-coal combustion. They found that maintaining primary mass flow-rate or momentum when switching from air-firing to oxy-firing would maintain a stable flame, whereas, maintaining primary velocity would lead to slight detachment. Interestingly, this study also found that the primary stream could consist of purely recirculated flue gas and still achieve a stable flame, which could greatly impact the char/volatile split in the fuel-rich zone. However, this analysis was performed merely in terms of changes in the visual structure and radiation intensity along the flame length, and no principles in terms of minimising NO_x emissions were presented.

Correa da Silva, et al., (2014) investigated an industrial burner forming a type-1 flame finding that swirl and secondary/tertiary flow ratio were the key attributes to stabilising an oxy-fired flame and that limits to stability were similar for both air-fired and oxy-fired flames. Further studies of this burner go on to show that high swirl and secondary/tertiary ratio also result in substantial NO reduction (Correa da Silva and Krautz, 2014). In-flame measurements showed that NO formation was axially delayed in oxy-fired flames due to reduced mixing of oxygen into the penetrating jet and the presence of high temperature oxygen-lean regions (Correa da Silva and Krautz, 2018). Detailed emission analysis was also performed on another burner at 21 vol% and 25 vol% O_2 and a fixed swirl highlighting trends between increasing O_2 utilisation and decreased NO formation (Hees, et al., 2016). Although these studies perform detailed analysis of swirling flames and confirm the significant impact of increasing swirl on a reduction in NO formation, there is very little discussion of any impact on the destruction rates of recycled NO or reburning. It should also be mentioned that the investigation into altering the secondary/tertiary ratio showed

that type-1 oxy-fired flames are less impacted by this than air-fired flames, perhaps highlighting that type-1 flames are not as easily optimised and type-2 oxy-fired flames should have the same level of scrutiny.

In-furnace staging was previously discussed in the context of overfire air, creating a reducing (fuel-rich) zone initially around the burner and then introducing overfire air in an oxidising zone to complete combustion. This concept has been studied for use in oxy-coal combustion to show that the fuel-rich zones cause far greater NO reduction in oxy-combustion than in air and the NO concentration in the flue gas shows less sensitivity to the reducing zone stoichiometry than air (Mackrory and Tree, 2012). Further to this, it is believed that staged combustion in an O_2/CO_2 environment would lead to a significant reduction in NO_x emissions (Wantanabe, et al., 2011). However, the issue with in-furnace staging is that NO_x, from the recirculated flue gas, would be present in all streams and injecting a portion of it downstream would potentially decrease NO_x reduction rate (Toftegaard, et al., 2012).

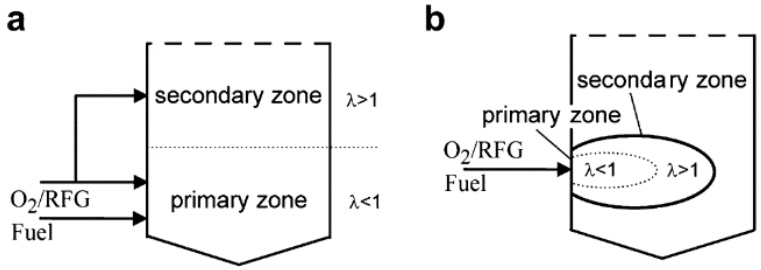

Figure 2.7 – Diagrams of (a) in-furnace staging and (b) burner staging (adapted from Normann, et al., 2009)

2.2.4 Summary of Gaps in the Research

Section 2.2.1 introduced how NO evolves during pulverised coal combustion, with particular attention to the processes involved with fuel-NO. It was then discussed how these processes can be manipulated towards the nitrogen production pathways by primary NO_x abatement technologies. Finally, the carbon capture process oxy-fuel combustion was discussed due to its inherent use of flue gas recirculation and the attributed phenomena of NO reburning that only significantly occurs during oxy-coal combustion. There is great discussion around oxy-coal flame stability, but sometimes this leads to a compromise with regards to NO emissions.

However, there appears to be an opportunity with oxy-coal flames with regards to minimising NO formation and maximising NO reburning in that, due to the lack of nitrogen, the reducing zones are far more reducing and, due to the comparably reduced mass flow rates, an oxy-coal flame's swirl is different to that of air flames. Minimising NO formation is not often a primary objective, while maximising NO reburning is seldom discussed. An effort should be made to marry the two concepts whilst maintaining flame stability, so that a flame is visibly still rooted and burnout is not compromised. This could prove important in that an operator could minimise the NO concentration at the input of a SCR unit, thus minimising the operational capacity and hence, the cost of the unit, which would aid the appearance of financial feasibility for this technology.

2.3 Fe Interactions with NO

Hayhurst and Lawrence's study (1997) showed that the presence of iron oxides in a fluidised bed led to an 80% reduction in NO emissions. The mechanism was initiated by the reduction of Fe_2O_3 by CO. The subsequent Fe ions were then oxidised by NO to produce N_2 and regenerate the Fe_2O_3. Therefore, the iron catalyses and increases the selectivity of the reduction of NO by CO.

$$3CO + Fe_2O_3 \rightarrow 3CO_2 + 2Fe \qquad (2\text{-}9)$$

$$2Fe + 3NO \rightarrow \frac{3}{2}N_2 + Fe_2O_3 \qquad (2\text{-}10)$$

Lissianski, et al., (2001a) investigated the technique of injecting iron additives into the combustion zone and reburning zone of a down-fired burner. The iron additives of interest were described as Fe metal, Fe waste, Fe_2O_3 and Fe_3O_4. When the additives were co-injected with the reburning fuel, each additive showed the tendency to increase the NO_x reduction compared to reburning without any additives. The order of increasing effectiveness, when reburning was set at 18%, was: Fe_3O_4 (4% increase), Fe metal (6%), Fe waste (13%) then Fe_2O_3 (16%). Whereas, when reburning was set at 35%, the order of increasing effectiveness was: Fe metal (6% increase), Fe_3O_4 (9%), Fe waste (19%) then Fe_2O_3 (20%). Fe_2O_3 was tested in a variety of injection locations, including: co-injection with the main fuel, co-injection with the reburning fuel and injection into the reburning zone. The highest NO_x reduction was observed when Fe_2O_3 was injected with the reburning fuel; whereas the smallest increase in NO_x reduction was observed when Fe_2O_3 was injected into

the reburning zone. The latter is probably due to the greater degree of mixing that is achieved when injected with the fuel; while the former is probably due to the sub-stoichiometric conditions caused by the reburning fuel in the reburning zone, leading to higher concentrations of CO than in the main combustion zone. This is confirmed in Lasek (2014), where they investigated Fe-related NO_x reduction in fuel-lean and fuel-rich environments. It was found that NO_x reduction is far higher in fuel-rich atmospheres and the presence of oxygen slightly inhibits Fe NO_x reduction mechanisms. The presence of high levels of CO_2 in the fuel-rich zones has been found to have no effect on the rate of NO destruction (Gradon and Lasek, 2010).

In a separate study, Lissianski, et al., (2001b) studied the effect of injecting Na, K and Ca containing additives and fly ash on NO_x reduction and combustion when injected into the main fuel, the reburning fuel or the reburning zone. They found that when the additives were injected into the main fuel, there was a reduction in NO_x emissions regardless of whether reburning was also used; the order of effectiveness being Na, K then Ca. When the additives were injected into the reburning fuel, there was still NO_x reduction but this was smaller; a similar effect was noted for fly ash addition to the reburning fuel. The Ca additives also had the notable effect of reducing the SO_2 emissions by 50% when included in the main fuel. Modelling showed that the NO_x reduction observed when using Na-based additives was due to inhibition of the local combustion environment. The authors, however, concluded that iron containing additives provided far more effective NO_x reduction.

Fennell and Hayhurst (2002) studied the kinetics of the NO reduction reaction in the presence of iron. Using their detailed rate expressions, they described a possible mechanism involving NO dissociating while adsorbed onto Fe_2O_3. The adsorbed N atoms either re-associate with O atoms or combine with other adsorbed N atoms to produce N_2, leaving the O atoms to diffuse into the Fe_2O_3 matrix. However, Reddy and Khanna (2004) detailed a different mechanism, where the initial step involves a CO or NO adsorbing to the Fe_2O_3. This process weakens the O-Fe bonds leading to a CO being oxidised at one of the O atoms; this reduces the Fe_2O_3 to Fe_2O_2. NO then oxidises the reduced Fe_2O_2, forming N_2 in the process.

Fe has also been found to have a significant effect on coal pyrolysis. In Yan, et al., (2005), they investigated the effect of inherent minerals on coal pyrolysis. Demineralisation of the coal was found to inhibit conversion of char to volatiles, therefore decreasing nitrogen formation. Fe was found to be the most important mineral for NH_3 formation and decreasing char-N yield, therefore promoting N_2 formation instead of NO. Tsubouchi and Ohtsuka (2008) confirm that Fe has a catalytic role in not only NH_3 formation, but also the secondary decomposition of tar-N, NH_3 and HCN to N_2, as well as the conversion of char-N to N_2.

Sowa and Fletcher (2011) attempted to take advantage of the effect of Fe on coal pyrolysis by investigating the effect of an Fe-based additive in a pulverised coal burner. A coal was treated with two different loadings of the Fe-based catalyst to produce the treated coals KYT1 and KYT2; KYT2 has roughly twice as much catalyst loading as KYT1. Both of the treated coals were found to lead to a substantially increased volatile yield compared to the untreated coal; precisely a 37% and 49% increase in volatile yield for KYT1 and KYT2 respectively. When char oxidation was observed, KYT2 was found to display a 47% increase in char reactivity, while KYT1 only displayed an increase of 5% compared to untreated coal.

Daood, et al., (2014a) investigated a commercialised fuel additive technology consisting of iron, aluminium, calcium and silicon on both a pilot scale 100 kW_{th} down-fired combustion test facility and a full-scale commercial 260 tons/hr boiler. The effect of this additive on coal pyrolysis led to an increase in flame temperature of 12-30 °C, which led to a 1-5% increase in combustion efficiency. This, in turn, led to a decrease in the carbon content of the fly ash. In Daood, et al., (2014b), they explain that this is due to the additive's finer particle size and greater heat transfer properties, causing heavy hydrocarbons in the coal matrix to break down into lighter hydrocarbons. This is shown in Figure 2.8:

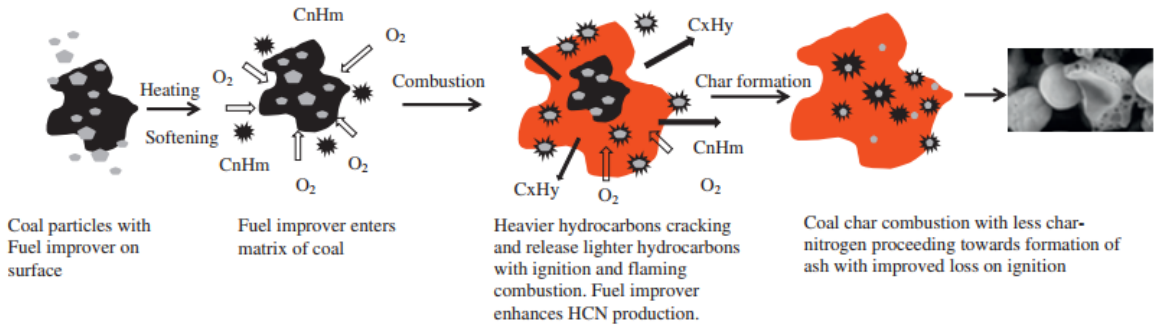

Figure 2.8 – Effect of additive on coal pyrolysis and char/volatile split (Daood, et al., 2014b)

This impact on coal pyrolysis has the same effect with fuel-N evolution; greater volatile-N release increases the rate of N_2 formation over NO formation. The increased volatile-N formation and the interaction between NO and Fe led to an observed 25% NO reduction (Daood, et al., 2014a).

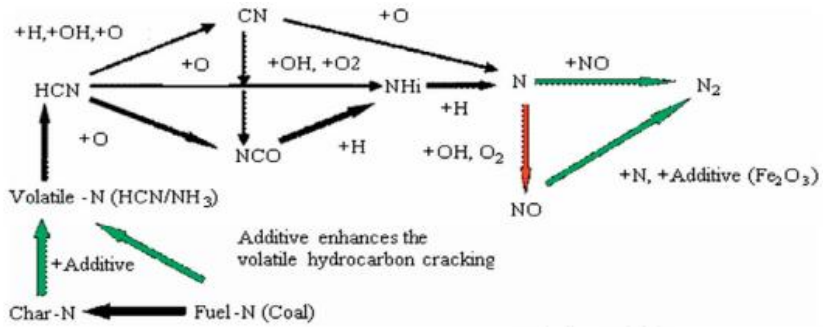

Figure 2.9 – Effect of additive on fuel-N evolution (Daood, et al., 2014a)

2.4 Post-Combustion NO_x Abatement

2.4.1 Selective Non-Catalytic Reduction

Alternative approaches to reduce NO_x emissions involve installing technologies post combustion. The two most common post-combustion techniques are selective non-catalytic reduction (SNCR) and selective catalytic reduction (SCR). Selective non-catalytic reduction involves the addition of typically ammonia, urea or cyanuric acid at a suitable temperature where NH_3 will selectively react with NO. In the mid-1970s, first tests showed that ammonia or urea would react with NO to produce N_2 (Lyon and Longwell, 1976) (Muzio, et al., 1977). However, if the temperature was too high (>1000 °C) then the reagent would be oxidised by O_2, and NO emissions would increase but if the temperature was too low (<800 °C), then the reagent would not react at all, resulting in ammonia slippage (Lyon and Longwell, 1976). Javed, et al., (2007) gives a summary of the mechanism investigated in detail by several researchers. The mechanism is initiated by ammonia reacting with hydroxyl radicals:

$$NH_3 + OH \leftrightarrow NH_2 + H_2O \qquad (2\text{-}11)$$

Alternatively, if there is a lack of OH radicals (possibly due to a lack of water vapour), the amidogen (NH_2) radical can be formed by ammonia reacting with an oxygen atom:

$$NH_3 + O \leftrightarrow NH_2 + OH \qquad (2\text{-}12)$$

The creation of amidogen radicals is critical as they selectively react with NO:

$$NH_2 + NO \leftrightarrow N_2 + H_2O \quad (2\text{-}13)$$

$$NH_2 + NO \leftrightarrow NNH + OH \quad (2\text{-}14)$$

However, the creation of amidogen radicals depends on OH and O concentrations. Therefore, for this mechanism to be self-sustaining, OH and O must be regenerated through chain reactions. The NNH radical from reaction (2-14) is key to making this mechanism self-sustaining through chain branching reactions:

$$NNH + NO \leftrightarrow N_2 + HNO \quad (2\text{-}15)$$

$$HNO + M \leftrightarrow H + NO + M \quad (2\text{-}16)$$

The H atom then reacts with oxygen:

$$H + O_2 \leftrightarrow OH + O \quad (2\text{-}17)$$

The O atom produced can then be used in reaction (2-12) or can react with water:

$$O + H_2O \leftrightarrow OH + OH \quad (2\text{-}18)$$

Therefore, assuming water vapour is present, reaction (2-11) will be dominant over reaction (2-12), reactions (2-13) and (2-14) proceed and four hydroxyl radicals will be produced for every two consumed and the mechanism is self-sustaining.

Javed, et al., (2007) then goes on to explain the vital effect of the previously mentioned temperature variation on the reaction mechanism and how the optimal temperature range is where we see a balance between chain branching and termination reactions. At temperatures below the optimal range, reactions (2-17) and (2-18) slow down, HNO radicals stop being consumed as the concentration of H atoms increases and chain termination reactions (2-13), (2-19) and (2-20) start to compete with the chain branching reactions. This has the effect of consuming amidogen and hydroxyl radicals and creating further NO.

$$NH_2 + HNO \leftrightarrow NO + NH_3 \quad (2\text{-}19)$$

$$OH + HNO \leftrightarrow H_2O + NO \quad (2\text{-}20)$$

As the hydroxyl radicals are ultimately depleted, ammonia will start to pass through the reactor unreacted and the ammonia slip that is inherent below the optimal temperature window will be observed.

During the optimal temperature window, the selective amidogen oxidation reactions (2-13) and (2-14) are dominant over the non-selective amidogen reactions (2-21) and (2-22).

$$NH_2 + OH \leftrightarrow NH + H_2O \quad (2\text{-}21)$$

$$NH_2 + NH_2 \leftrightarrow NH_3 + NH \quad (2\text{-}22)$$

The aforementioned balance of chain branching and chain termination reactions is active so that enough hydroxyl radicals are created to sustain the chain reaction. This is in part due to reaction (2-16) becoming dominant over reaction (2-20), leading to hydrogen atoms to react in reactions (2-17) or (2-23).

$$H + H_2O \leftrightarrow OH + H_2 \quad (2\text{-}23)$$

Above the temperature window, the rate of hydroxyl formation reactions (2-17) and (2-18) increases, leading to an increase in the concentration of hydroxyl radicals. This, in turn, leads to increased reaction rate for reaction (2-21) leading to NH formation, which, when oxidised, leads to NO formation. The HNO formed in reactions (2-24) and (2-25) is converted to NO by reaction (2-20).

$$NH + O_2 \leftrightarrow HNO + O \quad (2\text{-}24)$$

$$NH + OH \leftrightarrow HNO + H \quad (2\text{-}25)$$

$$NH + O_2 \leftrightarrow OH + NO \quad (2\text{-}26)$$

The amount of NO formed through this sequence will equal the amount destroyed at a temperature of around 1230 °C (Javed, et al., 2007).

The kinetic modelling of ammonia based SNCR is well developed and reported (Glarborg, et al., 2018), largely due to the reliance on H/N/O chemistry developed for larger combustion modelling needs. The greatest developments, and also uncertainty, in the model comes from the role of NNH in nitrogen chemistry, with Klippenstein, et al., (2011) recently decreasing the NNH lifetime significantly compared to the established works of Miller and Bowman (1989) and Konnov, et al., (2000).

The focus of many researchers' studies has been to try to maximise the NO_x reduction during SNCR. It could be assumed that increasing the ammonia input would lead to more NO_x reduction by pushing reaction (2-11) in the forward direction. However, early studies by Muzio, et al., (1977) revealed that at a temperature of ~1240 K the maximum NO reduction is achieved when the ratio between added ammonia and initial NO concentration reaches 2 and when further ammonia is added, ammonia slip increases dramatically (Lodder and Lefers, 1985) and the NO reduction remains constant. They also found that the initial NO concentration has a great effect on the NO reduction; when the initial NO concentration is 1050 ppm, an 80% reduction in NO is seen at a NH_3/NO ratio of 1, compared to only 40% when the initial NO concentration is 100 ppm. The NH_3/NO ratio can be compared to urea usage by using a normalised stoichiometric ratio (NSR) which takes into account the number of amidogens produced by the reagent, i.e. a urea/NO ratio of 0.5 is equivalent to an NSR of 1 and a NH_3/NO ratio of 1 (Javed, et al., 2007).

Lyon and Hardy (1986) discuss a phenomenon, discovered by Lyon and Benn (1979), named the self-inhibition effect that leads to limited NO reduction at high ammonia input levels. They state that the process described by reactions (2-11)-(2-18) produces 1.6 NH_2 radicals per NH_2 consumed. When the ammonia input is high enough that the ammonia concentration in the reaction zone is nearing the oxygen concentration, then the following reaction becomes active:

$$H + NH_3 \leftrightarrow NH_2 + H_2 \qquad (2\text{-}27)$$

Lyon and Hardy (1986) state that reaction (2-27) will start to compete with reaction (2-17), reducing the number of hydroxyl radicals and oxygen atoms in the system and causing only 0.8 NH_2 radicals to be produced for every one consumed. In this case, NH_2 is produced in alternative slower reactions:

$$NH_3 + O_2 \leftrightarrow NH_2 + HO_2 \qquad (2\text{-}28)$$

$$HO_2 + H \leftrightarrow OH + OH \qquad (2\text{-}29)$$

This results in the NO reduction being delayed and a longer than usual residence time being required. Lyon and Benn (1979) claim that the NH_3 concentration, required for the self-inhibition effect, increases with O_2 content in the flue gas, temperature and reduction time. In Muzio, et al., (1977), they found that the reaction sequence was completed in 200 ms,

therefore measurements in a standard high NH_3 study are likely to find disparaging results. However, this is of little concern as the cost of running a high NH_3 SNCR system would be infeasible to many operators.

Among published results for maximum NO reduction through SNCR, there is a distinct discrepancy between tests depending on the system in which the tests were taking place. In Muzio, et al., (1977), for example, tests were conducted using a plug flow combustion tunnel fired with natural gas with a flue gas containing 300 ppm NO, and they achieved ~80% NO reduction at 1240 K and NH_3/NO ratio of 1. However, in Muzio, et al., (1979) a larger combustion facility was used producing a flue gas containing 500 ppm. When gas fired, this led to a decreased NO reduction of ~65% at a similar temperature (~1200 K) and the same ratio NH_3/NO. In Muzio, et al., (1977), they report that a higher initial NO concentration leads to a greater NO reduction; therefore, the NO reduction in the later test should be greater. This situation highlights how engineering parameters, such as the dimensions of the reactor vessel and reagent flowrate, can lead to changes in mixing conditions and therefore different SNCR performances.

In Lee, et al., (2008), they state the lack of information on effects of mixing conditions to SNCR performance as motive for their research. They find that to achieve the highest NO reduction, the NH_3 must be premixed with the NO containing gas prior to entry to the reactor; this leads to a uniformly distributed mixture of NO and NH_3. This is simply not a feasible situation in an operational environment and so the NH_3 must be injected downstream of the burner. Lee, et al., (2008) then tested a range of injection flow rates (10-500 mL/min) with four NSRs (1-4) and three initial NO conditions (100, 300, 500 ppm). The conditions of interest are NSRs 1 and 2 at an initial NO of 500 ppm. At a NSR of 1, the increasing injection flow rate leads to an increased NO reduction (up to 20%). However, at a NSR of 2, the NO reduction increases (from 35% to 50%) with injection flow rate until the optimum is reached at 100 mL/min; past this point, NO reduction decreases slightly to 45%. This was caused by the higher injection flow rate allowing some of the NH_3 to escape the reactor before reacting. Nevertheless, this study highlights the importance of a degree of turbulence in the reacting section of a furnace to improve reduction efficiency. This study also attempted to gain some insight regarding the influence of momentum ratio (J), which they describe as a correlation between injected fluid and bulk gas (Lee, et al., 2008). They

found an ideal range of 8-130. This is in contrast to an earlier study on mixing by Østberg, et al., (1997) that says the ideal range is 20-30.

In this study by Østberg, et al., (1997), they also contrast the use of air and nitrogen as carriers for the ammonia. They conclude that the absence of oxygen from the carrier gas has a negligible effect on NO reduction, but that the presence of O_2 in the flue gas is vital to SNCR performance. In a study by Irons, et al., (1991), oxygen content in the flue gas was varied between 1-5 % for tests at 908 °C and 1000 °C. They showed that at 1000 °C there is little change in SNCR performance when oxygen is varied but at 908 °C there is a substantial variation; however, between 3-4%, which is the standard oxygen content in a coal-fired flue gas, there is very little change in SNCR performance. If an operator were to consider altering the process so that there is more oxygen in the flue gas, this would negatively affect the plant efficiency due to a cooler flue gas.

Wenli, et al., (1989) investigated the impact of varied water vapour addition in the flue gas. Three addition concentrations were investigated: 0%, 2.7% and 10%. When 2.7% was added, SNCR performance was increased and the optimum temperature range was widened. When 10% was added, SNCR performance was increased compared to the 0% condition but had decreased compared to 2.7%; also, the optimum temperature range had shifted up slightly. Therefore, it may prove worthwhile to consider adding water vapour if an operator is working at the upper end of the temperature range.

Researchers have tried to influence the performance parameters of SNCR using process additives; the majority of which are reducing agents that would theoretically reduce NO in a non-selective process. This idea may have grown from early attempts to explain the kinetics of the SNCR reactions such as in Wendt, et al., (1973). In this study, methane and ammonia are compared as reburning fuels for the reduction of sulphur trioxide and nitric oxide; they suggested that the high NO reduction seen with the addition of ammonia was due to reduction from hydrogen produced by ammonia pyrolysing on the stainless steel wall. Lyon (1975) debunked this and claimed they had merely achieved non-selective reduction; nevertheless, hydrogen was tested as a process additive in this patent and was said to reduce the optimum temperature range by ~170 °C. This is later proved in Lyon and Hardy (1986), where they show that with an increasing addition of hydrogen decreases and slightly narrows the optimum temperature range. This addition of hydrogen increases the

rate of temperature dependent reaction (2-17) causing more hydroxyl radicals to be produced and, therefore, more NH_2 radicals to be produced. At temperatures below the standard optimum range, enough hydroxyl radicals are created to proceed with the SNCR mechanism. At temperatures around the standard optimum, too many hydroxyl radicals are being created and reaction (2-21) becomes competitive leading to NO formation.

Azuhata, et al., (1982) investigated another method to influence SNCR performance through increasing hydroxyl radical formation; this time through addition of hydrogen peroxide. Hydrogen peroxide would decompose upon heating into two hydroxyl radicals. Similar to the use of hydrogen, the primary impact of this additive is reducing the optimum temperature range by ~300 °C. However, a secondary consequence was also noted; this was the formation of NO_2, which has an obvious negative effect on the overall NO_x reduction. Nitrogen dioxide is thought to be produced through the following mechanism (Azuhata, et al., 1982):

$$H_2O_2 + OH \leftrightarrow H_2O + HO_2 \qquad (2\text{-}30)$$

$$HO_2 + NO \leftrightarrow NO_2 + OH \qquad (2\text{-}31)$$

Azuhata, et al., (1982) then hypothesised that the NO_2 would oxidise NH_2 radicals to both create more NO and inhibit the NO destruction mechanism. While Miller and Bowman (1989) state that NO_2 could be attacked by hydrogen or oxygen atoms to form NO.

Wenli, et al., (1991) tested a range of combustible additives, including a range of alkanes, alcohols and amines, to find that every additive had the effect of reducing the optimum temperature range. The amines, when used in conjunction with ammonia, also decreased the width of the temperature range. When used alone, the two amines had drastically different performances. CH_3NH_2 produced a slightly less NO reduction with a lower temperature range, when compared with ammonia. $(CH_2NH_2)_2$ produced a greatly decreased NO reduction with a much lower and wider compared to ammonia.

Banna and Branch (1981) noticed that carbon monoxide levels increased when ammonia was added in the SNCR configuration, indicating that the oxidation of CO is inhibited by ammonia. While testing the effect of CO injection on SNCR performance, Lodder and Lefers (1985) confirmed this and found that CO injection reduced the optimum temperature window by 150-200 K. The presence of extra CO was also shown to accelerate both NO

reduction and NO formation, through NH_3 oxidation, reactions; hence, decreasing the selectivity of ammonia. Lyon and Hardy (1986) provided an explanation for these effects. The oxidation of CO involves the following reaction:

$$CO + OH \leftrightarrow CO_2 + H \qquad (2\text{-}32)$$

The inhibited oxidation of CO was due to competition for OH radicals from ammonia. When CO was introduced in large quantities, more H atoms were produced and, therefore, reactions (2-17) and (2-18) were accelerated, forming more OH radicals and O atoms. However, a greater concentration of O atoms then led to a NH forming reaction:

$$NH_2 + O \leftrightarrow NH + OH \qquad (2\text{-}33)$$

Therefore, the introduction of CO led to the acceleration of NH_2 formation but the decrease in the selectivity of these radicals.

Further studies to improve SNCR performance involve the addition of metal additives that simulate an increased content of a specific mineral in the combusted coal. Hao, et al., (2015) tested the effect of sodium (NaCl and Na_2CO_3) and potassium (KCl) based additives, as well as fly ash addition, on SNCR performance. They found that these additives slightly increased NO reduction without the use of fly ash, but when fly ash is used in conjunction with the additives then a more substantial reduction was achieved. When only fly ash is used, there is a significant decrease in NO reduction. However, these tests were conducted using a quartz reactor and fly ash from a circulating fluidised bed combustor; therefore, any observations made from these tests are likely to differ substantially when tests are done on a pilot or industrial scale, as these would be conducted in a steel furnace the surface of which being able to catalyse ammonia reactions. Furthermore, fly ash from pulverised coal combustion would be formed at a higher temperature than during fluidised bed combustion and so the phase composition of the ash could be substantially different. Zamansky, et al., (1999) also studied the effect of sodium species on the SNCR process. By adding small amounts of sodium containing salts to the reducing agent, the SNCR temperature window was broadened and NO reduction was improved. When the amount of injected sodium was increased, there was a reduction in the observed promotion effect. Han and Lu (2007) conducted a kinetic study on the use of Na_2CO_3 during SNCR, finding that the increased performance was the net result of sodium species encouraging

conversion of H_2O and HO_2 to OH radicals. A further study by Guo, et al., (2012) set up a detailed model to investigate the effects of KOH and NaOH on the SNCR mechanism. This found that both these additives extended the temperature window by 100 K down by providing an alternative source of OH radicals.

Li, et al., (2010) tested the effect of using of CaO on SNCR performance at low temperatures (650-850 °C). They observed a catalytic effect on NH_3 decomposition, NH_3 oxidation and NO reduction, with an overall impact of increasing NO emissions through NH_3 oxidation. They also tested the effect of using $CaCO_3$ by maintaining a high CO_2 concentration in the reaction vessel. This proved to lead to less NH_3 oxidation but greater NH_3 decomposition; therefore, the overall impact was less NO produced than when using CaO but more than without additives. Further confirmation of the inhibitory effect of $CaCO_3$ on SNCR was published (Fu, et al., 2015) along with a mechanism and kinetic model detailing this phenomenon. The impact of sulphated CaO on SNCR was also investigated in order to design a process that combines SNCR with dry flue gas desulphurisation (Li, et al., 2010). The results confirmed that sulphated CaO had a catalytic effect on NO reduction by NH_3, however the study does not consider the effect of CO_2 or H_2O on the reaction mechanism and concedes that the un-sulphated CaO will catalyse NH_3 oxidation, as is confirmed elsewhere (Sun, et al., 2017).

Fu, et al., (2014) conducted a detailed study into the use of pure Fe_2O_3 during SNCR, including an experimental investigation and the construction of a kinetic model used to discuss the relationships between Fe_2O_3, NH_3 and NO. To study the impact on the SNCR mechanism, they measured NO and NH_3 emissions over temperatures ranging from 973 K to 1373 K when they injected 500 ppm NH_3, 500 ppm NO and 2% O_2 (balanced with N_2) through a fixed bed of 10 mg of Fe_2O_3. They found that NH_3 was increasingly catalytically oxidised to NO until the temperature reached 1173 K (the start of the SNCR temperature window), from this point NH_3 oxidation diminished but the presence of Fe_2O_3 was clearly inhibitory. In the absence of NO or O_2, NH_3 was found to be catalytically reduced to N_2 and H_2. However, when O_2 was added and NO remained absent, the NO concentration rose, displaying the catalytic oxidation of NH_3. When O_2 was absent, there was a slight catalytic activity increasing NO reduction by NH_3. The kinetic model fit sufficiently with the experimental results, although this model was heavily simplified so that a few reaction rate

constants were used to represent the entire complicated H/N/O mechanism. It should also be noted that the reacting atmosphere was chosen to mirror calcination and does not include CO_2 or water vapour, which could produce radicals that would greatly impact the SNCR mechanism.

2.4.2 Selective Catalytic Reduction

The idea of attempting to catalyse NO reduction is mature, and selective catalytic reduction is an established technology. SCR is said to be the most popular NO_x reduction technology due to its applicability in both power stations and automobiles and high NO_x reduction potential (60-85%) (Bosch and Janssen, 1988); however, SCR is accompanied by larger costs than any other NO_x abatement technique due to the high costs of the catalysts involved (McCahey, et al., 1999). SCR requires temperatures to be 400-850 K depending on the catalyst used (Gomez-Garcia, et al., 2005) and so is usually situated between the boiler and the electro-static precipitator (removing dust and particulate matter). However, SCR catalysts are liable to poisoning from dust and SO_2; therefore, SCR can be situated in other operational positions to prolong catalyst life. The other operational positions require the temperature of the flue gas to be raised in order to increase SCR performance, therefore requiring an increase in operational costs and power plant efficiency loss. Figure 2.10 shows the potential operational positions of SCR in an oxy-fired coal power plant:

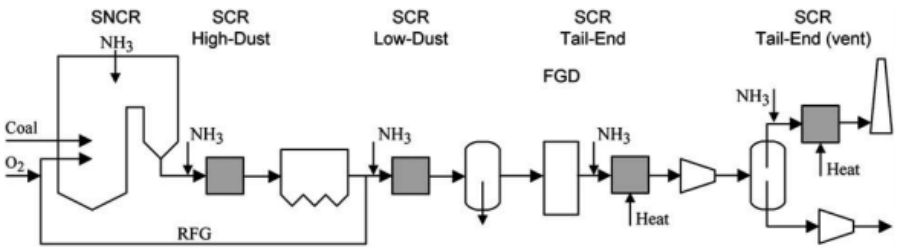

Figure 2.10 – Possible operational positions of SCR (Normann, et al., 2009)

In the presence of a catalyst, NSR~1 and T<400 °C, NO and NO_2 are reduced in the following reactions (Busca, et al., 1998, Parvulescu, et al., 1998):

$$4NH_3 + 4NO + O_2 \leftrightarrow 4N_2 + 6H_2O \quad (2\text{-}34)$$

$$4NH_3 + 6NO \leftrightarrow 5N_2 + 6H_2O \quad (2\text{-}35)$$

$$4NH_3 + 2NO_2 + O_2 \leftrightarrow 3N_2 + 6H_2O \quad (2\text{-}36)$$

$$8NH_3 + 6NO_2 \leftrightarrow 7N_2 + 12H_2O \qquad (2\text{-}37)$$

However, non-selective reactions can become competitive upon unfavourable conditions, such as temperatures above the temperature range of the catalyst:

$$2NH_3 + \frac{3}{2}O_2 \leftrightarrow N_2 + 3H_2O \qquad (2\text{-}38)$$

$$2NH_3 + 2O_2 \leftrightarrow N_2O + 3H_2O \qquad (2\text{-}39)$$

$$2NH_3 + \frac{5}{2}O_2 \leftrightarrow 2NO + 3H_2O \qquad (2\text{-}40)$$

Reaction (2-38), although undesirable in the context of NO reduction, is of interest to researchers due to the opportunity to reduce ammonia slip from SCR reactors; this has been called selective catalytic oxidation of ammonia (SCO) (Busca, et al., 1998).

Catalysts for SCR can be broadly divided into three groups: supported metal oxides, metal ion exchanged zeolites or supported noble metal. Figure 2.11 shows the operational variation between these groups of catalysts and the theoretical NO_x reduction of each group with respect to the operational temperature range. Figure 2.11 particularly highlights that the noble metals are generally unfavourable due to their vast limitations.

Operating characteristics of different SCR catalysts

Medium temperature – VNX™ catalyst (V_2O_5/TiO_2)
- 500–800°F (260–425°C)
- most broadly used
- 10–15 years of experience
- sulfur tolerant

High temperature – ZNX™ catalysts (zeolite)
- 650–1100°F (345–590°C)
- very high NO_x conversion
- very low NH_3 slip
- NH_3 destruction
- sulfur tolerant above 800°F (425°C)

Low temperature – LT catalyst (Pt-based)
- 300–520°F (150–300°C)
- narrow temperature window
- temperature window shifts
- not sulfur tolerant

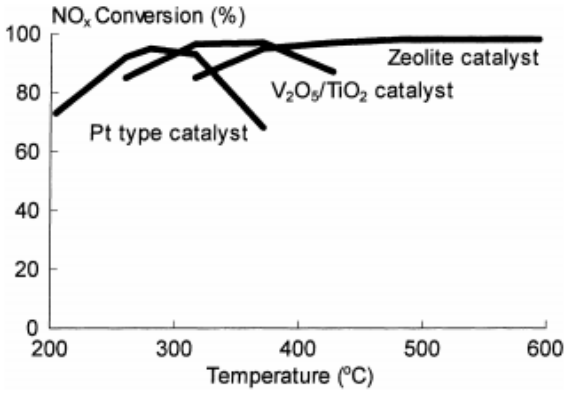

Figure 2.11 – Operating characteristics and ideal temperature ranges for popular SCR catalysts for popular SCR catalysts (Heck, 1999)

Commercial catalysts are typically of the supported metal oxide group consisting of an active component, usually V_2O_5-WO_3 or V_2O_5-MoO_3, layered on a support, usually TiO_2. The vanadium oxide provides the majority of the active sites for ammonia sorption, while tungsten oxide and molybdenum oxide increase the selectivity and activity of the catalyst.

The popularity of titanium oxide as the support is due to its resistance to sulfation and the effect of increasing catalyst activity (Busca, et al., 1998). Topsøe, et al., (1998) described the SCR mechanism as starting with NH_3 adsorption to a Brønsted acid site on the V^{5+}-OH. This ammonia is then 'activated' when an H atom is transferred to a V^{5+}=O site. NO is then reduced forming nitrogen and water and reforming the vanadium-based active sites. This is shown graphically in Figure 2.12:

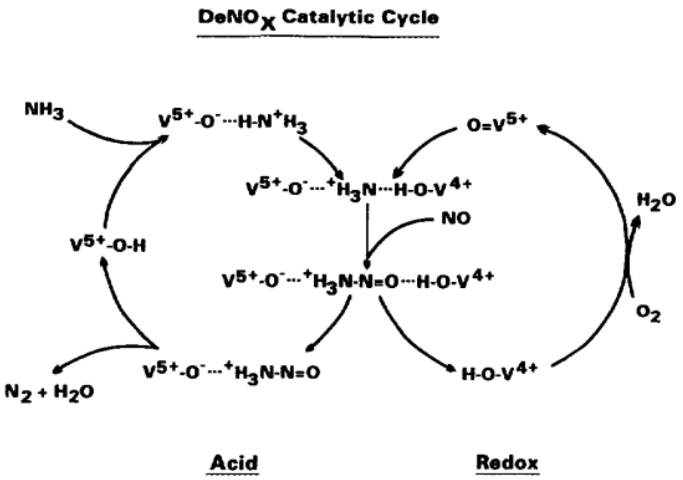

Figure 2.12 – $DeNO_x$ catalytic cycle (Topsøe, et al., 1995)

Due to concerns regarding the toxicity and low melting point of vanadium oxide, as well as the tendency to oxidise SO_2, which can be less easy to remove by flue gas desulphurisation, and produce N_2O at high temperatures, researchers have continued to develop and investigate new catalysts. Researching for high temperature SCR, zeolite based catalysts have been investigated. Zeolites are aluminosilicate lattices consisting of channels containing cations; these are activated through ion exchange with a solution whose cation is required for catalysis (Weitkamp, 2000). Preparation of a zeolite remains to be optimised; for example, Qi and Yang (2005) found that the Fe-ZSM-5 prepared by incipient wetness impregnation showed higher NO reduction (up to ~95%) than traditional Fe-ZSM-5 prepared by ion exchange (up to 90%). This catalyst also showed higher NO reduction when compared to a V_2O_5-WO_3 catalyst across the tested temperature range (300-500 °C), as opposed to the Fe-ZSM-5 prepared though aqueous ion exchange, which only showed a higher NO reduction at temperatures above 350 °C. The preparation method to produce higher catalyst activity was shown to be the two step method. They suggested that this

was because the ion exchange was incomplete from the one step method and some of the $FeCl_2$ was oxidised to Fe_2O_3 during the calcination in air; whereas the two step method used helium first, which inhibited any oxidation. However, they concluded that the Fe_2O_3 also contributed to the high activity of the catalyst.

Apostlescu, et al., (2005) tested a catalyst comprising of ZrO_2 coated with Fe_2O_3 and WO_3, developed to reduce NO_x from the exhaust of diesel engines, from which they found a 100% reduction in NO at 350 °C. They concluded that the zirconium oxide support is a more effective support than those previously tested. The use of tungsten with Fe_2O_3 increased both the catalyst activity and the thermal stability. They reported that the active sites were mainly found on Fe_2O_3, where an Eley-Rideal mechanism is initiated when the ammonia partially reduces the iron to form an amide species. These amides are highly reactive and react with the NO to form nitrogen and water. The partially reduced iron is then oxidised by oxygen to reactivate them. This Eley-Rideal mechanism can be seen in Figure 2.13:

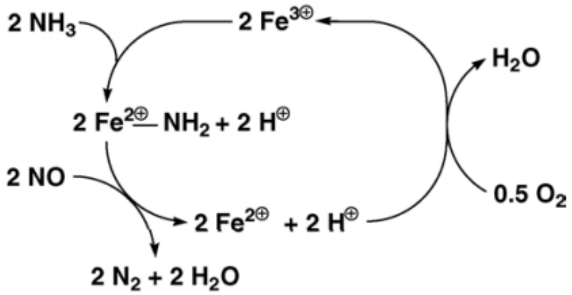

Figure 2.13 – Catalytic NO reduction mechanism for iron oxide (Apostolescu, et al., 2005)

In an effort to reduce costs associated with SCR, Gullett, et al., (1994) presented a pilot scale test combining the use SNCR with SCR in a hybrid technology. This hybrid technology involved injecting urea at an appropriate position within the furnace to achieve the primary NO_x reduction, then the remaining NO_x and ammonia slip would pass downstream to a vanadium-titanium SCR, where ammonia slip was reduced to >3 ppm and total NO_x reduction was increased to 85%. This study showed the opportunity to use higher NSRs during SNCR without fear of an unsuitable ammonia slip and to reduce the size (and, therefore, cost) of the SCR catalyst without compromising NO_x reduction. Urbas and Boyle (1998) performed tests on a utility boiler using a commercial hybrid SNCR/SCR technology; they increased reducing agent addition to the existing SNCR above normal operating conditions to induce an ammonia slip, which was then reduced in the new SCR. They

modelled the reduction in SCR catalyst volume based on desired overall reduction and maximum possible reduction from the SNCR in Figure 2.14:

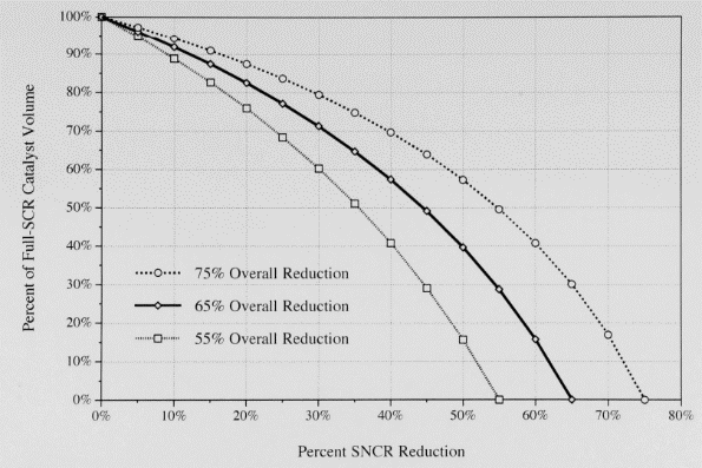

Figure 2.14 – Optimisation of hybrid SNCR/SCR (Urbas and Boyle, 1998)

Further successful experimentation and modelling of hybrid SNCR/SCR was achieved by Wendt, et al., (2001). However, this study found that this technology may not be as economically viable as previously claimed. Indications from their coal utility environmental cost model showed that the hybrid technology only becomes economical when SCNR is able to achieve over 60% NO_x reduction, which is highly difficult to achieve in practice due to mixing limitations. Therefore, for a system in which both high NO_x reduction (>95 %) and low ammonia slip (<5 ppm) is required, there was found to be little economic benefit in installing the hybrid technology over just SCR.

2.4.3 Summary of Gaps in the Research

As shown in section 2.3, there is a wealth of research into the in-flame benefits of utilising iron derivatives during pulverised combustion that gives some legitimacy to the idea of using them in industry, provided it is economically feasible for individual applications. Section 2.4.1 discussed the technology selective non-catalytic reduction as a post-combustion NO_x abatement technology. It was shown how the trend in research of this technology is surrounding a desire to improve NO reduction, shift/expand the temperature window and improve ammonia utilisation efficiency (to minimise ammonia slip/emissions), although not much progress to this intent has been made.

Instead, the focus has been on making selective catalytic reduction, the alternative technology, more economical and resilient. To this purpose, novel catalysts and a wide

range of catalyst supports were investigated. A common thread in these studies was the ability of iron to interact with ammonia, either in a zeolite structure or in addition to vanadia. This raises a question about whether an iron additive, used for its in-flame benefits, would interact with ammonia within the furnace, if selective non-catalytic reduction were to be used. One study explored this possibility to find a slight negative impact, however, as discussed, several concerns about the methodology and the accompanying kinetic modelling can be raised and the applicability of the results to pulverised coal furnace can be significantly doubted. Therefore, this remains an avenue that requires pilot-scale investigation and comprehensive kinetic modelling.

2.5 Fireside Corrosion in PF boilers

2.5.1 Fireside Corrosion Processes

Impurities in coal and high operating temperatures within PF boilers lead to mechanisms such as fireside corrosion, slagging and fouling, all of which shorten the lifespan of boiler tube walls. Fireside corrosion is defined as 'corrosion of tubes due to chemical attack occurring on the furnace or fireside of heat exchanging surfaces in fossil fuel-fired furnaces' (Harb and Smith, 1990). While slagging and fouling are phenomena that involve ash deposition on tube walls. These processes are caused by the presence in significant quantity of the inorganic elements shown in Figure 2.15 (Bryers, 1996):

	Element	Bituminous	Subbituminous	Lignite	Oil and Pet Coke	Refuse
Slag forming fluxing agents for aluminosilicates	Si	S		S		
	Al	S		S		
	Fe	S		S	Contribute to Fouling	
	Mg	S		S		
	Ca	S	S, F	S, F	Corrosive elements	
	Na	F, C	F	S, F	C, F	C, F
	K	S				C, F
	Pb	–	–	–		C, F
	Zn	–	–	–		C, F
	Ni	–	–	–	F	C, F
	V	–	–	–	C, F	C, F
	Cl	C				C, F
	S	C	S, F	F	C, F	C, F

C = corrosion—by Cl or S of metal surfaces in excess of 600°F under reducing conditions and 830°F under oxidizing conditions, by V above 950°F.
S = slagging—by partial or fully formed melts due to fluxing of quartz by heavy metals at flue gas temperature >1065°F.
F = fouling—fused or sintered ash due to condensation of volatile species, solid-gas reactions with SO_3 or Cl, solid-state reaction at flue gas temperatures from 648–1037°C between sulfates and oxides, and molten sulfates.

Figure 2.15 – Effect of coal impurities on corrosion, slagging and fouling (Bryers, 1996)

The inorganic components evolve from mineral matter in the coal that is either inherent or extraneous. Inherent mineral matter is closely associated with the pulverised coal, while extraneous mineral matter is separated from the coal during milling (Wall, 1992). During

coal devolatilisation, mineral matter is released and reducing environments are formed; within these areas, ash fusion temperatures are lower and mineral deposition increases (Harb and Smith, 1990). These reducing environments are characterised by high CO, low O_2 and moderate H_2S concentrations and the presence of only partially combusted coal particles; therefore, corrosion problems are exacerbated by NO_x reduction-led air/fuel staging. Reducing environments formed when burning a coal high in sulphur and iron were found to be contributing to corrosion by Manny, et al., (1978); these corrosion processes were reduced when the air flow was altered to increase oxygen concentration in these reducing environments. Within these reducing environments, reacted pyrite (FeS) and fuel-S exist as H_2S in the flue gas and can react with either the base metal iron or, due to the high CO concentration, the protective iron oxide layer to form iron sulphide, which leads to high metal wastage (Kung, 2006).

Ash deposition on boiler tubes leads to increased corrosion and decreased heat flux through the walls. For plant operators, this results in a reduction in plant efficiency as well as an increase in operating costs, as boiler tubes have to be replaced. In hot areas near the flame, ash deposition is due to ash melting on the tube wall. In cooler areas (such as on superheater walls), the volatile alkali salts condense forming a sticky layer that solid ash particles are able to attach to. As the fly ash particles collide with the sticky layer, the deposited ash thickens at an uneven rate around the tube. The temperature of this deposition will increase and the saturation temperature of the volatiles will be met; this results in the condensation rate falling to zero and, subsequently, no more ash deposition (Tomeczek and Wacławiak, 2009). This process to shown in Figure 2.16:

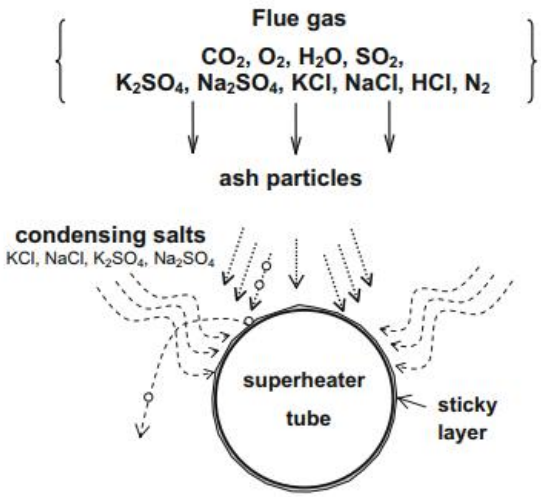

Figure 2.16 – Ash deposition mechanism (Tomeczek and Wacławiak, 2009)

Once ash has deposited on the tube walls, many new avenues for fireside corrosion become available. Significant corrosion rates can be caused by the formation of alkali-iron trisulphates through either pyrosulphates as intermediates or the mechanism described by Corey, et al., (Harb and Smith, 1990). The alkali-iron trisulphate mechanism devised by Corey, et al., and described in Harb and Smith (1990) is initiated by deposition of alkali sulphates, formed from reaction between alkali metals in the fly ash and SO_2 in the flue gas on the wall of the tubes. As this deposited layer thickens, it becomes sticky and traps ash, which then sinters, forming a molten slag and releasing SO_3. SO_3 is also formed through the molten sulphates catalysing SO_2 oxidation during the diffusion of O_2 and SO_2 through the molten slag (Hendry and Lees, 1980):

$$SO_2 + 0.5O_2 \leftrightarrow SO_3 \qquad (2\text{-}41)$$

As oxygen diffuses through the molten sulphates faster than SO_3, the base metal (iron) is oxidised to form a protective oxide film. The SO_3 then reacts with both the protective oxide film and the alkali sulphate to initiate metal wastage, as such:

$$3A_2SO_4 + Fe_2O_3 + 3SO_3 \rightarrow 2A_3Fe(SO_4)_3 \qquad (2\text{-}42)$$

As these reactions remove the iron oxide film, the base iron becomes oxidised and reaction (2-42) repeats, creating a cycle. Additionally, the trisulphates react with the base metal in a mechanism devised by Reid (1971):

$$9Fe + 2A_3Fe(SO_4)_3 \rightarrow 3A_2SO_4 + 4Fe_2O_3 + 3FeS \quad (2\text{-}43)$$

$$4FeS + 7O_2 \rightarrow 2Fe_2O_3 + 4SO_2 \qquad (2\text{-}44)$$

Reactions (2-41) and (2-42) then repeat.

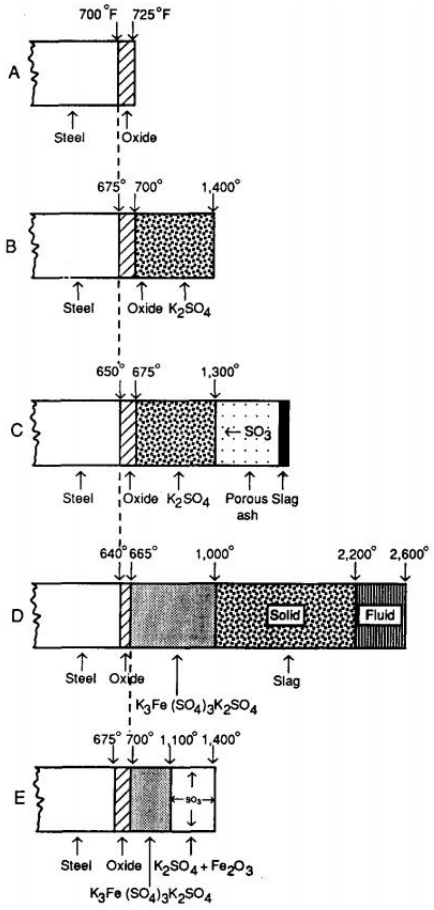

Figure 2.17 – Alkali-iron trisulphates formation mechanism (Reid, 1971)

Alternatively, the trisulphates attack the base metal in the following fashion (Zeng, et al., 2017):

$$19Fe + 2A_3Fe(SO_4)_3 \rightarrow 3A_2S + 6Fe_3O_4 + 3FeS \qquad (2\text{-}45)$$

The alkali and iron sulphides will then be oxidised to reform alkali sulphates, Fe_2O_3 and SO_3, continuing the cycle of metal wastage.

Tomeczek (2007) proposes a slightly different mechanism for trisulphate production and subsequent metal wastage (Figure 2.18) states that the mechanism involves SO_3 first reacting with iron oxide:

$$Fe_2O_3 + 3SO_3 \leftrightarrow Fe_2(SO_4)_3 \qquad (2\text{-}46)$$

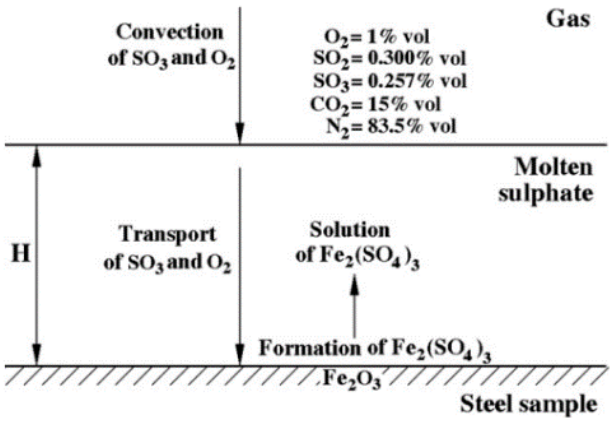

Figure 2.18 – Alternative trisulphate initiation mechanism (Tomeczek, 2007)

Due to the low activity of this compound, it is believed to be consumed upon dissolution in the molten sulphates:

$$3A_2SO_4 + Fe_2(SO_4)_3 \rightarrow 2A_3Fe(SO_4)_3 \qquad (2\text{-}47)$$

It is also possible for pyrosulphates to be stable on the walls of the tube, formed through reaction of the molten sulphates with SO_3 (Zeng, et al., 2017):

$$A_2SO_4 + SO_3 \rightarrow A_2S_2O_7 \qquad (2\text{-}48)$$

These pyrosulphates then react with the iron oxide film to produce another pathway towards trisulphate production when in the temperature range 672-755 K (Srivastava, et al., 1997):

$$3A_2S_2O_7 + Fe_2O_3 \rightarrow 2A_3Fe(SO_4)_3 \qquad (2\text{-}49)$$

Although, this route is believed to be more unlikely due to the high SO_3 and alkali metal concentration required (Hendry and Lees, 1980). Alternatively, the pyrosulphates can attack the base metal as such, creating a cycle of degradation (Zeng, et al., 2017):

$$3A_2S_2O_7 + 3Fe \rightarrow Fe_2O_3 + FeS + A_2SO_4 \qquad (2\text{-}50)$$

Fuels containing high levels of chlorine will emit substantial quantities of HCl on combustion. In the 1950s, chlorine impacts on corrosion became evident due to the high chlorine content in UK coals (Bryers, 1996). It is believed that the chlorine based corrosion mechanism is initiated through the oxidation of HCl (Grabke, et al., 2004):

$$2HCl + \frac{1}{2}O_2 \rightarrow H_2O + Cl_2 \qquad (2\text{-}51)$$

The chlorine then diffuses through the protective oxide film to react with the iron or the alloying metals:

$$Cl_2 + Fe \rightarrow FeCl_{2(s)} \rightarrow FeCl_{2(g)} \qquad (2\text{-}52)$$

Hydrogen chloride can also attack the protective metal oxide or the base metal directly (Zeng, et al., 2017):

$$2HCl + FeO \rightarrow FeCl_2 + H_2O \qquad (2\text{-}53)$$

$$2HCl + Fe \rightarrow FeCl_2 + H_2 \qquad (2\text{-}54)$$

The evaporation and diffusion of $FeCl_2$ is a steady process and is the rate-controlling step of the mechanism (Grabke, et al., 1995); the resulting gas diffuses through the scale and slagging until it comes in contact with an oxidative atmosphere, in which the chlorine gas is reformed:

$$FeCl_{2(g)} + \frac{3}{2}O_2 \rightarrow Fe_2O_3 + Cl_2 \qquad (2\text{-}55)$$

These oxides do not form as a film and provide no protection to the base metal. A diagrammatic representation is shown below:

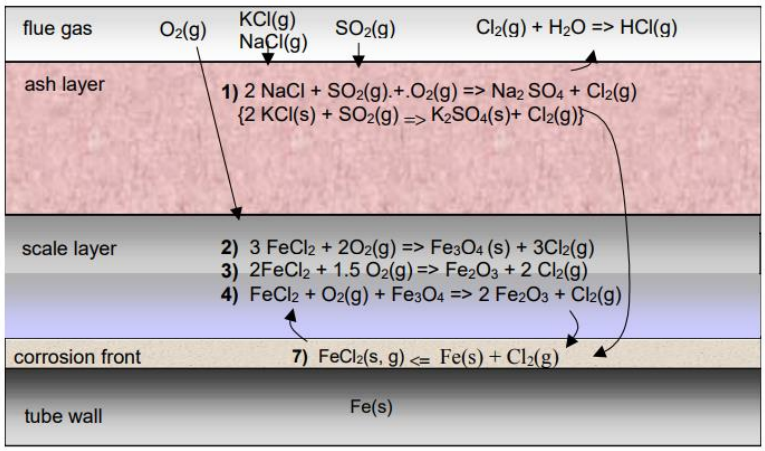

Figure 2.19 – Effect of chlorine attack on base metal (Reidl, et al., 1999)

Alternatively, alkali metal chlorides can be a source of chlorine and responsible for its migration to the tube wall. Gaseous alkali metal chlorides can attack the chromium in the tube metal alloy or facilitate the breakdown of the protective chromia layer, leaving the base metal exposed and providing a source of chlorine adjacent to the base metal (Niu, et al., 2016):

$$2ACl_{(g)} + Cr + 2O_2 \rightarrow 2A_2CrO_4 + 2Cl_2 \qquad (2\text{-}56)$$

$$4ACl_{(g)} + Cr_2O_3 + \frac{5}{2}O_2 \rightarrow 2A_2CrO_4 + 2Cl_2 \qquad (2\text{-}57)$$

Deposited alkali metal chlorides are usually found on the innermost section of a deposit (Niu, et al., 2010) and can melt with each other and alkali metal sulphates to form low temperature eutectics (Niu, et al., 2016). Both deposited and molten alkali metal chlorides can attack protective metal oxides, again leaving base metal exposed and creating a source of molecular chlorine adjacent to the base metal (Antunes and de Oliveira, 2013). The molten phase alkali metal chlorides are particularly aggressive, with the highest reaction rates and the formation of a conductive electrolyte that can lead to electrochemical attack (Nielsen, et al., 2000).

$$2ACl_{(s,l)} + Fe_2O_3 + \frac{1}{2}O_2 \rightarrow A_2Fe_2O_4 + Cl_2 \qquad (2\text{-}58)$$

$$4ACl_{(s,l)} + Cr_2O_3 + \frac{5}{2}O_2 \rightarrow 2A_2CrO_4 + 2Cl_2 \qquad (2\text{-}59)$$

Alkali metal chlorides can release chlorine through conversion to sulphates:

$$2ACl + SO_2 + O_2 \rightarrow A_2SO_4 + Cl_2 \qquad (2\text{-}60)$$

$$2ACl + SO_2 + \frac{1}{2}O_2 + H_2O \rightarrow A_2SO_4 + 2HCl \qquad (2\text{-}61)$$

Reaction (2-60) tends to occur nearer the surface of the scaling, leading to chlorine being lost through entrainment in the flue gas. Therefore, the presence of SO_2 actually partially mitigates the chlorine corrosion mechanism (Grabke, et al., 1995).

2.5.2 Inhibition Techniques

When burning biomass or co-firing with biomass and coal, fireside corrosion is drastically intensified. Biomass combustion produces higher levels of alkali content in the ash of differing species than coal (Antunes and de Oliveira, 2013), as well as higher levels of chlorine during the combustion of straw-type biomass (Baxter, et al., 1996). The higher level of chlorine not only has an adverse effect on chlorine related corrosion but also leads to the evolution of more volatile potassium species from the fuel (Nielsen, et al., 2000). For this reason, there has been a focus to research and develop techniques for the inhibition of all ash-related problems but, in particular, slagging and corrosion. Traditionally, research has surrounded novel materials for use as tubing but recently, the utilisation of fuel

additives has become more popular. Fuel additives have the impact of changing the ash chemistry through the addition of minerals. They are either blended with the fuel prior to combustion, or delivered into the combustion chamber through dedicated sprayers (Wang, et al., 2012). There are thought to be four ways in which additives can mitigate ash problems:

- Chemical absorption: the sequestering of alkali metals within compounds with high melting temperatures.
- Physical adsorption: the trapping of volatile and molten compounds within inert compounds that are entrained in the flue gas.
- Alteration of the ash melting behaviour through the introduction of inerts such as SiO_2 and Al_2O_3.
- Dilution of the more problematic compounds.

The latter three are universal to all additives, however the nature of chemical absorption is individual to the type of additive being used. Wang, et al., (2012) defined four types of additive: alumino-silicate based additives, sulphur based additives, calcium based additives and phosphorus based additives.

Alumino-silicates are reportedly able to capture potassium and sodium from gaseous KCl and NaCl (Dayton, et al., 1999), which, as shown in Figure 2.16, can contribute to ash deposition; however, the capture of the alkali metals led to the liberation of gaseous HCl. This has resulted in significant research, using experimental and equilibrium modelling methods, both into the use of alumino-silicate based additives, especially kaolin, and into the abatement of alkali metal based issues during biomass and cofired combustion (Coda, et al., 2001 and Wei, et al., 2002), with findings suggesting the formation of $KAlSi_2O_6$ (leucite). Further study of the use of kaolin during coal combustion found additional benefits regarding the capture of volatile-K; KOH, produced during combustion, was captured by aluminosilicates and transferred to coarse fly ash particles, which could then be easily removed using an ESP (Zhou, et al., 2010). This resulted in a reduction in PM1 generation, as well as a reduction in the K content of the PM1; the consequences of which are beneficial to the environment and human health (Zhou, et al., 2010).

Further study of KOH capture by kaolin and mullite was performed by Wang, et al., (2018a), including equilibrium modelling using FactSage; they found that kaolin was being completely converted to K-aluminosilicates between 1100-1450 °C (including formation of kaliophilite ($KAlSiO_4$) above 1300 °C and amorphous K-aluminosilicates below 1300 °C), while the equilibrium calculations were accurate for low concentrations of KOH and temperatures above 1100 °C. Mullite, formed when kaolin is heated above 1100 °C (Chen, et al., 2000), was found to be less effective at capturing potassium below 1100 °C. However, when the temperature is increased past 1300 °C, the potassium capture rate starts to mirror that of kaolin. This group went on to also investigate capture of K_2CO_3, KCl and K_2SO_4 using kaolin (Wang, et al., 2018b). Almost complete capture of K_2CO_3 and KCl was witnessed experimentally and numerically above 1100 °C; however, below 1000 °C, the predicted formation of these species at equilibrium was greater than witnessed experimentally, indicating kinetic limitations to this potassium capture. Equilibrium predictions for K_2SO_4 capture were inaccurate because FactSage assumed kaliophilite to be the product as opposed to leucite, which was revealed to be the true product by XRD. The study concludes by recommending the use of a high Si content (relative to Al) for chlorine-rich fuels, due to this prevalence for leucite formation.

In addition to conventional alumino-silicates, it has been found that silica and alumina individually are able to capture alkali metals and mitigate some ash-related problems. However, they have been found by Llorente, et al., (2008) to offer inferior performance compared to alumino-silicates, in terms of reducing sintering. While, Kyi and Chadwick (1999) found that only ~50% of sodium could be retained when using alumina compared to ~95% at the same loading of kaolin and Liu, et al., (2020) found that silica and alumina could inhibit potassium emissions by a maximum of ~70%, compared to a maximum of ~90% for the alumino-silicates.

Sulphur based additives are used for the sole purpose of promoting reactions (2-60) and (2-61), converting KCl to K_2SO_4. This reduces the chlorine content in the deposit, causes more HCl to be carried out of the furnace in the flue gas and changes the nature of the corrosive threat, i.e. that potassium sulphate is believed to be less ‘sticky’ and corrosive than potassium chloride (Brostrom, et al., 2007). Sulphur based additives can prove unsuccessful in scenarios where a significant CaO content converts the SO_3 from the

additive to calcium sulphate, and alkali hydroxides convert the liberated HCl back into alkali chlorides (Aho, et al., 2008).

Calcium based additives and phosphorus based additives are used with the aim of sequestering potassium within calcium-rich phosphates rather than allowing the formation of potassium silicates. The former has a higher melting temperature thus hindering ash sintering and slagging (Wang, et al., 2012).

There may be yet another group of additives; Daood, et al., (2014a) noted that the investigated Fe-based additive would aid the mitigation of corrosion, slagging and fouling. This was studied in greater detail in Daood, et al., (2017); in which, they exposed portions of T22 boiler tube coated with an additive/coal fly ash mixture for 1000 hours to a simulated flue gas containing SO_2 and HCl gas at 833.15 K. The results indicated that the boiler tubes would last up to 4.2 years, compared to 3.2 years when no additive is used. Three reasons were cited for this improvement in life span: in the additive/coal fly ash mixture there is a lower concentration of potassium oxide, iron oxide in the additive could inhibit the direct chlorination of the base metal and chromia in the additive prevents metal oxidation.

It was theorised that the lower concentration of potassium oxide leads to less potassium sulphate being formed, which, in turn, leads to less alkali iron trisulphates being formed. These molten compounds are unstable and will react with the base metal, leading to loss of wall thickness. The higher concentration of Fe_2O_3 could also prevent the chlorination of the base iron by reacting with chlorine containing compounds prior to diffusion through the deposits, leaving the protective oxide layer untouched. Not only is there are a larger concentration of Fe_2O_3 but also the chromia content in the additive/coal fly ash mixture is approximately double the level in coal fly ash alone and the chromia protects the base metal by forming a protective layer; although it should be noted that the chromia content in the additive is very low and the authors may be overstating any impact from this. It is also important to note the appearance of alumino-silicates in the make-up of the Fe-based additive, with the alumina content being reported as 4.71% and the silica content as 34.69% (Daood, et al., 2014a); this could lead to a sizeable amount of potassium being sequestered.

2.5.3 Summary of Gaps in the Research

Section 2.5.1 discussed the processes responsible for ash-based fireside corrosion in pulverised fuel boilers, focussing on the role of sulphur and chlorine and the alkali metals that aid migration of the two. Section 2.5.2 then discussed the use of fuel additives to depress the corrosive processes, with alumino-silicates being the most widely researched and recognised as beneficial. However, the Fe-based additive that was discussed in section 2.3 was also shown to be beneficial when preliminary tests were carried out with coal ash, however the explanation for the reduced corrosion rates witnessed was weak. Additional research to identify how this additive is actually impacting the corrosive processes would be required, to enable a recommendation for using this technology in order to inhibit corrosion. Further, a comparison to the impact of alumino-silicates on fireside corrosion would shed light on just how ground-breaking the application of this technology is.

2.6 Conclusions and Summary of the Research Gaps

This chapter summarised the state of research with regards to NO_x production and abatement and fireside corrosion and its inhibition. After discussing the varying pathways responsible for producing NO, the technologies that are designed to manipulate or depress these pathways were discussed, with particular attention to low NO_x burners and their control of fluid dynamics to stage species transfer. Oxy-coal combustion was then discussed, due to its importance as a developed carbon capture technology and the presence of the NO reburning phenomenon. The emergence of loading coal with iron compounds to enhance combustion and reduce NO emissions was then discussed, along with a detailed examination of the secondary NO_x abatement technologies, SNCR and SCR. Finally, the processes responsible for fireside corrosion were analysed, as were the mitigation options, in the form of additives.

This review highlighted some research gaps that can be considered achievable avenues for study. First was the use of low-NO_x burners during oxy-coal combustion and the impact of varying burner settings on both NO formation and NO destruction (through reburning). The use of the Fe-based additive raised two prominent routes for investigation: how the Fe-based additive would interact with ammonia during SNCR and how it would impact fireside

corrosion. There were studies that had started to investigate these factors but had raised more questions than were answered, so further investigation is warranted.

Hence the aim stated at the close of the introduction is to be achieved through the following objectives:

- Improving confidence and understanding in the performance of low NO_x burners during oxy-coal combustion (for intended carbon capture purposes), with particular attention to maximising the rate of reburning of recycled NO.
- Improving the performance of selective non-catalytic reduction using an Fe-based additive, and investigating sensitivities of this new process.
- Improving the confidence of the proposed ability of the Fe-based additive to mitigate fireside corrosion of superheater tubes through comparison with a variety of established additives on a variety of fuels.

CHAPTER 3 EXPERIMENTAL SETUP AND COMPUTATIONAL SOFTWARE

3.1 Introduction

The following content of this chapter is a description of the facilities, software and methods used to harvest the data presented in chapters 4-6. This is presented in the same order as the analysis is presented and, due to the variety of facilities used, an effort has been made to be concise in their description. The 250 kWth combustion test facility discussed in this section was used to study a variety of oxy-coal flames and examine the impact of burner configuration on flame stability, NO formation and NO reburning rates. The 100 kWth combustion test facility was used to combust coal in air and study the impact of an Fe-based additive on NO reduction by selective non-catalytic reduction. This interaction was then studied further using a kinetic model of a continuously stirred tank reactor in Cantera. Finally, the equilibrium modelling software FactSage was used to study the impact of various fuel additives on the formation of corrosive species and the by-products of corrosion.

3.2 250 kW_{th} Oxy-coal Combustion Test Facility

3.2.1 Description of the Combustion Test Facility

A large pilot scale 250 kW_{th} combustion test facility (CTF) (Figure 3.1) at the UK carbon capture and storage research centre's pilot-scale advanced CO_2-capture technology centre (UKCCSRC - PACT) has been utilised for experimental data collection of an oxy-coal flame. The furnace of the 250 kW_{th} CTF measures approximately 4 m in height with an internal diameter of 0.9 m and contains a total of eight modular sections, the first six of which are water cooled and the first three contain viewing ports. Each section is 0.5 m high and lined with 100 mm thick light weight alumino-silicate refractory (Figure 3.2). A high density 96% alumina (thermally rated to 1850 °C) is used to cast the quarl section of the burner and the section connected to the quarl.

An induced draft fan (IDF) maintains a negative pressure inside the CTF and draws out the combustion products (fly ash and flue gas) from the bottom of the CTF; this then passes through a cyclone separator and a candle filtration unit (for fine particulate removal). This

negative pressure is achieved by sealing the bottom of the furnace with a water tray, which, in turn, provides a safe container to capture and quench falling bottom ash and slag, and allows for pressure release in the event that the IDF fails to maintain the negative pressure. The fly/bottom ash was collected, to be available for analysis, after each test from catch pots located at the exhaust point and at the cyclone. This analysis was executed externally and involved: heating to remove contaminants and moisture; weight measurements before and after the removal of moisture; heating in a muffle furnace to remove unburned carbon and then a final weighing. These values were then used to determine the quantity of unburned carbon in the sample under ISO:1171-2010.

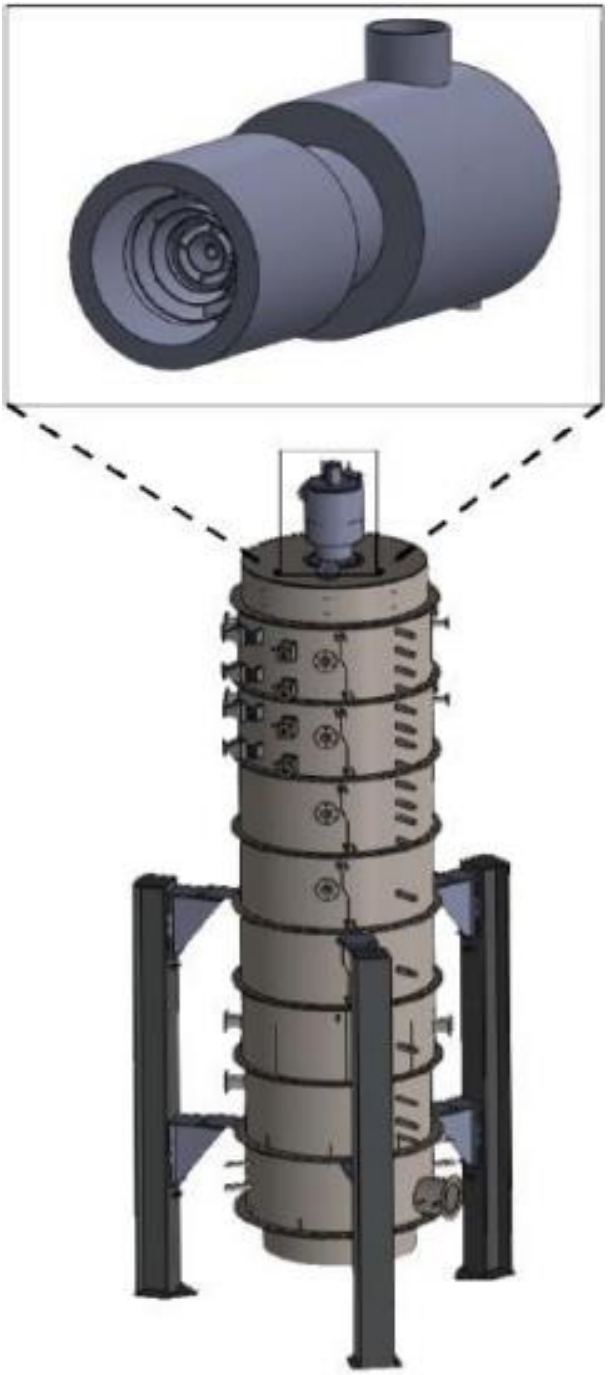

Figure 3.1 – Layout of UKCCSRC-PACT oxy fuel combustion testing facility (250 kW_{th}) (Szuhanszki, et al., 2017)

3.2.2 Sample Collection and Analysis

There are numerous ports of 1.5” diameter along the combustor which could be used for the measurement of process temperature and inflame emissions and recording flame shape. The first three sections contain four sampling ports and a viewing port; the next four sections each contain only one sampling port located at the centre point of the

section. Each section has a thermocouple for measuring the process temperature at the wall, although section 4's thermocouple was not operational during the tests.

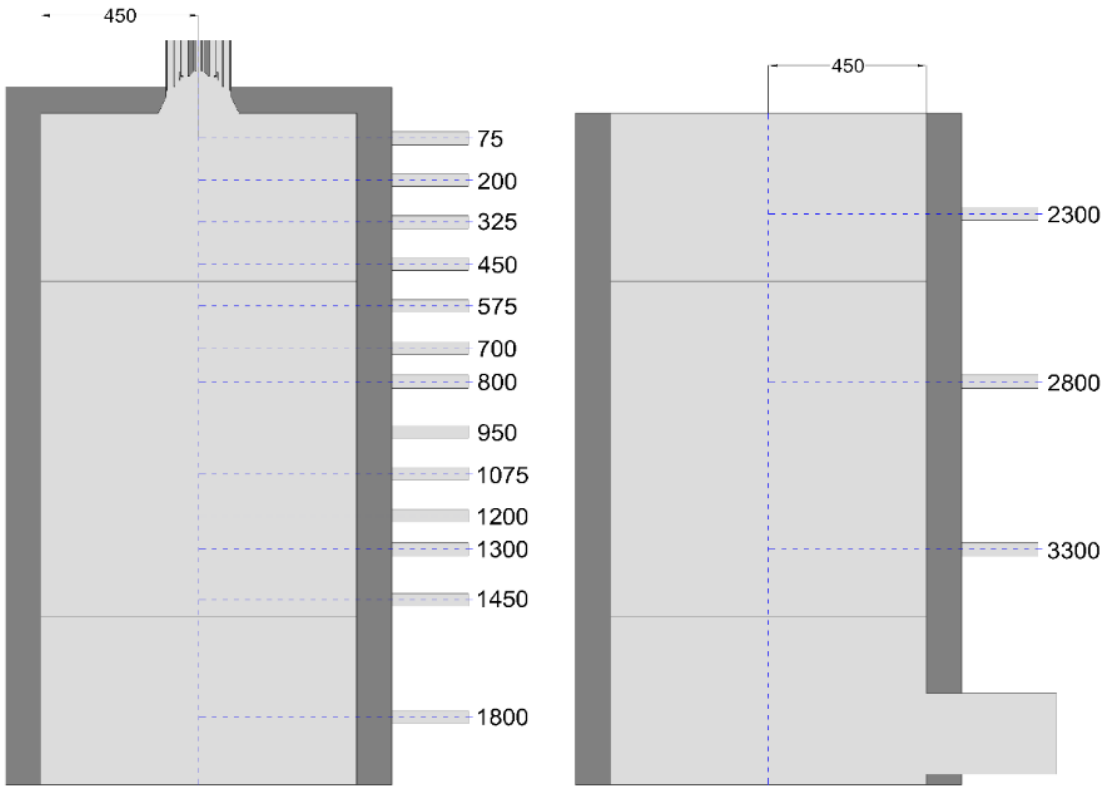

Figure 3.2 – Furnace geometry and position of measurement ports (all dimensions in mm)

Process thermocouples, along with continuous emission monitoring equipment (i.e. NO_x, CO_2, CO, O_2, SO_2, and THC), are utilised for data gathering purposes for specific test runs. The data collected during the test is logged every 5 seconds through a supervisory control and data acquisition system connected to a human-machine interface (HMI) (Figure 3.3), which displays past and present measurements over user preferred time periods.

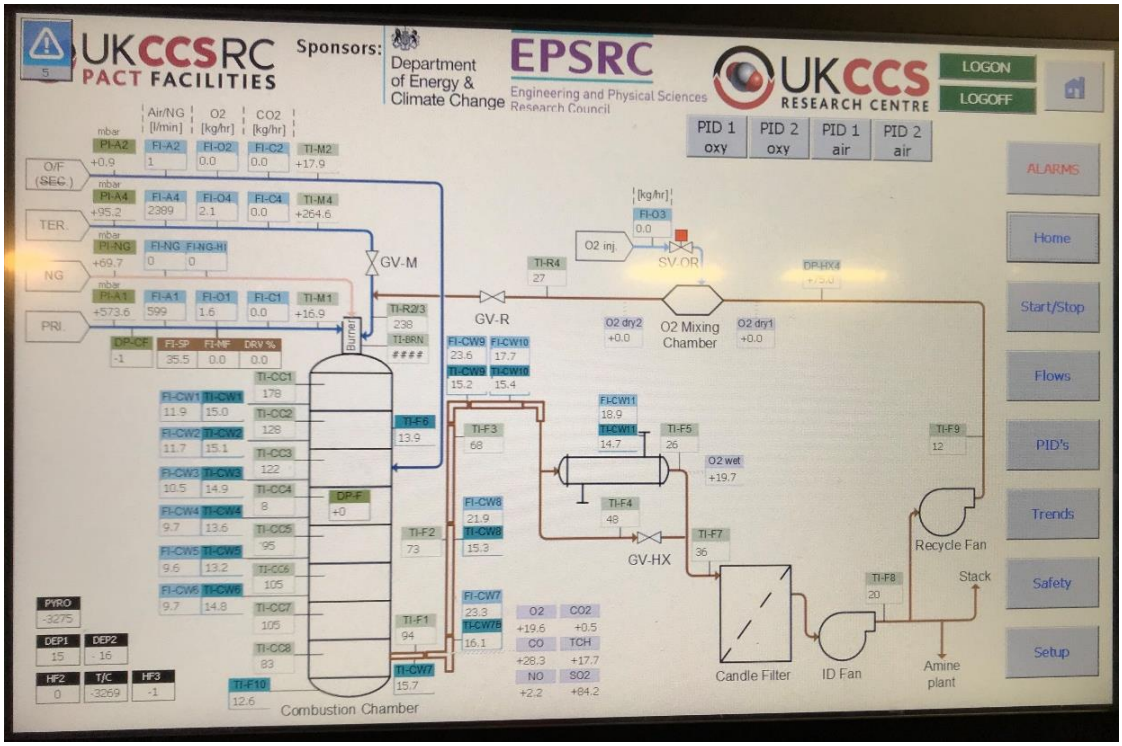

Figure 3.3 – HMI for monitoring online data measurements

In-flame and flue gas samples are continuously drawn through two water jacketed probes via a Drechsel bottle, to remove large particulates and moisture, and into a heated filter kept at 180 °C. From this heated filter, the sample passes through a heated line (191 °C), to prevent condensation, and to another heated fine filter element for further fine particle removal. The probes can only be used one at a time and a valve is used to switch between the probes. Both probes are supplied with a compressed air line that can be opened in the event of a blockage or deposit within the sample probe, usually recognised by an abnormal oxygen reading on the HMI. Following the fine particle filter, the gas is fed to a cooler (cooled to 5 °C), to remove any remaining moisture, and subsequently reheated to 191 °C and fed to the individual CO_2/O_2, NO/NO_2, CO and THC analysers at a rate of approximately 1 L/min, while any remaining sample is ejected along with the analysed sample.

The primary O_2 analyser was a 7208MG Signal paramagnetic analyser that was able to evaluate the dry O_2 concentration. A secondary Servomex 2700 O_2 analyser was also used to measure the wet O_2 concentration when gas was not being pulled through the sampling probes; this was used in case a problem occurred during this time. The NO/NO_2 analyser was a Signal 4000VM chemiluminescence analyser that utilises the reaction of NO with ozone; 10% of the subsequent NO_2 formed is in an excited state and emits photons that

are measured by the analyser, thus giving a measurement that is proportional to the NO concentration in the gas. The CO_2 (7208MG Signal Multi-Gas analyser) and CO (Signal 7000FM) analysers utilise the gas filter correlation non-dispersive infra-red technique and are able to present the concentrations of these compounds in various ranges from ppm to percent, which are automatically changed during measurement. The THC analyser (Signal 3000HM) utilises the principle of flame ionisation to measure VOCs in the gas, with the output also being displayed in ppmv or percent. To account for any drift in the instrument-related measurement, zero and span calibrations are periodically performed before and during each test using calibration gases permanently connected to the analyser rack.

Figure 3.4 – The gas analyser rack with preheater (top) and chiller (bottom)

During data analysis, all NO measurements collected from the flue are corrected to 6% O_2; whereas, all in-flame NO measurements are reported as collected accompanied by the local O_2 concentration. Instantaneous flame images were recorded using a water-cooled optical probe inserted into the upmost section of the furnace. This probe contains a wide-angle lens that focuses light onto a complementary metal oxide semiconductor (CMOS) sensor of an industrial camera. The CMOS sensor allows videos of the flame to be recorded on a nearby laptop computer. Further information on the optical probe can be found in Farias Moguel, et al., (2018).

3.2.3 Burner Description

The burner is a scaled down version of a Doosan Babcock Mk III low-NO_x burner, previously discussed in section 2.2.2; this consists of a primary annulus through which the coal is fed with a portion of the oxidant and the swirling secondary and tertiary annuli through which the remaining oxidant is delivered (Figure 3.5). A sliding partitioning damper controls the split between the secondary and tertiary oxidants; this enables a change in the stoichiometry in the near burner region and the overall swirl of the flame due to the larger swirl angle of the secondary register. The swirling primary oxidant, carrying coal particles, engages with the coal collectors for later mixing with swirling secondary and tertiary oxidant registers. A term, secondary oxidant proportion 'S', is used to denote the burner setting and represents the proportion of excess oxidant that is flowing through the secondary register.

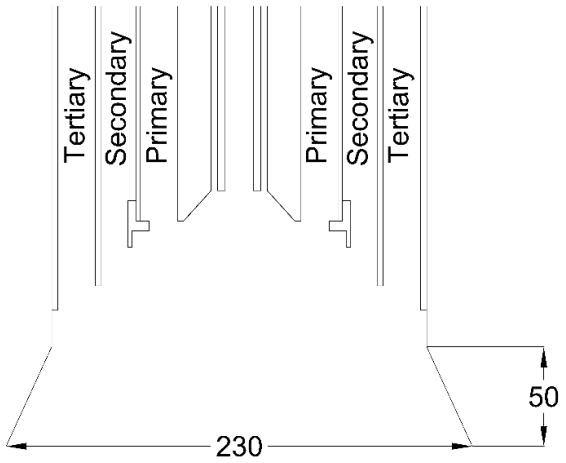

Figure 3.5 – CAD drawing of the investigated burner (all dimensions in mm) (Adapted from Clements, et al., 2015)

3.2.4 Oxidant Supply and Operational Method

The combustion air is sent from the on-site compressor to mass flow controllers controlling the primary and combined secondary/tertiary flows. The oxy-fuel oxidant is not contain actual recycled flue gas but uses pure O_2 and CO_2 to create a simulated dry oxy-fuel oxidant. This is supplied from dedicated cryogenic storage tanks of O_2 and CO_2 through a primary compressor to a mass flow controlled manifold with Coriolis mass flow meters and pneumatically actuated control valves, before entering to the primary, secondary and tertiary air registers. The desired air and O_2/CO_2 mass flow rates and O_2/CO_2 mass ratios are inputted using the HMI connected to a SCADA system (Figure 3.6). The temperature of all the oxidant streams can be maintained using bespoke electrical heaters. The primary stream is unheated and limited to containing 21% O_2 due to being responsible for entraining and transporting the coal to the burner, and to avoid auto-ignition of the fuel. This coal is loaded into a hopper on the mezzanine of the CTF prior to a day's test. This then passes into a lower hopper that is constantly vibrating in order to prevent bridging. Following the lower hopper, the coal is fed through a screw valve onto a vibrating plate, and finally into the primary line via a venturi. During air operation this venturi is open to the atmosphere; however, during oxy-fuel combustion, a small portion of the primary oxidant is routed to the venturi to eliminate the need for air, in order to prevent air ingress.

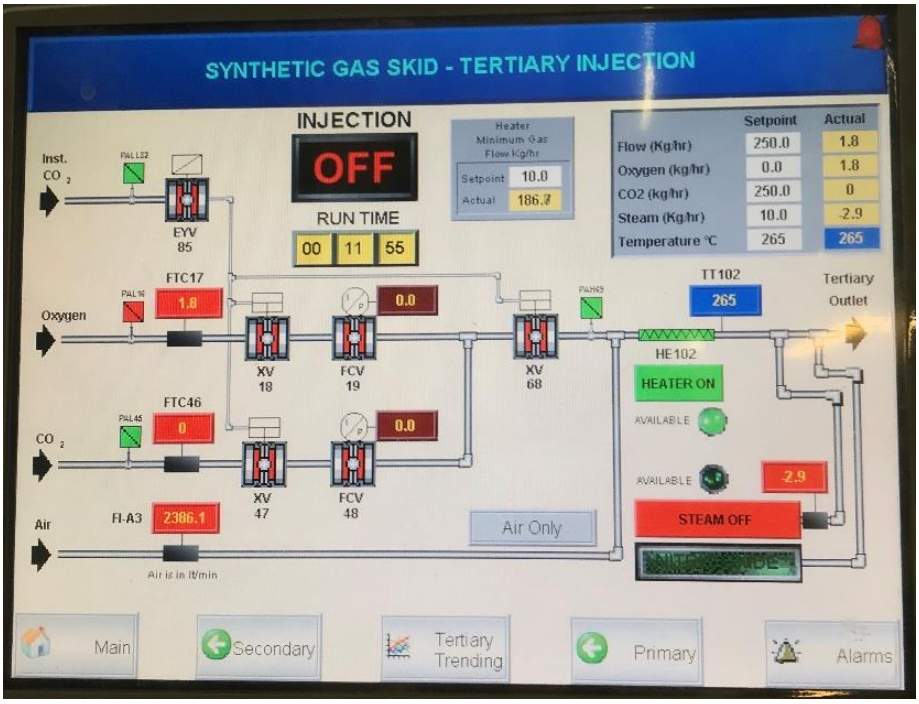

Figure 3.6 – HMI for controlling oxy-fuel oxidant mass flows

An issue in the operation of an air/oxy-fuel furnace is the setting of the primary flow rate during switchover from air to oxy-fuel. One method (as demonstrated in Smart, et al., (2010) and Zhang, et al., (2011)) is to maintain the primary flow rate, as this offers the most simple operational philosophy and guarantees that coal particles will remain entrained in suspension. This technique was found to delay flame ignition and lead to a lifted flame, which was only corrected when the primary volumetric flow rate was decreased (Fry, et al., 2011). Therefore, Gharebaghi, et al., (2011) instead maintained the primary volumetric flow rate as a ratio of the total oxidant flow and achieved a stable flame without jeopardising the entrainment of the coal. This same approach is used at the 250 kW_{th} CTF in this study; however, the ratio that is to be used had to be investigated in order to find the preferable option. Four ratios, 16%, 18%, 20% or 22% of the total oxidant, were tested using air over a range of burner staging environments while the NO emissions and unburned carbon in ash were monitored/analysed. Maintaining the primary flow rate at 20% of the total flow was found to be the most preferable option and this value was then maintained for all air-fired and oxy-fired tests henceforth. This is readdressed in full in chapter 4. The operating conditions for the baseline 200 kW_{th} and the core 170 kW_{th} tests can be found in Table 3.1, where OF is used as short-hand for oxy-fuel.

		Primary Stream	Combined Secondary/Tertiary Stream
Air (200 kW_{th})	Air (kg/hr)	56	235
	Temperature (°C)	20	260
	Coal Feed Rate (kg/hr)	24.35	
OF 28 (200 kW_{th})	O_2 (kg/hr)	9	56
	CO_2 (kg/hr)	52	182
	Temperature (°C)	20	260
	Coal Feed Rate (kg/hr)	24.35	
OF 27 (170 kW_{th})	O_2 (kg/hr)	8	44
	CO_2 (kg/hr)	42	152
	Temperature (°C)	20	260
	Coal Feed Rate (kg/hr)	20.7	
OF 30 (170 kW_{th})	O_2 (kg/hr)	7	44
	CO_2 (kg/hr)	37	126
	Temperature (°C)	20	260
	Coal Feed Rate (kg/hr)	20.7	

Table 3.1 – Operating conditions

Natural gas is primarily used to heat up the CTF for roughly 2-2.5 hours until the furnace temperature is greater than 1000 °C. At this point, the fuel is switched to pulverised coal but at a lower thermal rating than will be used for the test. The El Cerrejón coal analysis was carried out externally and is given in Table 3.2. This coal is a bituminous coal, well-known for its low sulphur and ash content and relatively high volatile content, which aids ignition substantially. The thermal rating is gradually increased as desired as the temperature of the furnace is increased. Conventional air-fired coal combustion takes approximately 1 hour to stabilise and reach thermal equilibrium, before the measurements can be recorded. This point is determined by monitoring the temperatures recorded by the thermocouples (~1500 °C measured at the thermocouple in section 2) as well as NO concentration in the flue gas. For the oxy-fuel cases, this is the point when the switchover from air to oxy-fuel is then initiated; this takes another hour to stabilise before measurements can be taken within the scope of the test. Each test is completed by

reverting back to air-fired combustion from oxy-fuel combustion in order to check the coal feeding and sampling stability.

Ultimate Analysis (%)					Proximate Analysis (%)				Calorific Value (MJ/kg)
C	H	N	O	S	Moisture	Volatile Matter	Fixed Carbon	Ash	
74.50	5.04	1.58	18.50	0.38	5.12	36.90	56.06	1.92	29.57

Table 3.2 – El Cerrejón Coal analysis (as received basis)

A separate 99.5% NO in N_2 injection manifold, with automatic shut-off safety valves, is used to inject NO into the O_2/CO_2 blend in order to simulate dry recycled flue gas. During the tests, a variety of levels of NO were injected and mixed into different streams to simulate the recycled NO for both air and oxy-fuel cases. The concentration of the simulated NO injected was in the range of 122-1500 ppm, chosen from a review of available literature (Stanmore and Visona, 2000, Al-Abbas and Naser, 2012, Backreedy, et al., 2005, Meij and te Winkel, 2004, Cao, et al., 2010, Ling, et al., 2014), and the reported NO destruction rates were calculated using (3-1):

$$NO\ destruction\ \% = 100 \times \frac{NO_{baseline} + NO_{recycled} - NO_{measured}}{NO_{recycled}} \qquad (3\text{-}1)$$

Where $NO_{baseline}$ are measurements taken without any recycled NO, $NO_{recycled}$ is the concentration of NO in the oxidant, and $NO_{measured}$ are measurements taken when the NO concentration in the oxidant is equal to the value $NO_{recycled}$.

3.3 100 kW_{th} Fe-based Additive Combustion Test Facility with Selective Non-Catalytic Reduction Capability

3.3.1 Description of the Combustion Test Facility

This pulverised fuel (PF) combustion test facility was located at the former industrial partner, International Innovative Technologies Ltd, in Gateshead, UK. It was a 4 m tall down-fired furnace consisting of 8 sections of 500 mm height and 650 mm outer diameter, with interior diameters of 400 mm, and a quarl of 450 mm height and 500 mm outer diameter. The dimensions can be viewed in Figure 3.8. The burner arrangement is two-stage, with the primary air entraining the coal and the Fe-based additive and the secondary air completing burnout. The CTF is designed up to 100 kW_{th} input of coal ranging from 15-20 kg/hr based on the calorific value of the fuel. The coal is fed onto a vibratory tray feeder

using a Rospen twin-screw feeder, with a nominal uncertainty of ±0.5%, while the Fe-based additive (if in use) is also fed onto this tray using a single fine pitch screw feeder. This smaller feeder can be calibrated to feed the Fe-based additive from 0.27 kg/hr to 1 kg/hr; a 3 point calibration is done on this feeder to give repeatability confidence. The vibratory tray feeds this mixture into the primary air where it is entrained and, due to the turbulence of the primary air flow and the distance to the burner (9-10 m), it can be assumed to be fully mixed when it arrives at the burner. The majority of the combustion air is split between the primary (carrier) air and secondary air, which is supplied through a dedicated compressor and a blower fan. The configuration is shown in Figure 3.7:

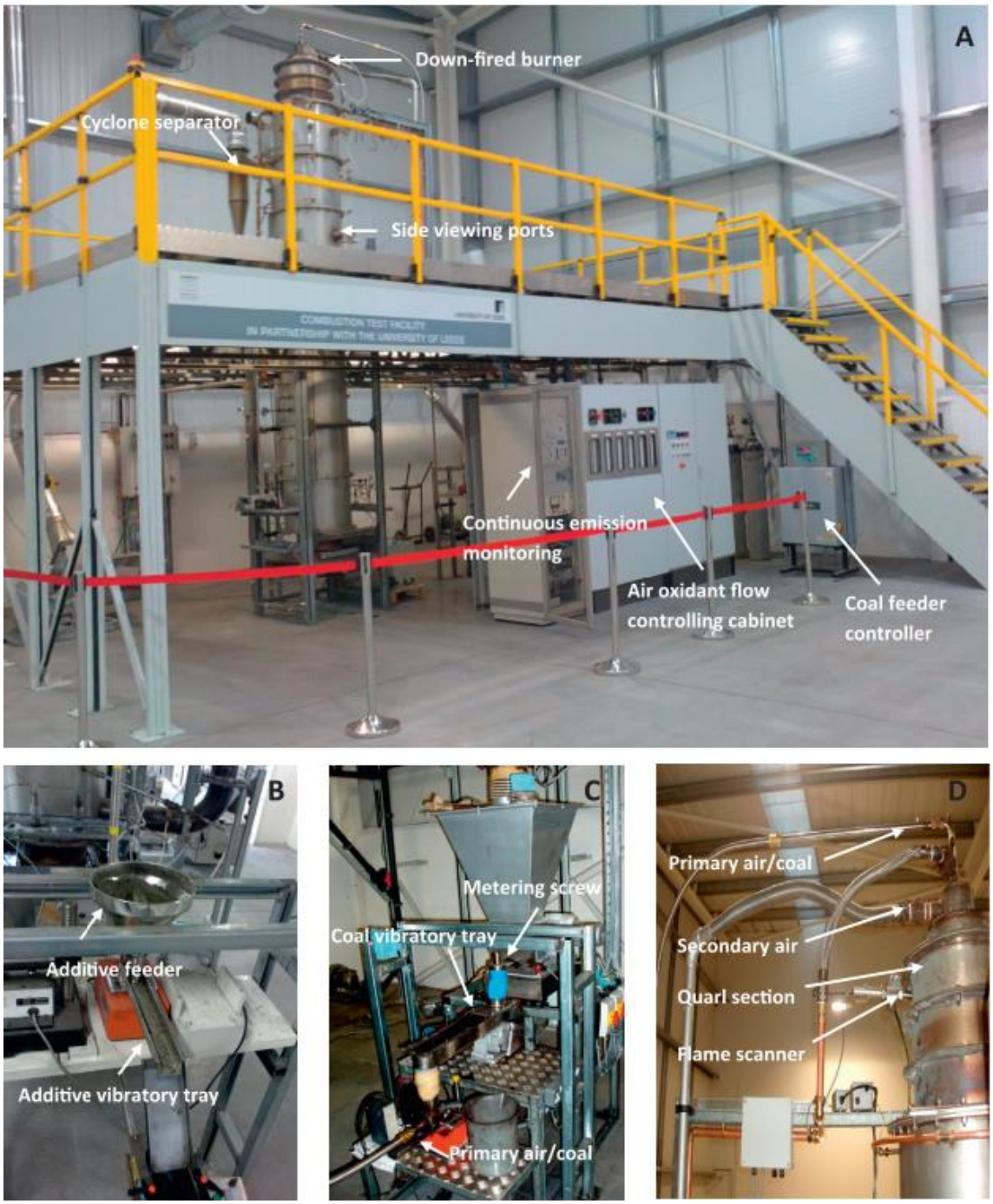

Figure 3.7 – A: Broad view of the 100kW$_{th}$ CTF, B: Additive feeding system, C: Coal feeding system, D: Burner and quarl (Daood, et al., 2014a)

A water-cooled probe is used to sample the gaseous constituents of the flue gas at a sample point in the eighth section. The sample is fed through a series of Drechsel flasks and filters to remove moisture and large particulates to a series of gas analysers. NO was measured using a chemiluminescence-based Signal series 440 analyser. CO_2 was measured using a non-dispersive infra-red based Signal 7000FM GFC analyser. CO was measured using a non-

dispersive infra-red based Analytical Development Company and O_2 was be measured using paramagnetic-based Servomex 570A analyser. The sampling probe is periodically purged using compressed air to remove condensed water and deposited fly ash, which may block the probe or influence measurements. Thermocouples are installed in each of the top seven sections to measure the temperature at the wall, and there are viewing ports in the top four sections for visual inspection of the flame.

The arrangement for the injection of ammonia, the reagent in use for selective non-catalytic reduction, consisted of a specialized mixing skid with calibrated flowmeters for the measurement of both pure ammonia and nitrogen used as a carrier. The momentum induced by the entraining nitrogen helps induce thorough mixing of the injected ammonia into the hot gas mixture inside the furnace. The ammonia and nitrogen mixture, through a water-cooled injection probe, is introduced at the module that provides a compromise between highest possible NO reduction and lowest possible ammonia slip, as discussed in Section 3.3.2. This arrangement benefits in the maximum reactivity of the reducing amides with the oxides of nitrogen within the optimum temperature window (850 °C to 1100 °C). The appropriate ammonia flow rate (AFR) is calculated using:

$$AFR = (NO_{initial} \times 10^{-6}) \times Q \times NSR \qquad (3\text{-}2)$$

Where Q is the volumetric flow rate of air (mL/min) and $NO_{initial}$ is the concentration of NO in the flue gas prior to ammonia injection (ppm). The NSR is a term used to standardise the desired NO reduction between different reagents, e.g. a NSR of 1 will theoretically reduce 1 mole of NO and requires 1 mole of ammonia or 0.5 moles of urea. The calculated ammonia flow rate is converted to an arbitrary flow value using the manufacturer's calibration chart.

A general arrangement drawing with accurate dimensions with respect to the furnace, port locations and thermocouple locations is presented in Figure 3.8; the dimensions and locations of pipes and other equipment is not exact.

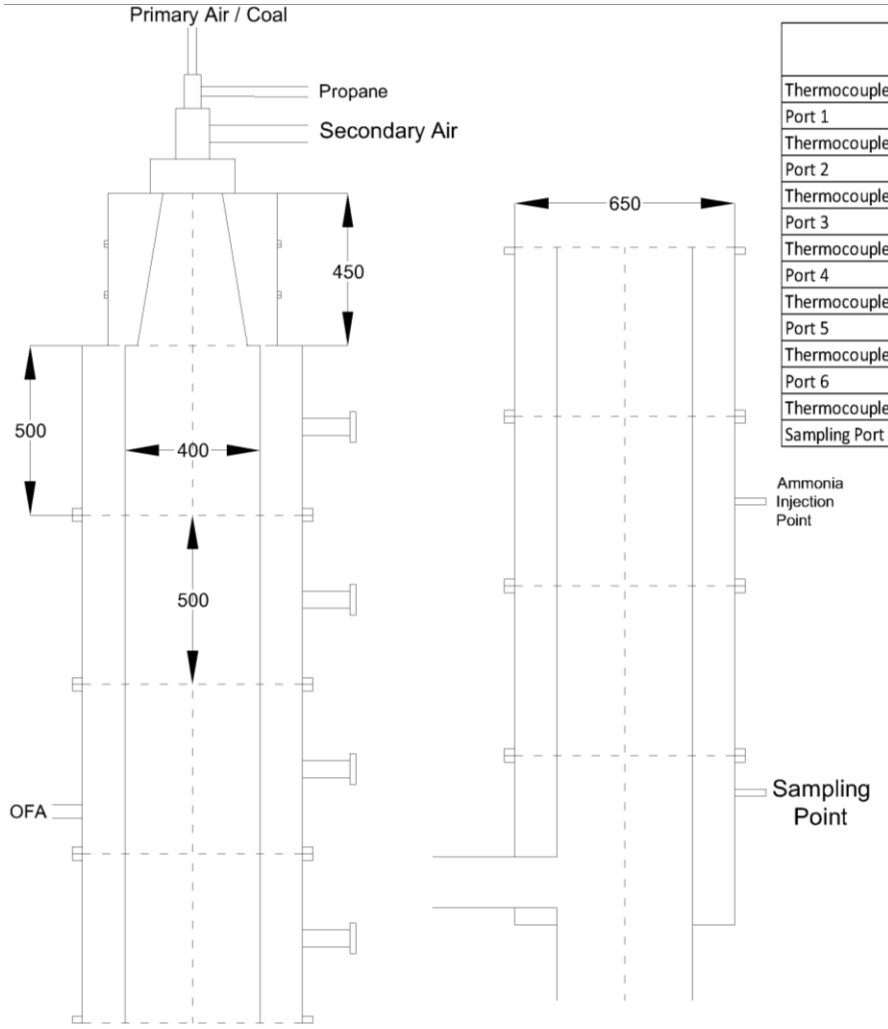

	Distance from the Quarl/ mm	Diameter/ mm
Thermocouple 1	240	20
Port 1	355	20
Thermocouple 2	740	20
Port 2	855	20
Thermocouple 3	1240	20
Port 3	1240	20
Thermocouple 4	1860	20
Port 4	1740	20
Thermocouple 5	2360	20
Port 5	2240	20
Thermocouple 6	2860	20
Port 6	2740	20
Thermocouple 7	3360	20
Sampling Port	3600	20

Figure 3.8 – General arrangement drawing of the 100 kW_{th} CTF

3.3.2 SNCR Optimisation

The injection point and the flow rate of the nitrogen was investigated in order to optimise the SNCR. Four injection points (four different axial locations for the intrusive probe) within the literature temperature range for SNCR were studied along with two nitrogen flow rates. The NO reduction and ammonia slip were measured for each of these axial locations at a NSR of 2.5 to find that ammonia slip decreased as the temperature at the injection point increased and as the nitrogen flow rate increased, while the NO reduction reaches a peak at 1050 °C and 30 L/min of nitrogen (as shown in Figure 3.9); therefore, this axial location was chosen as the ammonia injection site. The higher nitrogen flow rate is likely to aid the penetration of the turbulent combustion gas; while at the higher temperatures, it is likely that the ammonia to NO pathways are incentivised, therefore decreasing the ammonia utilisation efficiency, and at the 950 °C injection point, the flue gas point is too close in

proximity and the reaction time is insufficient for a higher NO reduction or lower ammonia slip.

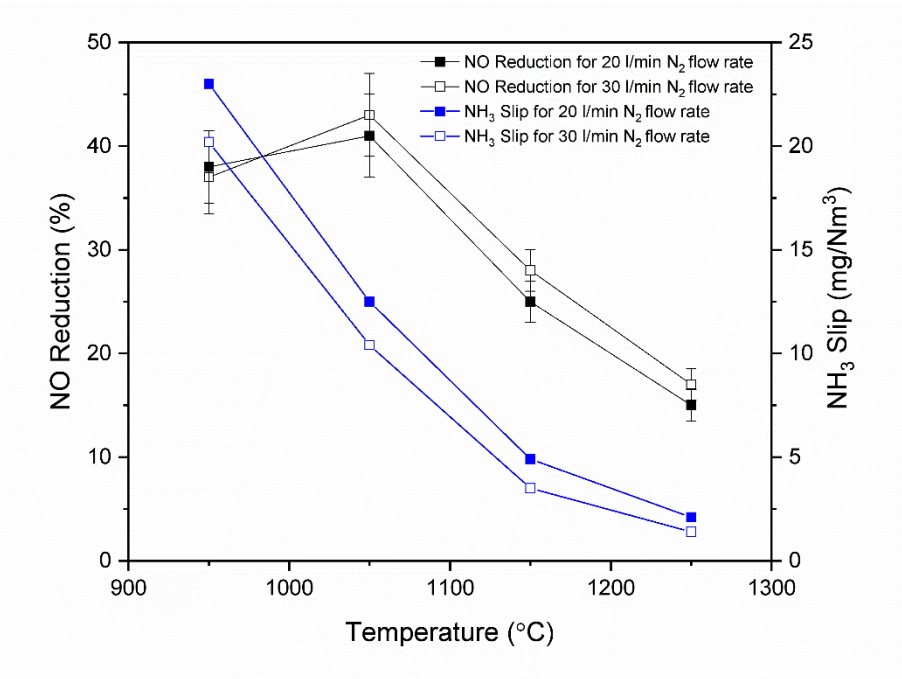

Figure 3.9 – SNCR performance at various axial injection positions

The radial position of the injection probe also has to be optimised for the highest possible NO reduction. For the previous optimisation a radial position of 150 mm was used; for this optimisation, the NO reduction was measured at every 50 mm of probe insertion (bar the 50 mm point) into the furnace until a maximum of 350 mm. The maximum NO reduction was measured for the 150 mm position; at this position, it is likely that the ammonia/nitrogen mix is able to fully penetrate and mix with the turbulent combustion gas. Past this 150 mm point, it is likely that the ammonia/nitrogen mix is overly penetrating the combustion gas and so a portion of ammonia escapes at the far wall. This is displayed in Figure 3.10:

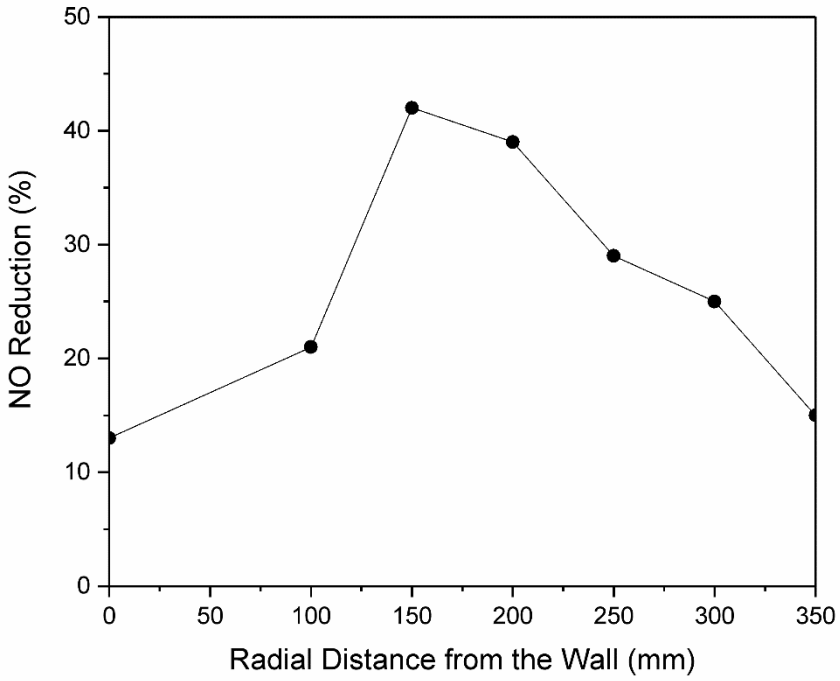

Figure 3.10 – SNCR performance at various radial positions

3.3.3 Operational Method

The actual commencement of the test starts by using propane as the main fuel at around 50 kW_{th} thermal input. When the temperature of the modules near the burner reach around 1000^{o} C then the fuel is switched to pulverised coal. This fuel transition causes a temperature ramp that continues until the temperature near the burner stabilises at around 1300 ^{o}C. The walls of the top section behind the refractory are water-cooled to avoid temperature creep and provide stable operating conditions. The combustion test facility is operated under slight negative pressure (8–12 mmH_2O) achieved with the help of an induced draft fan and a water seal maintained at the lower section of the rig.

Once the aforementioned temperature ramp from the switch to coal from propane has levelled off at ~1300 °C, steady state is assumed to be achieved and the NO concentration in the flue gas is designated as the coal baseline level. Following the acquisition of sufficient data points, approximately 100-120 points (with one reading every ten seconds), at the coal baseline, ammonia is added at a flow rate to give a desired NSR. The NSR range under investigation is between 0-3. This is because during preliminary tests, it was discovered that above a NSR of 3 the self-inhibition effect is observed and NO reduction is greatly decreased. After all the desired NSRs have been investigated, the ammonia addition ceases

and there is a return to coal baseline. This confirms that no reduction in NO can be attributed to a change in initial conditions. The Fe-based additive is then added and the steady state NO reduction is observed. Using the NO concentration in the flue gas for the Fe-based additive baseline as $NO_{initial}$, ammonia is re-introduced to the system at the same NSRs as before. Each combination of NSR and Fe-based additive concentration is observed and recorded for approximately ten minutes. This gives a direct indication of the effect of the Fe-based additive on the NO reduction by SNCR. A simplified infographic of the experimental procedure can be seen in Figure 3.11:

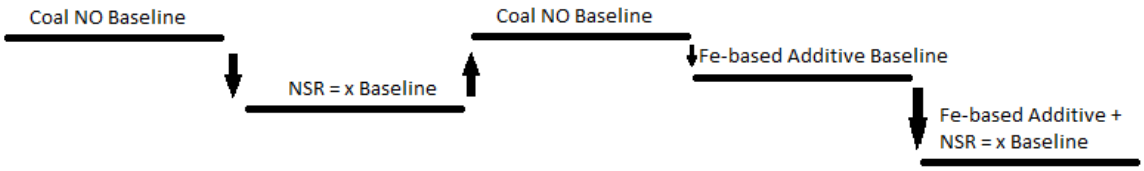

Figure 3.11 – Operational procedure

The coal under investigation was Durrans grade 240 coal, and the as-received ultimate analysis and calorific value is presented below.

Ultimate Analysis (%)							Calorific Value (MJ/kg)
C	H	N	O	S	Moisture	Ash	
69.2	4.4	0.8	18.0	0.6	4.0	3.0	29.57

Table 3.3 – Ultimate analysis and net calorific value of Durrans grade 240 coal

3.4 Cantera's CSTR Model

Cantera is an open-source software package for use in the solution of problems regarding chemical kinetics, thermodynamics and transport processes. Cantera can be used with Python, Matlab or programs using C/C++ and Fortran 90. For work done here, Cantera was used in the Python environment Spyder. It is essentially a package of functions allowing the user to simply define species, phases and reactions and then use this information to kinetically model reactors without having to resort to any complex mathematics.

Cantera's continuously stirred tank reactor (CSTR) function was used to represent the section of the 100 kW_{th} CTF into which the ammonia was added. A CSTR was chosen to be modelled instead of a plug flow reactor (PFR) as this section of the furnace was considered to be well mixed both radially and axially, due to the injection of ammonia in a radial direction as well as eddies present in this section. This CSTR is simply defined to have an

inlet, an outlet, a constant volume and for the species (and energy) to be homogeneously distributed, with the governing equations for single reactors applying. The first step to initiating a Cantera CSTR is to define a solution, which is the mixture that is flowing through the reactor. The solution contains the list of species and reactions, the thermodynamic and transport properties of the species and the kinetic properties of the reactions. Then the initial temperature, pressure and composition of the gas must be inputted and an upstream reservoir must be created containing this gas. The reactor is then created with a set volume (in this case the volume of the section under investigation). An environment is created into which heat is lost from the reactor, along with the wall of the reactor through which the heat is lost. The wall has properties that must be defined: area (A) and heat transfer coefficient (U). The area is inputted as the area of the wall surrounding the section. The heat transfer coefficient was not changed from the example value for two reasons: this U led to an almost isothermal (±5 C) reactor, which was desired in order to assess the impacts of the independent variables, and changing U had little impact on the finishing temperature anyway.

The upstream reservoir is then connected to the reactor through a simulated mass flow controller set to a desired mass flow rate. The exhaust of the reactor is designated as a downstream reservoir and a valve is created to connect the two. A co-efficient, K, must be entered to designate 'how open' the valve is; this was designated as 1, as K must be sufficiently large otherwise there will be a spike in the temperature and pressure, and seeing as the next section in the CTF would have a similar temperature and pressure, this is undesirable. A network is then created combining all the defined operations and, from here, one is able to integrate with time. The model was run for a total time of 10 s with calculations every 1E-04 s. This is displayed in Appendix 2.

How Cantera was utilised and the specific inputs used are described in detail in section 5.3.1. Appendix 1 contains the CTI file used to describe the thermodynamic, transport and kinetic data for all the species and reactions that could be present in an N/H/O system. The species' thermodynamic characteristics are described using NASA 7-coefficient polynomial parameterisation. This is used to compute the specific heat capacity, enthalpy and entropy of a species between a specified temperature range. The transport characteristics for a species is described by inputting parameters relating to collision diameter, atomic

geometry, well depth and polarity. Kinetic data is described using the stoichiometric equation, Arrhenius co-efficient, pre-exponential factor and the activation energy of the reaction.

3.5 FactSage and Deposit Model Design

3.5.1 FactSage Overview

The thermodynamic equilibrium modelling software FactSage was used to investigate theoretical ash deposits. This proprietary software contains thermodynamic databases with thousands of pure substance compounds and hundreds of evaluated and optimised metal oxide and molten and solid salt solutions, as well as many other solutions not applicable in this case (Bale, et al., 2016), which are easily accessible due to a user-friendly GUI. The FactSage 'Equilib' module utilises these databases to model complex multi-phase equilibria using the Gibb's free energy minimisation technique. The limitations to the utilisation of the FactSage databases have been well discussed by Becidan, et al., (2009). These limitations include: the lack of influence of kinetic constraints, residence times and temperature/concentration gradients; a lack of consideration of physical processes; an assumption of perfect mixing; and the results are completely dependent on the input variables and the selected databases. Measures to minimise the impact of these limitations have also been discussed by Becidan, et al., (2009) but, simplified, any model requires careful consideration and full disclosure of input conditions and solution selection in order to grant the ability to compare and contrast with alternative and experimental results.

For predicting ash behaviour within real boilers, laboratory data can prove difficult to collect and utilise; therefore, equilibrium modelling can be used instead as the full composition of the ash and flue gas are taken into account (Rizvi, et al., 2015). This technique has played a leading role, or has even been the sole basis, in a multitude of important studies covering fireside corrosion (Becidan, et al., 2009, Jabaz, et al., 2017, Paneru, et al., 2017), biomass ash challenges (Nordgren, et al., 2013, Zheng, et al., 2007) and additives (Zhou, et al., 2015, Stam and Brem, 2019, Liao, et al., 2015).

3.5.2 Ash Deposit Model

This model is used to study the corrosive potential of ash deposits with varying loadings of fuel additives on stainless steel tubing in the superheater region of a furnace. The corrosive

potential of the ash deposits will be determined by the presence and yield of alkali chlorides and sulphates. It is assumed that the alkali chlorides will be able to diffuse to the metal wall and aid in the production of metal chlorides, however, for simplification, the condensation process is not taken into account. The results of the calculations are not expected to give exact verifiable yields but rather provide trends and information regarding the probability of these additives to impede corrosion under the investigated ash deposit.

A single coal and three biomass fuels (Rizvi, et al., 2015) were investigated. The biomass fuels represent a range of fuels with regard to the silica and potassium contents, with the sunflower husk ash containing very little silica and almost 50% K_2O, while the peanut shell ash and miscanthus husk ash contain much greater silica contents but retain considerable potassium levels. The ash compositions, detected using XRF analysis, are displayed in Table 3.4.

	El Cerrejón (Ca-rich) Coal	Peanut Shell (Rizvi, et al., 2015)	Sunflower Husk (Rizvi, et al., 2015)	Miscanthus Husk (Rizvi, et al., 2015)
Ash (%AR)	2.00	3.20	2.69	3.61
SiO_2 (%)	31.87	35.51	3.21	49.55
TiO_2 (%)	0.50	0.83	0.03	0.01
Al_2O_3 (%)	15.88	8.25	0.48	0.45
Fe_2O_3 (%)	8.59	3.24	0.84	0.41
MgO (%)	2.20	5.16	15.24	2.86
CaO (%)	18.28	9.29	27.16	7.95
Na_2O (%)	2.00	1.33	0.21	2.39
K_2O (%)	0.70	31.10	45.10	30.49
P_2O_5 (%)	0.40	4.52	5.30	5.76
SO_3 (%)	19.58	0.78	2.43	0.13

Table 3.4 – Ash content of each fuel and the composition of each ash

The composition of the Fe-based additive (Daood, et al., 2014a, Daood, et al., 2014b, Daood, et al., 2017) was derived from Daood, et al., (2014b) by taking an average of all the individual components and then normalising the mixture. The ash from the tested coal was used for comparison with the Fe-based additive and named Ca-rich coal ash for its

considerable calcium content; this was chosen for convenience and due to the relatively high content of alumina and silica in the ash, making it an appropriate candidate for use as reuse in actual boilers. Another coal ash (Al-rich coal ash), with a greater Si/Al content, was tested as a comparison to highlight the impact of contaminants within the coal ash, along with 'pure' alumina to test that reduced activity would in fact be reported by FactSage. The compositions of the additives used are presented below.

	Fe-based Additive (Daood, et al, 2014)	Ca-rich Coal Ash	Al-rich Coal Ash (Daood, et al., 2017)	Alumina (Llorente, et al., 2008)
SiO_2 (%)	38.04	31.87	56.28	0.87
TiO_2 (%)	0.20	0.50	1.04	0.00
Al_2O_3 (%)	4.60	15.88	23.38	97.63
Fe_2O_3 (%)	49.24	8.59	6.62	0.37
MgO (%)	1.44	2.20	2.10	0.35
CaO (%)	3.94	18.28	6.31	0.22
Na_2O (%)	0.79	2.00	0.37	0.39
K_2O (%)	0.64	0.70	2.19	0.02
P_2O_5 (%)	0.44	0.40	0.58	0.02
SO_3 (%)	0.67	19.58	1.13	0.11

Table 3.5 – Composition of each additive

Reactants were inputted into the module so that each model contained flue gas from the combustion of 1 kg of the respective fuel with an excess air of 18% (the compositions of which are shown in Table 3.6), 5 g of T22 steel (the composition of which is shown in Table 3.7) and 100 g of accumulated ash deposit.

	Coal	Peanut Shell	Sunflower Husk	Miscanthus Husk
CO_2 (g)	2786.96	1555.40	1644.28	1597.20
H_2O (g)	459.36	530.82	547.02	523.44
N_2 (g)	8954.09	4518.06	4852.41	4565.29
O_2 (g)	415.36	209.48	224.89	211.43
SO_2 (g)	8.00	3.32	2.19	1.86
HCl[a] (g)	1.19[b]	1.08[c]	1.44[d]	1.44[e]

Table 3.6 – Composition of the flue gas for each fuel ([a] Based on typical flue gas values [b] Kurkela, 1996 [c] Perea-Moreno, et al., 2018 [d] Jagustyn, et al., 2011 [e] Hallgren, et al., 1999)

	C	Si	Mn	P	S	Cr	Mo	Fe
T22	0.05-0.15	≤0.50	0.30-0.60	≤0.025	≤0.025	1.90-2.60	0.87-1.13	Bal.

Table 3.7 – Composition of T22 Steel (ThyssenKrupp Materials International, 2011)

Six additive fuel loadings were investigated (0%, 1.5%, 3.0%, 5.5%, 6.6%, 8%); the last four being chosen due to their use in Chapter 5, 0% being chosen in order to set a baseline behaviour and 1.5% being chosen in order to investigate any transitory behaviour between 0% and 3.0%. Ash mixtures were calculated by combining the masses of the individual ash components within 1 kg of each fuel with the masses of the individual additive components needed to load the fuel to the specified loading. The calculated compositions are presented below:

	Coal (%)	Fe-based Additive				
		1.5% (%)	3.0% (%)	5.5% (%)	6.6% (%)	8.0% (%)
SiO2	31.87	32.67	33.29	34.06	34.32	34.61
TiO2	0.50	0.46	0.43	0.39	0.38	0.37
Al2O3	15.88	14.41	13.28	11.88	11.40	10.87
Fe2O3	8.59	13.89	17.97	23.01	24.74	26.65
MgO	2.20	2.10	2.02	1.93	1.90	1.86
CaO	18.28	16.41	14.97	13.20	12.58	11.91
Na2O	2.00	1.84	1.72	1.57	1.52	1.46
K2O	0.70	0.69	0.69	0.68	0.68	0.67
P2O5	0.40	0.40	0.41	0.41	0.42	0.42
SO3	19.58	17.12	15.22	12.87	12.07	11.18

Table 3.8 – Calculated compositions of the coal cases

	Peanut	Fe-Based Additive					Ca-rich Coal Ash				
	Shell (%)	1.5% (%)	3.0% (%)	5.5% (%)	6.6% (%)	8.0% (%)	1.5% (%)	3.0% (%)	5.5% (%)	6.6% (%)	8.0% (%)
SiO2	35.51	36.32	36.74	37.11	37.22	37.32	34.34	33.74	33.20	33.05	32.90
TiO2	0.83	0.63	0.52	0.43	0.41	0.38	0.72	0.67	0.62	0.61	0.59
Al2O3	8.25	7.08	6.48	5.93	5.78	5.64	10.70	11.96	13.09	13.40	13.71
Fe2O3	3.24	18.00	25.58	32.40	34.30	36.17	4.96	5.84	6.63	6.85	7.07
MgO	5.16	3.97	3.35	2.80	2.65	2.50	4.21	3.72	3.28	3.16	3.04
CaO	9.29	7.57	6.69	5.90	5.68	5.46	12.17	13.65	14.99	15.36	15.72
Na2O	1.33	1.16	1.07	0.98	0.96	0.94	1.54	1.65	1.75	1.78	1.81
K2O	31.10	21.33	16.31	11.79	10.54	9.30	21.35	16.34	11.83	10.58	9.34
P2O5	4.52	3.21	2.54	1.93	1.77	1.60	3.20	2.52	1.91	1.74	1.57
SO3	0.78	0.74	0.72	0.71	0.70	0.70	6.81	9.91	12.69	13.47	14.23
	Peanut	Al-rich Coal Ash					Alumina				
	Shell (%)	1.5% (%)	3.0% (%)	5.5% (%)	6.6% (%)	8.0% (%)	1.5% (%)	3.0% (%)	5.5% (%)	6.6% (%)	8.0% (%)
SiO2	35.51	42.17	45.60	48.68	49.53	50.38	24.40	18.69	13.56	12.13	10.72
TiO2	0.83	0.89	0.93	0.96	0.97	0.98	0.56	0.42	0.30	0.27	0.23
Al2O3	8.25	13.10	15.60	17.84	18.46	19.08	36.91	51.66	64.91	68.59	72.23
Fe2O3	3.24	4.33	4.88	5.38	5.52	5.66	2.32	1.85	1.42	1.31	1.19
MgO	5.16	4.17	3.67	3.22	3.09	2.97	3.62	2.82	2.11	1.91	1.72
CaO	9.29	8.33	7.84	7.40	7.28	7.16	6.38	4.88	3.54	3.16	2.80
Na2O	1.33	1.02	0.86	0.72	0.68	0.64	1.03	0.88	0.74	0.70	0.66
K2O	31.10	21.83	17.06	12.77	11.58	10.40	21.13	16.01	11.40	10.12	8.85
P2O5	4.52	3.26	2.61	2.02	1.86	1.70	3.08	2.34	1.67	1.48	1.30
SO3	0.78	0.89	0.95	1.00	1.02	1.03	0.56	0.45	0.36	0.33	0.30

Table 3.9 – Calculated compositions of the peanut shell cases

	Sunflower	Fe-Based Additive					Ca-rich Coal Ash				
	Husk (%)	1.5% (%)	3.0% (%)	5.5% (%)	6.6% (%)	8.0% (%)	1.5% (%)	3.0% (%)	5.5% (%)	6.6% (%)	8.0% (%)
SiO2	3.21	15.68	21.57	26.60	27.95	29.27	13.47	18.32	22.46	23.57	24.66
TiO2	0.03	0.09	0.12	0.15	0.15	0.16	0.20	0.28	0.35	0.36	0.38
Al2O3	0.48	1.95	2.65	3.25	3.41	3.56	5.99	8.60	10.82	11.42	12.01
Fe2O3	0.84	18.17	26.36	33.35	35.23	37.06	3.61	4.93	6.05	6.35	6.64
MgO	15.24	10.30	7.97	5.98	5.44	4.92	10.57	8.36	6.48	5.97	5.48
CaO	27.16	18.85	14.92	11.57	10.66	9.78	23.98	22.48	21.20	20.85	20.52
Na2O	0.21	0.42	0.51	0.60	0.62	0.64	0.85	1.15	1.41	1.48	1.55
K2O	45.10	29.18	21.66	15.24	13.51	11.83	29.20	21.69	15.28	13.56	11.87
P2O5	5.30	3.56	2.74	2.04	1.85	1.66	3.55	2.72	2.01	1.82	1.63
SO3	2.43	1.80	1.50	1.25	1.18	1.11	8.57	11.47	13.95	14.61	15.26
	Sunflower	Al-rich Coal Ash					Alumina				
	Husk (%)	1.5% (%)	3.0% (%)	5.5% (%)	6.6% (%)	8.0% (%)	1.5% (%)	3.0% (%)	5.5% (%)	6.6% (%)	8.0% (%)
SiO2	3.21	22.21	31.19	38.85	40.92	42.93	2.37	1.98	1.64	1.55	1.46
TiO2	0.03	0.39	0.56	0.71	0.75	0.79	0.02	0.01	0.01	0.01	0.01
Al2O3	0.48	8.68	12.55	15.86	16.75	17.62	35.26	51.70	65.72	69.50	73.19
Fe2O3	0.84	2.91	3.89	4.72	4.95	5.17	0.67	0.59	0.53	0.51	0.49
MgO	15.24	10.53	8.31	6.41	5.90	5.40	9.91	7.39	5.24	4.66	4.10
CaO	27.16	19.70	16.17	13.16	12.35	11.56	17.51	12.96	9.07	8.02	7.00
Na2O	0.21	0.27	0.30	0.32	0.33	0.33	0.28	0.31	0.33	0.34	0.35
K2O	45.10	29.74	22.47	16.28	14.61	12.98	28.96	21.33	14.82	13.07	11.36
P2O5	5.30	3.61	2.81	2.13	1.95	1.77	3.41	2.52	1.75	1.55	1.35
SO3	2.43	1.97	1.75	1.56	1.51	1.46	1.60	1.21	0.87	0.78	0.70

Table 3.10 – Calculated compositions of the sunflower husk cases

	Miscanthus Husk (%)	Fe-Based Additive					Ca-rich Coal Ash				
		1.5% (%)	3.0% (%)	5.5% (%)	6.6% (%)	8.0% (%)	1.5% (%)	3.0% (%)	5.5% (%)	6.6% (%)	8.0% (%)
SiO2	49.55	46.17	44.32	42.60	42.11	41.62	44.36	41.52	38.87	38.12	37.37
TiO2	0.01	0.07	0.10	0.13	0.13	0.14	0.15	0.23	0.31	0.33	0.35
Al2O3	0.45	1.67	2.33	2.95	3.13	3.31	4.98	7.45	9.77	10.43	11.09
Fe2O3	0.41	14.74	22.57	29.89	31.98	34.06	2.81	4.12	5.35	5.70	6.05
MgO	2.86	2.44	2.22	2.00	1.94	1.88	2.67	2.56	2.46	2.43	2.40
CaO	7.95	6.77	6.13	5.53	5.36	5.19	10.98	12.64	14.19	14.63	15.07
Na2O	2.39	1.92	1.66	1.42	1.35	1.28	2.27	2.21	2.15	2.14	2.12
K2O	30.49	21.73	16.94	12.47	11.19	9.92	21.75	16.97	12.50	11.23	9.96
P2O5	5.76	4.20	3.35	2.55	2.32	2.09	4.19	3.33	2.52	2.29	2.07
SO3	0.13	0.29	0.37	0.46	0.48	0.50	5.84	8.96	11.87	12.70	13.53
	Miscanthus Husk (%)	Al-rich Coal Ash					Alumina				
		1.5% (%)	3.0% (%)	5.5% (%)	6.6% (%)	8.0% (%)	1.5% (%)	3.0% (%)	5.5% (%)	6.6% (%)	8.0% (%)
SiO2	49.55	51.53	52.61	53.62	53.90	54.19	35.26	27.46	20.16	18.08	16.01
TiO2	0.01	0.31	0.48	0.63	0.68	0.72	0.01	0.01	0.00	0.00	0.00
Al2O3	0.45	7.18	10.86	14.29	15.27	16.25	28.98	44.56	59.12	63.27	67.42
Fe2O3	0.41	2.23	3.23	4.16	4.42	4.69	0.40	0.39	0.39	0.39	0.39
MgO	2.86	2.64	2.51	2.40	2.37	2.33	2.12	1.72	1.35	1.24	1.13
CaO	7.95	7.47	7.21	6.96	6.89	6.82	5.68	4.44	3.28	2.95	2.62
Na2O	2.39	1.80	1.47	1.17	1.09	1.00	1.80	1.48	1.19	1.10	1.02
K2O	30.49	22.18	17.64	13.40	12.19	10.99	21.55	16.66	12.09	10.79	9.49
P2O5	5.76	4.24	3.41	2.63	2.41	2.19	4.08	3.16	2.30	2.05	1.81
SO3	0.13	0.42	0.59	0.74	0.78	0.82	0.13	0.12	0.12	0.12	0.12

Table 3.11 – Calculated compositions of the miscanthus husk cases

A temperature range was chosen in order to simulate the possible temperature range witnessed in an ash deposit, from 400 °C at the tube wall to 900 °C in the flue gas in steps of 10 °C (Figure 3.12), while the step change was chosen so as not to omit any results that may have a short but pivotal formative temperature window. This temperature range also allows for analysis of superheaters of differing operating temperatures.

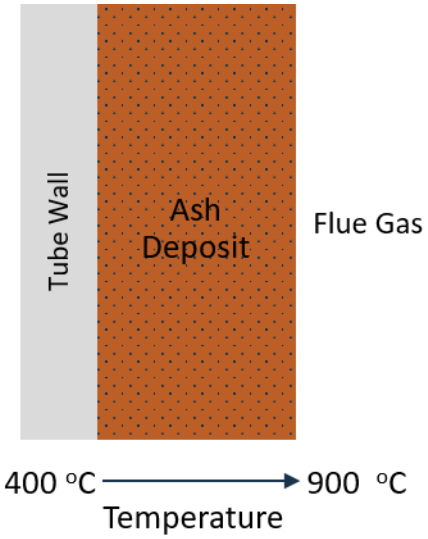

Figure 3.12 – The possible temperature gradient through an ash deposit

This study utilises four databases within FactSage:

- FactPS, a collection of data related to pure substances,
- FToxid, a collection of pure oxides and oxide solutions, including various slag solutions,
- FTsalt, a collection of pure salts and salt solutions,
- FTpulp, a database designed for the paper and pulp industry but very applicable to solid fuel combustion due to the collection of sodium and potassium compounds (including chlorides, sulphates and pyrosulphates).

Four solutions are used in combination:

- FTpulp-MeltB, containing liquid phase alkali salts, hence simulating corrosive melt formations,
- FTpulp-Hexa, containing solid phase alkali sulphates, carbonates and sulphides (this solution must be dilute in sulphides and high temperature to be valid),
- FTpulp-ACl, containing solid phase alkali chlorides (with dissolved alkali hydroxides),
- FTpulp-OrtB, a low temperature solid phase solution of alkali sulphates and carbonates requiring a high concentration of K_2SO_4.

The selection of these solutions allows for the monitoring of the production of species that are either responsible for the initiation of corrosive processes or are by-products of this corrosion. The yields of these species act as metrics representing corrosive potential, and any changes in these yields indicate an impact of the addition of additive to the tested ash deposits.

CHAPTER 4 THE IMPACT OF BURNER STAGING ON NO REDUCTION BY REBURNING DURING OXY-COAL COMBUSTION

4.1 Introduction

In pulverised fuel combustion systems for power generation, there are a number of primary NO_x abatement technologies employed, including low-NO_x burners, overfire air staging and flue gas recirculation, and they rely, to an extent, on reburn reactions, whereby NO is reduced in the flame/boiler through reaction with fuel fragments. Many investigations into oxy-coal combustion are either unstaged or utilise overfire air (furnace staging). However, the rate of NO reduction by reburning in the overfire stream would be far lower than that of the tertiary stream of a staged flame, due to the crucial role of the external recirculation zone returning oxidant from the tertiary stream to the root of the flame. Not to mention, the primary zone during furnace staging (overfire air) is an extremely corrosive location, therefore it is both preferable and necessary to minimise the contact of this corrosive (fuel-rich) atmosphere with the furnace walls. Thus, it would be more desirable to utilise low NO_x burners as the primary NO_x abatement technology of choice and to optimise their operation, in order to reduce load on a selective catalytic reduction (SCR) unit that would be required to achieve zero-emission combustion.

This chapter focuses on investigating the performance of a down-scaled model of a popular industrial low-NO_x burner during oxy-coal combustion with a simulated dry recirculated flue gas. The low-NO_x burner will be optimised for the minimisation of NO formation and the greatest destruction of recycled NO, while maintaining combustion efficiency. This will be assessed through measurements in the flame and the flue gas, as well as imaging, giving insight into the changing conditions inside the furnace and structure of the flame. This work aims to deliver a greater grasp on the impact of changes in flame structure and, subsequently, local stoichiometry within regions of the flame on NO destruction, ultimately improving confidence in this carbon capture technology and highlighting its inherent low NO_x nature. The burner setting is described with the term 'secondary oxidant proportion' (S), which represents the proportion of the total oxidant flow flowing through the burner's

secondary register. The process for changing the secondary oxidant proportion is described in Chapter 3. This chapter has been published in its entirety in Energy and Fuels.

4.2 Commissioning

Before beginning the investigation, it must be determined how the rig will be operated in terms of two variables that should be kept constant; these are the proportion of oxidant to flow through the primary register and the registers through which NO should be injected. The burner tested has 3 air registers; primary (containing fuel), secondary and tertiary. To simulate oxy-coal combustion NO can be injected into any of the burner flow registers. The NO concentration in the primary stream can be varied independently of the secondary/tertiary line to allow for NO staging in the flame and making it possible to inject NO into either only one line or both. Baseline tests were carried out at 200 kW_{th} to first determine the impact of varying the proportion of primary oxidant and to find an optimum, which would remain constant for all future tests. This method of maintaining the primary oxidant proportion when moving from air-firing to oxy-firing is endorsed by literature as promoting flame stability (Fry, et al., 2011 and Gharebaghi, et al., 2011) and is in opposition to the method of maintaining a fixed primary velocity. The proportion of primary oxidant was varied between 16% and 22% (using the input controls on the HMI) of the total air flow for air-coal combustion across a range of secondary oxidant proportions (varied by changing the position of the portioning sliding damper), this is presented in Figure 4.1. The 20% option for the proportion of primary oxidant was visually perceived as leading to the most distinct and stable flames, as well as to a marginally lower NO concentration in the flue gas and unburned carbon in the ash. From Figure 4.1, it can also be observed that a secondary oxidant proportion of 0.36-0.39 leads to both optimal combustion efficiency and adequate NO, when compared with the other cases.

The firing regime was then changed to 28% O_2/CO_2 (OF 28), but the proportion of primary oxidant was maintained at 20% due to the consensus regarding flame stability formed from the air combustion case. Compared to the air case, the NO emissions, reported as ppm, at OF 28 are expected to be greater than air due to lack of dilution by N_2. However, due to a possible greater CO and hydrocarbon concentration in the fuel-rich region of the flame, a greater destruction of initially produced NO is witnessed, resulting in decreased NO concentration in the flue gas. The trends from both the air and the OF 28 case indicate that

by operating the burner in order to increase flow of the tertiary stream controls NO formation, by creating a flame with less swirl, hence influencing the char-volatile split in favour of volatile-N formation.

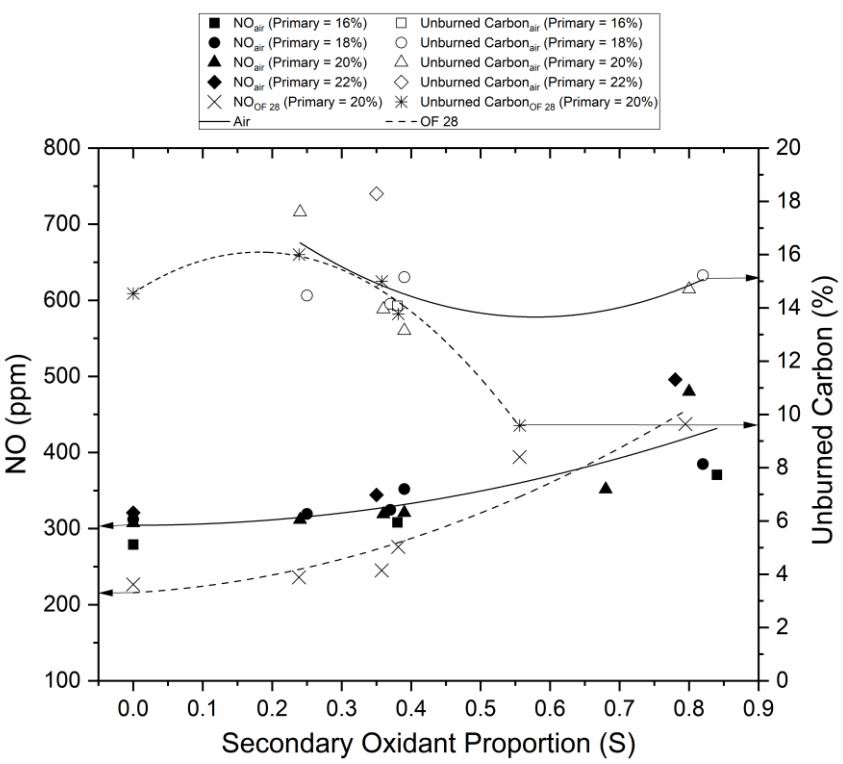

Figure 4.1 – The impact of varying the secondary oxidant proportion and the primary oxidant proportion on NO concentration in the flue gas and unburned carbon in the ash for the air and OF 28 cases

In order to address the issue of differing flue gas volume between the air and OF 28 case, the change in NO_x emission rate with changing secondary oxidant proportion is presented in Figure 4.2. One highlight from this graph is that the OF 28 case produces only ~50% of the NO per unit of thermal input that the air case produces when S: 0.35, which is a similar observation to that made in Liu, et al., (2005b) where a staged OF 30 flame was compared to air and found to cut the conversion of fuel-N to NO in half. A lower secondary oxidant proportion reduces the secondary flow rate causing less transfer of O_2 into the fuel-rich region and hence decreasing O_2 availability and causing less NO formation. Furthermore, this lack of O_2 availability will also increase the CO concentration in the fuel-rich region, increasing the reduction of recently formed NO on char (Levy, et al., 1981). The lack of nitrogen in the oxy-fuel case would also lead to a negligible thermal-NO process, although,

on an industrial scale, it would be difficult to completely prevent air ingress and hence the thermal-NO process. These phenomena optimally combine with acceptable combustion efficiency between an S: 0.30 and 0.40 to give the emission rate and unburned carbon in ash seen in Figures 4.1 and 4.2.

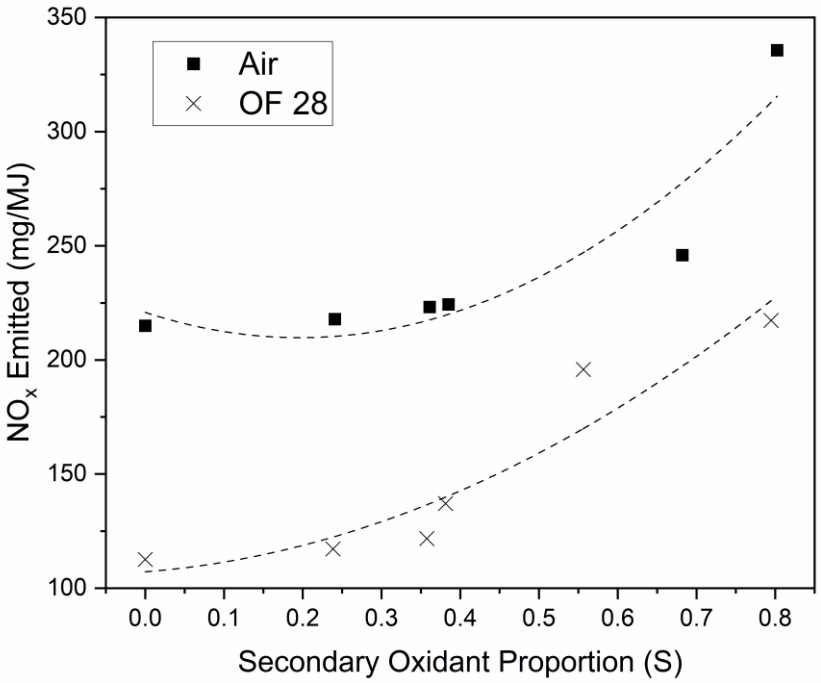

Figure 4.2 – The impact of changing the secondary oxidant proportion on the NO_x emission rate, reported as NO_2, for the air and OF 28 case

In order to simulate the presence of dry NO (recycled from the stream post-condenser in a conventional air combustion plant) in the recycled flue gas, 160-1016 ppm NO (28-700 mg/MJ NO_x reported as NO_2) was injected into the air stream while using an S: 0.36. The injection of the recycled NO was varied between only the primary, only the secondary and tertiary, and each stream proportionally, with the objective of studying the effect of each injection method on eventual destruction of recycled NO. The recycled NO seems to undergo complete conversion to N_2 when it was injected only in the primary stream, resulting in 100% NO destruction being recorded and presented in Figure 4.3; this is believed to be due to the strong fuel-rich zone in the route of the primary air, presenting a greater concentration of volatile-C and volatile-N which plays a critical role in reducing the NO. Furthermore, there is even a slight decrease in the NO_x emission rate when NO is recycled into the primary stream; this is in agreement with Spinti and Pershing's (2003)

findings that the presence of NO in the initial combustion zone decreases char-N to NO conversion, due to the higher partial pressure of NO inside the pores of the coal particles.

When recycled NO was injected into all the air streams to the burner (Figure 4.3 and Figure 4.4), over 80% of the recycled NO was destroyed. The total NO emissions measured in the flue gas with this configuration ranged from 350-473 ppm (245-330 mg/MJ) for S: 0.36. This drop in NO destruction is most likely due to the comparative lack of reburning reactions in the pathway of the secondary and tertiary streams, with a portion of these streams being lost to the flue gas rather than being caught up in the external recirculation zone. This is made evident by the lowest recorded NO destruction being observed when NO is recycled into these streams only (Figure 4.3). Figure 4.3 compares the measured NO_x values to a theoretical NO_x measurement where no reburning mechanisms are taking place, this theoretical value is calculated assuming the injected NO is oxidised to NO_2 in:

$$NO_{x_{Theoretical}} = NO_{x_{Baseline}} + (\frac{46}{30} \times NO_{x_{Injected}}) \qquad (4\text{-}1)$$

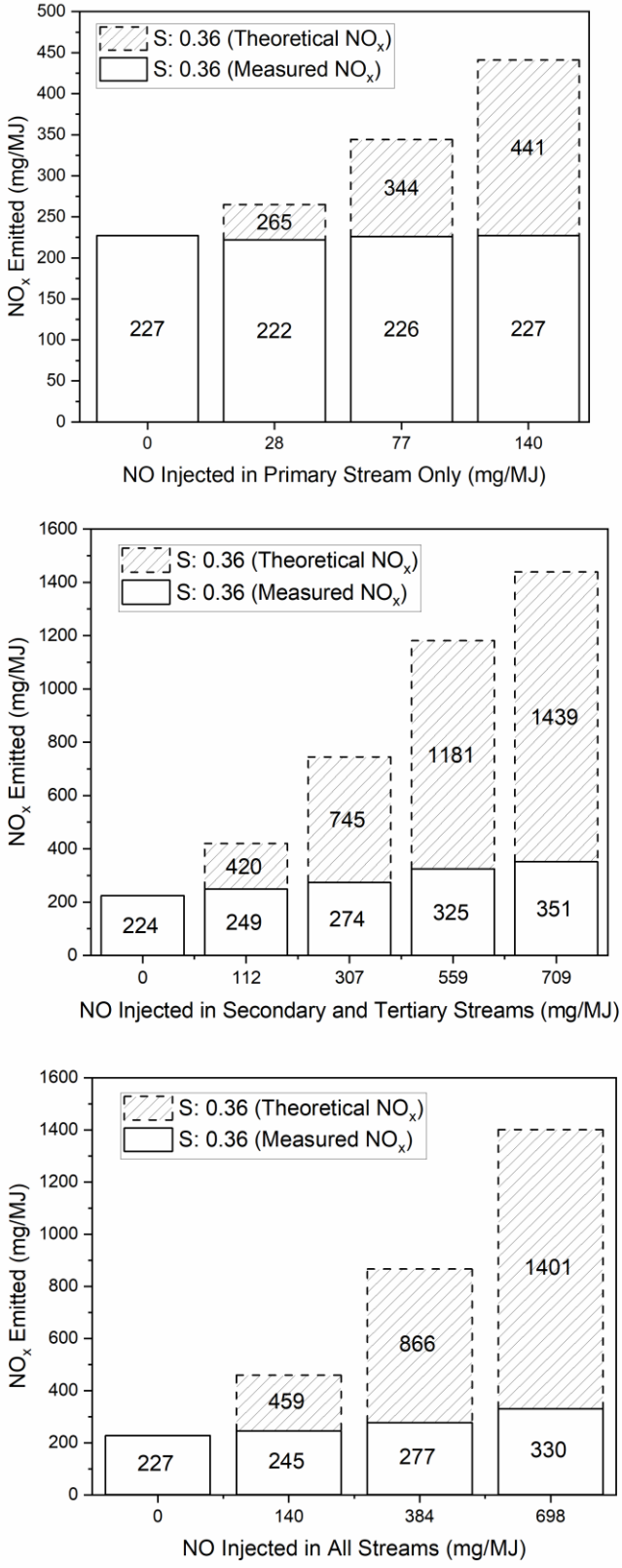

Figure 4.3 – Theoretical and actual NO_x, reported as NO_2, emissions for the air case when NO is recycled into the oxidant either into the primary stream, the secondary and tertiary streams or all streams

Figure 4.4 summarises and compares the impact on NO destruction when both the concentration of recycled NO (from 160-1016 ppm) and the secondary oxidant proportion (from 0.00 – 0.68) are altered. This shows that NO destruction remains high at around 80% for a range of secondary oxidant proportions, while the greatest NO destruction is seen for the moderate secondary oxidant proportions, S of 0.36 and 0.39 and the moderate NO recycling regime (440 ppm). Furthermore, the lowest recorded NO destruction rates are always seen when the NO recycling is 160 ppm, with the highest secondary oxidant proportion presenting the worst set of NO destruction rates.

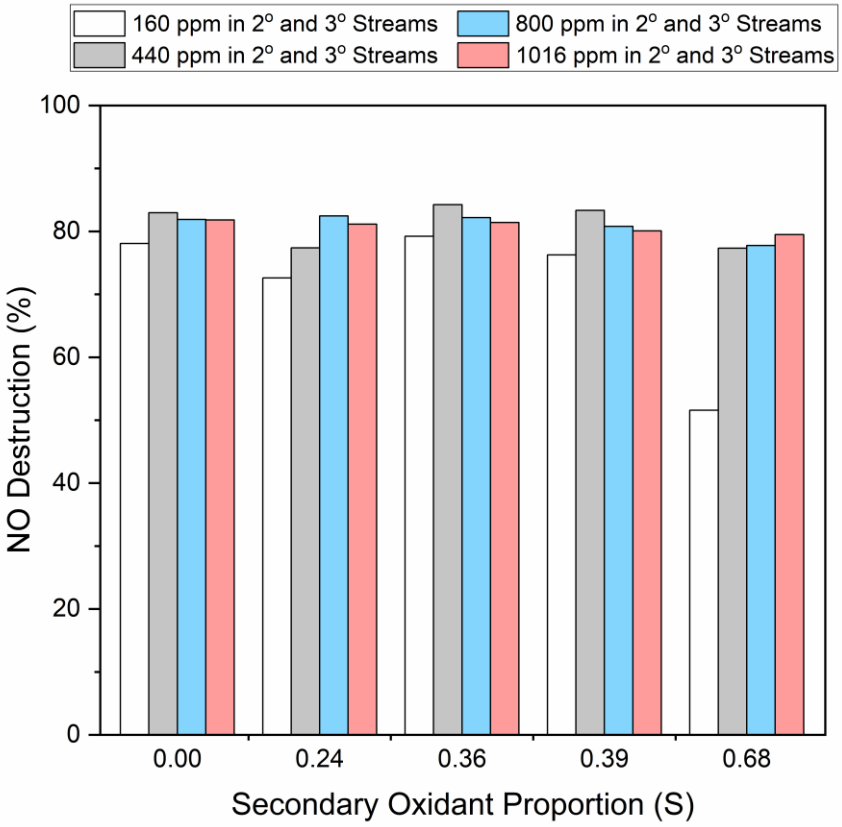

Figure 4.4 – The effect of varying secondary oxidant proportion (and recycling regime) on the destruction of recycled NO for the air case

Figure 4.5 outlines the overall impact of a range of recycled NO injections into either just the secondary and tertiary oxidant registers or all the oxidant registers for the OF 28 case. The overall emissions of NO measured in the flue gas when recycled NO was injected into each oxidant stream ranged from 168-203 mg/MJ resulting in ~80% of the recycled NO being destroyed for S of 0.36; while when the injection was only into the secondary and

tertiary streams, the rate of NO destruction decreased as more NO was recycled away from ideal reburning conditions. The observed destruction of simulated recycled NO is most likely caused by reactions similar to reburning, where the NO would be reduced in the fuel-rich zone by hydrocarbon radicals formed from volatile-C to generate amine and cyanide intermediates, similar to volatile-N (Toftegaard, et al., 2010). This mechanism is believed to account for 50-80 % of the NO reduction with the remaining reduction (10-50 %) caused by reaction with volatile-N to form N_2, as well as contributions from reduction on char (Toftegaard, et al., 2010). When the secondary oxidant proportion is decreased, the secondary/tertiary oxidant partitioning is split in favour of the tertiary stream, enabling limited initial NO formation and greater hydrocarbon radical generation due to the reduced oxygen present in the fuel-rich zone. This phenomenon, also reported by Mackrory and Tree (2012, 2009) for oxy-fuel combustion, supports greater rate of NO destructions due to temperature rise and faster conversion of fuel-N to volatile-N. This results in an increased probability of N_2 formation rather than NO formation, especially in the O_2-starved fuel-rich zones.

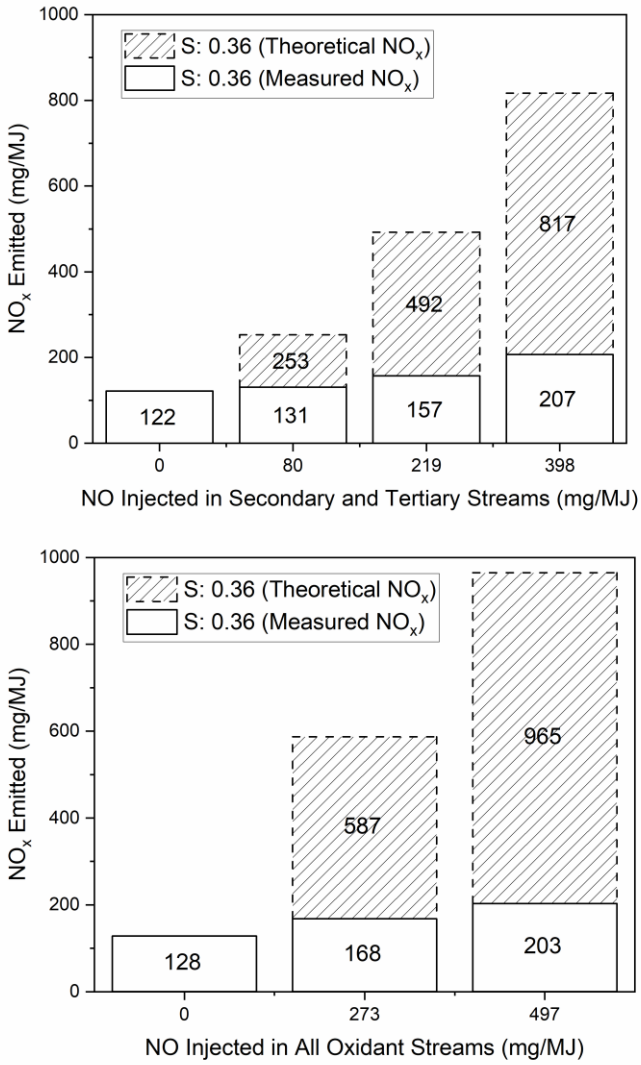

Figure 4.5 – Theoretical and actual NO_x, reported as NO_2, emissions for the OF 28 case when NO is recycled into the oxidant either into the secondary and tertiary streams or all streams

The impact of changing the secondary oxidant proportion on the destruction of recycled NO during the OF 28 regime is displayed in Figure 4.6. When NO is injected into the secondary and tertiary streams only, there is a slight increase in NO destruction with decreasing S values. Whereas, when NO is injected into all the oxidant streams, the NO destruction is greatest at the moderate S values (0.36 and 0.38) which coincide with the optimum values seen in Figure 4.1. There is much greater stability in the NO destruction rate over the range of burner configurations when NO is injected into all streams, as compared to solely the secondary and tertiary streams. A comparison of Figure 4.4 and Figure 4.6 shows that there are only minor differences in the rate of NO destruction

between air and OF 28 cases. Further to this, regardless of the regime, the same trend is witnessed, where the highest NO recycling case, when injected into solely the secondary and tertiary streams, provides the lowest NO destruction rate when a high secondary oxidant proportion is used. Due to these observations and the logic that in an operating oxy-fuel plant there would be recycled flue gas in each stream (and operating otherwise would be complicated and expensive), it can be concluded that it is necessary to inject NO into each stream during the post-commissioning tests, in order to gather a comprehensive understanding of the impact of burner configuration on NO reburning.

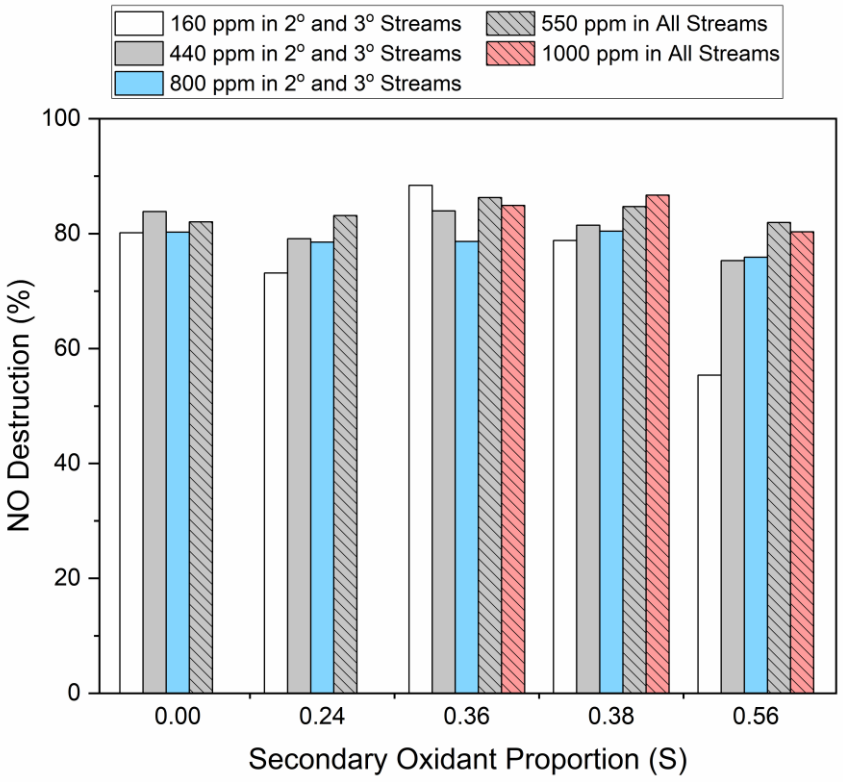

Figure 4.6 – The effect of varying secondary oxidant proportion (and recycling regime) on the destruction of recycled NO for the OF 28 case

Figure 4.7 shows a plot depicting NO_x emission rates at varying levels of NO recycling for a single burner configuration during the air and OF 28 regimes. This highlights that the difference in the NO_x emission rates for the air and OF 28 regimes at the flue results from the difference in initial NO production in the two flames, while the NO_x destruction rate remains similar.

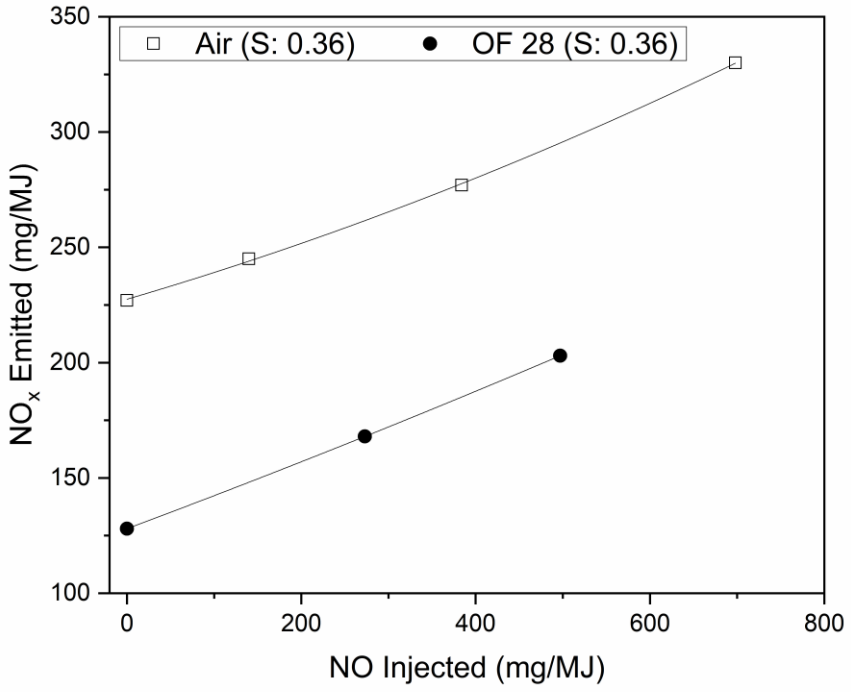

Figure 4.7 – The effect of varying recycled NO on emissions of NO_x, reported as NO_2, for the air and OF 28 cases at equivalent secondary oxidant proportion

As seen in Table 4.1, the data collected for the OF 28 case showed far greater standard deviations for the OF 28 case than the air case. To combat this, the burner output was decreased 15% (from 200 kW_{th} to 170 kW_{th}) in order to reach steady state more swiftly each test day and, therefore, be able to collect a greater amount of data; furthermore, the oxygen concentration in the primary stream was increased from 18.5% to 21% in order to increase flame stability thus reducing any variation in the data caused by an unstable flame. Now at 170 kW_{th}, 27% O_2/CO_2 was swapped for the 28% O_2/CO_2 in order to discourage comparison between the data at 170 and 200 kW_{th}, which would have different O_2 concentrations in the primary stream. In addition, using a 27% O_2/CO_2 case would also provide greater variance between the two planned oxy-fuel cases, one high (OF 30) and one low (now OF 27), highlighting conflicting trends.

	CO_2 (vol%, dry)	NO (ppmv, dry)	O_2 (vol%, dry)
Air (200 kW_{th})	15.53 ± 0.16	329.80 ± 7.81	3.25 ± 0.12
OF 28 (200 kW_{th})	94.26 ± 0.51	281.94 ± 27.00	4.17 ± 0.90

Table 4.1 – Raw flue gas composition when ratio of secondary to tertiary oxidant flow is 45:55

4.3 Experimental Results

4.3.1 Recycling NO into OF 27 and OF 30 at 170 kW_{th}

Moving to 170 kW_{th} and OF 27, the proportion of the total oxidant flowing through the primary register was maintained at 20% and a variety of secondary oxidant proportions and NO injection rates were investigated. Figure 4.8 shows the NO concentration in the flue gas and the unburned carbon in the ash at these different conditions, along with data points from two OF 30 cases at secondary oxidant proportion values chosen for achieving satisfactory NO concentrations and unburned carbon values at OF 27. The trendlines in the figure are for the OF 27 cases only. As seen in Figure 4.8, unburned carbon in particular is significantly affected by the burner configuration, decreasing markedly with an increase in secondary oxidant proportion; the increased burnout can be attributed to better mixing of oxygen into the fuel-rich region caused by both the increased flow of the secondary stream and the subsequent intensification of the flame's swirl.

The best performing burner configuration for the OF 27 case was found to be at S: 0.50; however, when this configuration was used at OF 30, the NO concentration in the flue gas was far greater than for the other tested OF 30 case at a S value of 0.36. The increase in NO emissions between these two OF 30 conditions can be attributed to the same conditions that cause low unburned carbon at OF 27, better mixing of oxygen into the fuel-rich region caused by both the increased flow of the secondary stream and the subsequent intensification of the flame's swirl causing greater fuel-N to NO conversion. This impact on NO is not seen for the OF 27 case until a greater secondary oxidant proportion of S: 0.57; this is due to the OF 30 case having a smaller overall gas volume and greater oxygen concentrations in the secondary and tertiary streams, resulting in more efficient fuel-N oxidation. When directly comparing the two S: 0.36 cases, one can conclude that the OF 30 regime leads to a lower NO concentration in the flue gas than the OF 27 regime; this can be thought to be due to the oxidant, during the OF 30 regime, having a lower density and mass flow, coupled with lower volumetric flow, thus forming a flame with less swirl momentum. This would result in reduced mixing of oxygen into the fuel-rich region and less fuel-N oxidation.

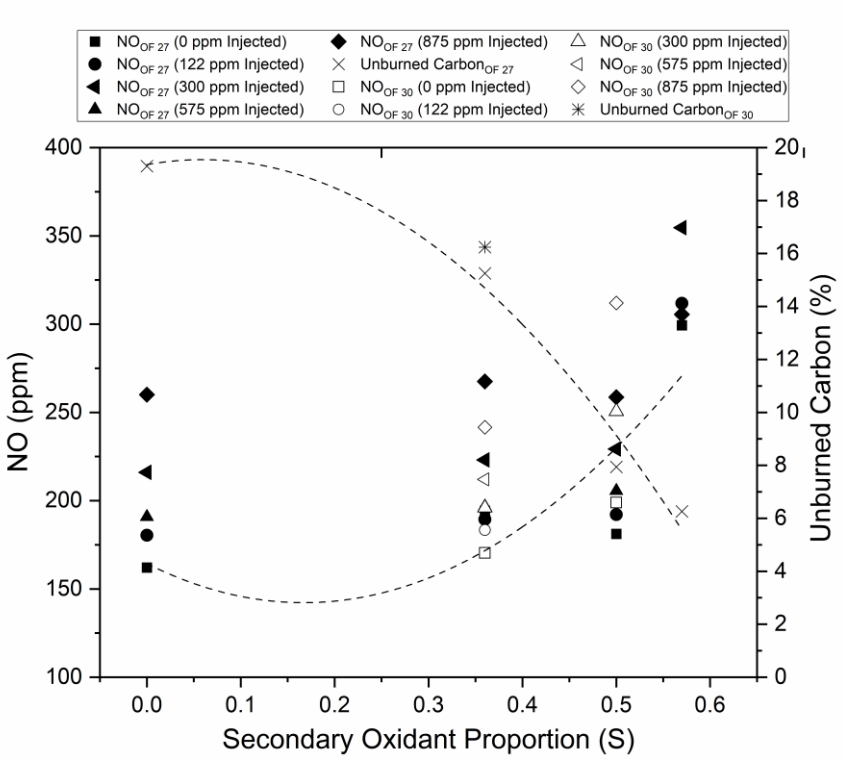

Figure 4.8 – The impact of varying the secondary oxidant proportion and NO recycling regime on NO concentration in the flue gas and unburned carbon in the ash for the OF 27 and OF 30 cases

In addition, the variation in NO concentration between the OF 27 case and the OF 30 case at S: 0.36 could be due to the greater temperature of the OF 30 flame as seen in Figure 4.9. This would cause the char/volatile partitioning to be in favour of volatile formation (Kambara, et al., 1993) (Mackrory and Tree, 2009) and the char-N to NO conversion rate to decrease slightly. The combination of these phenomena has a greater impact than the increase in char-N to NO conversion that would be caused by the elevated oxygen concentration in the OF 30 flame (Spinti and Pershing, 2003), hence leading to net lower NO formation.

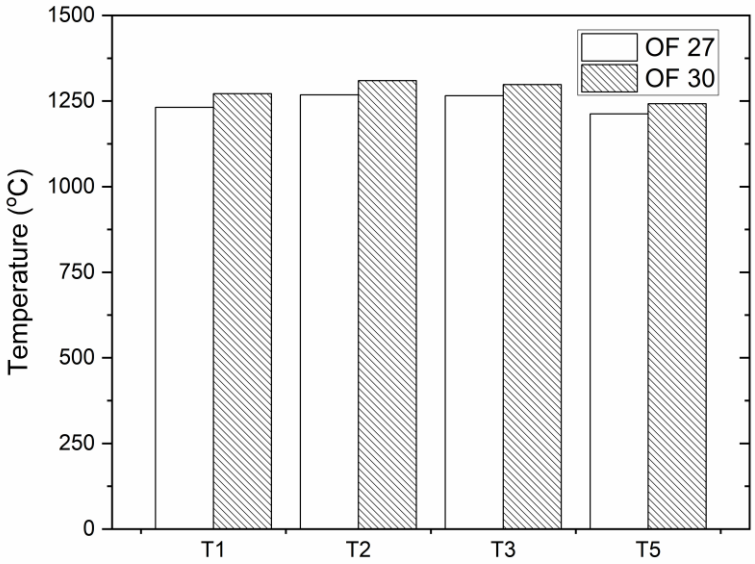

Figure 4.9 – Temperature readings at the wall of the upper section of the furnace for the OF 27 case and OF 30 case at S: 0.36

Presented in Figure 4.10 are instantaneous flame images of the investigated OF 27 flames. As the secondary oxidant proportion is increased, there is a clear change in the flame shape, which amplifies the analysis of Figure 4.8 as discussed prior. As the sliding partitioning damper is adjusted in order to increase the secondary flow and reciprocally decrease the tertiary flow, the swirl of the flame is improved due to the greater swirl angle of the secondary register in comparison to the tertiary register. This increased swirl results in a visibly shorter and broader flame and an increase of oxygen mixing into the fuel-rich region, which, as mentioned, increases fuel-N to NO conversion, combustion efficiency and flame stability.

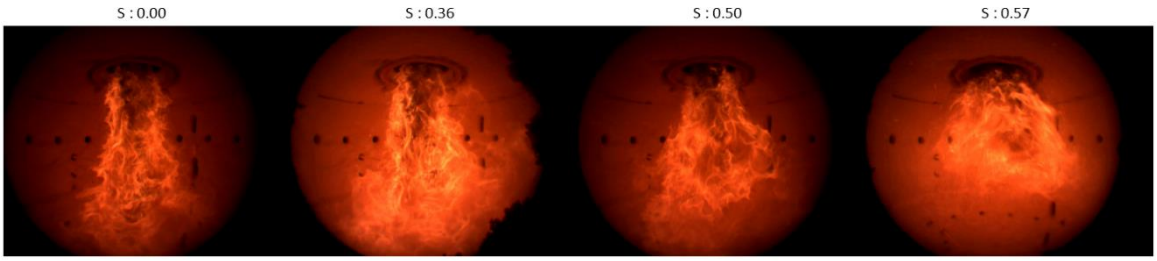

Figure 4.10 – Instantaneous flame images of OF 27 flames at 170 kW_{th}

In Figure 4.11 are instantaneous flame images of the investigated OF 30 flames. The change in flame shape between the two burner configurations can be viewed to be less

pronounced than for the OF 27 flames. This is likely to be due to the OF 30 flames having a lower volumetric flow through it and the secondary and tertiary oxidant having a decreased density (due to the increased oxygen concentration), causing a weaker swirl and hence less change in flame width.

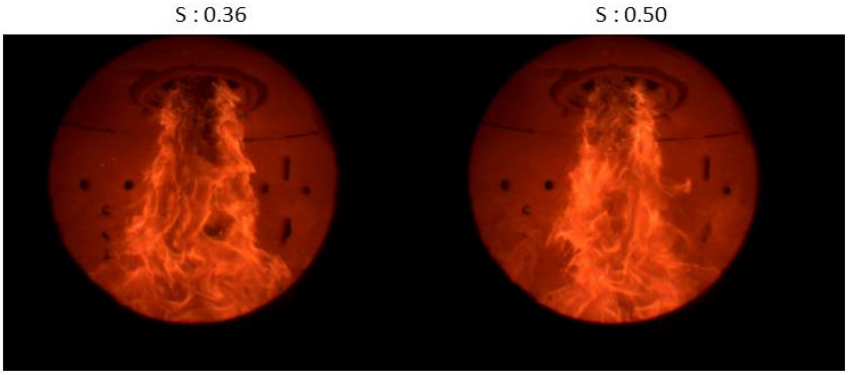

Figure 4.11 – Instantaneous flame images of OF 30 flames at 170 kW_{th}

Figure 4.12 presents a comparison of the destruction of recycled NO across the various burner configurations tested and the two oxy-fuel regimes, therefore highlighting impact of burner configuration on NO reburning. Across every tested case, NO destruction remains high at over 80% destruction; while, across the OF 27 cases, only a minor sensitivity to secondary oxidant proportion can be witnessed. The S: 0.00 and S: 0.57 cases are the only ones to vary meaningfully from the 90% destruction mark. Curiously, the higher secondary oxidant proportion of the two comes close to 100% destruction at the 300 ppm and 875 ppm recycling regimes; this could be caused by the increased flow of the secondary improving NO migration into the fuel-rich zone. It should be mentioned that the growing presence of NO in the fuel-rich region caused by an increase in NO injection, would increasingly inhibit NO formation from char-N (Spinti and Pershing, 2003), thus artificially boosting the rate of NO destruction and misrepresenting the impact on NO reburning. It can be noted that NO destruction remains relatively stable as the level of NO recycling is increased; this suggests that NO destruction is limited by reaching a reduction/oxidation equilibrium, where NO is reduced by volatile-C to form volatile-N, which is then oxidised to reform NO and so on. When comparing the two oxy-fuel regimes, it can be seen that the S: 0.36 case offers both lower NO formation and greater NO destruction when 30% O_2 is

used. However, the same trend is not seen for the S: 0.50 case, which proved to perform significantly worse with regard to both NO formation and destruction.

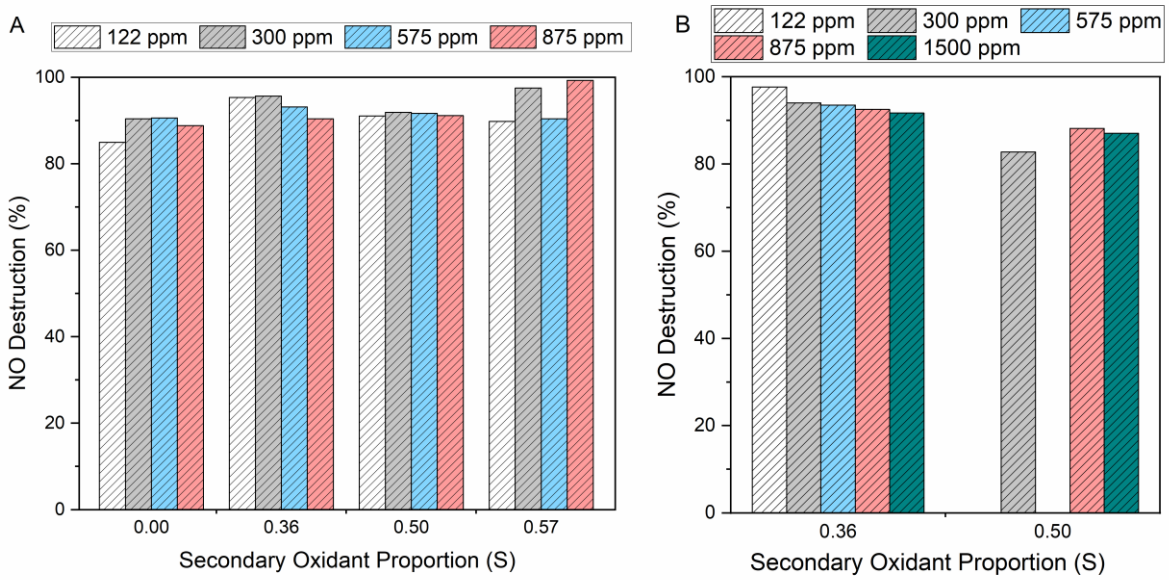

Figure 4.12 – Impact of varying the secondary oxidant proportion and NO recycling regime on NO destruction for the (A) OF 27 case and the (B) OF 30 case

This can be confirmed by Figure 4.13, through analysis of the change in NO_x emission rate with increasing NO recycling for the two common secondary oxidant proportions across both oxy-fuel regimes. For the S: 0.36 case, there is a growing difference between the NO_x emission rate from both oxy-fuel regimes as NO recycling is increased, with the OF 30 regime being vastly superior. However, for the S: 0.50 case, the OF 30 NO_x emission rate is only improved when there is no NO recycling, implying that when the gas volume is taken into account, NO formation is actually improved; and when NO recycling is increased, the NO_x emission rate for the OF 30 regime becomes significantly greater than for the OF 27 regime. This could be due to the decreased total oxidant flow of the OF 30 case creating a flame with a weaker swirl than the equivalent OF 27 flame and, thus, reducing the residence time of recycled NO in the fuel-rich region and reducing migration to recycled NO from the secondary stream into the fuel-rich region when compared to the OF 27 flame.

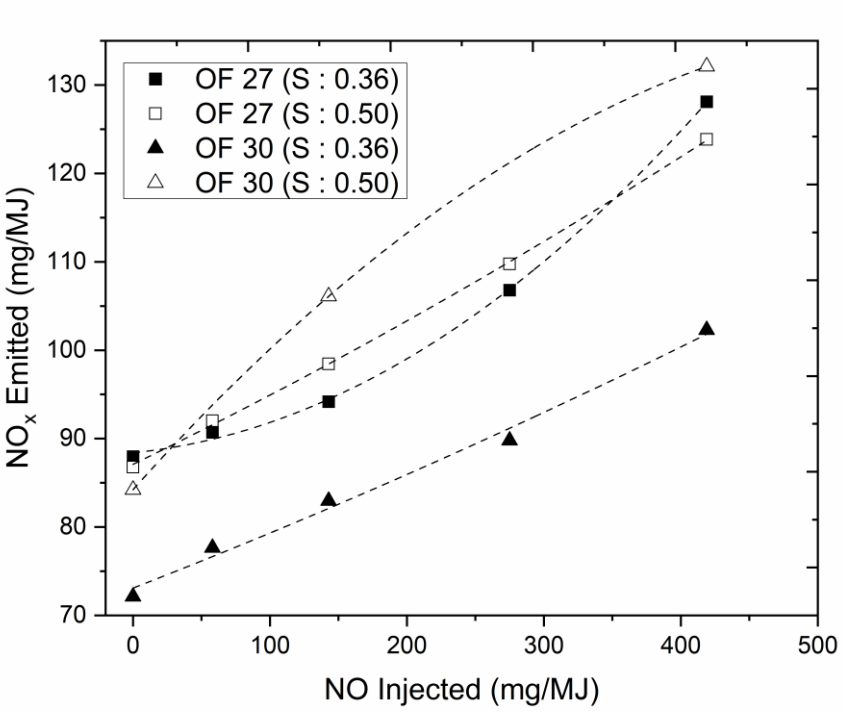

Figure 4.13 – Impact of varying the recycled NO in the emission rate of NO_x, reported as NO_2, for the OF 27 and OF 30 cases at equivalent burner configurations

4.3.2 In-Flame Analysis of NO Recycling into OF 27 and OF 30 at 170 kW_{th}

Figure 4.14 shows in-flame radial profiles of key gas constituents at 75 mm downstream of the burner for the S: 0.36 case and OF 27 regime across a variety of NO recycling levels. These represent the impact of the presence of recycled NO on processes within the flame that contribute either passively or actively to the production and destruction of NO. The greatest variation can be witnessed in the NO radial profiles. When there is not any NO being recycled, there exists a reducing zone between 0 and 25 mm, which leads to the destruction of approximately half of the NO; however, when the level of NO recycling is increased, the decrease from 0 to 25 mm becomes less, until, at a recycling regime of 1500 ppm, there is an increase in NO. The more extreme the recycling regime, the greater the volatile-N production from the reduction of excess NO; a portion of this volatile-N will be oxidised and, hence, this NO reformation grows with increasing NO recycling, resulting in this trend seen between 0 and 25 mm.

Another interesting highlight of Figure 4.14 can be found at 75 mm from the centreline, where the impact of the shear boundary can be witnessed; there is a significant rise in NO from 25 to 75 mm, as volatile-N is oxidised by oxygen rapidly diffusing into the fuel-rich

region from the bulk secondary stream. This rise, however, becomes less as the rate of NO recycling is increased. This implies that there is less volatile-N present for the 1500 ppm case, highlighting the importance of the advanced reburn reactions (reducing NO with specifically NH_3 and HCN), but could also be due the likelihood of there being reduced char-N to NO conversion due to the increasing presence of recycled NO (Spinti and Pershing, 2003). When analysing the CO and O_2 radial profiles, one can surmise that there is a lack of consistent trends to imply any impact of the NO recycling on these constituents; however, it is also possible that any effect on local CO concentration brought about by the reaction with NO in the presence of char is cancelled out by any impact on the increased presence of NO on the combustion processes.

In contrast, there is a drastic change in THC (total hydrocarbon) concentration when varying NO recycling regimes are used. When 1500 ppm NO is recycled, the THC concentration is far below that of the baseline case, showing that the recycled NO is oxidising hydrocarbon fragments; this observation is in support of Okazaki and Ando (1997), which states that the reactions of NO with volatile-C and volatile-N are far more noteworthy than the reduction of NO on char.

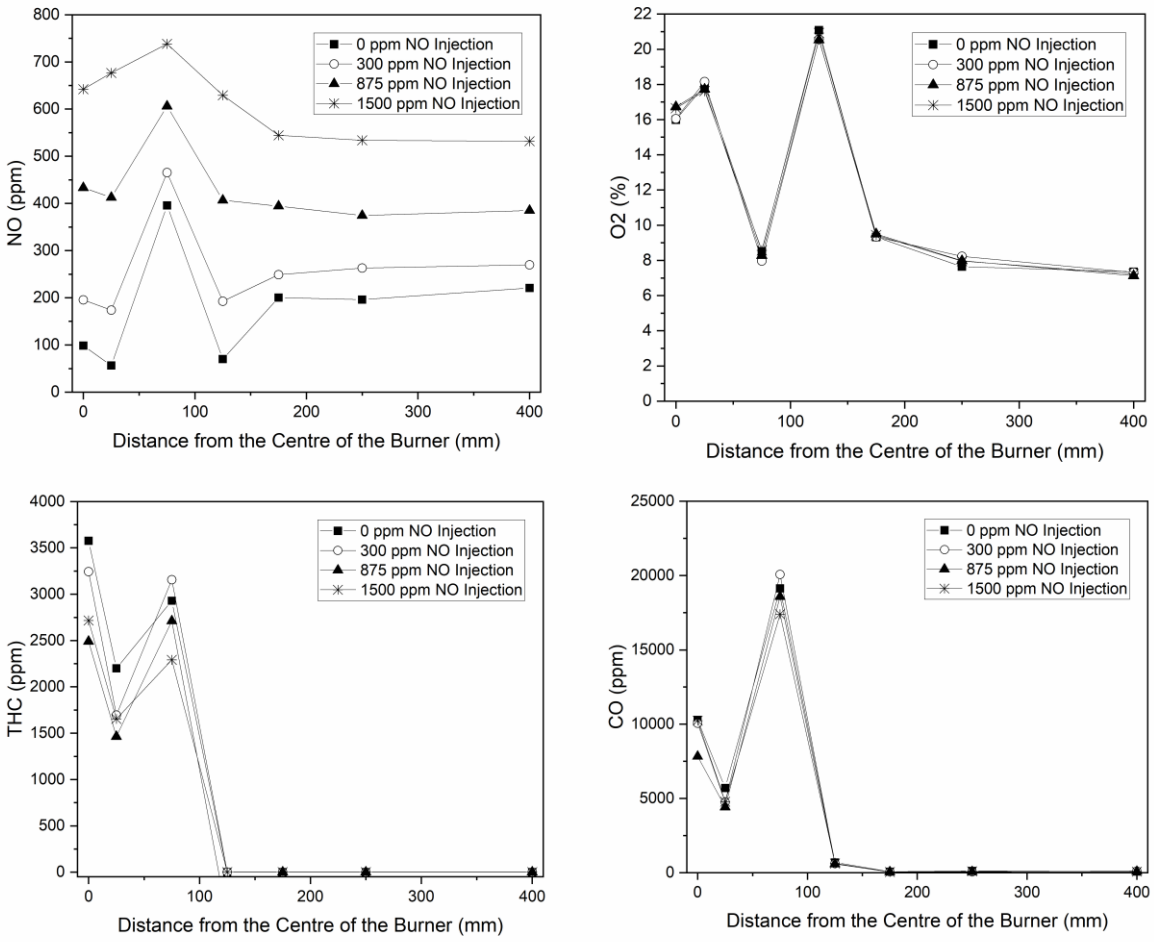

Figure 4.14 – Radial profiles from the centreline of the burner to the wall of key flame constituents at 75 mm from the burner for the OF 27 case at S: 0.36 for a variety of NO recycling regimes

Figure 4.15 shows radial profiles of key gas constituents at two burner configurations, S: 0.36 and S: 0.50, and two NO recycling regimes, 0 ppm and 300 ppm, for OF 27. It can be observed that when there is no NO being recycled, there is less NO measured for the S: 0.36 case than the S: 0.50 across the entire profile, bar the 125 mm point, which is similar due to dilution caused by the bulk secondary oxidant as shown by the extremely high O_2 concentration at this point. The THC and CO concentrations are far higher for the S: 0.50 case at the points that can be considered within the inner recirculation zone (IRZ) (0 and 75 mm) than the S: 0.36, implying poorer combustion but also that this region is more fuel-rich.

To analyse the impact on NO reburning in these graphs, one can consult the difference between the values recorded with and without NO injection for the respective burner

configuration. At 0 mm, this difference is less for the S: 0.50 case than the S: 0.36 case; this indicates that there was greater NO reburning at this point, most likely a result of the region being more fuel-rich. This is coming about due to the decreased tertiary flow of the S: 0.50 case, creating an external recirculation zone (ERZ) that is weaker and has a lower O_2 concentration, as can be observed at the points between 175-400 mm. When this weaker ERZ recirculates to the root of the flame, less oxygen will be transferred into the IRZ, resulting in the lower O_2 and higher THC and CO witnessed for the S: 0.50 case at 0 mm.

Furthermore, although there is more O_2 being transferred to the root via the ERZ for the S: 0.36 case, the rate of NO formation appears to be lower; this seems to indicate that the rate of transfer of O_2 from the secondary stream into the IRZ is more critical to NO formation than the rate of transfer of O_2 from the ERZ to the root of the flame. As opposed to the case at S: 0.36, the presence of recycled NO for the S: 0.50 case results in a slightly increased CO and THC concentration and, therefore, lower combustion efficiency. During the OF 27 regime and at a burner configuration of S: 0.50, although a more fuel-rich IRZ is created and the rate of NO reburning appears to increase as a result, the increase in NO formation is too substantial to make a significant improvement.

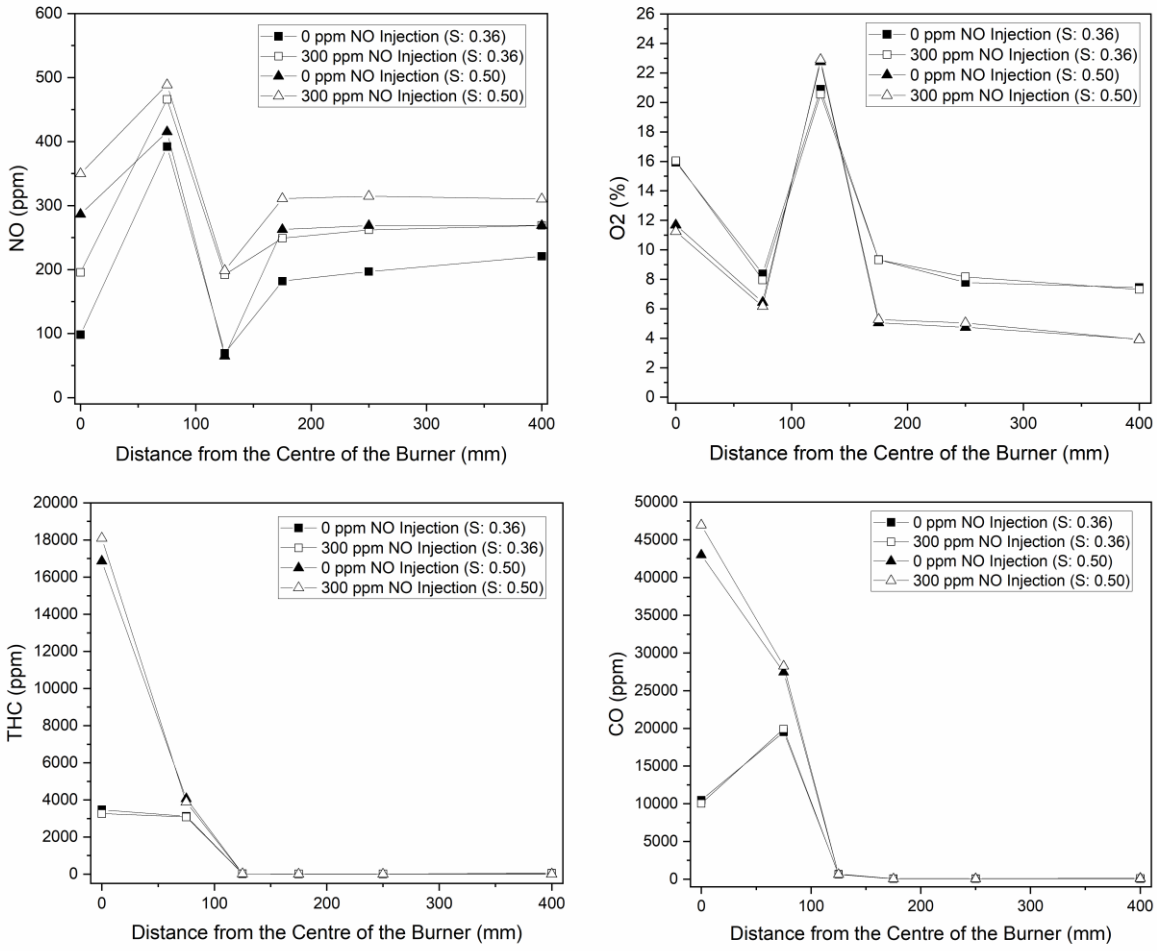

Figure 4.15 – Radial profiles from the centreline of the burner to the wall of key flame constituents at 75 mm from the burner for the OF 27 case at S: 0.36 and S: 0.50 with and without NO recycling

Figure 4.16 displays a comparison of radial profiles of the same key gas constituents and variables as in Figure 4.15 but during the OF 30 regime. When there is no NO being recycled, the S: 0.36 case produces less NO in the area between 0-75 mm from the centreline of the burner than the S: 0.50 case. Furthermore, when there is NO being recycled, the increase in measured NO, THC and CO concentrations of the S: 0.50 case at 0 mm is far greater than that of the S: 0.36 case. This runs contrary to the trends found for OF 27 regime and is most likely due to an anomalous deficiency in O_2 at this point, which can be caused by some compacted coal entering the flame, which in turn could be caused by a bridging collapse in the fuel hopper or simply from topping up the fuel hopper (uneven coal feeding).

The change in NO concentration in the flue gas between the dilution point at 125 mm and the start of the ERZ at 175 mm differs depending on the injection regime. There is a larger increase for the 0 ppm case, implying that there is a greater amount of volatile-N present to be oxidised in the burnout oxidant. Whereas for the 300 ppm case, the recycled NO must be undergoing advanced reburning, therefore depleting the volatile-N content and reducing this increase in NO. For each burner configuration, the NO concentration in the ERZ (past the 175 mm point) is largely similar and depends only on the NO recycling regime; this suggests that the reduced tertiary flow rate of the S: 0.50 case has a minimal impact on the ERZ, which is in opposition to the observations of the OF 27 regime. This could be attributed to the fact that the total mass flow rate of oxidant used at OF 30 is markedly less than at the OF 27 regime, and as a result, the flame is of a smaller volume. This aspect makes it likely that the flue gas recirculating in the ERZ originates from a location in the furnace where the chemistry can be described as more resolved, compared to the OF 27 regime. This phenomenon has the impact of decreasing the difference between the measured concentrations of the different burner configurations at 0 mm for the OF 30 regime compared to OF 27 and, therefore, of showing that burner configurations can have different impacts at different oxy-fuel regimes.

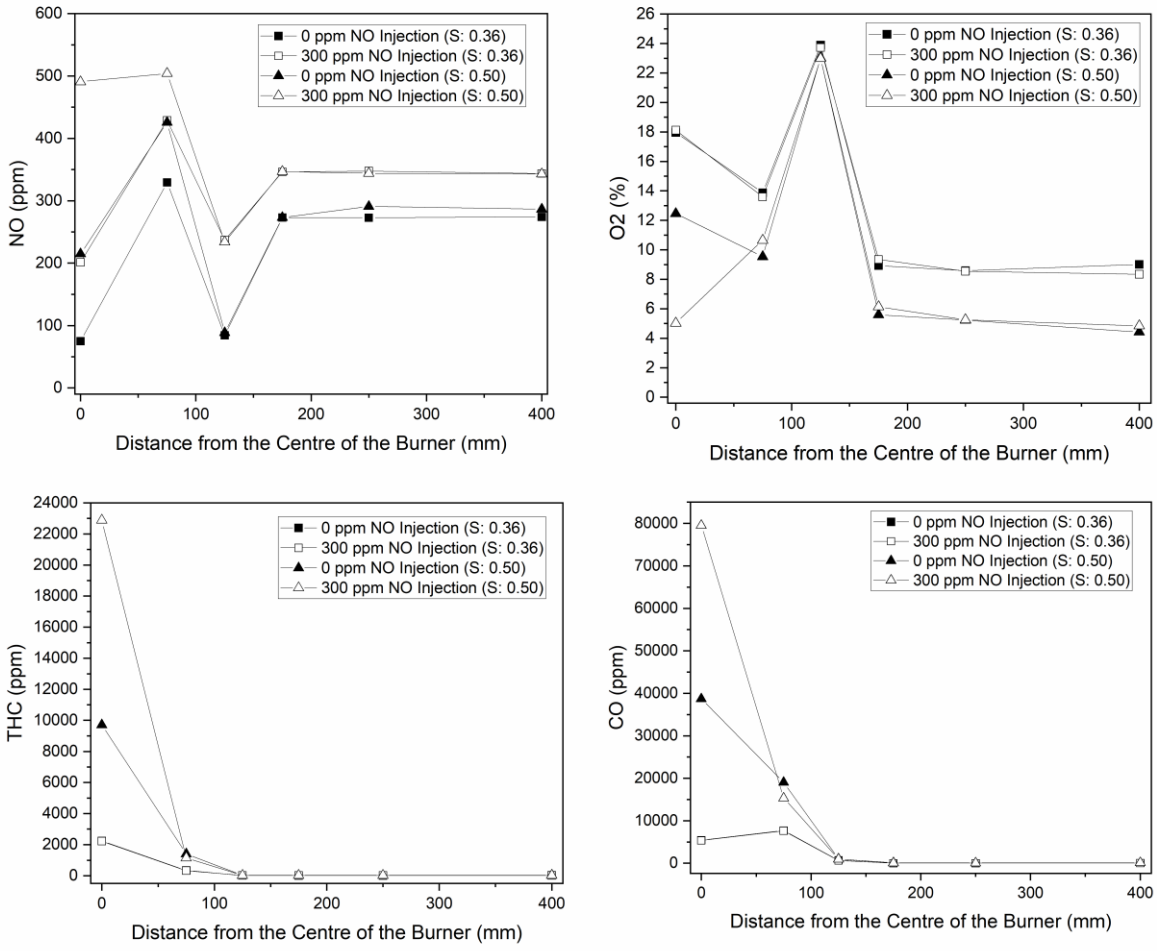

Figure 4.16 – Radial profiles from the centreline of the burner to the wall of key flame constituents at 75 mm from the burner for the OF 30 case at S: 0.36 and S: 0.50 with and without NO recycling

Figure 4.17 shows axial profiles down the centreline of the furnace of key gas constituents at two burner configurations, S: 0.36 and S: 0.50, and two NO recycling regimes, 0 ppm and 300 ppm, for OF 30. At the 75 mm point (as with Figure 4.16), it can be observed that NO formation is higher for the S: 0.50 case compared to the S: 0.36 case. When the furnace is descended to 375 mm, there is a peak in NO and the NO concentration for the S: 0.36 case rises further than for the S: 0.50 case, implying that NO formation might actually be delayed for the S: 0.36 case. However, this delay in NO formation seems not to have an impact on NO reduction by reburning, as the cases with NO recycling are only marginally greater than the cases without and so destruction is high for both burner configurations. The minimum NO concentration in the profile is found at 800 mm and coincides with a substantial drop in the THC concentration from the peak at 375 mm, most likely caused by the reburning of

recently formed NO; the depleted O_2 at this point would facilitate this NO destruction at both burner configurations. There is a return of a considerable O_2 concentration from 800 mm down and this coincides with a rise in NO, which can be attributed to oxidation of any remaining volatile-N either originating from the fuel or from the reaction of NO with volatile-C.

These profiles can be broken down into three zones: the first zone encompasses the evolution of the reducing species and is located at 75-325 mm, the second zone involves the destruction of these reducing species in an oxygen deficient environment and is located at 325-800 mm, while the third zone covers the oxidation of any remaining reducing species and is located from 800 mm to the flue. This simplified breakdown is complicated by the introduction of recycled NO. This recycled NO is almost entirely destroyed within the first zone and is likely to cause a great increase in volatile-N, compared to a flame without recycled NO; this is then oxidised in the oxidation zone causing a greater increase in NO concentration from 800 mm onwards for the cases with recycled NO. This observation could also be due to the destruction rate of NO in the tertiary stream being lower than the other streams; however, literature shows that the destruction rate of NO in the secondary and tertiary streams should remain significant (Liu, et al., 2005b). Nevertheless, it is preferable and necessary to control this additional volatile-N using the second zone to minimise conversion back to NO.

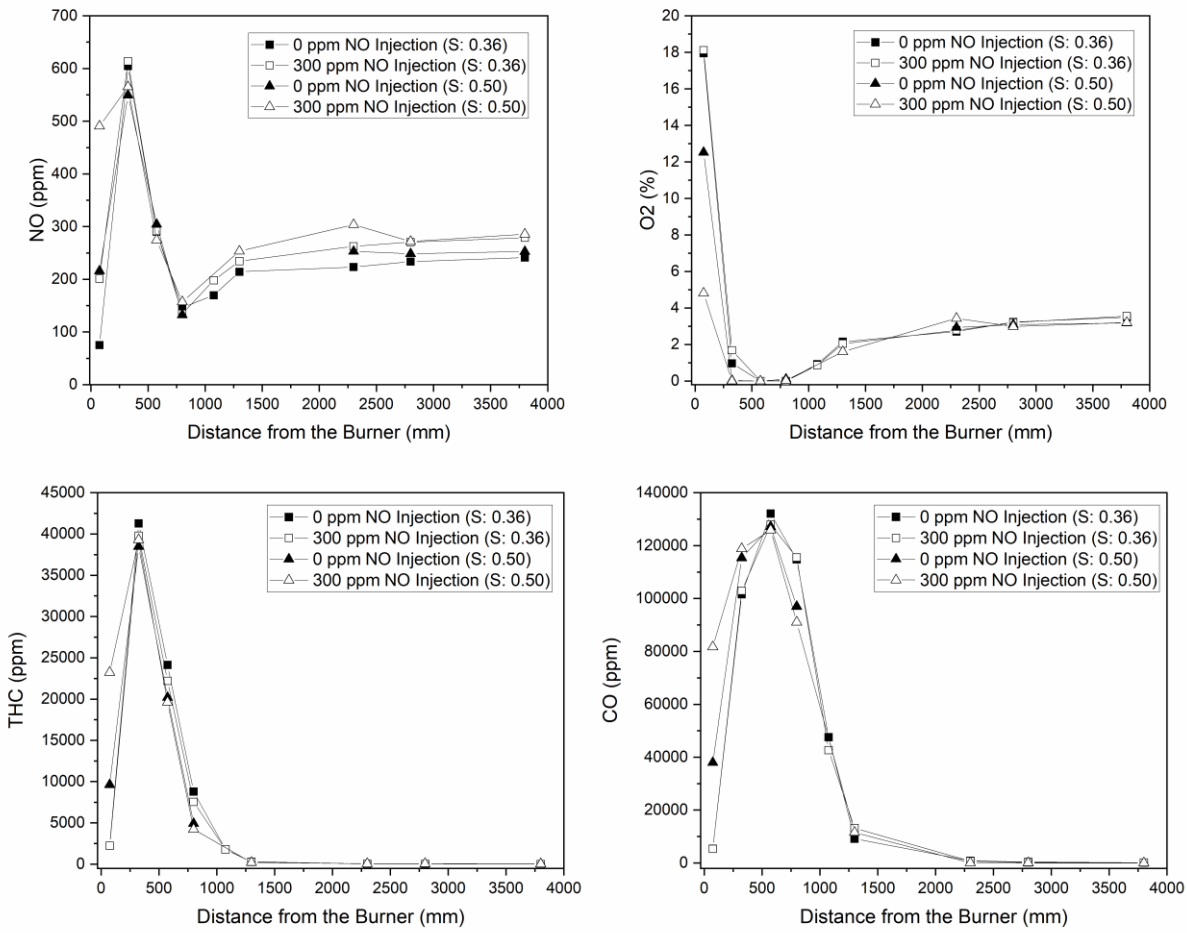

Figure 4.17 – Axial profiles down the centreline of the furnace of key flame constituents for the OF 30 case at S: 0.36 and S: 0.50 with and without NO recycling

Figure 4.18 presents an illustration identifying the major aerodynamic zones within a furnace utilising a single swirled flame. The relative size and intensity of these zones will affect the chemistry within the fuel-rich zone and, hence, the ability to minimise NO_x formation and achieve the highest possible combustion efficiency. This study only investigated a single burner furnace but the majority of practical industrial boilers will utilise many burners in an array, and the flames they produce are likely to affect each other aerodynamically and chemically. As this cannot be replicated in the CTF and it is outside of the scope of this study to model, it is important to theoretically explore possible divergences to the trends presented in this study. One apparent difference would be a nominal change in the composition of the JEZ (jet expansion zone); this would be caused by the invasion of flue gas from parallel or opposite flames. The impact of this would in turn be a change in the composition of the ERZ, which is crucially returned to the root of

the flame and has been shown to have an important impact on the flame properties in this study; thus, any trends related to the ERZ from this study may be slightly compromised in a boiler. There will also be a disruption of the eddies within the ERZ, varying the speed at which heat and species are recirculated to the root of the flame. It is likely, however, that the IRZ and processes at the shear surfaces within the flame would be mostly protected from the effects of flames in series, and, therefore, the described impacts of burner configuration on NO reburning in particular would remain valid for a full-scale boiler.

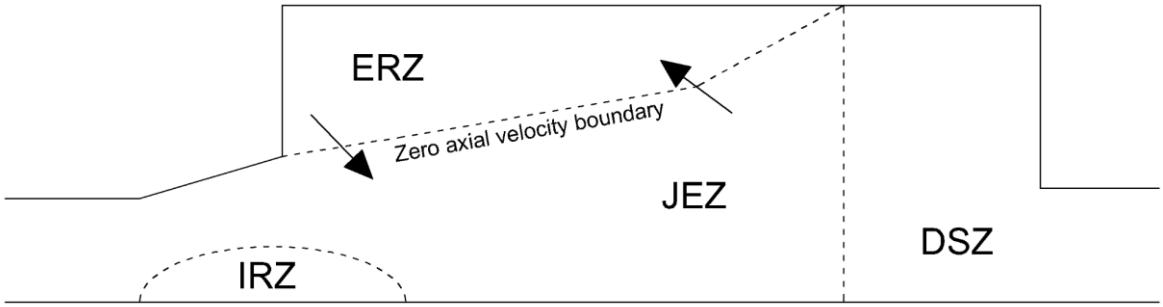

Figure 4.18 – Distinct zones within a furnace with a single swirled flame (Adapted from Pedersen, et al., 1997)

4.4 Conclusions

This chapter studied the impact of varying burner configuration on NO formation and NO reburning during oxy-coal combustion. The burner configuration was varied by altering the partitioning of the combined burnout oxidant between the secondary and tertiary using a sliding damper on the burner. This was considered to have the impact of altering the stoichiometry within the fuel-rich zone by increasing/decreasing the swirl of the flame and, hence, increasing/decreasing mixing of oxygen into the fuel-rich zone. Commissioning tests were carried out prior to progression through the test matrix, in order to establish a desirable proportion for the primary oxidant flow rate and to establish whether NO should be injected into solely the primary stream, just the secondary and tertiary streams, or all streams. These attributes were established as 20% of the overall oxidant and the injection of NO into all oxidant streams, but the commissioning tests highlighted issues with the stability of the flame under the pre-conceived settings. In order to increase stability, the thermal capacity was decreased from 200 kW_{th} to 170 kW_{th} and the oxygen content in the primary oxidant was increased to 21%. It was theorised that reducing the thermal rating

would aid flame stability as the lower oxidant flow rates required would reduce flame lift-off and increase attachment of the flame root to the burner.

It was shown that the rate of destruction of recycled NO remained stable around 90% across the range of burner configurations during the OF 27 regime; however, during the OF 30 regime, there was a prevalent reduction in the rate of destruction of recycled NO when the secondary oxidant proportion was increased. This was explained by taking into account that the OF 30 regime involves an oxidant with a decreased density/volume flow compared to that of the OF 27 regime; this would create a flame with a weaker swirl, which would compromise residence time of recycled NO within the fuel-rich region compared to the OF 27 case.

The NO formation rates, as well as burnout of the fuel, varied greatly over the range of burner configurations tested. Between secondary oxidant proportions of 0.00-0.57 for the OF 27 regime, the NO_x emission rate rose from 77 to 143 mg/MJ, while the unburned carbon in ash fell from around 19% to 6%. During the OF 30 regime, the NO_x emission rate was found to be 72 mg/MJ when the secondary oxidant proportion was 0.36, but when this was increased to 0.50, the NO_x emission rate rose to 84 mg/MJ. This was believed to be due to the increased flow rate of the secondary stream providing more oxygen to, and increasing mixing into, the fuel-rich zone.

Radial profiles at 75mm from the burner of key flame constituents were taken at a range of NO recycling regimes, at two burner configurations (S: 0.36 and S: 0.50) and two oxy-fuel regimes (OF 27 and OF 30). In addition, an axial profile of key flame constituents was taken down the centreline of the furnace for the same two burner configurations at OF 30. From these profiles, it was theorised that not only is burner staging preferable for controlling NO formation but it also acts to manage the products of NO reburning in order to prevent the reformation of NO. Through studying two moderate burner configurations, which differ through slightly variant secondary and tertiary oxidant flow rates (and, hence, also swirl), it was shown how slight changes in flame structure affect the progress of NO related mechanisms during oxy-coal combustion.

CHAPTER 5 THE IMPACT OF AN FE-BASED ADDITIVE ON SELECTIVE NON-CATALYTIC REDUCTION

5.1 Introduction

The literature review found that an Fe-based additive had been tested for use during pulverised coal combustion and was shown to significantly improve combustion efficiency, decrease NO and CO emissions and decrease loss on ignition. As there are tightening restrictions on NO emissions due to policy concentration on improving air quality, it stands to reason that this technology could be seen as very appealing, considering that the only retrofitting required to deploy this technology would involve enabling the addition of an additive to the coal once it is ground. The literature review also investigated current NO abatement technologies, finding that the two most popular secondary NO_x abatement technologies were selective non-catalytic reduction (SNCR) and selective catalytic reduction (SCR), both of which can involve ammonia as the reagent. In some cases, iron oxide was used as a component of the catalyst during SCR. When coupling this information with other known interactions between iron and ammonia, a question arises over how the Fe-based additive would interact with ammonia during SNCR, which has a significantly different temperature range and flue gas composition from SCR.

5.2 Experimental Results and Discussion

5.2.1 Experimental Studies

Using the method and pilot scale combustion test facility (CTF) described in section 3.3, an experimental investigation was launched to study how NO reduction due to SNCR changes with the introduction of the Fe-based additive. Figure 5.1 displays the NO reduction by SNCR across a range of NSRs and Fe-based additive loadings. For clarity, the NO reduction given for the 0% Fe-based additive is with respect to the coal baseline NO concentration; while, the NO reduction values presented for the additive cases are with respect to the Fe-based additive baseline NO concentrations, which are different for each additive loading. Therefore, it is pertinent to mention that the Fe-based additive baseline NO concentrations will be lower and if there was no interaction between the Fe-based additive and the ammonia, then the NO reduction due to SNCR should be decreased to the 0% Fe-based additive case (Javed, et al., 2007).

Figure 5.1, instead, shows that the Fe-based additive considerably improves the SNCR process for the majority of cases tested, signifying that the presence of the Fe-based additive within the ammonia injection zone facilitates NO reduction by ammonia. At the NSR of 0.5, the NO reduction is similar for all cases where the Fe-based additive is present and higher than the 0% Fe-based additive case. This indicates that, although the mechanism facilitating the interaction between ammonia and the Fe-based additive is active, it is largely independent of the rate of loading at this point. When NSR is increased to 1, the rate of Fe-based additive loading starts to show an impact; the 6.6% Fe-based additive case has a markedly improved NO reduction compared to the lower Fe-based additive loadings, indicating that the additive may act as an active site for ammonia to reduce NO. When the loading is lower, a reduced NO reduction is observed; this could result from the additive's active sites becoming occupied, leading to a limit on the NO reduction mechanism. This may even lead to a negative impact on NO reduction, such as that witnessed at a NSR of 1.5 for the 3% Fe-based additive loading case. However, this will be examined further at the end of this sub-section with a discussion regarding a possible structure of the active mechanism. Error bars representing two standard deviations from the mean were added to Figure 5.1 to represent the variation in the operational data. This variation could be viewed to be quite extreme and be the cause of misperception regarding any conclusions; however, this variation is a natural consequence of the coal's inherent heterogeneity and the trends presented for each case remain valid due to the clear difference in mean values.

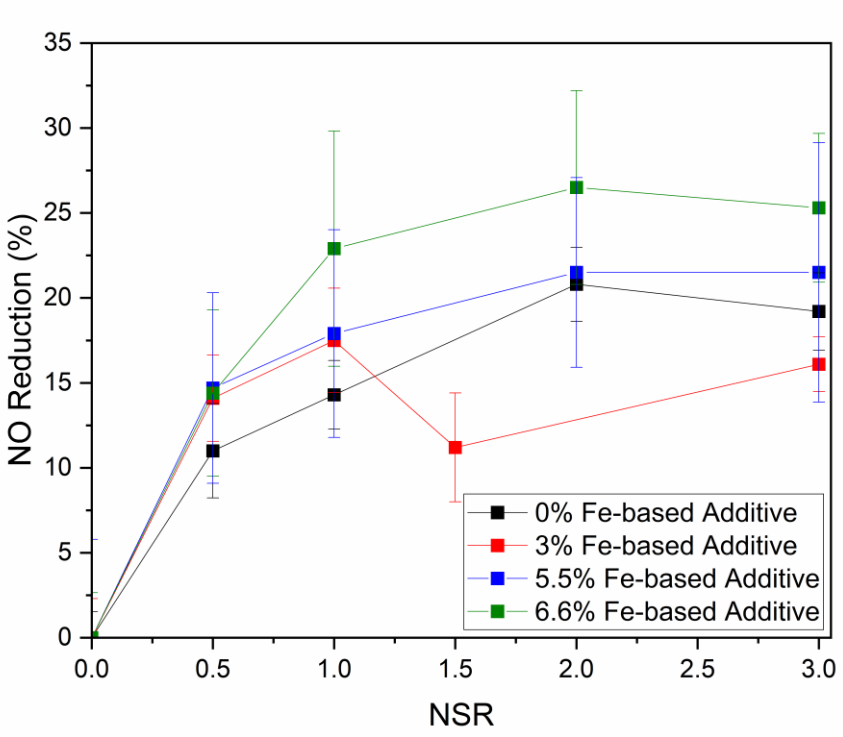

Figure 5.1 – The impact of the Fe-based additive on NO reduction by SNCR as a function of NSR

Figure 5.2 presents the impact of the Fe-based additive on ammonia utilisation efficiency, which is defined using the following equation (Daood, et al., 2013):

$$\eta NH_3 = \frac{NO_{initial} - NO_{final}}{NO_{initial} \times NSR} \qquad (5\text{-}1)$$

This value describes the share of ammonia that is productively used to reduce NO, instead of being oxidised or lost to entrainment in the flue gas, known as slip. As with the calculations to discern NO reduction, the initial NO concentration is relative to the additive loading; if no additive is used, then the initial NO concentration is the NO concentration of the flue gas when the coal is combusted unaided, but if a certain additive loading is used, then the initial NO concentration is the NO concentration of the flue gas when the coal is combusted with that loading of additive.

From Figure 5.2, it can be observed that the NH_3 utilisation efficiency is much improved when the Fe-based additive is utilised, especially in the low NSR region. When the NSR is increased, the NH_3 utilisation efficiencies all decrease, appearing to begin to converge; this indicates that as ammonia input is increased, the proposed active sites become fully

occupied and the classic SNCR mechanism becomes dominant. This effect is seen earlier, at lower NSR values, for the 3% Fe-based additive case, thus reaffirming the occupied active sites theory. As with the prior figure, Figure 5.2 includes error bars representing two standard deviations from the mean, which adds confidence to the conclusion that NH_3 utilisation efficiency is improved in the presence of the Fe-based additive.

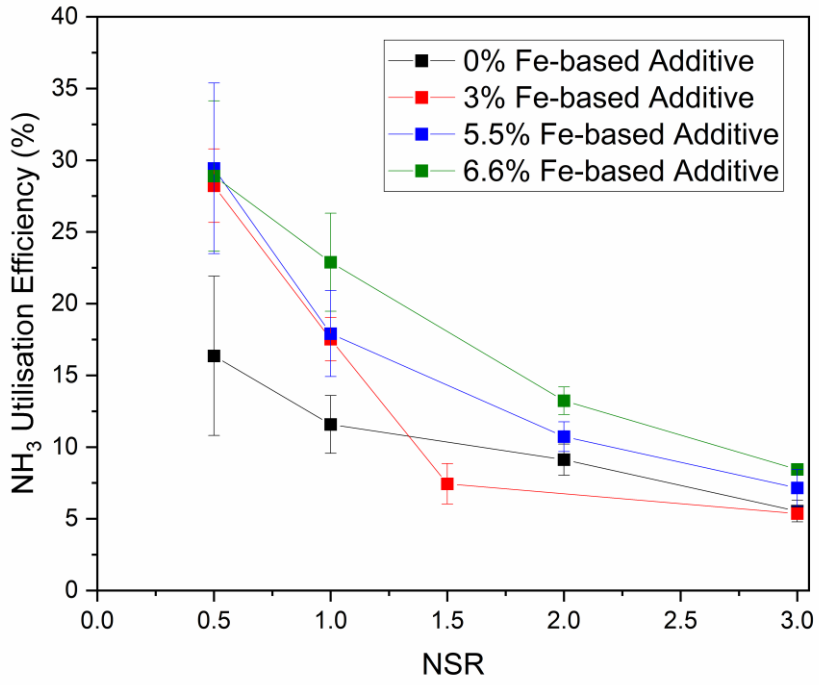

Figure 5.2 – The impact of the Fe-based additive on NH_3 utilisation efficiency of SNCR as a function of NSR

It should be mentioned that the reductions witnessed in this investigation are unlikely to be as high as an industrial application, let alone a laboratory setup. The measured temperature of the section at which ammonia was injected was around 1100 °C; this is known to be at the upper end of the typical SNCR temperature window, and so competition between the NH oxidation and NO reduction mechanisms may start to occur. Furthermore, the temperature measurement would not be accurate because the thermocouple will measure the temperature at the wall, which will be lower than at the centre of the furnace, and heat will be lost between the thermocouple and its surroundings, thus further underestimating the true gas temperature. Therefore, it is acceptable to speculate that the gas temperature is high enough for the aforementioned mechanism competition to hinder

NO reduction. Another reason for reduced NO reduction may be that the residence time between the injection of the ammonia and the extraction of the flue gas in this CTF is not enough for sufficient mixing and maximum reduction. It is certain that attempting to increase the residence time by moving the ammonia injection site up-stream in the furnace would result in greater NH_3 oxidation. Attempting to solve the temperature issues by moving the ammonia injection site down the furnace would just complicate the residence time issue further.

The combination of the Fe-based additive and SNCR was expected to have a cumulative reduction capability consisting of the in-flame reduction caused by the additive reported in Daood, et al., (2014a, 2014b) and then chemical reduction from the ammonia injection site downwards. This chemical reduction by SNCR was expected to be lower in the cumulative case, than when solely SNCR was used, due to the in-flame reduction caused by the additive leading to a lower initial NO concentration (Javed, et al., 2007). Figure 5.3 was created to investigate how the observed trends differed from the expected trends and whether there was enough variance to justify conclusions theorising a positive interaction between the Fe-based additive and the ammonia. In Figure 5.3, the observed trends for each Fe-based additive loading were plotted with five variations of the expected trend using a k factor; where, a k factor of 0.85 would signify a SNCR efficacy of 85% as compared to the case where the Fe-based additive is not present and a k factor of 1 would signify that SNCR is 100% as effective, with or without the additive. The predicted NO concentrations ($[NO]_{NSR,k}$) were calculated using:

$$[NO]_{NSR,k} = [NO]_{additive} \times (1 - (k \times SNCR\%_{NSR})) \qquad (5\text{-}2)$$

Where, $[NO]_{additive}$ is the additive baseline NO concentration for a particular loading of Fe-based additive and $SNCR\%_{NSR}$ is the NO reduction by SNCR at a particular NSR.

Figure 5.3 implies that the cumulative reduction theorised prior to the experimental investigation is not occurring here. The observed NO concentrations outperform even the k=1 predictions, proving that there is no drop in SNCR effectiveness. Further to this, when the Fe-based additive loading is increased, the divergence between the predicted trends and the observed trends grows until, for the 6.6% Fe-based additive case, the predicted trends are so far removed from the observed trends that there is even very little overlap

within two standard deviations. The observed trends from the 3% Fe-based additive case show, however, less clarity. Above a NSR of 1, the NO concentration is within the range of, or lower than, the predicted values but it remains unlikely that the cumulative reduction theory is occurring, due to the two prior points at a NSR of 0.5 and 1 showing, on account of their error bars, that 95% of the data is outside of the predicted region for this point.

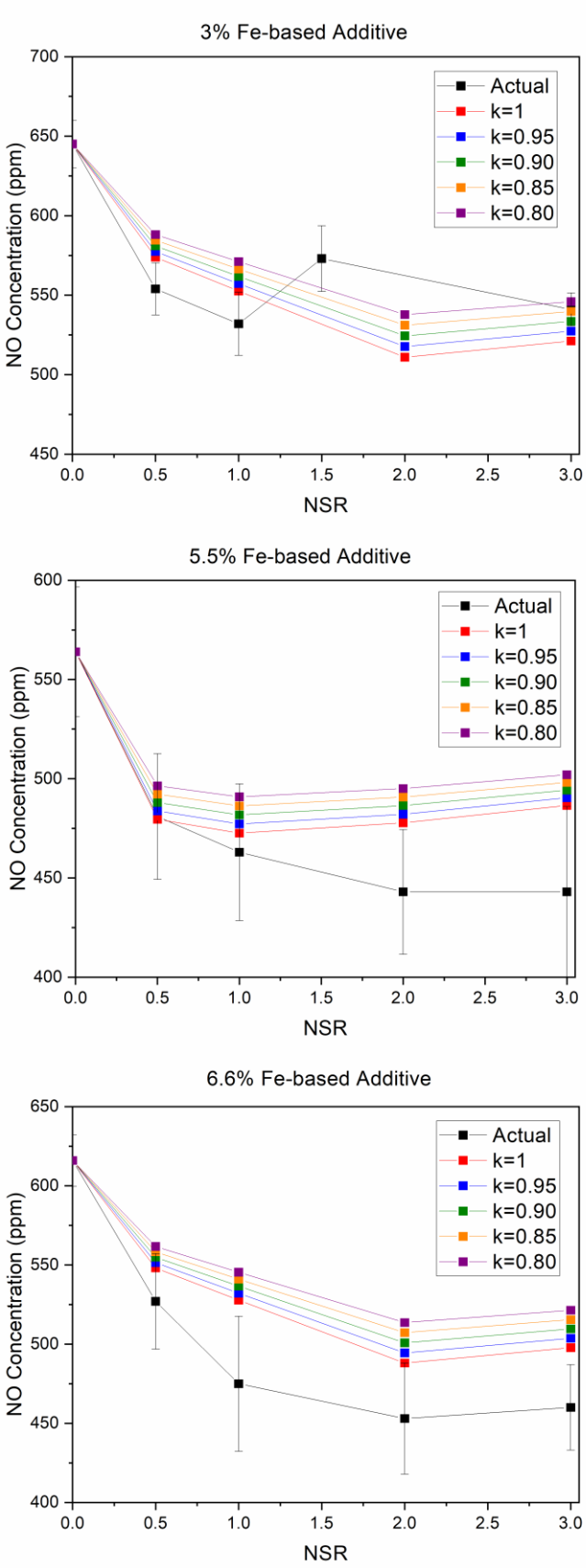

Figure 5.3 – Actual impact of the Fe-based additive compared with a variety of predicted effects

Figure 5.4 presents a mechanism suggested by Apostlescu, et al., (2006) to explain an interaction between iron oxide and ammonia when the authors had used iron oxide within a catalyst for SCR. They theorised an Eley-Rideal mechanism, where ammonia was binding to an ionised iron atom to create an amide. This amide then reduced the NO to N_2, thereby simplifying the reduction of NO by reducing the reliance on the balance of O and OH radicals to convert ammonia to amidogen, without then converting that amidogen (NH_2) to imidogen (NH), which can lead to NO production.

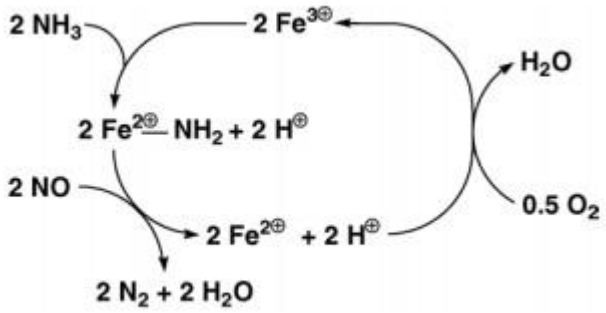

Figure 5.4 – Possible mechanism representing interaction between ammonia and the Fe-based additive (Apostolescu, et al., 2006)

This may be used to explain why the 3% Fe-based additive case produces strange trends at and above a NSR of 1.5. As the number of active sites becomes depleted, due to the lower loading, the SNCR mechanism starts to become competitive again and the amidogen production reaction rate increases:

$$NH_3 + OH \rightarrow NH_2 + H_2O \qquad (5\text{-}3)$$

However, similar to a condition where the NSR was very low or the temperature was much higher than optimum, the ratio of hydroxyl radicals to free ammonia is very high; this causes further hydroxyl reactions to propagate, such as the imidogen (NH) production reaction mentioned prior:

$$NH_2 + OH \rightarrow NH + H_2O \qquad (5\text{-}4)$$

The imidogen is subsequently oxidised to form NO, greatly reducing NO reduction and NH_3 utilisation. The NO reduction, for the 3% Fe-based additive case, increases when NSR is increased from 1.5 to 3; the increase in ammonia concentration in the reaction zone increases the reaction rate of the amidogen (NH_2) production reaction and reduces the

ratio of hydroxyl radicals to free ammonia, thus reducing the rate of the imidogen (NH) production reaction and starting to stabilise the system.

From the trends presented here, the Fe-based additive seems to introduce a catalytic effect on the selective non-catalytic reduction; however, there is doubt over whether this can be truly considered selective catalytic reduction (SCR). In the high temperature zone for SCR (>750 °C), ammonia combustion reactions become competitive with NO reduction reactions (Horvath, 2003); therefore, NO reduction and NH_3 utilisation efficiency drops as the system no longer becomes selective, and this is why SCR is not used at higher temperatures. The nature of the Fe-NH_3 interaction will be further investigated in a kinetic study presented in section 5.3 of this chapter.

5.2.2 Analysis of Possible Economic Impact

The impact of the Fe-based additive SNCR hybrid technology can be economically realised in two ways. The first of which involves an analysis of the shift in optimum NSR, where NO reduction and NH_3 utilisation is observably highest. As seen in Figure 5.5, the optimum NSR can be seen to fall from 2 to 1 when the Fe-based additive is added. This is an opportunity to markedly reduce their ammonia usage, and therefore chemical costs, while maintaining their NO reduction and continuing to meet NO_x emission regulations. Furthermore, reducing ammonia usage would reduce the chance and magnitude of an ammonia slip; this could become pertinent, should ammonia become a regulated pollutant for systems using post combustion NO_x control measures.

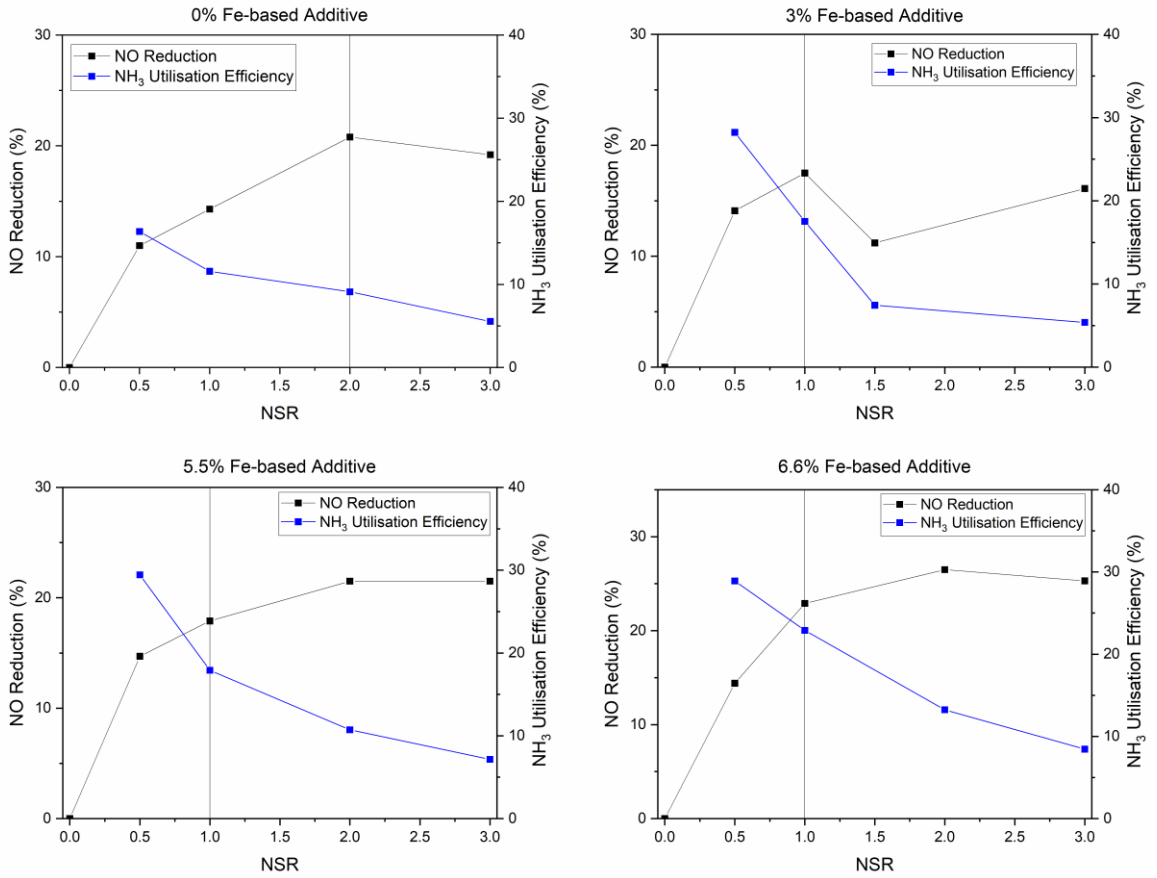

Figure 5.5 – Change in optimum NSR with the addition of the Fe-based additive

The second method for realising an economic benefit from this hybrid technology involves maintaining the ammonia usage but greatly increasing NO reduction due to SNCR. This magnitude of NO reduction would only be possible by greatly increasing ammonia usage and would be accompanied by very low NH_3 utilisation efficiency and high ammonia slip. Furthermore, the presence of the Fe-based additive will also give in-flame benefits such as 10-15% NO reduction. In Figure 5.6, the impact of four NO_x abatement systems are analysed, with low NO_x burners being present in all cases, to highlight the benefit of the hybrid technology with regard to NO_x reduction. It can be shown that the combination of reduction due to low NO_x burners, the in-flame benefits of the Fe-based additive and the modest increase in effectiveness of SNCR would be able to meet NO_x regulations in most circumstances.

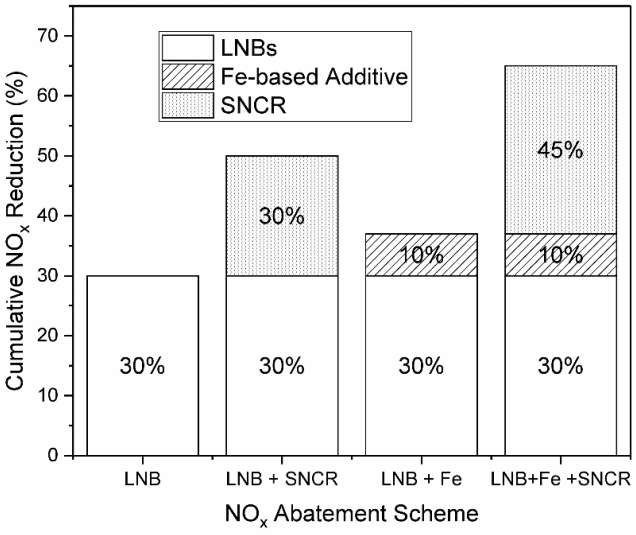

Figure 5.6 – Cumulative impact on NO reduction of the Fe-based additive-SNCR hybrid technology

In order to economically investigate these arrangements, Carnegie Mellon University's 'Integrated Environmental Control Model' (IECM) (CMU, 2020) was used to model a 650 MW pulverised coal fired boiler with a capacity factor of 47%, burning a coal identical to the Durrans grade 240 coal used in the experimental tests. A NO_x emission rate was defined as 0.5202 mg/kJ in order to lead to a NO concentration in the model's flue gas, similar to that seen at the coal baseline in the experimental tests. A number of environmental controls are offered within the model and, in order to imitate a large coal boiler, wet FGD, cold side ESP, low NO_x burners and SNCR were chosen. The effectiveness of the low NO_x burners was set at 30% NO reduction (Skalska, et al., 2010) as was SNCR (Gomez-Garcia, et al., 2005). The effectiveness of the SNCR was then increased to 45% while recording the change in OPEX (operating expenditure); this upper NO reduction limit was chosen as a likely comparison with the hybrid technology's ability to reduce NO during SNCR at a loading of 5.5%. The recorded OPEX values are plotted in Figure 5.7, with the scenario in which the Fe-based additive is used at 5.5% loading to achieve 45% NO reduction by SNCR, using an estimated additive cost of £45/tonne (from private communications). Figure 5.7 shows that the Fe-based additive offers a much more economical alternative to increase NO reduction in place of increasing ammonia usage. Use of the Fe-based additive will only increase OPEX by ~$5 M/yr (using an exchange rate of £1:$1.24) as opposed to a cost of

~$30 M/yr associated with the increased ammonia usage, which does not take into account any fines associated with unacceptable ammonia emissions from slip.

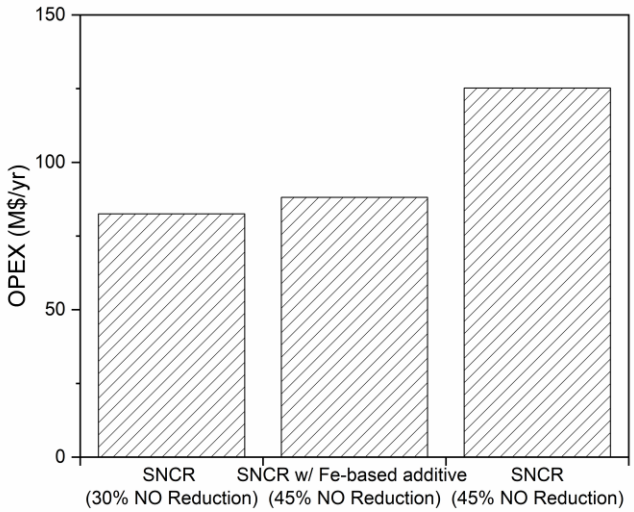

Figure 5.7 – Comparison of the total process OPEX between plants with basic SNCR, the hybrid technology and SNCR with the ammonia required to match NO reduction by the hybrid technology

The hybrid technology was then compared to SCR. Although SCR is an incredibly effective option to meet NO_x emission limits, it is also accompanied by extensive operating and capital costs. The IECM was used with the previously modelled plant but SCR was chosen instead of SNCR at a NO_x reduction of 80% and a catalyst cost of \$10,000/m^3 (EPA, 2003). It was found that the OPEX of a plant with SCR was only marginally higher than a plant using the hybrid technology but the annualised CAPEX was ~$5 M/yr, thus leading to a TOTEX three times greater than that of the hybrid technology. There is, of course, uncertainty in this calculation, with the cost likely to be far larger as the EPA has claimed that retrofitting a boiler with SCR will likely lead to a much higher CAPEX (EPA, 2000), due to processes such as the demolition of existing structures accounting for as much as 30% of this increased CAPEX (Cochran, et al., 1993). In comparison, the hybrid technology would require very little retrofit and down-time. Hence, there would only be a minimal loss of revenue and very little capital investment required; thus proving to be an attractive alternative even to SCR.

5.3 Kinetic Modelling

5.3.1 SNCR-Fe-based Additive Hybrid Technology

In order to investigate further the phenomenon witnessed in the experimental tests, a kinetic model describing the selective non-catalytic reduction mechanism was set up using Cantera (Goodwin, et al., 2018). At the heart of the model was the comprehensive H/N/O mechanism discussed and published in Klippenstein, et al., (2011); this was chosen due to the consistent accuracy in comparison with experimental Thermal De-NO_x process results. The mechanism located in Appendix 1 of this thesis was configured to the exact Chemkin format and converted into a file that Cantera was able to read (a CTI file) using the ck2cti.py script provided in the Cantera package. The newly created CTI (presented in Appendix 1) then provided thermodynamic properties of all 25 species in the H/N/O mechanism as well as Arrhenius coefficients for all 207 reactions. The suspected Fe_2O_3-NH_x reactions were added using kinetic data published in Fu, et al., (2014), for the reactions:

$$NH_3 + Fe^{3+} + O^{2-} \rightarrow Fe^{2+} - NH_2 + OH^- \qquad (5\text{-}5)$$

$$Fe^{2+} - NH_2 + O_2(ads) \rightarrow Fe^{2+} + NO + H_2O \qquad (5\text{-}6)$$

$$Fe^{2+} - NH_2 + NO \rightarrow Fe^{2+} - NH_2NO \qquad (5\text{-}7)$$

$$Fe^{2+} - NH_2NO \rightarrow Fe^{2+} + N_2 + H_2O \qquad (5\text{-}8)$$

However, due to the limited availability of species input data, these reactions were simplified to:

$$NH_3 + Fe + O \rightarrow Fe + NH_2 + OH \qquad (5\text{-}9)$$

$$Fe + NH_2 + O_2 \rightarrow Fe + NO + H_2O \qquad (5\text{-}10)$$

$$Fe + NH_2 + NO \rightarrow Fe + N_2 + H_2O \qquad (5\text{-}11)$$

To complicate matters, Fu, et al., (2014) provides kinetic data to calculate rate constants for reaction 5-9 and the ratio of reaction 5-10 to reaction 5-11. The provided pre-exponential factor (A) related to reactions 5-10 and 5-11 was a ratio of the pre-exponential factors for reactions 5-10 and 5-11; while the provided activation energy (E) was the difference in activation energy between reactions 5-10 and 5-11. Therefore, the Arrhenius coefficients were estimated for these two reactions by attempting to match the

experimental relationship witnessed at 1123 K and 1223 K in Fu, et al., (2014). The activation energies were set at $E_{NH2\rightarrow NO}$ of 0 J/mol and $E_{NH2\rightarrow N2}$ of 109928 J/mol, and the pre-exponential coefficients were varied until SNCR was effectively completely halted at 1123 K and NO reduction was reduced to 30% at 1223 K; this resulted in pre-exponential coefficients of $A_{NH2\rightarrow NO}$ of 3.43E+09 mol/m^2·s and $A_{NH2\rightarrow N2}$ of 2.77E+15 m/s. Unlike the experimental results, a resultant NO production would not occur at 1123 K, consequently a drop in NO reduction from ~64% to ~2% was deemed as sufficient to approximate the published behaviour. This process was also conducted for another set of activation energies, but the produced relationship between temperature and NO reduction was very similar.

Using this collection of species and reactions, a continuous stirred tank reactor (CSTR) model was created using Cantera (presented in Appendix 2), designed to mimic the section of the 100 kW CTF into which the ammonia was added during the experimental tests. A temperature range of 1100-1600 K is used to investigate the impact of the Fe-based additive across the entire SNCR temperature window and above, with results every 25 K. The allotted time for the reaction to complete is 10 seconds with calculation made every 1E-04 seconds. The flue gas, at input, is simplified to a composition of roughly 70% N_2, 20% CO_2, 7% H_2O, 3% O_2, 500 ppm NO and 20 ppm CO, with the NH_3 and Fe concentrations dictated by the test variables. These were four NSRs of 0.5, 1.0, 1.5 and 2.0 and four Fe-based additive loadings of 0%, 3%, 5.5% and 6.6%, which roughly equated to Fe concentrations of 4500, 8000 and 10000 ppm.

As witnessed in Figure 5.8, the baseline selective non-catalytic reduction mechanism is most effective over a temperature range of 1125-1300 K. From 1300 K onwards, NO reduction decreases greatly until the temperature window ends at around 1400 K, when the NH_3 reduction/oxidation equilibrium starts to tip in favour of NH_3 oxidation. This is emphasised in Figure 5.9 as being the point where the NH_3 utilisation efficiency becomes less than half of maximum NH_3 utilisation efficiency for the respective NSR, due to the improbability of an NH_3 slip at this temperature and excess air. When the Fe-based additive is used in conjunction with ammonia, there is an increase in NO reduction, a shift in the temperature window towards a higher range and a widening of this new temperature window. In addition, a greater Fe-based additive loading furthers these effects, so much so

that when 6.6% Fe-based additive loading is used, the SNCR mechanism only becomes active at ~1350 K and continues to be viable throughout the usual SNCR temperature range, i.e. up to 1600 K.

This impact on temperature range is consequential for two reasons. The first is that it may help explain why there were indications of a negative impact of Fe_2O_3 on the SNCR process in the study by Fu, et al., (2014). This paper focussed on a temperature range of 973-1373 K, which could be viewed as misguided when the previously mentioned observations made from the baseline SNCR model are considered along with the observed extension of the temperature range, which would mean that the comprehensive impact of Fe_2O_3 could not have been discovered. If this is the case, then the authors' assertion that Fe_2O_3 has an inhibitory effect on the thermal deNO_x process is inaccurate and could have an adverse impact on future research and development of this technology.

The second reason is that the increased and expanded temperature range offers options regarding the location of the injection of the ammonia, which will be discussed in section 5.2.3.2, and leeway regarding the issues caused by the heterogeneous nature of the temperature profiles at these injection points. Temperatures in the post-flame zone of a tangentially fired boiler can reasonably vary between 1100 K and 1800 K (Choi and Kim, 2009); atmospheres at the higher end of this spectrum can cause SNCR to perform considerably less well than in studies that took place using laminar/quartz reactors or modelling and, hence, reduce the reputation of the technology. Therefore, the use of the Fe-based additive technology would reduce the rate of ammonia oxidation within these high temperature zones.

It was previously discussed why the NO reduction, recorded experimentally, was lower than theoretically maximum experimental data; it should also be mentioned that this model produces higher baseline NO reductions than is ever likely to be witnessed experimentally. This is mainly due to the fact that the system is modelled on a continuously stirred tank reactor, so the species are perfectly mixed and there is no temperature gradient. This results in the model being a satisfactory tool for analysis of the mechanism but uncertainty should remain regarding accurate prediction of and comparison to experimental trends.

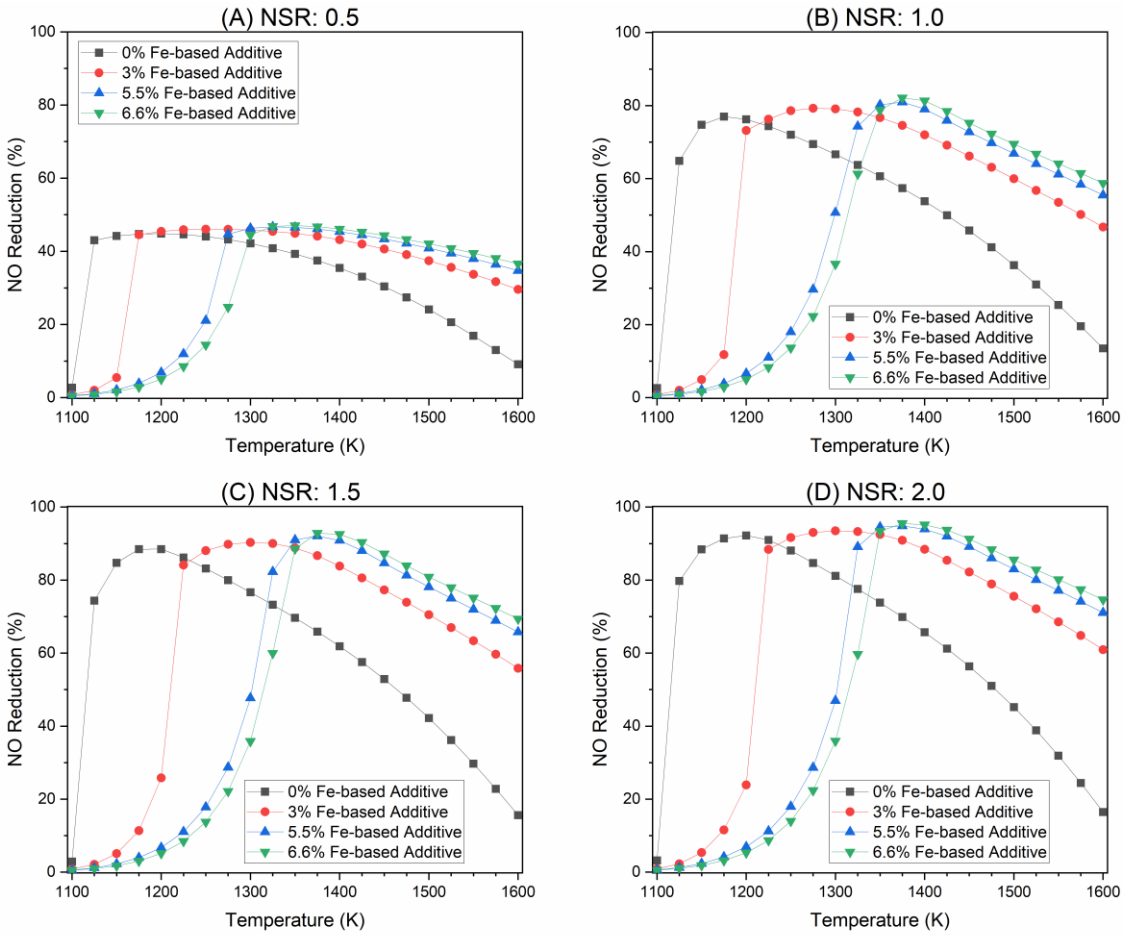

Figure 5.8 – The impact of the Fe-based additive on NO reduction as a function of temperature and NSR

Figure 5.9 shows impact of the Fe-based additive on NH_3 utilisation efficiency. These graphs present similar trends to those presented in Figure 5.8, as NH_3 utilisation efficiency is a function of NO reduction, but Figure 5.9 provides clarity on the state of the trade-off between increased NO reduction and increased ammonia usage. Under the zero Fe-based additive scenario modelled, which can be described as perfectly mixed and, therefore, unlike a commercial scenario, increasing the NSR from 1.5 to 2 only increases NO reduction by ~4% but leads to a decrease in NH_3 utilisation efficiency of ~15%, hence, due to this insight, this decision would be considered uneconomical. In practice, higher NSRs may be required to increase mixing of the reagent into the flue gas as well as increase NO reduction. The presence of the Fe-based additive increases the NH_3 utilisation efficiency, with greater benefit achieved as a greater loading of Fe-based additive is utilised. However, as NSR is increased, this benefit becomes less noticeable, indicating that the most efficient

application for the Fe-based additive is at lower NSRs. This would allow for lower ammonia usage leading to lower reagent costs and a lower chance of ammonia slip, the former of which was shown in section 5.2.2 to be capable of significantly deteriorating a plant's process economics.

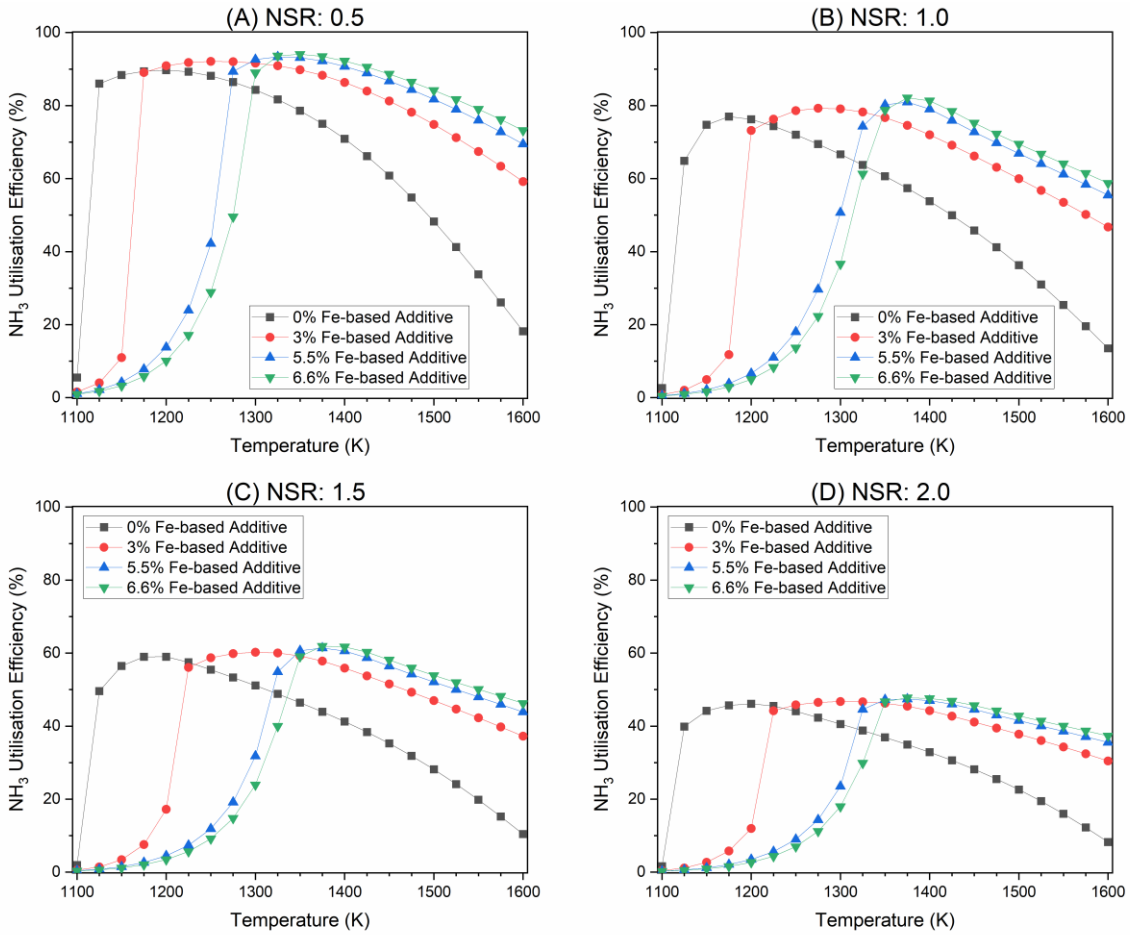

Figure 5.9 – The impact of the Fe-based additive on NH_3 utilisation efficiency as a function of temperature and NSR

5.3.2 Alternative Configurations

As mentioned previously, the increased and widened temperature window may provide leeway on the injection location of the ammonia. Figure 5.10 shows possible injection cases; where (A) is the traditional ammonia injection location, i.e. post flame and prior to the superheater, (B) is a location that implies injection with the overfire air, named here as reducing overfire air (ROFA), and (C) is a location where the top row of burners are taken out of service and ammonia is injected through these ports, named here as advanced SNCR (ASNCR). Location (A) was discussed in the previous section, and locations (B) and (C) will

be discussed here. Locations (B) and (C) have a temperature profile of 1400-1900 K (Choi and Kim, 2009) as well as heterogeneous species profiles. In order to accommodate this compositional ambiguity, an assortment of initial compositions was used to characterise these locations. At location (B), three compositions were considered: a fully combusted gas identical to that at location (A), an uncombusted gas (where only 10% of the overfire oxidant has been consumed) to represent the atmosphere around the overfire air stream and a semi-combusted gas (where 50% of the overfire oxidant has been consumed), all shown below:

	CO_2	O_2	NO	N_2	H_2O	CO
(A)	140000	30000	500	760000	70000	20
(B) Uncombusted	92000	97000	500	766000	44000	500
(B) Semi-combusted	136000	42000	500	755000	65000	1500

Table 5.1 – Array of compositions to represent heterogeneity at location (B) (All values are in ppm)

These compositions were run at a temperature range of 1400-1900 K with a 25 K step change and an average was taken, which is used to describe the impact of the Fe-based additive on reducing overfire air (ROFA) along with the minimum and maximum values present as error bars in Figure 5.11. As for location (C), there is still uncertainty regarding species composition but this uncertainty stems from the operator's preferred stoichiometric ratio; therefore, two stoichiometric ratios were simulated S: 1.025 and S: 1.1. These two cases had the following compositions:

	CO_2	O_2	NO	N_2	H_2O	CO
(C) S: 1.025	160000	5000	500	735000	80000	20000
(C) S: 1.1	155000	18000	500	750000	75000	2500

Table 5.2 – Array of compositions to represent uncertainty over operator stoichiometric preference at location (C) (All values are in ppm)

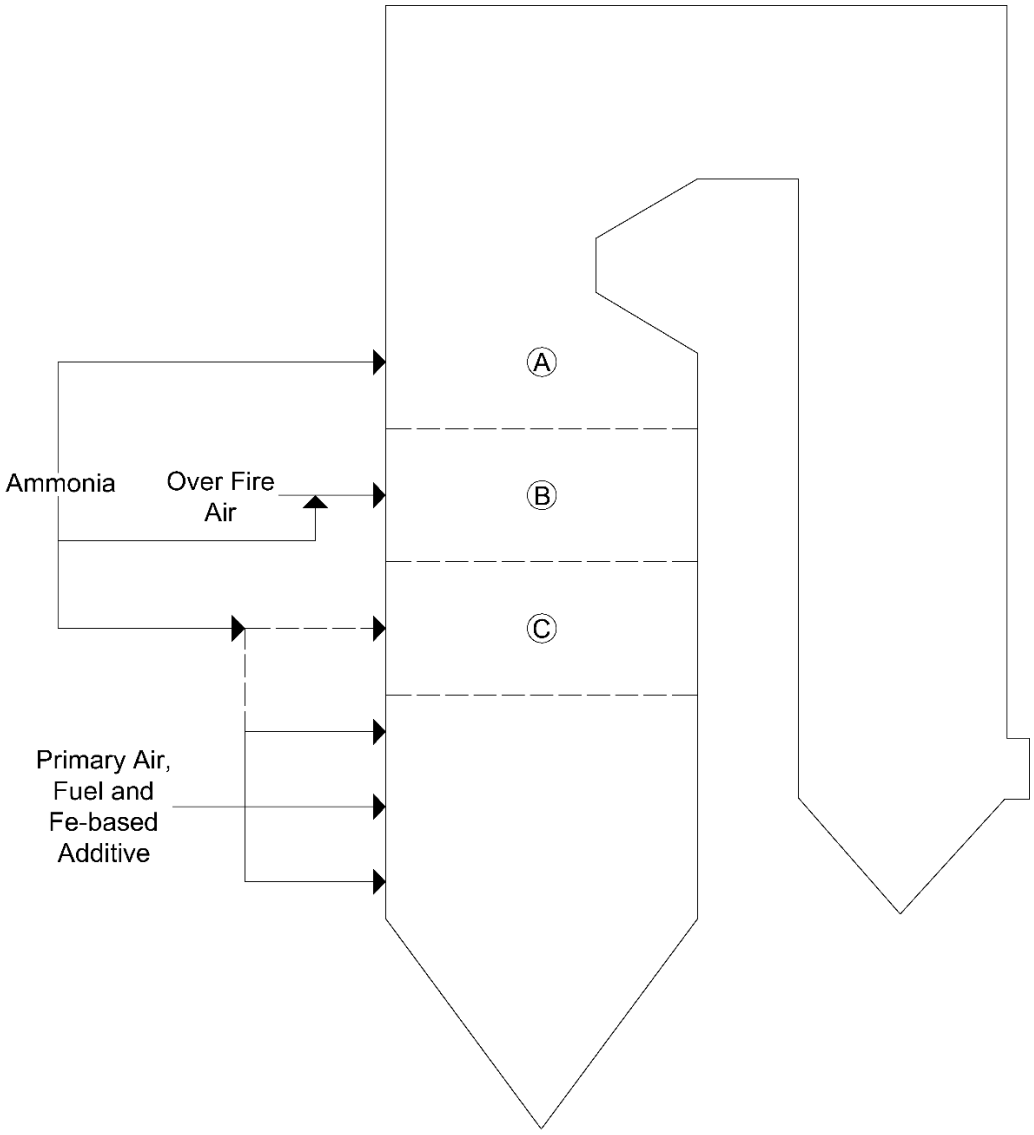

Figure 5.10 – Possible configurations for utilisation of the ammonia-Fe-based additive hybrid technology

Figure 5.11 presents the impact on NO reduction of the Fe-based additive at location (B). It can be observed that without any additive, NO reduction stops entirely at ~1650 K, regardless of the NSR, as all the injected ammonia is oxidised. When the Fe-based additive is present, net NO reduction occurs across the temperature window up to 1900 K;. Furthermore, for all cases tested with the additive, NO reduction remains above 20% until a minimum of 1700 K, greatly improving upon the baseline case. As with location (A), NO reduction significantly improves across the temperature range as Fe-based additive loading is increased. Although this may present as a feasible technology in its own right, it does not compare favourably with location (A) and should not be used as an alternative unless

experimental tests find otherwise. However, there may be an opportunity to use this location, or location (C), in conjunction with location (A) while maintaining ammonia usage; instead of using an NSR of 2 at location (A), an NSR of 1 could be used at location (A) and location (B)/(C).

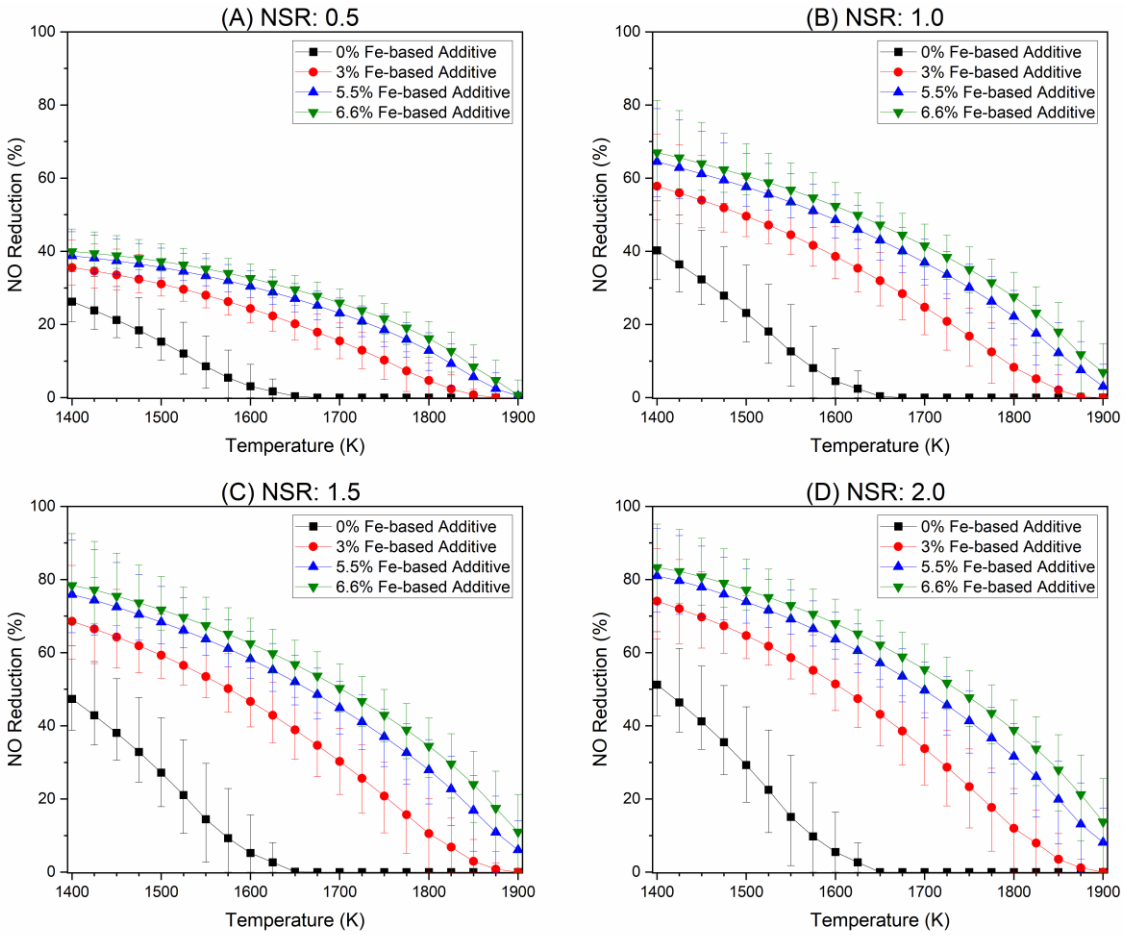

Figure 5.11 – The impact of the Fe-based additive on NO reduction as a function of temperature and NSR during reducing overfire air (ROFA)

Figure 5.12 presents the impact of the Fe-based additive on NH_3 utilisation. These figures differ in presentation to those in Figure 5.11 by comparing the NH_3 utilisation efficiency across NSRs at individual Fe-based additive loadings. This approach, in this circumstance, heavily advocates the use of the Fe-based additive and demonstrates just how wasteful and, therefore, unnecessary a high NSR can be when any loading of Fe-based additive is used; therefore, further advocating use as a supplementary technology with a low ammonia load. As for Fe-based additive preference, there is a clear advantage to a higher

loading (either 5.5% or 6.6%), allowing for continued mechanism activity at 1900 K and improved NH_3 utilisation across the temperature window.

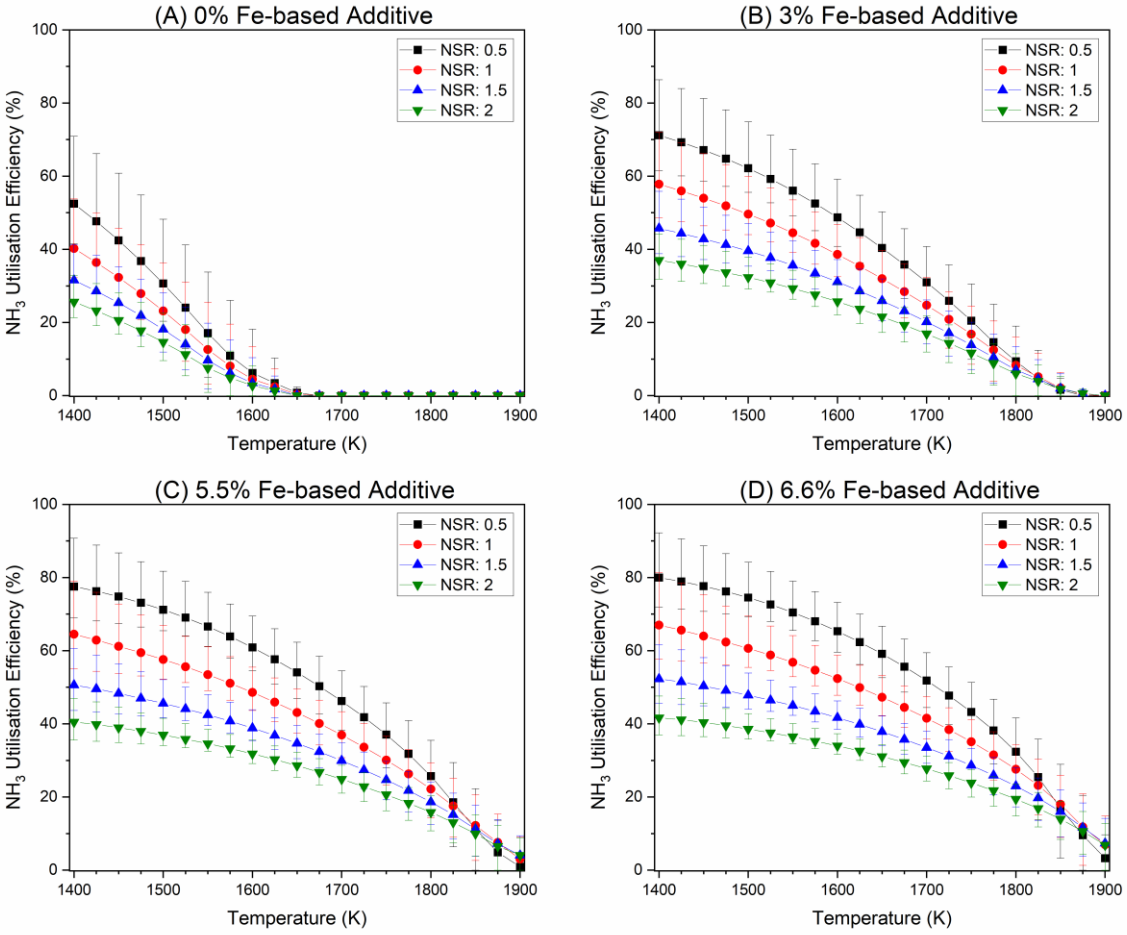

Figure 5.12 – The impact of the Fe-based additive on NH_3 utilisation efficiency as a function of temperature and NSR during reducing overfire air (ROFA)

Figure 5.13 displays the impact of the Fe-based additive on NO reduction at location (C). In terms of the baseline SNCR, NO reduction remains moderate across the higher temperature window for this composition; in comparison to location (B), this is a much improved baseline performance. However from a critical approach, this could also present a weakness in any conclusions derived from these models, as highlighted by the greater uncertainty present in error bars; because the major differences in the compositions used for locations (B) and (C) are the concentrations of O_2 and CO, which both play a vital role in the propagation of the SNCR mechanism. To combat any uncertainty stemming from this point, section 5.3.3 will investigate the sensitivity of SNCR-Fe-based additive hybrid technology to O_2 and CO.

When the Fe-based additive is used at location (C), NO reduction is further improved across the temperature window, even producing satisfactory NO reduction at 1900 K. To further highlight the greater suitability of location (C), a NSR of 2 and an Fe-based additive loading is predicted to reduce NO by ~50% at 1900 K compared to ~5% at location (B). The rate of improvement in NO reduction decreases as loading is increased, so, from an operator's point of view, the most efficient use of the Fe-based additive in this location would be 5.5%, as the greater loading of 6.6% would only increase NO reduction by a maximum of ~3%. However, this difference in NO reduction between the different loading cases increases as the temperature increases, indicating that the additive inhibits NH_3 oxidation and the benefit of a larger additive loading is more apparent at extreme temperatures. Ultimately if ASNCR were used in conjunction with the SNCR hybrid technology (both with an NSR of 1), a similar NO reduction could be achieved as when using solely the SNCR hybrid technology (with an NSR of 2) but with a lower ammonia usage and a lower ammonia slip.

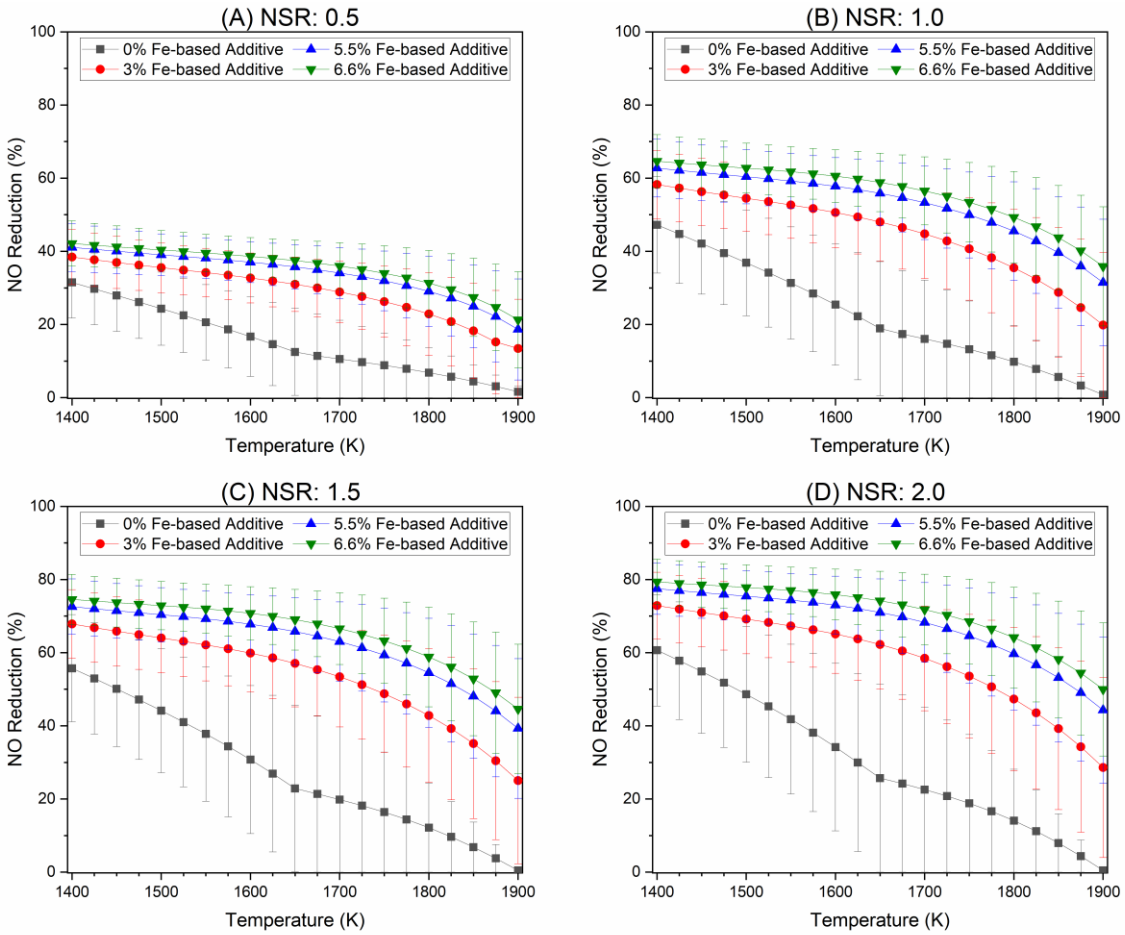

Figure 5.13 – The impact of the Fe-based additive on NO reduction as a function of temperature and NSR during advanced selective non-catalytic reduction (ASNCR)

Figure 5.14 presents the impact of the Fe-based additive on SNCR at location (C) in terms of NH_3 utilisation efficiency. The presence of the additive greatly increases the NH_3 utilisation efficiency for each NSR; however, the greatest benefits are achieved when using a smaller NSR. This provides juxtaposition to the related NO reduction trends, highlighting just how wasteful a higher NSR could be and reaffirming that an NSR of 1 would be the best compromise position in order to achieve high NO reduction and low ammonia usage and low ammonia slip. When compared to location (B), NH_3 utilisation efficiency is vastly increased at location (C), most likely due to the fuel-rich nature of the environment and, hence, much lower availability of O_2, reducing the rate of NH_3 oxidation reactions.

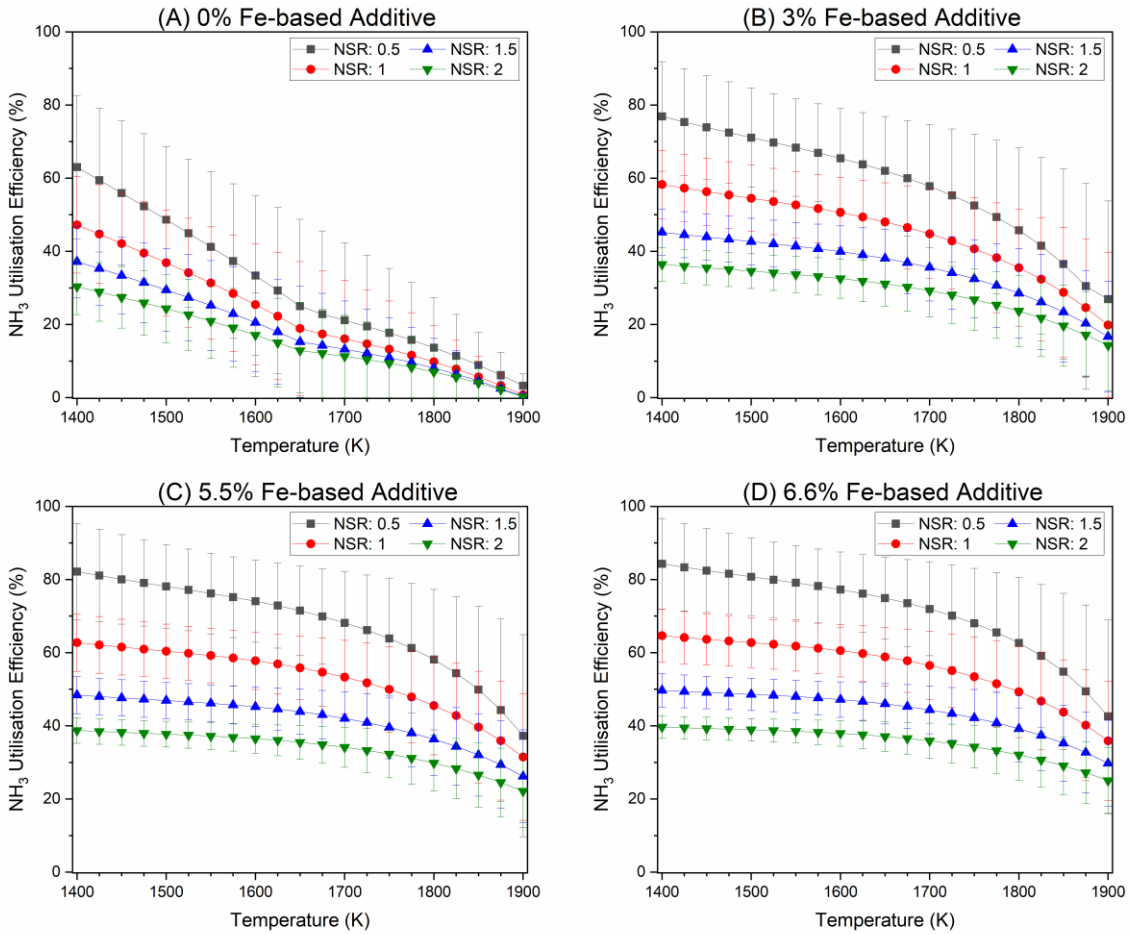

Figure 5.14 – The impact of the Fe-based additive on NH_3 utilisation efficiency as a function of temperature and NSR during advanced selective non-catalytic reduction (ASNCR)

5.3.3 Sensitivity to O_2 and CO

As mentioned prior, the compositions used to describe locations (B) and (C) have relatively extreme ranges of O_2 and CO values; this is just conjecture due to the impact of many factors affecting the point concentration of these gases, such as the primary stoichiometry, the thermal rating at which the furnace is being run affecting the turbulence and mixing within the furnace, and the composition and combustion efficiency of the fuel. It is pertinent, therefore, that it is understood how changing solely the O_2 and CO affects the SNCR process in terms of NO reduction. The importance of these compounds arrives from their key contribution to the chain initiation and branching reactions that form O and OH radicals, which are fundamental to the SNCR process and on which the balance between NH_3 oxidation and NO reduction depends.

Figure 5.15 presents the change in NO reduction and the temperature window of the SNCR process with variation in O_2 concentration for the baseline SNCR case and a case where the Fe-based additive is present solely for an NSR of 1. It can be observed that the impact of the O_2 concentration on the SNCR process is similar but inherently different when the Fe-based additive is present. The lower the O_2 concentration, the further the SNCR initiation temperature is driven up the temperature range by the presence of the additive. Furthermore, the temperature window for all oxygen concentrations is expanded dramatically and the peak NO reduction is increased across the board. Similarly, as in the case with no Fe-based additive, an increased O_2 concentration causes a lower SNCR initiation temperature, however the difference between each O_2 case is amplified by the presence of the additive.

As mentioned prior, oxygen plays a role in both initiating SNCR, through aiding the formation of NH_2 radicals, and NH_3 oxidation, through the formation of HNO and NH radicals which are associated with NO formation. This importance is highlighted in a number of relevant observations, as follows. When there is no additive present, too little O_2 (0.5%) negatively impacts SNCR initiation, resulting in a higher SNCR initiation temperature and lower overall NO reduction. However, when the concentration of O_2 is too great (10%), the SNCR initiation temperature is greatly lowered, which could be positive, but the overall NO reduction is reduced due to the increased rate of NO production reactions. When the additive is present, a very low oxygen concentration has an exaggerated effect on SNCR initiation temperature but does not have the same impact on NO reduction, with the latter possibly due to a low rate of Fe + NH_2 oxidation reactions. It is unclear as to why the differences between initiation temperatures are increased for the case where the Fe-based additive is present.

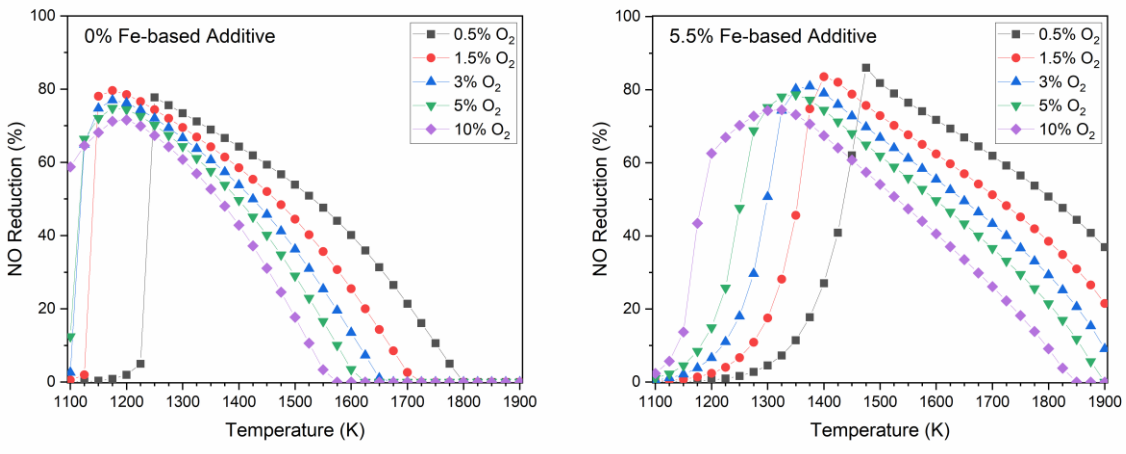

Figure 5.15 – The impact of the oxygen concentration on NO reduction due to SNCR with and without the presence of the Fe-based additive

Figure 5.16 displays the impact of varying the CO concentration on the SNCR process with and without the presence of the Fe-based additive solely for an NSR of 1. Under the classic SNCR process, an increased CO concentration will greatly shift the temperature window to a lower range, expand the temperature window and significantly decrease NO reduction. The shift in the temperature window is significant, as a CO concentration of 1000 ppm or greater will cause a portion of the temperature window to be below 1100 K, which is considerably lower than the typical SNCR temperature window. Furthermore, the decrease in maximum NO reduction is substantial; at 1250 K, the maximum NO reduction will decrease from ~75% at 20 ppm CO to ~25% at 10000 ppm CO. In comparison when the Fe-based additive is present, the expansion of the temperature window is greatly increased, with a CO concentration as little as 1000 ppm leading to a temperature window of over 800 K wide. The impact of CO concentration on NO reduction is similar whether or not the Fe-based additive is present, but due to the expanded temperature range caused by the Fe-based additive, SNCR remains viable despite this decrease; at 1400 K, the maximum NO reduction will decrease from ~80% at 20 ppm CO to ~38% at 10000 ppm CO.

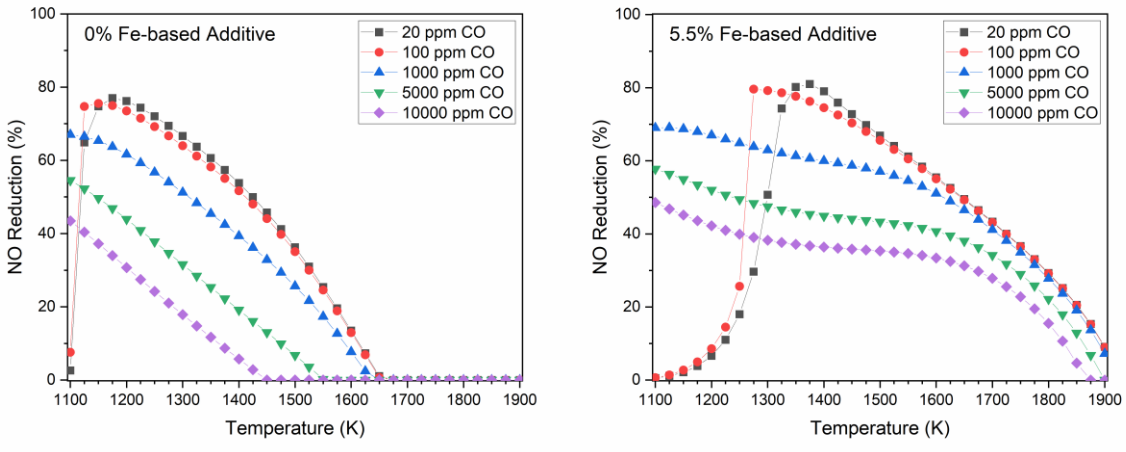

Figure 5.16 – The impact of the CO concentration on NO reduction due to SNCR with and without the presence of the Fe-based additive

When combining the observations regarding the sensitivity of these processes to O_2 and CO, a contradiction arises; the impact of an increased O_2 concentration is similar to that of an increased CO concentration but it is unlikely that there will be a region in the boiler with both extremes. Rather, it is likely that a low O_2 region will have a high CO concentration and vice versa. Fortunately, this concern was previously investigated in the form of the compositions used within section 5.3.2. In light of the data presented above, one can highlight the impact of O_2 and CO and how these trends combine; in particular for location (C), where the high CO and low O_2 combine to form a system with a wide temperature range that maintains a stable and moderate NO reduction. Overall, the presence of the Fe-based additive is shown to create a more robust SNCR system that should reliably deliver an increased and more stable NO reduction.

5.4 Conclusions

Following a comprehensive literature review, a study was envisioned where a fuel additive, the largest component of which is iron oxide, was utilised in conjunction with the conventional secondary NO_x abatement technology selective non-catalytic reduction (SNCR). An experimental investigation was initiated on a 100 kWth down-fired combustion test facility with continuous emissions monitoring as Fe-based additive loading was adjusted between 0%, 3%, 5.5% and 6.6% of the coal feed rate. Meanwhile, the strength of the SNCR process was altered by changing the normalised stoichiometric ratio (NSR) between 0, 0.5, 1, 1.5, 2 and 3. It was found that the presence of the Fe-based additive coincided with an increase in NO reduction due to SNCR and an increase in ammonia utilisation efficiency of the SNCR process. Further to this, the benefit was found to increase as the loading of Fe-based additive was increased. An argument was formed stating that the Fe-based additive will cause a lower initial NO concentration for the SNCR process and that since NO reduction decreases as the initial NO concentration decreases, if there was no interaction between the Fe-based additive and the ammonia, then NO reduction should decrease. It was shown beyond doubt, that the increased NO reductions witnessed were not within the realms of possibility for normal functioning SNCR. This was achieved by plotting the measured NO emissions alongside predicted NO emissions based on equal and decreased SNCR performance seen during coal combustion without the additive.

The interaction witnessed in these trends was theorised to work by ammonia molecules binding to the iron oxide, creating an active site for NO reduction and reducing the reliance on radical production to initiate NO reduction. This theory was then used to explain the more complex observations, such as why there was a decrease in NO reduction as NSR was increased for the 3% Fe-based additive case.

The Fe-based additive-SNCR hybrid technology was then investigated to examine whether the practical benefit can be economically utilised. A tool built by Carnegie-Mellon University called the 'Integrated Environmental Control Model' (IECM) was used to determine the change in OPEX required to provide extra ammonia in order to increase the NO reduction capacity of SNCR from 30% to 45% in a full-scale plant. This was then compared to the extra OPEX required to use the Fe-based additive, which was implied to

improve the NO reduction due to SNCR from 30% to 45%. Using the Fe-based additive was found to be a far more economical and environmentally favourable alternative to increasing ammonia usage.

In light of the promising experimental results and economic analysis, the mechanism was kinetically modelled using Cantera in order to further investigate changes to the temperature window and maximum NO reduction in ideal conditions. The model was built by combining pre-existing kinetic data for an ammonia-iron oxide interaction and the comprehensive N/H/O subset built by Klippenstein, Miller, Glarborg and others into a continuously stirred tank reactor (CSTR) designed to replicate the section of the combustion test facility into which ammonia was injected. It was found that the presence of the Fe-based additive significantly shifted the temperature window upwards, with this shift becoming greater as the Fe-based additive loading was increased. The increase in maximum NO reduction was not as great as experimental observations, rather it is more likely that the section into which ammonia was injected was at the upper end of the SNCR temperature window and the presence of the Fe-based additive reduced the impact of the increased NH_3 oxidation reactions.

This discovery regarding the impact of the Fe-based additive on the temperature window opens up debate over other possible locations for ammonia injection. Two further locations, in the overfire region (ROFA) and in the burner region (ASNCR), were defined using a range of possible compositions and these were investigated. Neither of these locations proved to be preferable to the standard location but ASNCR (advanced SNCR) did show improved performance compared to ROFA (reducing overfire air). Although, the variation in results shown through the error bars was considerably large, highlighting just how important the composition of the flue gas is.

In light of this, a final investigation was carried out to study the sensitivity of the hybrid technology to changing O_2 and CO concentration. When there is no additive present, an increased O_2 concentration is associated with a lower SNCR initiation temperature and a decreased maximum NO reduction. However, when the Fe-based additive is present, there is still a decrease in SNCR initiation temperature with increasing O_2 concentration, but this change is far more substantial, with a difference of almost 500 K between the 0.5% O_2 and 10% O_2 cases. With regards to CO when there is no additive present, an increase in CO is

accompanied by a great decrease in maximum NO reduction and a shift of the temperature window downwards, so that a portion of the temperature window is below 1100 K when the CO concentration is greater than 1000 ppm. A great change is seen when the Fe-based additive is present; the temperature window is greatly expanded, so much so that it becomes over 800 K wide for some of the tested conditions.

To conclude, the Fe-based additive was experimentally shown to have a positive impact on ammonia based SNCR. This interaction was shown to be economically viable in comparison with when SNCR effectiveness is increased by raising ammonia usage. The interaction was also shown to have a substantial impact on the temperature window, which, in addition, could increase the practicality of SNCR as a technology. This technology is well placed to be used in advanced coal power generation, in conjunction with other traditional technologies, to increase combustion efficiency and reduce NO_x emissions to appropriate levels.

CHAPTER 6 THE USE OF EQUILIBRIUM MODELLING TO COMPARE CORROSION INHIBITING FUEL ADDITIVES

6.1 Introduction

In the previous chapter, it was shown how the Fe-based additive could increase the efficiency and performance of the ammonia based selective non-catalytic reduction process for NO_x reduction. However, its use in industry could see the ash levels in the furnace increase, ash deposition accelerate and the composition of these deposits change, depending on the loading used. In section 2.5.2 of the literature review, it was shown how there are some preliminary findings regarding the impact of the Fe-based additive on slagging, fouling and fireside corrosion, but these findings are restricted to a single loading and the analysis of the chemistry is very limited. Under the knowledge that the Fe-based additive has been found to inhibit coal ash related corrosion, a more comprehensive examination of the impact of the Fe-based additive on coal ash related corrosion was undertaken using FactSage, which, along with the methods used, is described in Chapter 3. Due to the relatively inert nature of the studied coal ash (to be discussed in section 6.2), the investigation was widened to study three biomass ashes of varying perceived activity and three other additives. These three additives, two different coal ashes (designated the Ca-rich coal ash and the Al-rich coal ash) and alumina, were studied due to the practice of including coal ash with the fuel during biomass combustion in industry to help reduce slagging, improve radiation properties of the flame (Drax Power Ltd, 2014) or decrease poisoning of SCR systems (IEA Bioenergy, 2016). Section 6.3 compares the impact of the Fe-based additive and the Ca-rich coal ash on the corrosivity of the peanut shell, sunflower husk and miscanthus husk ashes. This is followed by a comparison of the impact of the Ca-rich coal ash with the Al-rich coal ash on the biomass ashes in section 6.4, and a comparison of the impact of the Al-rich coal ash and alumina on the biomass ashes in section 6.5.

6.2 Fe-based Additive Addition to Coal Ash

Figure 6.1 presents the yield of KCl and $FeCl_2$ from a mixture of a coal ash and its respective predicted flue gas with varying loadings of Fe-based additive. Studying these chlorine

containing compounds can give an indication of how Cl-based fireside corrosion is impacted by the change in composition of the deposited ash, caused by the addition of the additive. KCl can act to transport chlorine to the metal surface or to the protective oxide interface, or, alternatively, it can condense and more aggressively attack the metal as a liquid, hence signalling a form of relative corrosivity. $FeCl_2$, on the other hand, can be viewed as an indication of the extent of chlorination occurring, whether it be chlorination of the base metal, protective oxide layer or just loose iron oxide in the deposit. It can be assumed that a reduction in KCl is attributable to potassium being sequestered in a stable silicate; however, this will lead to a release in chlorine in the form of HCl or Cl_2 that may contribute to $FeCl_2$ formation or could just be harmlessly entrained in the flue gas. An increase in $FeCl_2$ does not guarantee an increase in corrosion of the base metal, but instead represents the impact of the aforementioned side-effect to capturing potassium.

There is little impact of the Fe-based additive on the yield of KCl until the end of the temperature range (>800 °C), where there is a decrease in yield with increasing addition of the Fe-based additive; however, this does not significantly impact the $FeCl_2$ yield at this temperature, indicating that the decrease in the KCl, and hence increase in free chlorine, is not great enough to cause any adverse effects. In addition to the minimal change in KCl and $FeCl_2$ yields, none of the selected liquid or solid solutions are formed in any cases studied using this coal ash. This implies that the studied coal ash is already very unreactive and the reduced corrosion witnessed by Daood, et al., (2017) is most likely due to physical processes such as adsorption, that cannot be quantified within FactSage (Becidan, et al., 2009), in addition to the reduction in gaseous KCl yield.

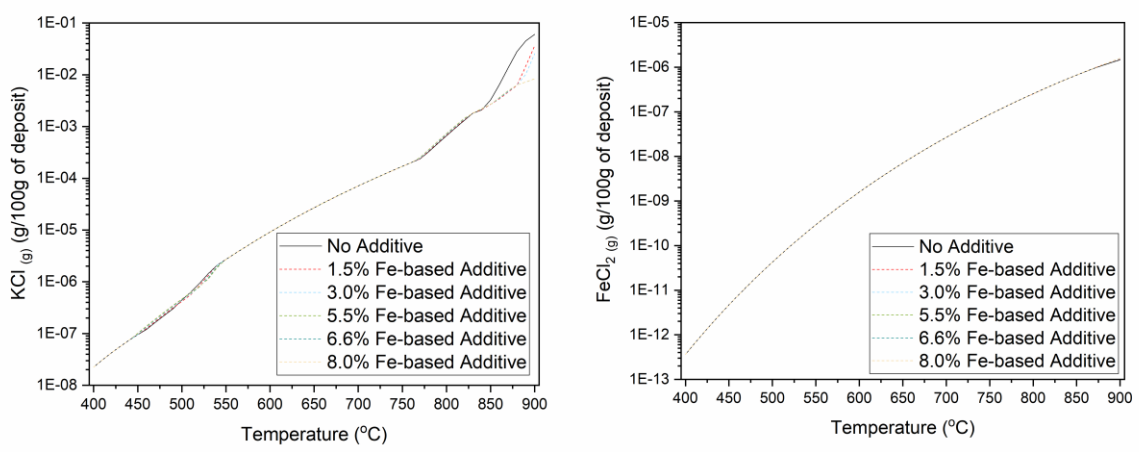

Figure 6.1 – The impact of loading of the Fe-based additive on the yield of KCl and $FeCl_2$ from a coal ash/flue gas mixture across the working temperature range

6.3 A Comparison of the Fe-based Additive and Ca-rich Coal Ash Addition to Biomass Ashes

In order to assess the capability of the Fe-based additive to reduce fireside corrosion, it is necessary to simulate its usage with ashes that cause more rapid and severe operational issues, such as ashes from biomass combustion. Biomass fuels vary greatly in their ash composition and consequently their corrosivity, therefore, three biomass fuels containing varying levels of silica, alumina, sulphur and potassium content were assessed. Drax power station, the UK's largest renewable electricity generator, primarily uses biomass fuels originating from Canadian forestry, but also has acknowledged using agricultural waste products, such as sunflower seed husks and peanut husks, and energy crops, of which miscanthus is a common choice (Drax, 2016). For this reason, the following biomass fuels were collected from literature and the compositions are presented in Table 6.1. A white wood also went through preliminary analysis, but did not present sufficient corrosive capability for there to be inhibition by the additives and, hence, sufficient trends to analyse.

	Peanut Shell (%) (Rizvi, et al., 2015)	Sunflower Husk (%) (Rizvi, et al., 2015)	Miscanthus Husk (%) (Rizvi, et al., 2015)
SiO_2	35.51	3.21	49.55
TiO_2	0.83	0.03	0.01
Al_2O_3	8.25	0.48	0.45
Fe_2O_3	3.24	0.84	0.41
MgO	5.16	15.24	2.86
CaO	9.29	27.16	7.95
Na_2O	1.33	0.21	2.39
K_2O	31.10	45.10	30.49
P_2O_5	4.52	5.30	5.76
SO_3	0.78	2.43	0.13

Table 6.1 – Composition of fuel ashes tested

A second additive, the previously analysed coal ash that will be known from here on as the Ca-rich coal ash, was tested in conjunction with the Fe-based additive; this was chosen in order to compare the effects of the Fe-based additive with the effects of an additive that is low cost, has a high silica content and is likely to be used for reasons other than corrosion inhibition, such as increasing heat transfer performance in industrial boilers. The compositions of these two additives are presented in Table 6.2.

	Fe-based Additive (%)	Ca-Rich CA (%)
SiO_2	38.04	31.87
TiO_2	0.20	0.50
Al_2O_3	4.60	15.88
Fe_2O_3	49.24	8.59
MgO	1.44	2.20
CaO	3.94	18.28
Na_2O	0.79	2.00
K_2O	0.64	0.70
P_2O_5	0.44	0.40
SO_3	0.67	19.58

Table 6.2 – Composition of additives tested

6.3.1 Peanut Shell Ash

Figure 6.2 presents the impact of various loadings of Fe-based additive and Ca-rich coal ash on the yield of gaseous KCl and $FeCl_2$ from a peanut shell ash deposit. There is an apparent pronounced impact of the additives on reducing KCl yield, with ever greater reduction in yield being witnessed, as additive loading is increased. Furthermore, the Ca-rich coal ash appears to have a far greater impact on the KCl yield at each additive loading in comparison to the Fe-based additive. The Fe-based additive required a loading of 5.5% to have a significant impact on the KCl yield, whereas the Ca-rich coal ash was shown to be beneficial at only 1.5%. Also of note, is the fact that the temperature, at which the additives were starting to decrease the KCl yield, decreased as the additive loading increased.

The mechanism for KCl capture by coal ash is well understood (Wang, et al., 2012) and is due to the significant Al_2O_3 and SiO_2 concentrations in the coal ash leading to reactions with either silicates or alumino-silicates. However, the addition of the Fe-based additive does not greatly increase the alumina concentration in the deposit. Therefore, the reasons for the decreased KCl yield are either due to dilution, a separate interaction with KCl, the catalysis of the alumino-silicate reactions by the iron oxide or the preferential chlorination of iron oxide over potassium oxide. Although, dilution is unlikely to be the sole cause of the decrease in yield due to the far greater decrease in KCl than K_2O.

Furthermore, the decreased KCl for each case is accompanied by a substantial increase in $FeCl_2$ production from the peanut ash deposit, with a significant increase regardless of which additive is used and an increasing rise in $FeCl_2$ production with additive loading; this implies that the drop in KCl arises from chemical absorption that results in HCl liberation. However, the increase in $FeCl_2$ between 1.5% and 8% Ca-rich coal ash is far smaller than the respective increase when using the Fe-based additive, even though more KCl is being captured. It stands to reason that this is either due to the far greater Fe_2O_3 content in the Fe-based additive loaded deposit, aiding the increased $FeCl_2$ formation, or, as seen in literature, that the increased CaO content of the Ca-rich coal ash loaded deposit is leading to neutralisation reactions with the liberated HCl (Liao, et al., 2015). It should also be mentioned that the rise in $FeCl_2$ compared to the baseline case is significant but orders of magnitude smaller than the fall in KCl, hence implying that the $FeCl_2$ increase is an acceptable side effect.

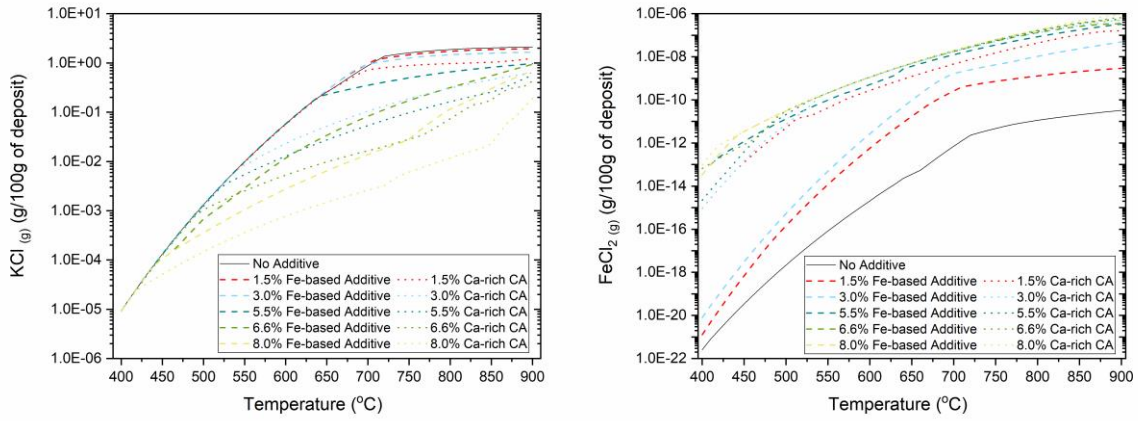

Figure 6.2 – The impact of loading of the Fe-based additive and the Ca-rich coal ash on the yield of KCl and $FeCl_2$ from a peanut shell ash/flue gas mixture across the working temperature range

Figure 6.3 presents the impact of the Fe-based additive and the Ca-rich coal ash on the yield and formative temperature range of corrosive liquid salts from a peanut shell ash deposit. A greater formative temperature range and yield of these liquid salts would inevitably lead to greater corrosion of the base metal through the processes described in Section 2.5.1, whereas a reduction in either of these metrics would be considered an indicator of reduced corrosivity of the ash deposit. Loading the deposit with increasing amounts of Fe-based additive narrows the temperature window at which the corrosive

liquid salts can form dramatically, until these liquid salts are eliminated at 5.5% loading. Use of the Ca-rich coal ash at 1.5% loading, although positive, does not have as big an impact as the Fe-based additive on the temperature window; however, only 3% loading of the Ca-rich coal ash is required to prevent liquid salt formation.

With regard to the yield of liquid KCl and K_2SO_4, yield decreases with respect to the baseline case as increasing Fe-based additive loading is used and the yield is lower for the single Ca-rich additive case in comparison to the same loading of Fe-based additive. Peculiarly, the yield of the liquid pyrosulphate increases dramatically for each case, showing greater formation with increased additive loading and with the use of the Ca-rich coal ash over the Fe-based additive. This is likely a side-effect of the capture of K_2SO_4, which will lead to a release of SO_3 and SO_2 that will react with remaining K_2SO_4 to produce potassium pyrosulphate. This leads to a several orders of magnitude rise in the formation of this troublesome compound; however, the yield is still very low compared to the other prominent corrosive liquid salts. It should also be noted that the Ca-rich coal ash also has a high sulphur content, which could contribute to the greater increase in pyrosulphate yield.

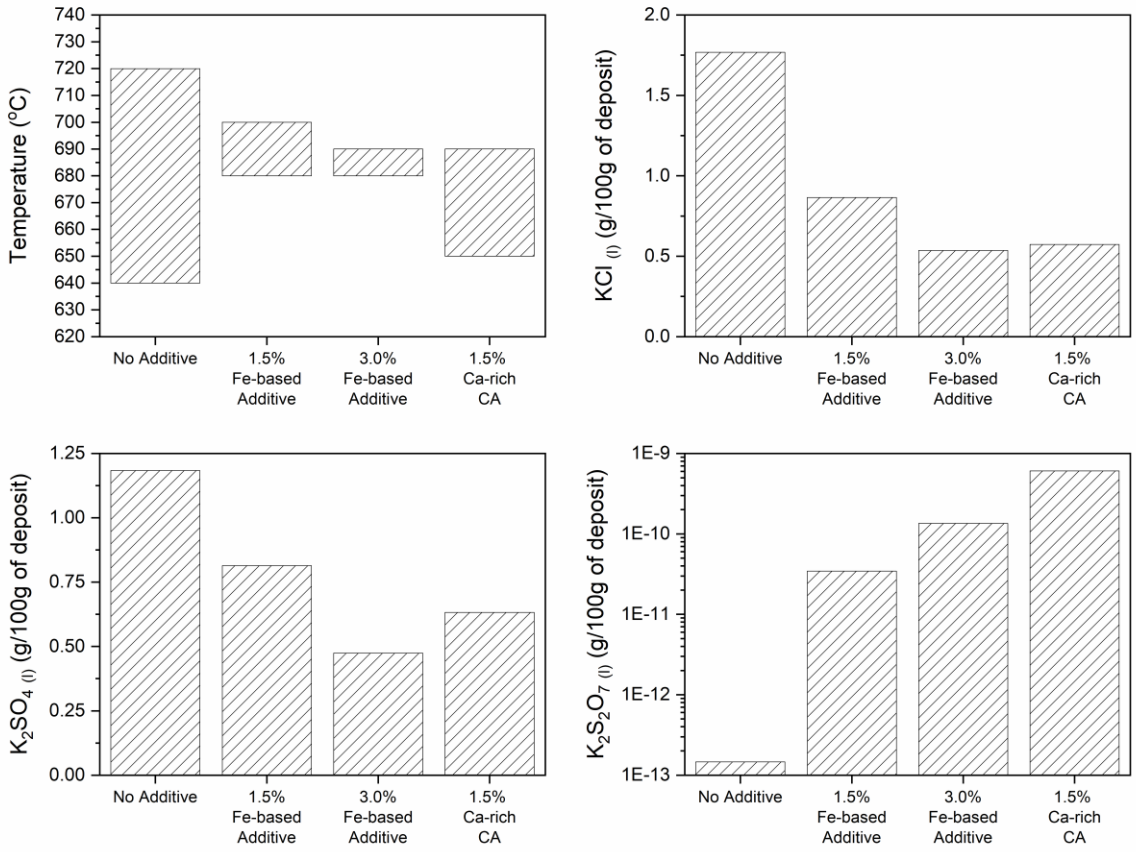

Figure 6.3 – The impact of loading of the Fe-based additive and the Ca-rich coal ash on the yield of liquid salts and the formative temperature range in a peanut shell ash/flue gas mixture

Figure 6.4 presents the impact of the Fe-based additive and the Ca-rich coal ash on the yield and formative temperature range of solid KCl from a peanut shell ash deposit. The presence of solid alkali chlorides and sulphates is less problematic than the liquid phase species in terms of corrosion but reducing their formation will still have a significant impact on corrosion rates, in addition to issues such as fouling. The decreased formative temperature range of the liquid salt solution during the use of 1.5% and 3% Fe-based additive has the impact of increasing the temperature range where solid KCl is present; however, the yield compared to the baseline is lower from 500 °C to 640 °C. As the Fe-based additive loading is increased further to 5.5%, the yield decreases substantially and the formative temperature range is the same as the baseline case. Increasing the loading further to 6.6% and 8% decreases the yield even further and shrinks the temperature range immensely so that the KCl no longer forms above 450 °C. The Ca-rich coal ash performs slightly better at each loading, with yield and temperature range decreasing steadily with

each increase in loading. However, there are periods at which the Fe-based additive performs marginally better at certain periods, such as 400-480 °C for the 5.5% loading and above 420 °C for the 6.6% loading.

Very visible kinks are seen in the lines for the 1.5% Ca-rich coal ash case and the 5.5% Fe-based additive case at 520 °C and 570 °C respectively. These occur at the same point as the phase transition between the potassium sulphate containing OrtB and Hexa solutions, and these kinks are most likely a consequence of this, as it becomes energetically favourable for some potassium to be sulphated rather than chlorinated.

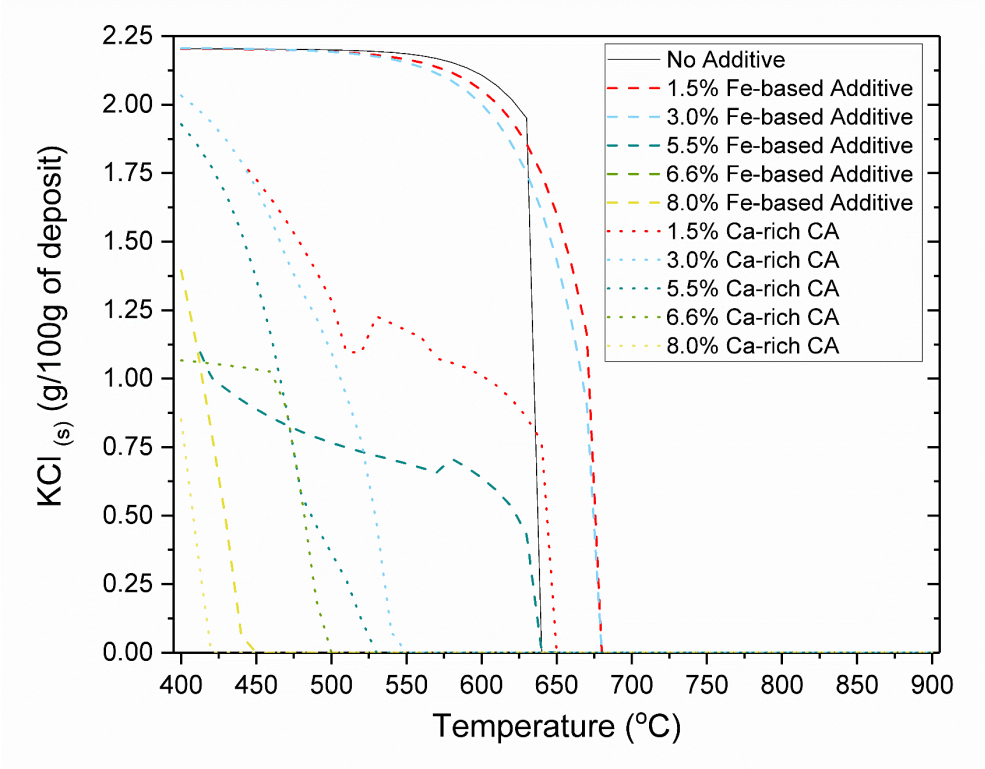

Figure 6.4 – The impact of loading of the Fe-based additive and the Ca-rich coal ash on the yield of solid KCl and the formative temperature range in a peanut shell ash/flue gas mixture

Figure 6.5 presents the impact of the Fe-based additive and the Ca-rich coal ash on the yield and formative temperature range of solid K_2SO_4 from a peanut shell ash deposit. The addition of the Fe-based additive leads to marginal improvements in K_2SO_4 yield with increasing loading, the rate of which implies that it is most likely a result of potassium dilution. The Ca-rich coal ash, on the other hand, intensifies the formation of K_2SO_4 greatly at 1.5% loading and less so at 3% loading; improvements are only witnessed once the

loading has been increased to 5.5% but at this point, the K_2SO_4 yield is far less than even the 8% Fe-based additive case. These initial increases may be a result of the relatively sizeable SO_3 content in the Ca-rich coal ash and the comparative lack of potassium dilution at these loadings. This can be seen as a warning over the use of additives containing sulphur; the resulting increase in K_2SO_4, especially when it is as great as seen during the 1.5% case, may cause more damage than it prevents from the conversion of KCl to K_2SO_4. The 6.6% Ca-rich coal ash case decreases the yield even further than the 5.5% case and also reduces the formative temperature range. When the loading is increased to 8%, the solid solution is eliminated altogether.

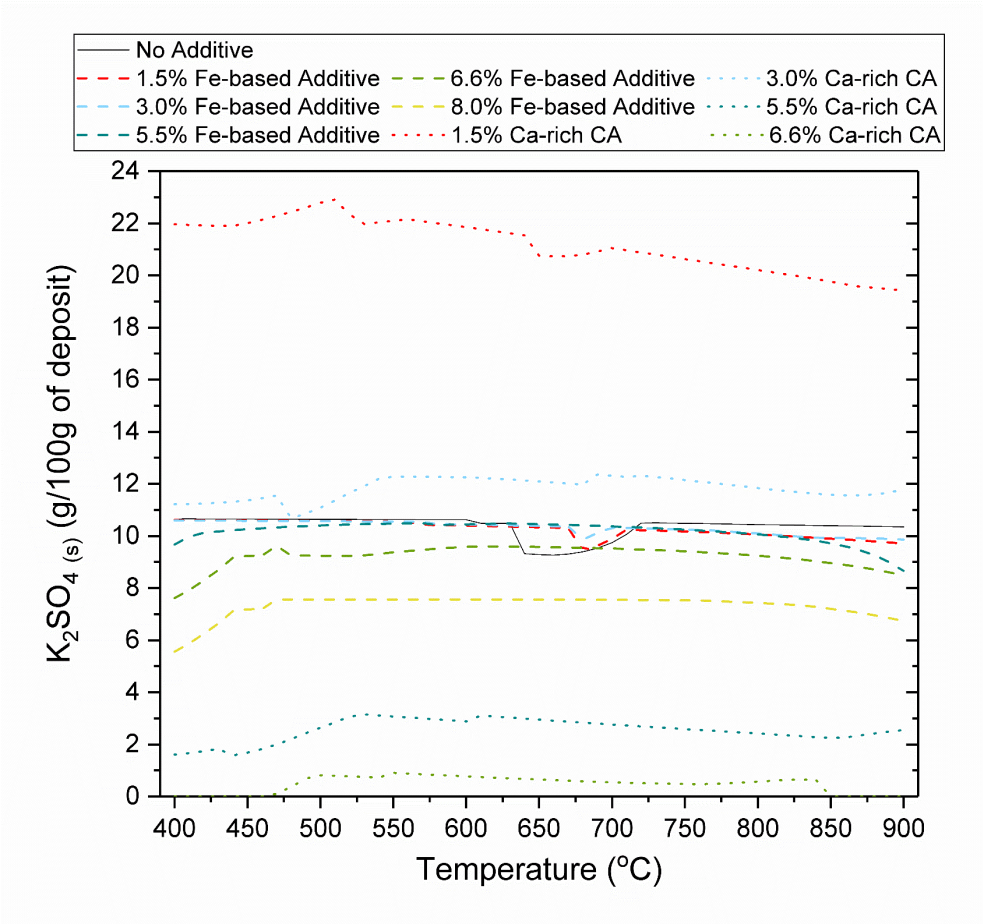

Figure 6.5 – The impact of loading of the Fe-based additive and the Ca-rich coal ash on the yield of solid K_2SO_4 in a peanut shell ash/flue gas mixture

6.3.2 Sunflower Husk Ash

Figure 6.6 presents the impact of various loadings of Fe-based additive and Ca-rich coal ash on the yield of gaseous KCl and $FeCl_2$ from a sunflower husk ash deposit. This ash, when no

additive is being used, contains the greatest amount of potassium out of those tested; that being noted, this ash is also arguably the least impacted by either of the additives. Not until 5.5% loading of Ca-rich coal ash is the KCl yield significantly impacted, and increasing the loading further does not lead to any considerable improvement. This is slightly mirrored in the trends seen with the $FeCl_2$ yield in that the greatest deviation from the baseline occurs for the 5.5% and greater loadings of the Ca-rich coal ash; although, the 5.5% and greater loadings of Fe-based additive do also lead to significantly greater $FeCl_2$ yield without presenting any considerable reduction in KCl, which would be considered an improvement. This is most likely just a function of the markedly increased Fe_2O_3 content in these deposits.

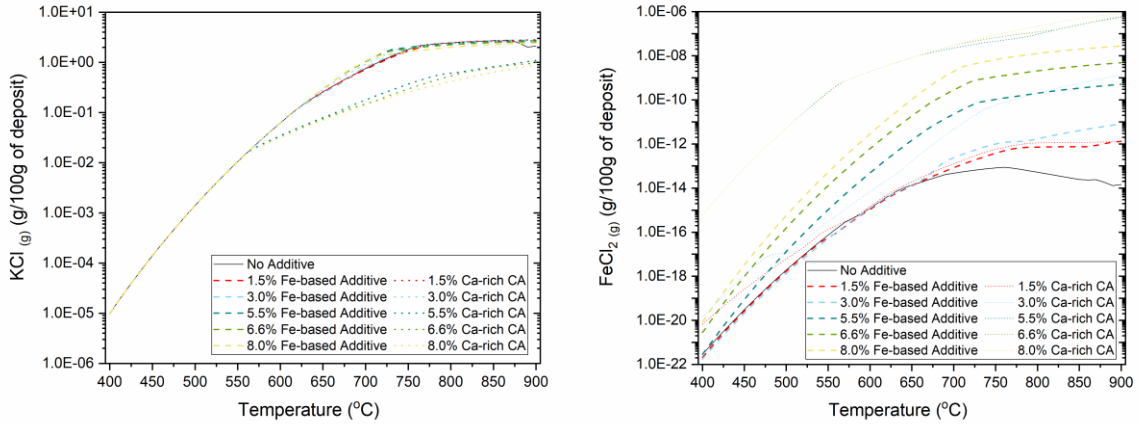

Figure 6.6 – The impact of loading of the Fe-based additive and the Ca-rich coal ash on the yield of KCl and $FeCl_2$ from a sunflower husk ash/flue gas mixture across the working temperature range

Figure 6.7 presents the impact of the Fe-based additive and the Ca-rich coal ash on the yield and formative temperature range of corrosive liquid salts from a sunflower husk ash deposit. In contrast to the impact on the gaseous KCl, both additives have a positive impact on the formative temperature range of corrosive liquid salts within the deposit. Increasing the loading of the Fe-based additive narrows the temperature range dramatically from 130 °C for the baseline case to 20 °C for the 8% loading case. In comparison, the Ca-rich coal ash proves even more effective, tightening the temperature range as the loading is increased to 3% and then eliminating the formation of the deposit altogether at any increased loading.

As for the yield of the liquid KCl, there is not much impact in utilising either additive until the loading is at least 5.5% for the Fe-based additive or 3% for the Ca-rich coal ash; although, when 8% Fe-based additive is utilised, the yield of liquid KCl is less than half the baseline case. The impact of the additives on the yield of liquid K_2SO_4 is less clear. The yield increases from the baseline as loading of the Ca-rich coal ash is increased, while the introduction of the Fe-based additive initially decreases the yield when loading is 1.5% but as this is increased to 3%, there is a large increase. From here on, the yield decreases as loading is increased but 8% Fe-based additive is required to fall below the baseline level again. As with the peanut shell ash, the use of the additives increases the yield of potassium pyrosulphate; this issue is aggravated by the additive loading and the use of the Ca-rich coal ash over the Fe-based additive, most likely due to the much greater sulphur content in the prior additive.

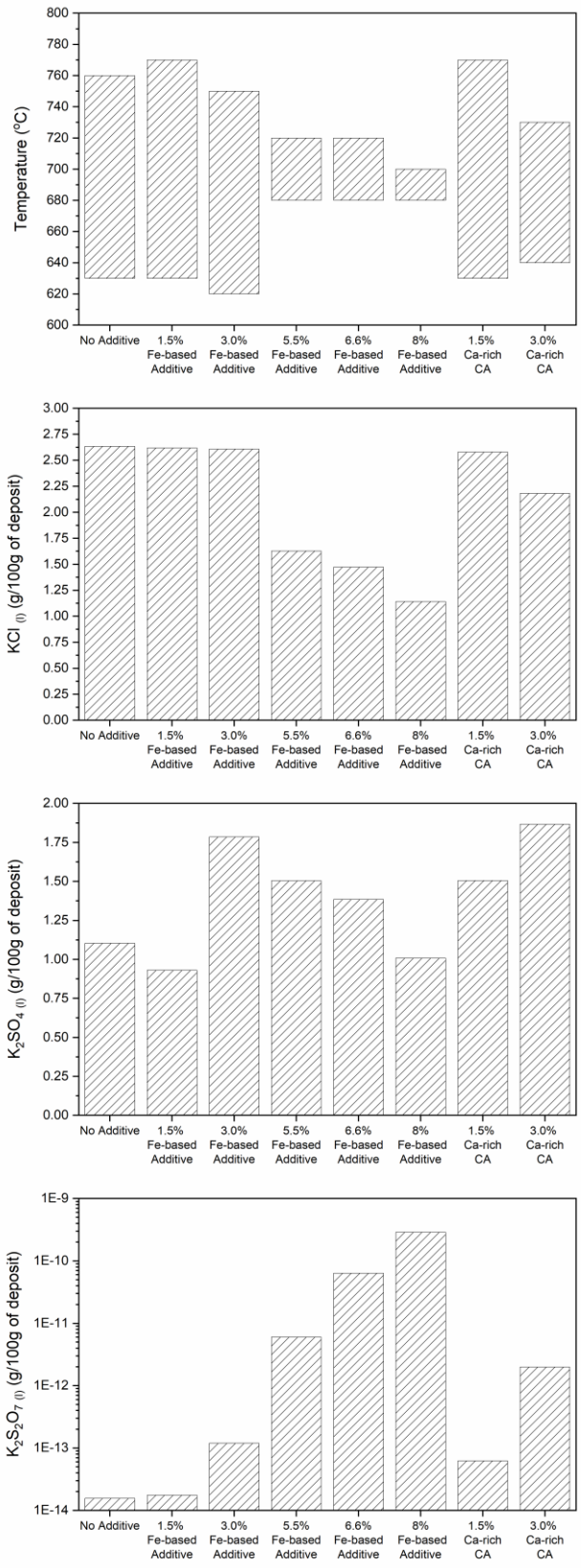

Figure 6.7 – The impact of loading of the Fe-based additive and the Ca-rich coal ash on the yield of liquid salts and their formative temperature range in a sunflower husk ash/flue gas mixture

Figure 6.8 presents the impact of the Fe-based additive and the Ca-rich coal ash on the yield and formative temperature range of solid KCl from a sunflower husk ash deposit. Introducing the Fe-based additive results in a slight decrease in yield that grows with increasing loading. The formative temperature range changes with the changing initial melt temperature witnessed in Figure 6.7. The Ca-rich coal ash has a minor impact on yield when the loading is 1.5% or 3%, although this decrease in yield is greater than any of the Fe-based additive cases from 400-550 °C. Increasing the loading further to 5.5% decreases the yield substantially, while also decreasing the formative temperature range by ~100 °C. There is no great benefit to increasing the loading of Ca-rich coal ash further than 5.5% for this ash.

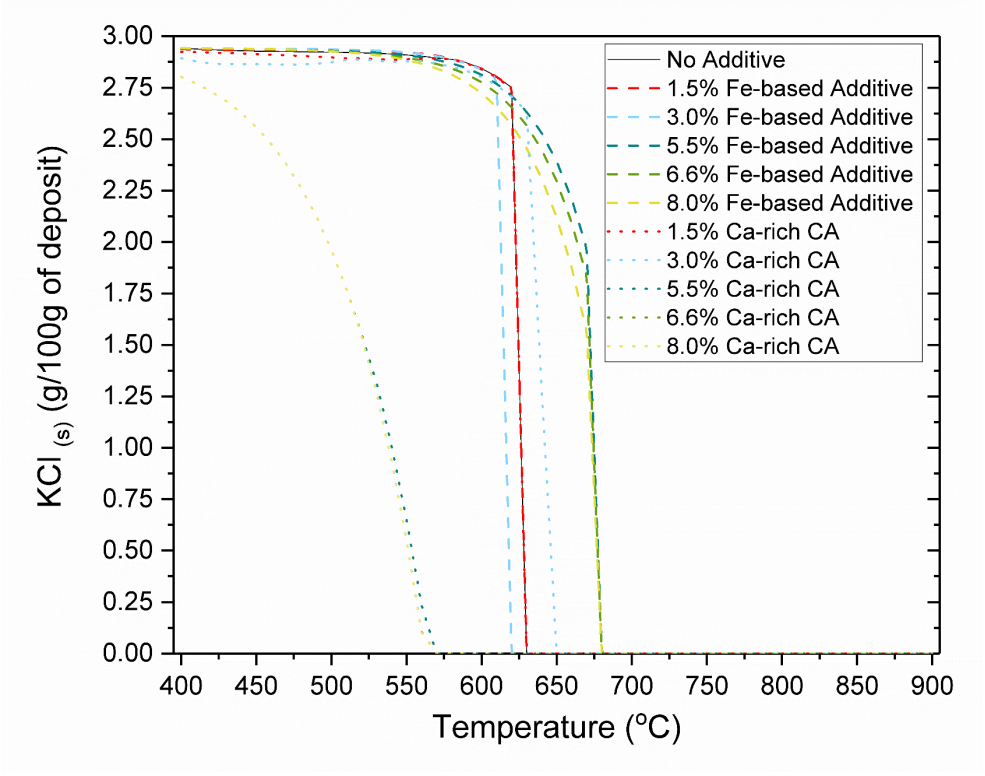

Figure 6.8 – The impact of loading of the Fe-based additive and the Ca-rich coal ash on the yield of solid KCl and the formative temperature range in a sunflower husk ash/flue gas mixture

Figure 6.9 presents the impact of the Fe-based additive and the Ca-rich coal ash on the yield and formative temperature range of solid K_2SO_4 from a sunflower husk ash deposit. As with the peanut shell ash, the Fe-based additive has a slight positive impact on K_2SO_4 yield, with the yield decreasing by smaller rates as the loading is increased. The impact of

the Ca-rich coal ash is erratic. At first, there is a rise in solid K_2SO_4 yield with increasing loading, with the maximum yield being witnessed at 3% Ca-rich coal ash. Increasing loading further leads to a decrease in yield, but not even during the 8% loading case does the yield fall below the baseline. The issue of the significant SO_3 content in the Ca-rich coal ash is far more noteworthy with an increased native potassium content.

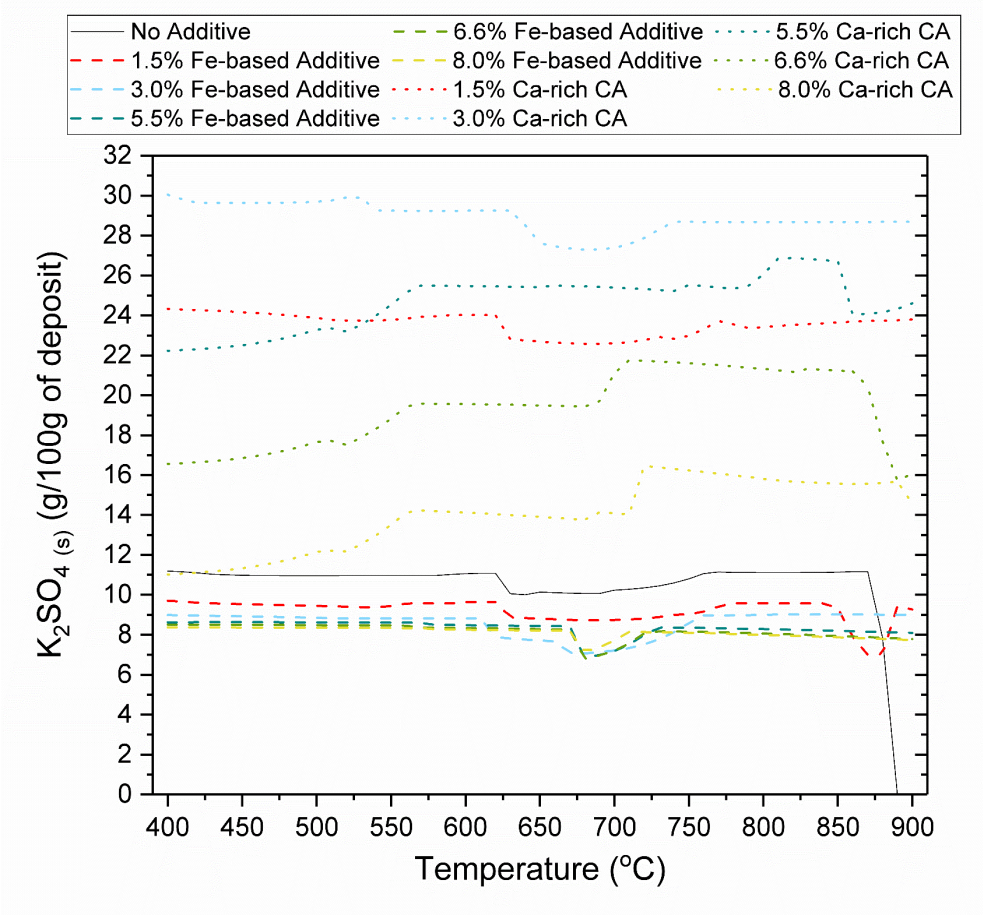

Figure 6.9 – The impact of loading of the Fe-based additive and the Ca-rich coal ash on the yield of solid K_2SO_4 in a sunflower husk ash/flue gas mixture

6.3.3 Miscanthus Husk Ash

Figure 6.10 presents the impact of various loadings of Fe-based additive and Ca-rich coal ash on the yield of gaseous KCl and $FeCl_2$ from a miscanthus husk ash deposit. The Fe-based additive appears to have only a modest impact on the yield of KCl and the height of this impact is reached at only 5.5% loading, after which there is no more change in the yield (the 5.5% and 6.6% Fe-based loading dashed lines on Figure 6.10 appear behind the 8% line). Comparatively, the Ca-rich coal ash has a much greater impact on KCl for all additive

loadings greater than 1.5%, which displays similar yields to its Fe-based additive counterpart. Similar trends can also be observed for the $FeCl_2$ yield. However, it is worth highlighting how close the 5.5-8% Fe-based additive and the 3-8% Ca-rich coal ash are in terms of $FeCl_2$ yield; displaying again that, although the Ca-rich coal ash is more capable at capturing potassium and liberating chlorine, the resulting rate of iron chlorination (wherever the iron may originate from) is proportionally lower for this additive.

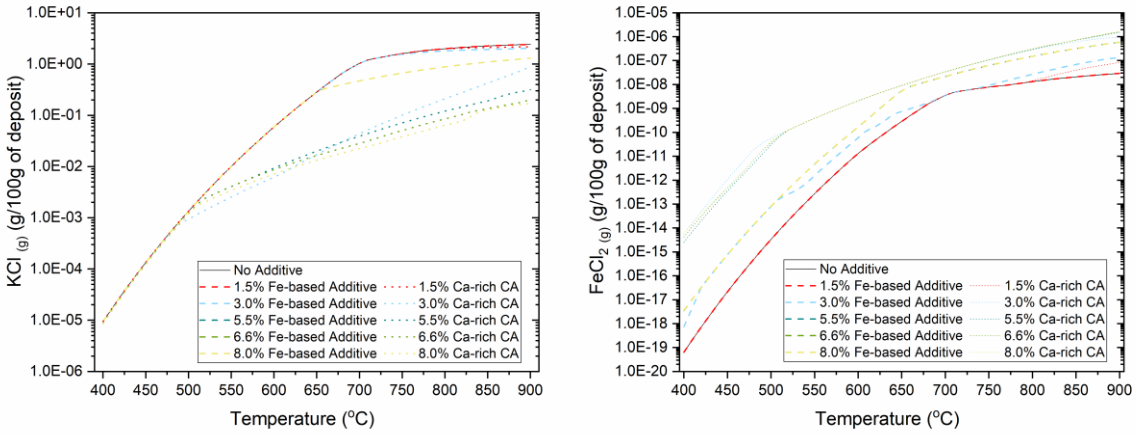

Figure 6.10 – The impact of loading of the Fe-based additive and the Ca-rich coal ash on the yield of KCl and $FeCl_2$ from a miscanthus husk ash/flue gas mixture across the working temperature range

Figure 6.11 presents the impact of the Fe-based additive and the Ca-rich coal ash on the yield and formative temperature range of corrosive liquid salts from a miscanthus husk ash deposit. As can be witnessed, these trends are curiously more uniform than those liquid solutions discussed prior, in that the temperature ranges and yield do not change with additive addition whilst the liquid solution remains formed; this is most likely due to the fact that the miscanthus husk ash contains, by far, the largest amount of silica of all the studied biomass ashes. This means that following a method of increasing the silica concentration in the deposit, in order to add stability and impact the liquid salt formation, is futile. That being said, the liquid salt does stop forming when either 5.5% Fe-based additive or 3% Ca-rich coal ash is used. This miscanthus ash also has a very low alumina content (0.45%) and the improvement of this property, even marginally by the Fe-based additive, likely causes the liquid salt to stop forming. This is in opposition to the belief that

potassium dilution could be the cause, which is discounted due to the lack of decrease in the yield of any of the studied liquid salts.

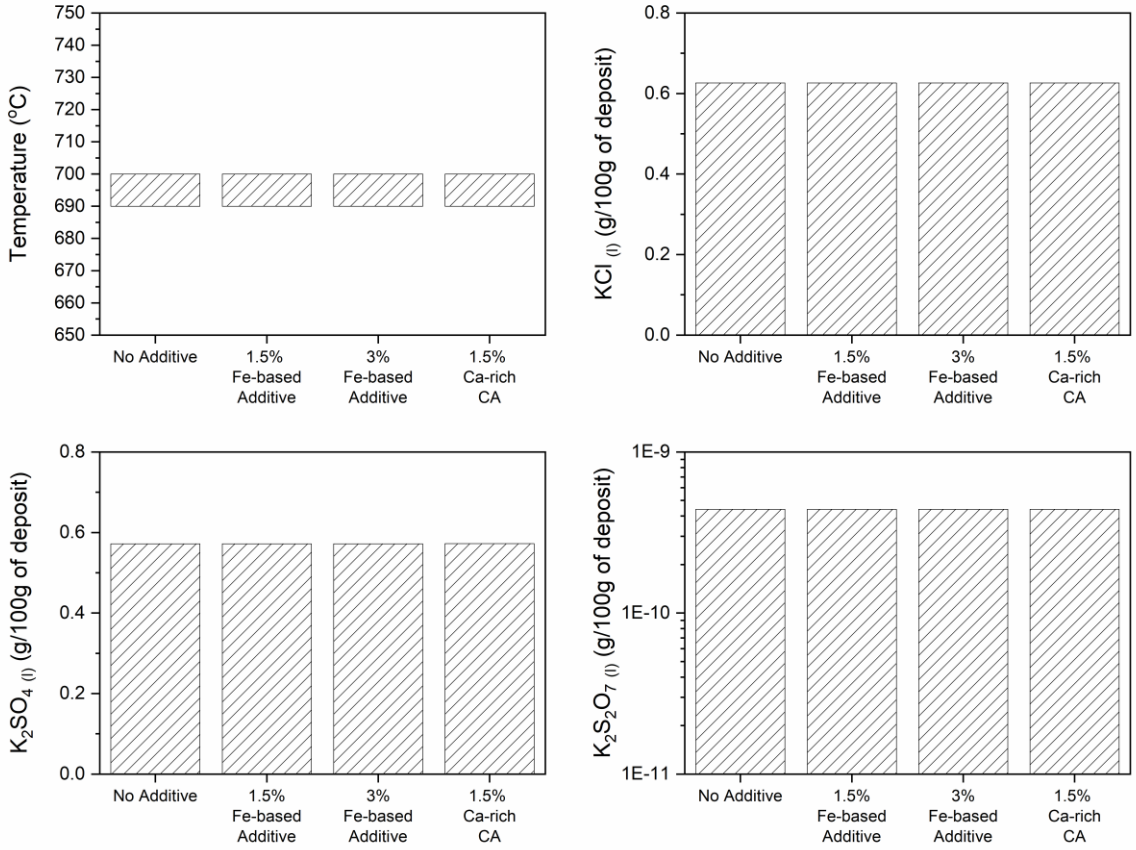

Figure 6.11 – The impact of loading of the Fe-based additive and the Ca-rich coal ash on the yield of liquid salts and their formative temperature range in a miscanthus husk ash/flue gas mixture

Figure 6.12 presents the impact of the Fe-based additive and the Ca-rich coal ash on the yield and formative temperature range of solid KCl from a miscanthus husk ash deposit. When adding 1.5% Fe-based additive, there is no change from the baseline case; however, increasing the loading to 3% decreases the yield and increasing it further to 5.5% decreases the yield and the formative temperature range, while any further increase in loading does not have any impact. Similar to the Fe-based additive, the 1.5% Ca-rich coal ash case does not deviate from the baseline. All further Ca-rich coal ash cases decrease the yield and the formative temperature range substantially, with arguably the best performing loading being 3% (interesting as this is neither the highest or lowest loading tested). This may, however, be linked to the K_2SO_4 formation witnessed in Figure 6.13, as the fall in solid KCl

at 3% Ca-rich coal ash is accompanied by a rise in solid K_2SO_4; at higher loadings of Ca-rich coal ash, there is greater inhibition of the solid K_2SO_4 and so there may be marginally more potassium available for chlorination, hence slightly greater solid KCl yields.

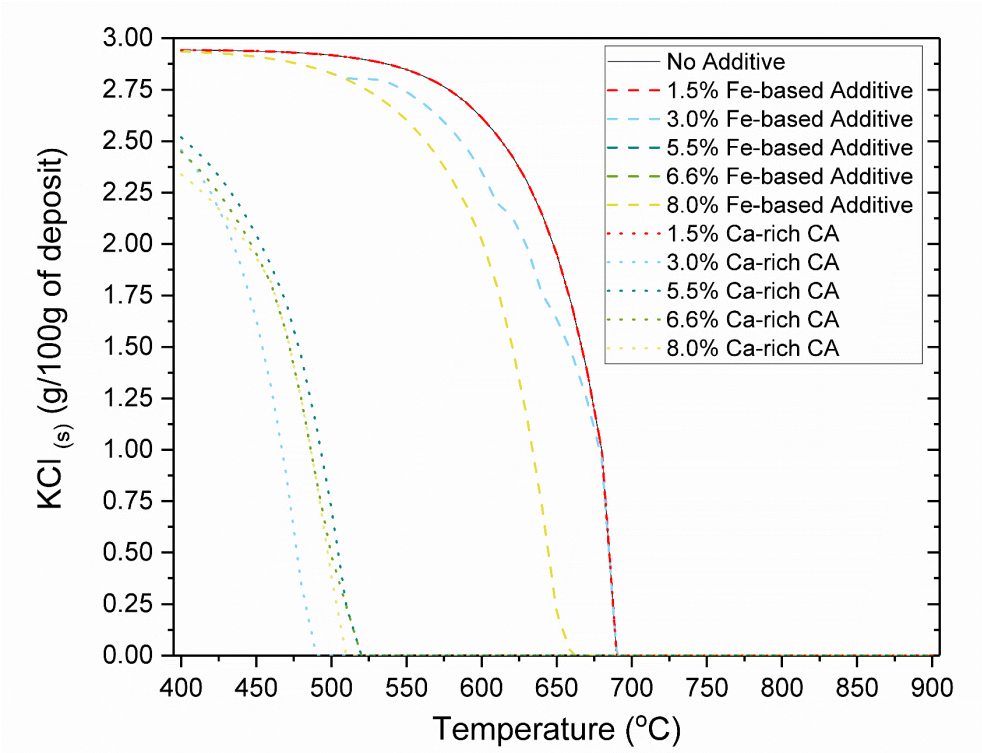

Figure 6.12 – The impact of loading of the Fe-based additive and the Ca-rich coal ash on the yield of solid KCl and the formative temperature range in a miscanthus husk ash/flue gas mixture

Figure 6.13 presents the impact of the Fe-based additive and the Ca-rich coal ash on the yield and formative temperature range of solid K_2SO_4 from a miscanthus husk ash deposit. Unlike the previous two fuel ashes, the addition of the Fe-based additive increases the yield of solid K_2SO_4, with the rise growing with increasing loading. This is likely due to the extremely low native SO_3 content in the miscanthus husk ash (0.13%) and the fact that the addition of the Fe-based additive actually increases the SO_3 content in the deposit (to 0.5% at 8% loading); therefore, the entire composition of the native fuel ash should be considered in practice if one is to use dilution as the method for mitigating the formation of corrosive species, as there can be side effects that one should be aware of.

Similar to the two previous fuel ashes, the 1.5% and 3% Ca-rich coal ash cases produce a greater yield of solid K_2SO_4 than the baseline, with the 3% case producing the highest yield

for the majority of the temperature range. Increasing the loading further leads to a decrease in yield and temperature range, so that the yield from the 5.5% case is only slightly greater than the 8% Fe-based additive cases and the solid K_2SO_4 stops forming at 880 °C, while the 6.6% and 8% Ca-rich coal ash cases offer lower yields than the baseline and smaller formative temperature ranges (disappearing at 830 °C). The contraction of the temperature range in these last three cases is not simply due to the return of the K_2SO_4 to the gas phase but rather due to the formation of a high temperature melt; these are not included in Figure 6.13 due to their perceived position within the deposit (likely away from the steel) but they may impact ash deposition or have the ability to migrate through the deposit, so should be avoided if possible.

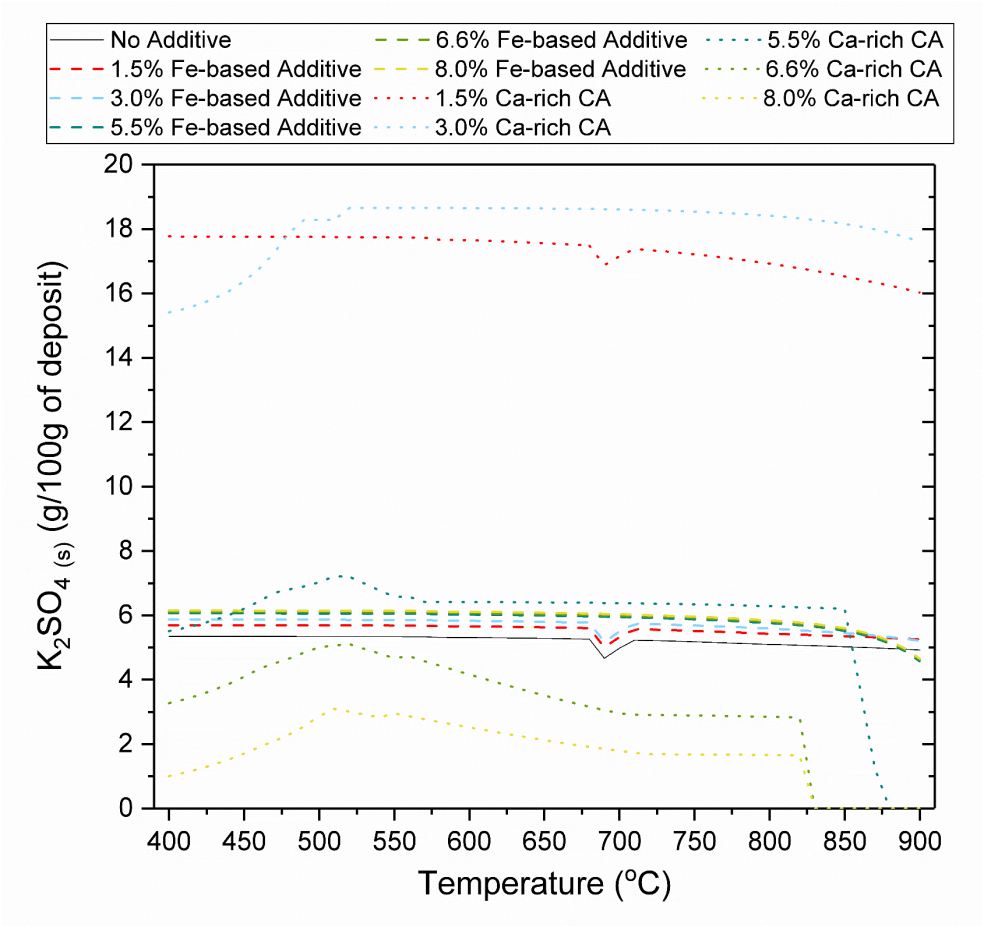

Figure 6.13 – The impact of loading of the Fe-based additive and the Ca-rich coal ash on the yield of solid K_2SO_4 in a miscanthus husk ash/flue gas mixture

6.4 A Comparison of Ca-rich Coal Ash and Al-rich Coal Ash Addition to Biomass Ashes

The Ca-rich coal ash proved capable of reducing the yield of corrosion inducing compounds, however there are significant impurities within this ash, which may impact its effectiveness, namely the calcium oxide and sulphur components. Kaolin is widely discussed in literature as being a choice additive for corrosion inhibition (Wang, et al., 2012) but is likely to be too expensive to be utilised in an industrial setting. Rather, it would be preferable to utilise a coal ash that resembles kaolin in having a high concentration of alumina and silica and without any significant levels of impurities. Such an 'Al-rich' coal ash can be found in (Daood, et al., 2017) and will be compared to the Ca-rich coal ash in order to highlight the importance of the presence of impurities and to discuss to what degree 'any' coal ash can be used in biomass boilers.

	Ca-rich CA (%)	Al-rich CA (%)
SiO_2	31.87	56.28
TiO_2	0.50	1.04
Al_2O_3	15.88	23.38
Fe_2O_3	8.59	6.62
MgO	2.20	2.10
CaO	18.28	6.31
Na_2O	2.00	0.37
K_2O	0.70	2.19
P_2O_5	0.40	0.58
SO_3	19.58	1.13

Table 6.3 – Comparison of the two tested coal ashes

6.4.1 Peanut Shell Ash

Figure 6.14 presents the impact of various loadings of Al-rich coal ash and Ca-rich coal ash on the yield of gaseous KCl and $FeCl_2$ from a peanut shell ash deposit. The Al-rich coal ash can be observed to be far more proficient at reducing KCl yield than the Ca-rich coal ash at all loadings except 1.5%, where there is little deviation from the baseline. Most interestingly for the uptake of this technology, the Al-rich coal ash is capable of

dramatically reducing KCl yield across the entire temperature range when a loading of 6.6% or greater is used. As for the $FeCl_2$ yield, all cases greatly deviate from the baseline except the 1.5% Al-rich coal ash case, mirroring the lack of impact that this loading causes. The fact that the other cases are bunched together, even though a varying amount of potassium has been captured, indicates a maximum rate for the iron chlorination cycle within this deposit. It stands to reason that if the $FeCl_2$ is unable to rise any further, it would be desirable to maximise potassium capture, safe in the knowledge that the excess chlorine will most likely be entrained in the flue gas and removed.

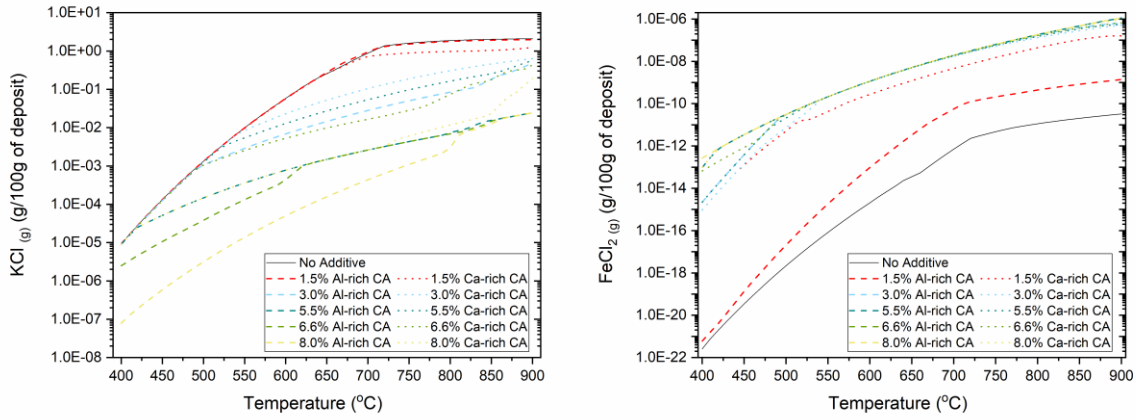

Figure 6.14 – The impact of loading of the Al-rich coal ash and the Ca-rich coal ash on the yield of KCl and $FeCl_2$ from a peanut shell ash/flue gas mixture across the working temperature range

Figure 6.15 presents the impact of the Al-rich coal ash and the Ca-rich coal ash on the yield and formative temperature range of corrosive liquid salts from a peanut shell ash deposit. The formative temperature range shrinks from 80 °C to 40 °C by the addition of 1.5% of either additive; although, the new temperature range during the use of the Al-rich coal ash is higher than its Ca-rich coal ash counterpart, which may prove useful if a plant is utilising older boilers working with steam at lower temperatures. However, increasing the loading of either additive will eliminate the formation of the liquid salt solution altogether. The yield of KCl and K_2SO_4 is far lower for the Ca-rich coal ash case, but the yield of potassium pyrosulphate is almost two orders of magnitude greater than the Al-rich coal ash, an effect seen also in the previous additive comparison.

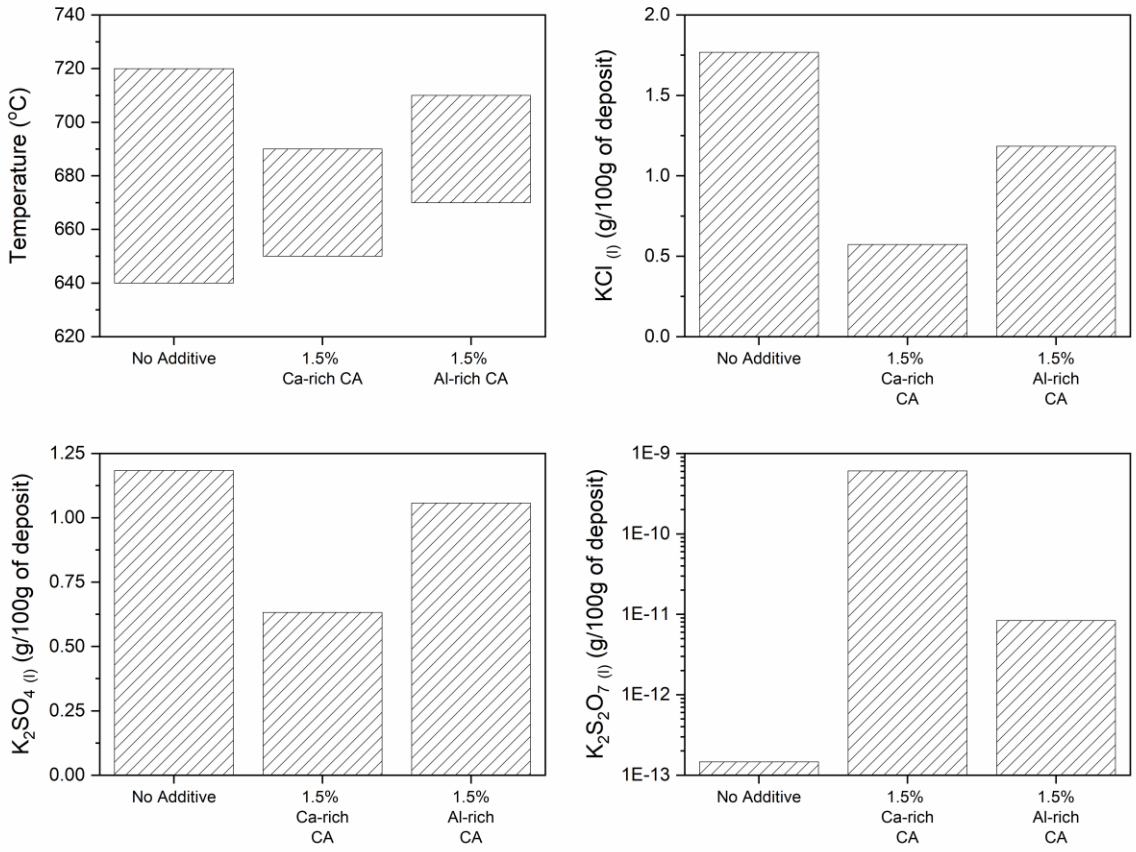

Figure 6.15 – The impact of loading of the Al-rich coal ash and the Ca-rich coal ash on the yield of liquid salts and their formative temperature range in a peanut shell ash/flue gas mixture

Figure 6.16 presents the impact of the Al-rich coal ash and the Ca-rich coal ash on the yield and formative temperature range of solid KCl from a peanut shell ash deposit. The Al-rich coal ash only has a slight positive impact on yield when 1.5% loading is used, while the increased temperature range, compared to the baseline, is due to the shifted and contracted temperature range of the liquid solution. Both the yield and the temperature range greatly improve with an increase in Al-rich coal ash loading. The 3% Al-rich coal ash case produces an equivalent yield to the 5.5% Ca-rich coal ash case but with the same temperature range as the 6.6% case; while, the 5.5% Al-rich coal ash case behaves as effectively as the 8% Ca-rich coal ash case and any further increase in loading leads to the elimination of the solid solution.

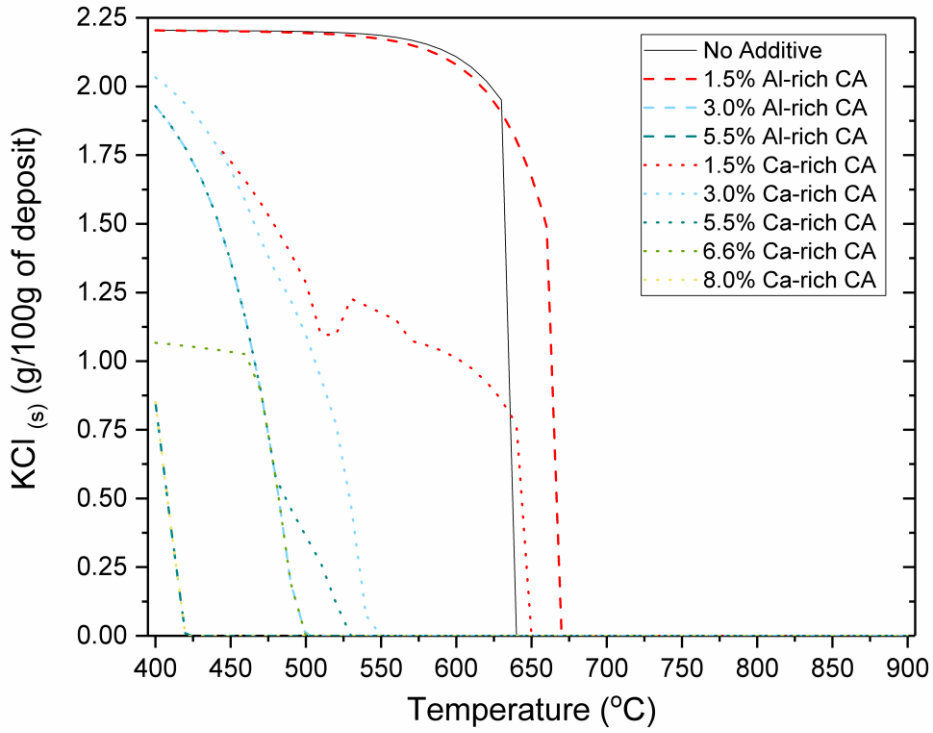

Figure 6.16 – The impact of loading of the Al-rich coal ash and the Ca-rich coal ash on the yield of solid KCl and the formative temperature range in a peanut shell ash/flue gas mixture

Figure 6.17 presents the impact of the Al-rich coal ash and the Ca-rich coal ash on the yield and formative temperature range of solid K_2SO_4 from a peanut shell ash deposit. Unlike the Ca-rich coal ash, the 1.5% Al-rich coal ash case produces a yield similar to the baseline, rather than significantly greater. Further to this, increasing the loading of Al-rich coal ash to 3% decreases the yield by over half and any additional increase in loading leads to the elimination of the solid solution, thus eliminating corrosion reaction pathways originating from alkali sulphates and, hence, reducing overall corrosion rates associated with this ash.

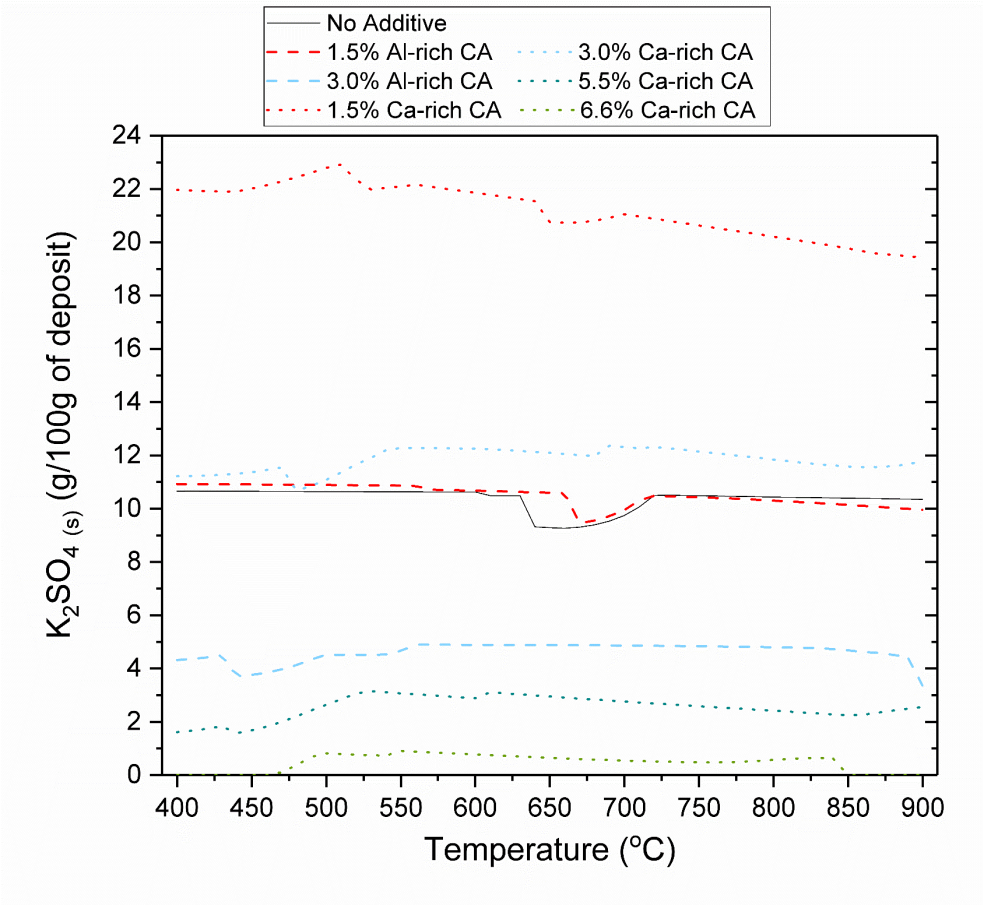

Figure 6.17 – The impact of loading of the Al-rich coal ash and the Ca-rich coal ash on the yield of solid K_2SO_4 in a peanut shell ash/flue gas mixture

6.4.2 Sunflower Husk Ash

Figure 6.18 presents the impact of various loadings of Al-rich coal ash and Ca-rich coal ash on the yield of gaseous KCl and $FeCl_2$ from a sunflower husk ash deposit. Both the additives perform similarly across the temperature range, with improved KCl capture at higher loadings. The exception to this is from ~450 °C to ~700 °C, where the 8% Al-rich coal ash case performs better than the equivalent Ca-rich coal ash case. The lack of disparity in the trends from each additive may be related to the fact that the sunflower husk ash has the highest initial potassium concentration; therefore, once potassium is sequestered by an alumino-silicate, more KCl may be formed by the chlorination of the present excess potassium. This phenomenon would seem to require a sufficiently large native potassium content and may also be used to explain the relative lack of impact by the lower additive loadings on KCl yield from the other biomass ashes. The $FeCl_2$ yield trends mirror the KCl trends well; the 5.5-8% cases are closely grouped for the majority of the temperature

range, with the notable exception of the 8% Al-rich coal ash exceeding the other cases across a similar temperature window to the KCl divergence, due to the sequestering of potassium, leading to the liberation of chlorine and greater $FeCl_2$ formation.

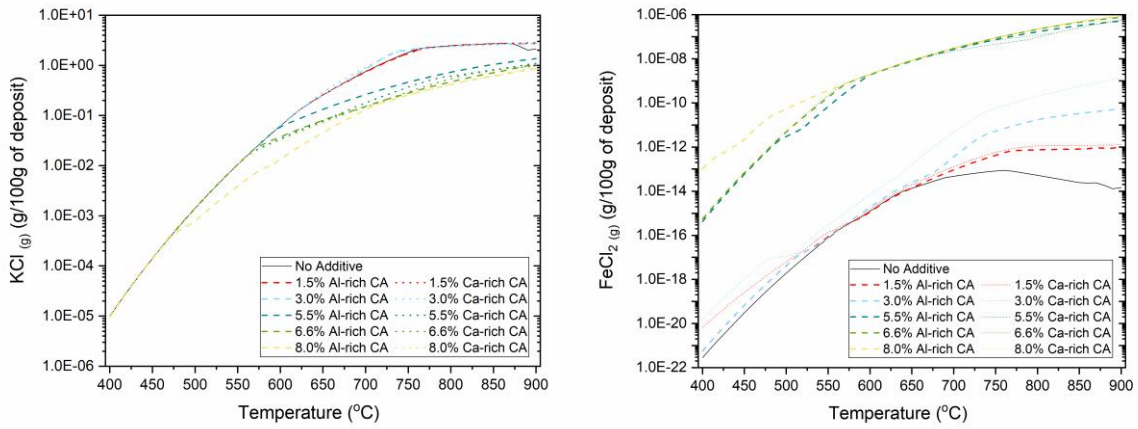

Figure 6.18 – The impact of loading of the Al-rich coal ash and the Ca-rich coal ash on the yield of KCl and $FeCl_2$ from a sunflower husk ash/flue gas mixture across the working temperature range

Figure 6.19 presents the impact of the Al-rich coal ash and the Ca-rich coal ash on the yield and formative temperature range of corrosive liquid salts from a sunflower husk ash deposit. The impact on the temperature range is similar for both the additives, first expanding the temperature range when a loading of 1.5% is used and then contracting when 3% of either additive is used; any addition greater than 3% is enough to seemingly prevent any corrosive liquid salts from forming. Both additives only have a minimal impact on the KCl yield, with the Ca-rich coal ash being slightly superior in this respect; however, the opposite is observed with respect to liquid K_2SO_4, where both additives increase the yield of this compound and the Ca-rich coal ash increases it the most. Regardless of the increase in K_2SO_4, the yield of potassium pyrosulphate increases dramatically in all cases, but particularly during the use of 3% Ca-rich coal ash. The cause of the increases in the sulphur related compounds is likely due to the combination of the increased sulphur content of the deposit under the utilisation of the Ca-rich coal ash and the impact of the excess potassium mentioned earlier; however, it is unclear why this same increase is seen when the Al-rich coal ash is used, as the impact on SO_3 under the utilisation of this additive is only minor and, in fact, leads to a decrease. The increase in liquid sulphates and pyrosulphates during the use of Al-rich coal ash may instead be a result of a phase

transition from solid to liquid, as seen with the significant dip in solid K_2SO_4 yield in Figure 6.21 across the liquid solution's formative temperature window.

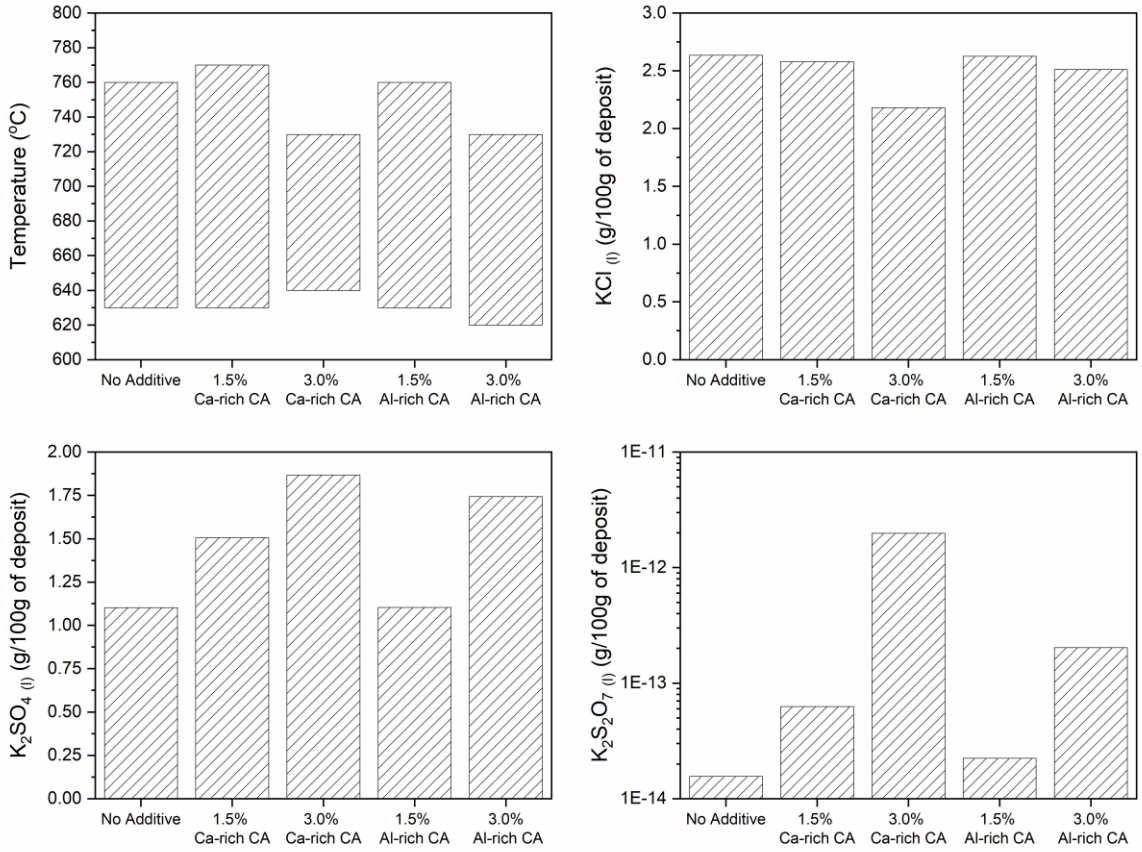

Figure 6.19 – The impact of loading of the Al-rich coal ash and the Ca-rich coal ash on the yield of liquid salts and their formative temperature range in a sunflower husk ash/flue gas mixture

Figure 6.20 presents the impact of the Al-rich coal ash and the Ca-rich coal ash on the yield and formative temperature range of solid KCl from a sunflower husk ash deposit. The 1.5% and 3% Al-rich coal ash cases only present minor improvement to the baseline case; this is similar to the impact of the same loadings of Ca-rich coal ash. Increasing the loading of Al-rich coal ash to 5.5% and 6.6% will decrease the yield and the temperature range but to less of an extent as the equivalent Ca-rich coal ash cases. However, increasing the loading of Al-rich coal ash to 8% produces a much reduced yield (over 50% reduction) and a decrease in end temperature, 480 °C compared to 570 °C for the 8% Ca-rich coal ash and 630 °C for the baseline.

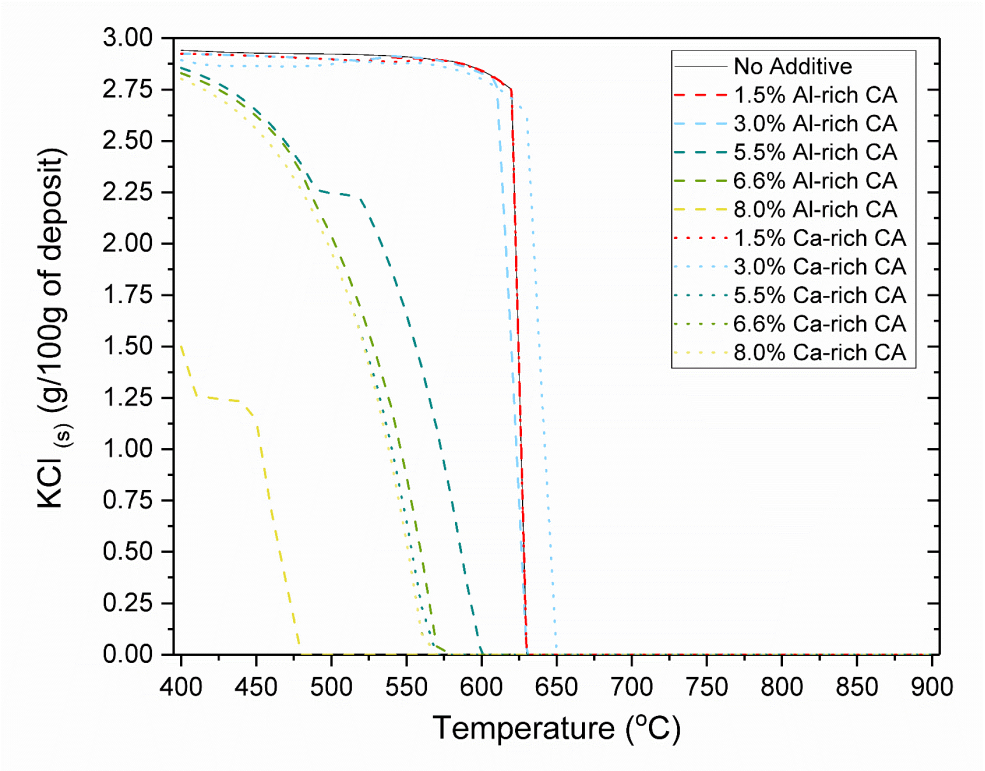

Figure 6.20 – The impact of loading of the Al-rich coal ash and the Ca-rich coal ash on the yield of solid KCl and the formative temperature range in a sunflower husk ash/flue gas mixture

Figure 6.21 presents the impact of the Al-rich coal ash and the Ca-rich coal ash on the yield and formative temperature range of solid K_2SO_4 from a sunflower husk ash deposit. The Ca-rich coal ash arguably performs almost as well as the Al-rich coal ash at reducing solid KCl yield, this is not the case for solid K_2SO_4. As was observed in Figure 6.9, all Ca-rich coal ash cases perform worse than the baseline case; whereas each Al-rich coal ash case performs better than the baseline, with performance improving as loading increases and the 8% loading case proving able to substantially reduce the yield and the temperature range, so that solid K_2SO_4 only forms from 710-820 °C. Importantly, the 6.6% Al-rich coal ash case is not able to restrict the formative temperature range but it can reduce the yield specifically in the lower half of the temperature range, which may prove vital for plants using an older generation of boiler.

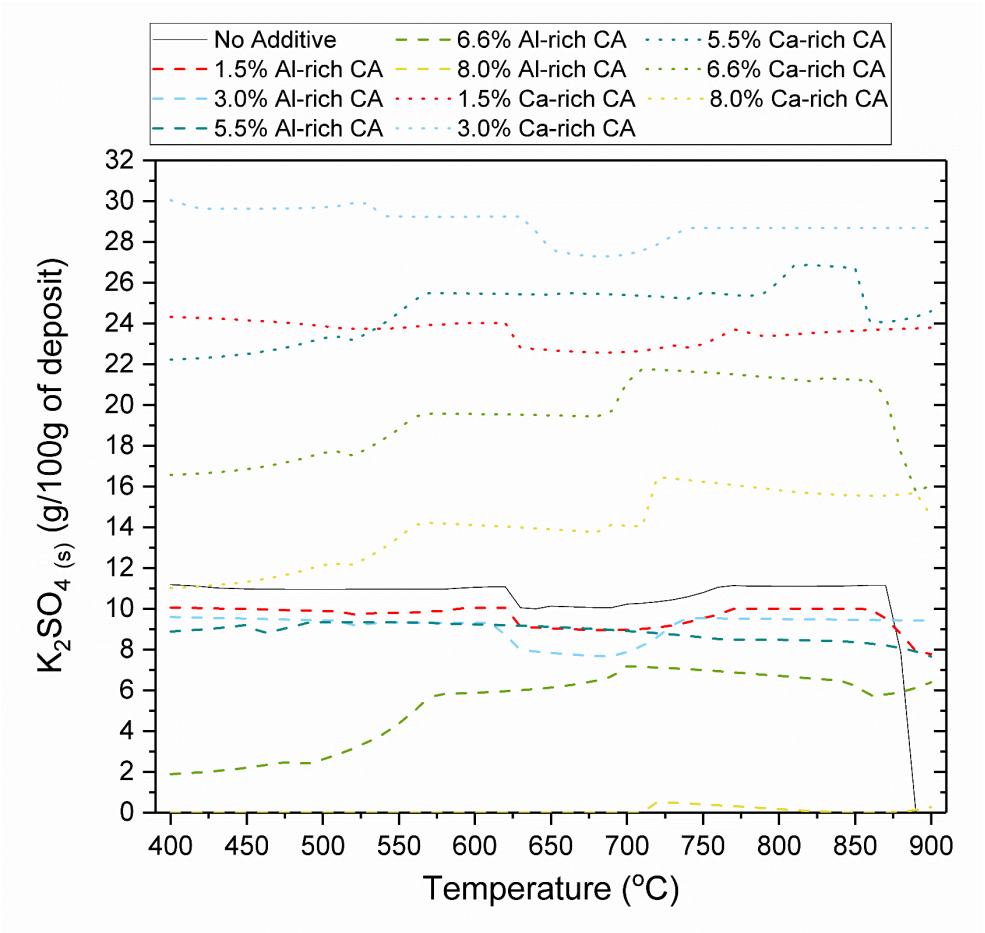

Figure 6.21 – The impact of loading of the Al-rich coal ash and the Ca-rich coal ash on the yield of solid K_2SO_4 in a sunflower husk ash/flue gas mixture

6.4.3 Miscanthus Husk Ash

Figure 6.22 presents the impact of various loadings of Al-rich coal ash and Ca-rich coal ash on the yield of gaseous KCl and $FeCl_2$ from a miscanthus husk ash deposit. The yield of KCl is much lower when using the Al-rich coal ash rather than the Ca-rich coal ash. Using a loading of 6.6% or greater also offers improvements to the KCl yield across the temperature range, rather than just above the 500 °C mark. However, the Al-rich coal ash also requires a loading of greater than 3% to have any noticeable impact at all. The Ca-rich coal ash, on the other hand, starts to become active above 1.5%, but there is only minimal improvement between the 3% and 8% cases for this additive, with all improvements in KCl yield being comparable to the 5.5% Al-rich coal ash case. When observing the impact on $FeCl_2$ yield, the same phenomenon that is present within the peanut shell ash is present here, in that there seems to be an achievement of a maximum rate of iron chlorination; so,

although the 6.6% and 8% Al-rich coal cases sequester more potassium and, hence, liberate more chlorine, a similar amount of $FeCl_2$ is produced as with the other active, but less impactful, cases.

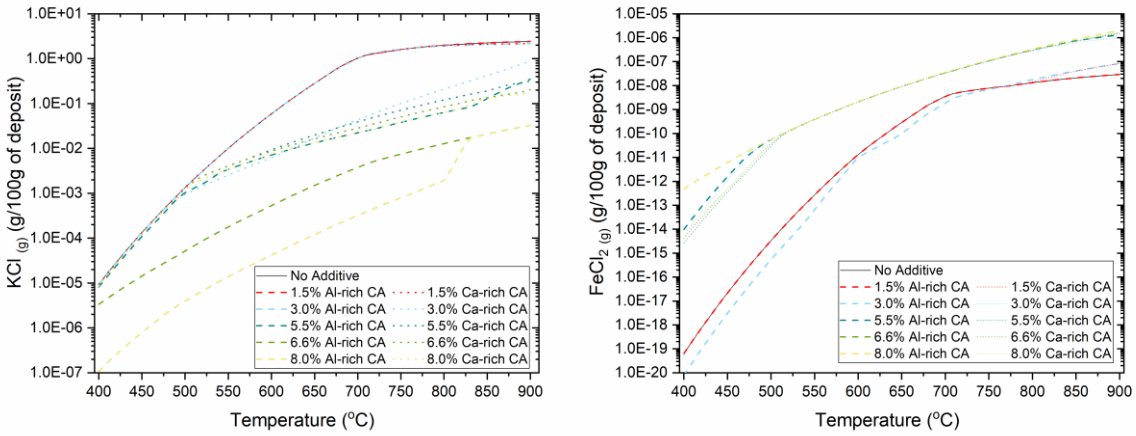

Figure 6.22 – The impact of loading of the Al-rich coal ash and the Ca-rich coal ash on the yield of KCl and $FeCl_2$ from a miscanthus husk ash/flue gas mixture across the working temperature range

Figure 6.23 presents the impact of the Al-rich coal ash and the Ca-rich coal ash on the yield and formative temperature range of corrosive liquid salts from a sunflower husk ash deposit. As with the previous analysis of the miscanthus husk ash in section 6.3.3, the additives have little impact on either the formative temperature range or the yields of the liquid salts when 1.5% loading is used and, when a greater loading is used, the melt is eliminated altogether. However, an exception occurs when using 3% Al-rich coal ash, where each one of the measured metrics is increased, except the yield of pyrosulphate, which is ever so minimally decreased (i.e. minimal in comparison to other witnessed changes to pyrosulphate yield). The increased yields and temperature range must be due to the changed composition of the deposit at 3% Al-rich coal ash aiding eutectic liquid solution formation, but as to why the formation is aided is unclear and highlights a need to be able to examine the calculation processes or, even, to map the reaction pathways within FactSage. As seen with the yields of other metrics in this section, there is little impact of the Ca-rich coal ash or Al-rich coal ash at 1.5%; therefore, the corrosivity of the miscanthus husk ash is simply unaffected by such little addition of mitigant, even though the change in composition is quite dramatic.

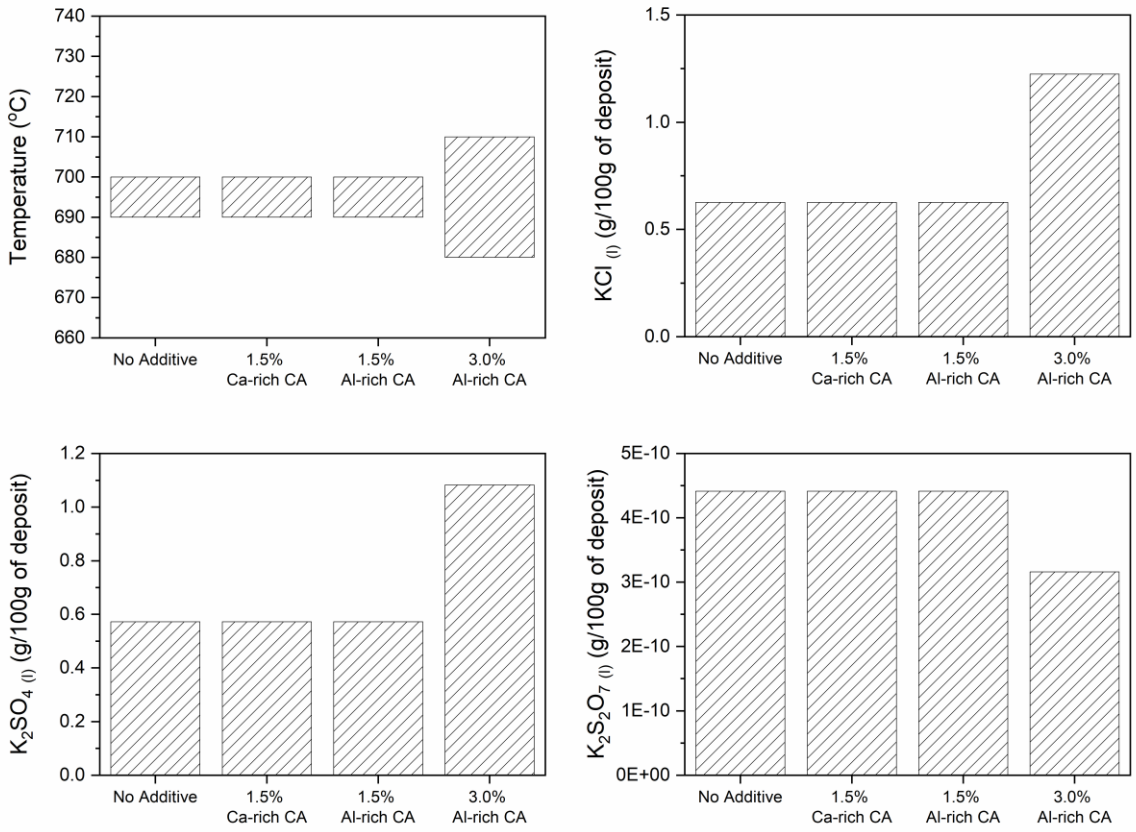

Figure 6.23 – The impact of loading of the Al-rich coal ash and the Ca-rich coal ash on the yield of liquid salts and their formative temperature range in a miscanthus husk ash/flue gas mixture

Figure 6.24 presents the impact of the Al-rich coal ash and the Ca-rich coal ash on the yield and formative temperature range of solid KCl from a miscanthus husk ash deposit. As with the sunflower husk ash, the 1.5% and 3% Al-rich coal ash cases have minimal impact on the KCl yield or temperature range. However, when increasing the loading to 5.5%, major improvements in both the yield and the temperature range are witnessed, so much so, that both metrics are superior to the best Ca-rich coal ash case (which is curiously a loading of 3%). Increasing the loading of Al-rich coal ash any further will lead to the inhibition of the formation of the solid solution altogether.

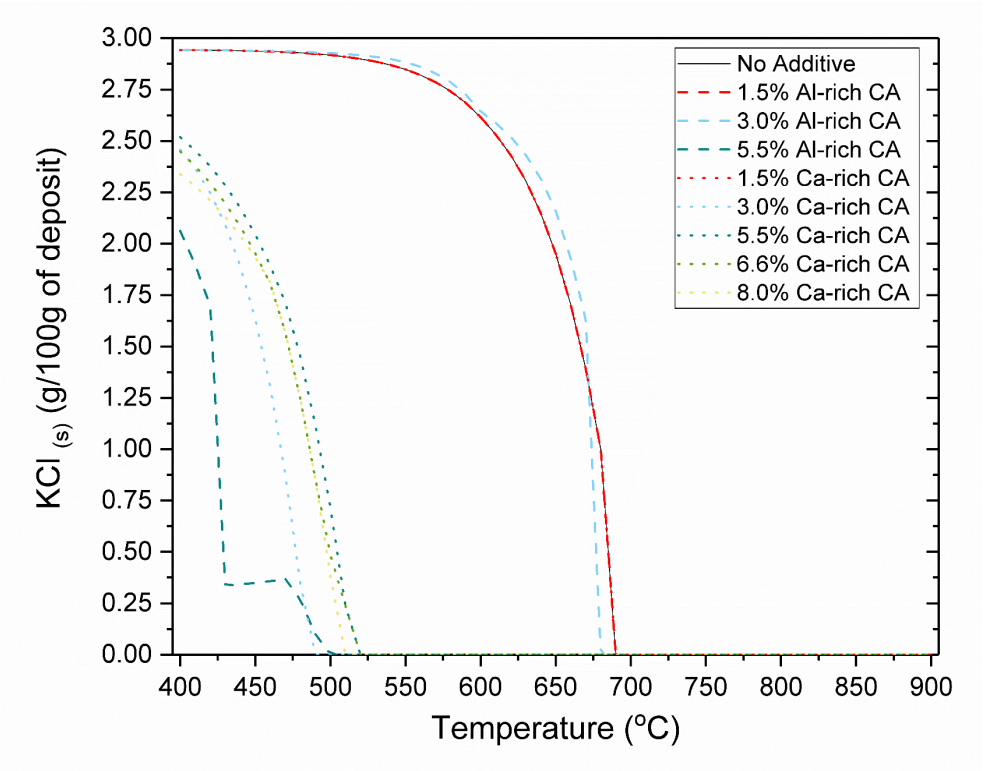

Figure 6.24 – The impact of loading of the Al-rich coal ash and the Ca-rich coal ash on the yield of solid KCl and the formative temperature range in a miscanthus husk ash/flue gas mixture

Figure 6.25 presents the impact of the Al-rich coal ash and the Ca-rich coal ash on the yield and formative temperature range of solid K_2SO_4 from a miscanthus husk ash deposit. At loadings of 1.5% and 3%, the behaviour of the Al-rich coal ash is similar to that of the Fe-based additive, with minor increases in the yield with increasing loading. This is also due to a slight increase in the SO_3 content of the deposit by the addition of the additive. However, increasing the loading further to 5.5% seems to add enough alumina to the deposit to mitigate this rise in SO_3 by capturing potassium, and results in a considerable drop in yield compared to the previous loadings and the baseline. In comparison to the Ca-rich coal ash, the 5.5% Al-rich coal ash case performs better in terms of yield and equal in terms of temperature range, compared to the best performing case of its competitor.

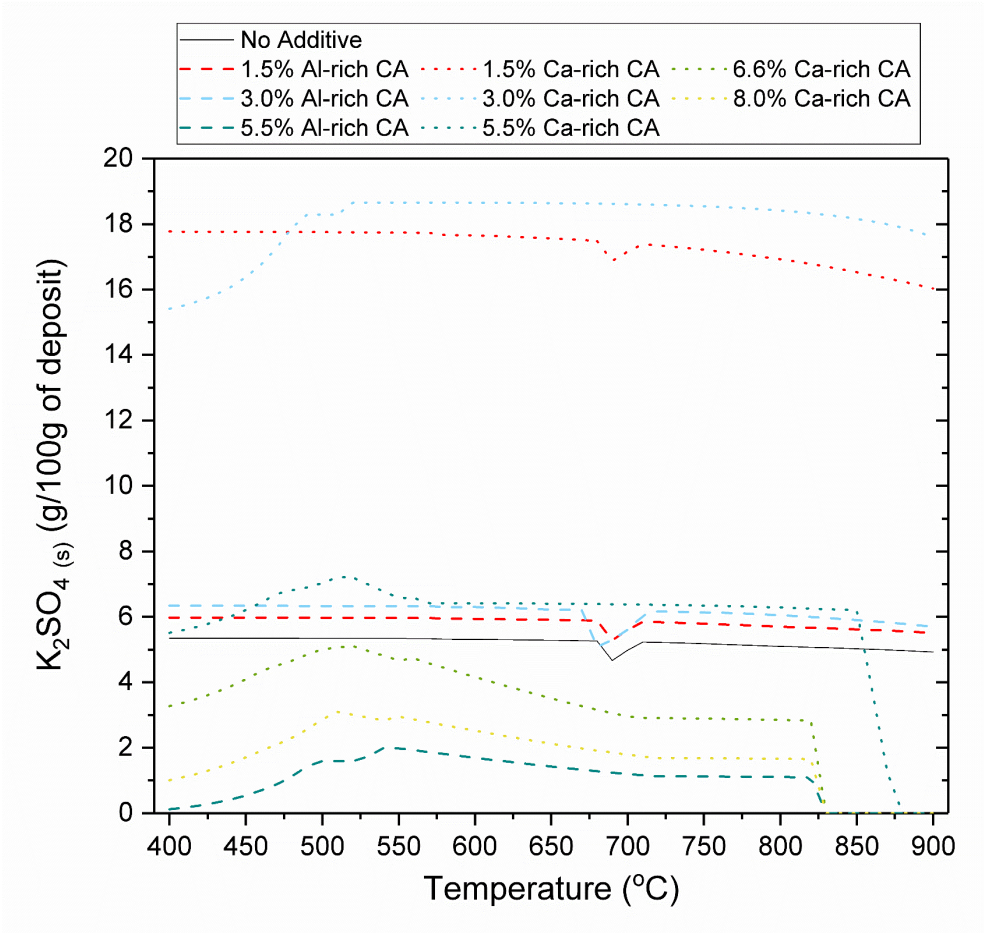

Figure 6.25 – The impact of loading of the Al-rich coal ash and the Ca-rich coal ash on the yield of solid K_2SO_4 in a miscanthus husk ash/flue gas mixture

6.5 A Comparison of Al-rich Coal Ash and Alumina Addition to Biomass Ashes

From comparison of the additives studied so far, an argument can be formed that there is an improvement in corrosion inhibition with increasing alumina content. There is also a wide range of sources in literature (Kyi and Chadwick, 1999, Llorente, et al., 2008, Uberoi, et al., 1990) who have studied using pure alumina as an additive in order to reduce corrosion, commonly in comparison with kaolin, which is studied here in a crude form called the Al-rich coal ash. The aim of this portion of the chapter is to highlight the importance of the silica portion of the Al-rich coal ash and to validate the previous trends by comparing subsequent observations with those made experimentally in literature.

	Al-rich CA (%)	Alumina (%)
SiO_2	56.28	0.87
TiO_2	1.04	0.00
Al_2O_3	23.38	97.63
Fe_2O_3	6.62	0.37
MgO	2.10	0.35
CaO	6.31	0.22
Na_2O	0.37	0.39
K_2O	2.19	0.02
P_2O_5	0.58	0.02
SO_3	1.13	0.11

Table 6.4 – A comparison of the compositions of the Al-rich coal ash and 'pure' alumina

6.5.1 Peanut Shell Ash

Figure 6.26 presents the impact of various loadings of Al-rich coal ash and alumina on the yield of gaseous KCl and $FeCl_2$ from a peanut shell ash deposit. The difference between these two additives is abundantly clear when viewing the impact on the KCl yield; the inclusion of the Al-rich coal ash leads to much lower KCl yields at each loading and the 8% alumina case performs at a similar rate to the 3% Al-rich coal ash case. Kyi and Chadwick (1999) found, when researching the ability of alumina to retain sodium, that the majority of alkali retention by minerals was a result of silica and alumino-silicate reactions, while NaCl retention by alumina was found to be the least significant reaction. Thus, the impact on KCl yield highlights the importance of a corrosion inhibiting additive to increase the silica concentration.

Of interest is the fact that the 1.5% alumina case outperforms its competitor; this is likely due to the fact that the peanut shell ash already has a considerable silica content and so more is gained in terms of corrosion inhibiting potential by solely increasing the alumina concentration. There is little difference in terms of $FeCl_2$ yield for the active cases past 600 °C; however, prior to this point, all the alumina cases (bar the 8% case) produce less $FeCl_2$ than their active Al-rich coal ash loaded counterparts but then again the improvement in

KCl yield is only minor in this region, so the increased $FeCl_2$ yield seen for the Al-rich coal ash cases is justified.

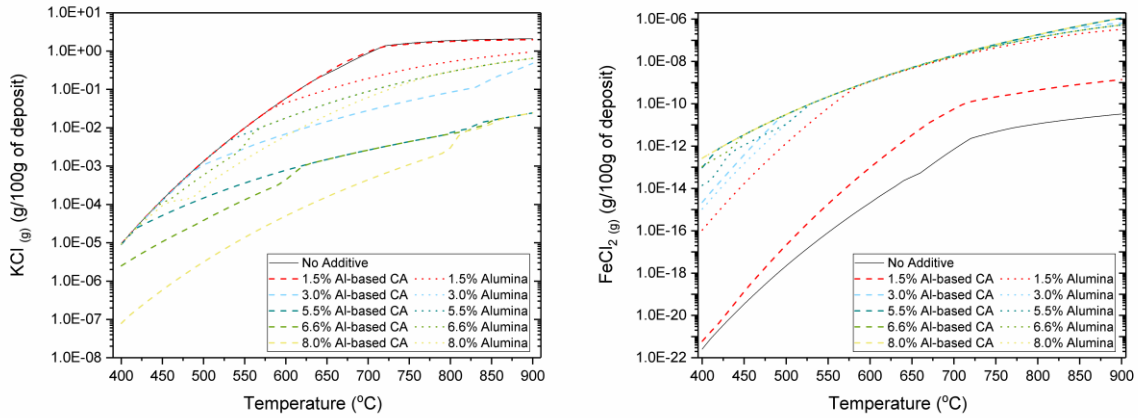

Figure 6.26 – The impact of loading of the Al-rich coal ash and alumina on the yield of KCl and $FeCl_2$ from a peanut shell ash/flue gas mixture across the working temperature range

As seen back in Figure 6.15, both the Ca-rich coal ash and the Al-rich case prevented the formation of the liquid solution when 3% of either additive was included. When alumina addition was investigated, the liquid solution failed to form at even 1.5% loading; this suggests that the addition of alumina as an inert material in order to disrupt liquid formation is very effective.

Figure 6.27 presents the impact of the Al-rich coal ash and alumina on the yield and formative temperature range of solid KCl from a peanut shell ash deposit. The addition of alumina has an immediate impact on the yield and temperature range of the solid KCl when the loading is 1.5%, proving more beneficial than Al-rich coal ash at this loading. The behaviour improves as loading is increased, with further reductions in yield and contractions of the temperature range, although the Al-rich coal ash does perform better once it truly becomes 'active' at 3% loading. For all intents and purposes, the 8% alumina case leads to all but the elimination of this solid solution, with the yield dropping to negligible levels and the formative temperature range ending at 410 °C.

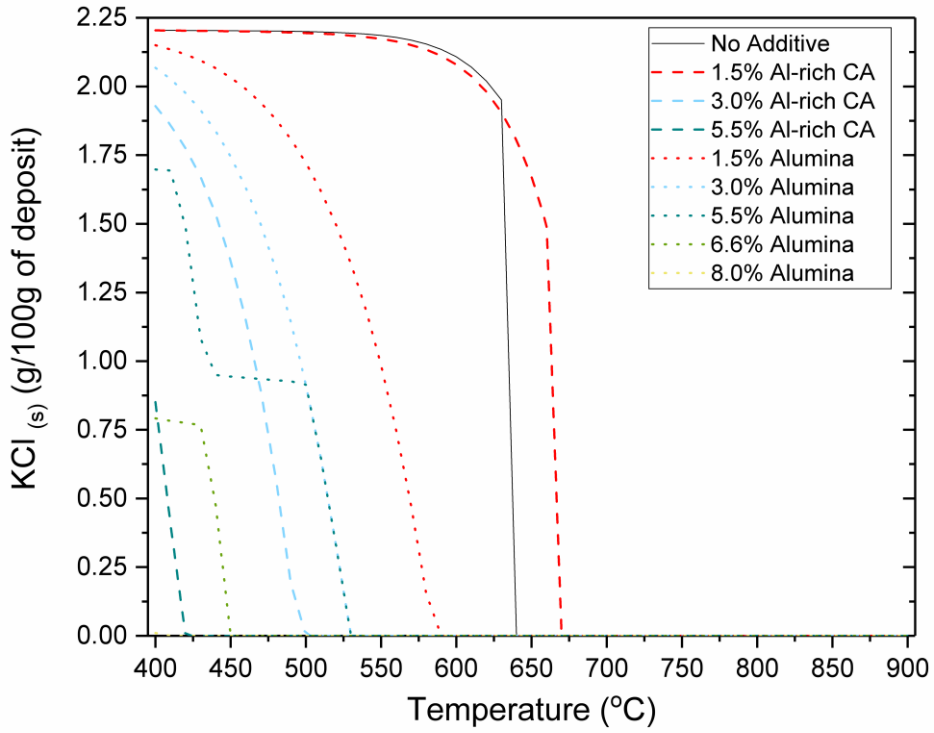

Figure 6.27 – The impact of loading of the Al-rich coal ash and alumina on the yield of solid KCl and the formative temperature range in a peanut shell ash/flue gas mixture

Figure 6.28 presents the impact of the Al-rich coal ash and alumina on the yield and formative temperature range of solid K_2SO_4 from a peanut shell ash deposit. The impact of alumina on the yield of solid K_2SO_4 mirrors both the impact of alumina on gaseous KCl and the impact of the Fe-based additive on solid K_2SO_4, with steady incremental improvements in yield with increasing loading but no dramatic benefits being present. The presence of 1.5% alumina appears to be more beneficial than the same loading of its competitor, but as loading increases to 3%, the Al-rich coal ash is vastly superior. The greater activity of alumina at 1.5% may be due to the larger increase in Al_2O_3 caused by loading 1.5% alumina rather than 1.5% Al-rich coal ash; this may cause the potassium capture reactions to successfully occur for the alumina case as opposed to the Al-rich coal ash case. In addition, further loading of alumina dilutes the silica content in the deposit, hampering its ability to take advantage of the increasing Al_2O_3 content and capture more potassium.

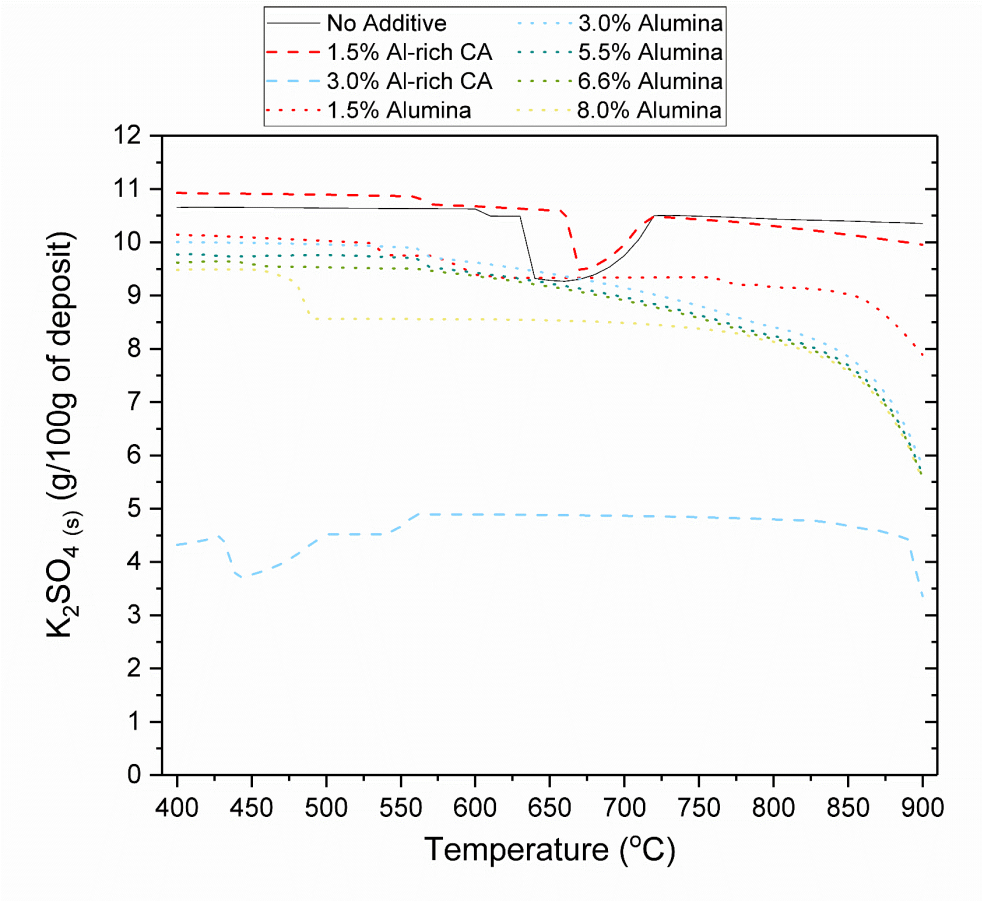

Figure 6.28 – The impact of loading of the Al-rich coal ash and alumina on the yield of solid K_2SO_4 in a peanut shell ash/flue gas mixture

6.5.2 Sunflower Husk Ash

Figure 6.29 presents the impact of various loadings of Al-rich coal ash and alumina on the yield of gaseous KCl and $FeCl_2$ from a sunflower husk ash deposit. The addition of alumina does not have a positive impact on the KCl yield, no matter what loading is used, while, as seen prior, the Al-rich coal ash only becomes effective at a loading of 5.5%. Nevertheless, the addition of alumina still leads to a small amount of chlorine being liberated and forming $FeCl_2$, as seen most prominently in the post 600 °C region. As will be discussed further with the interpretation of the liquid results, the reason the alumina is not effective with this ash is the inherently low silica content. For an additive to be successful with a particularly problematic ash such as this, it must provide a source of both silica and alumina.

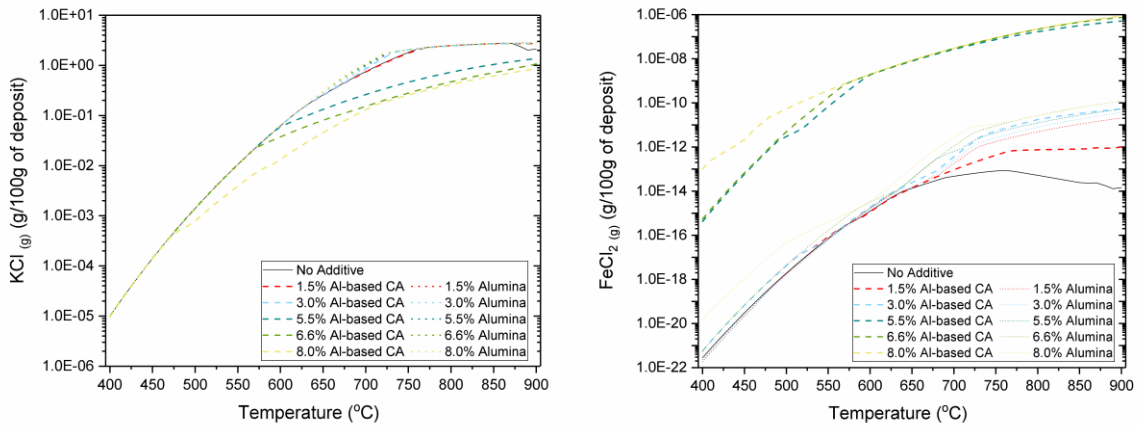

Figure 6.29 – The impact of loading of the Al-rich coal ash and alumina on the yield of KCl and $FeCl_2$ from a sunflower husk ash/flue gas mixture across the working temperature range

Figure 6.30 presents the impact of the Al-rich coal ash and alumina on the yield and formative temperature range of corrosive liquid salts from a sunflower husk ash deposit. The addition of alumina to the peanut shell ash was even more effective at preventing the liquid solution forming, than the other tested additives. This is not seen to be the case with the sunflower husk ash. Alumina is better at reducing the formative temperature range than the Al-rich coal ash at loadings of 1.5% and 3%, but the liquid solution is never fully eliminated, instead, just decreasing the temperature range further when loading is increased. A similar trend is seen with the KCl yield, as the yield marginally falls with increasing loading of alumina. The K_2SO_4 yield increases slightly from the baseline case but remains relatively stable as loading is increased. The pyrosulphate yield does increase with loading, but, unlike other cases in this chapter, the highest yield at 8% loading remains in the same order of magnitude as the initial increased yield at 1.5%. This performance, which, as mentioned, is contrary to the performance with the peanut shell ash, is most likely due to the very low silica content of the sunflower husk ash; although the addition of alumina does greatly increase the level of inert compounds within the deposit, the silica content is only decreased. As with decreasing the gas yields, the silica is necessary to form alumino-silicates that will capture enough potassium to prevent a critical mass of liquid salts forming that will enable a permanent liquid salt solution.

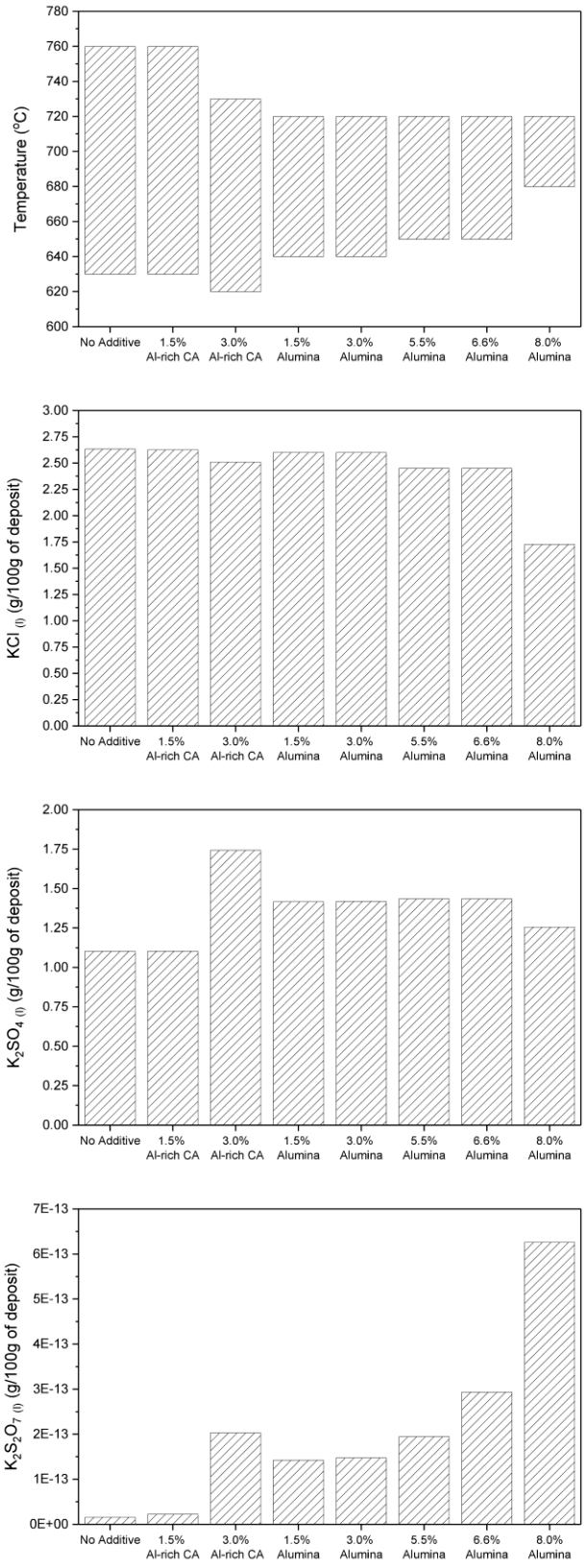

Figure 6.30 – The impact of loading of the Al-rich coal ash and alumina on the yield of liquid salts and their formative temperature range in a sunflower husk ash/flue gas mixture

Figure 6.31 presents the impact of the Al-rich coal ash and alumina on the yield and formative temperature range of solid KCl from a sunflower husk ash deposit. When adding alumina to sunflower husk ash, there is negligible impact on the yield of solid KCl. An increase in the temperature range can be seen, but this is a product of alumina's impact of delaying liquid formation until higher temperatures. This lack of impact is foreshadowed by the presented minimal effect on liquid yields, and further highlights the issue surrounding this additive's absence of silica content.

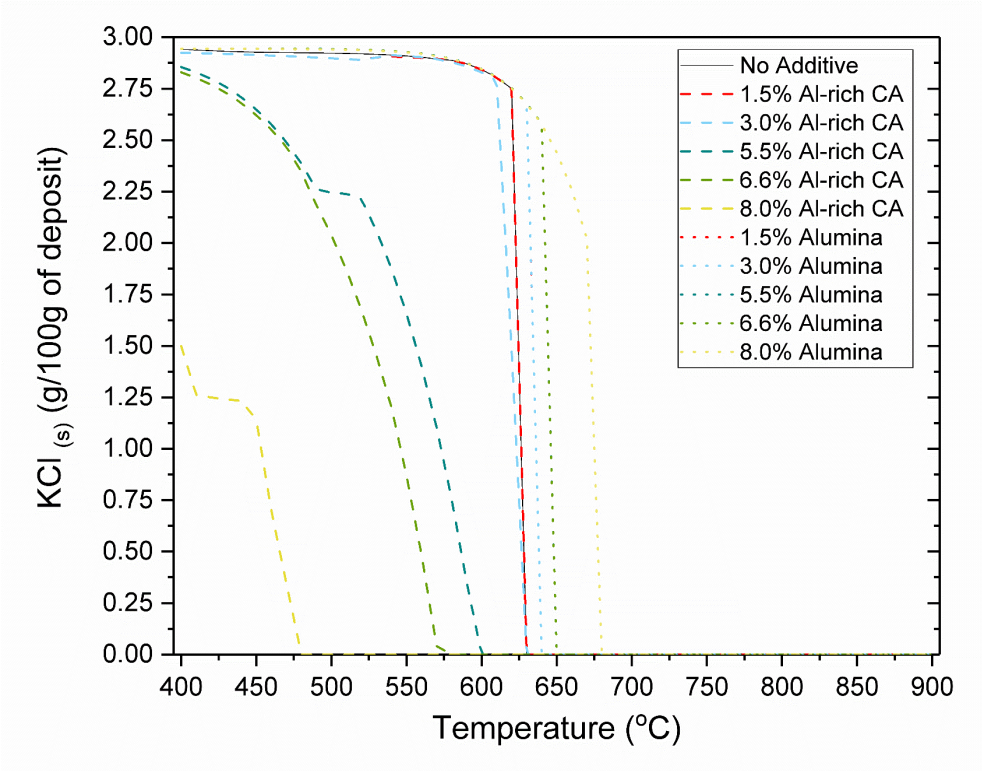

Figure 6.31 – The impact of loading of the Al-rich coal ash and alumina on the yield of solid KCl and the formative temperature range in a sunflower husk ash/flue gas mixture

Figure 6.32 presents the impact of the Al-rich coal ash and alumina on the yield and formative temperature range of solid K_2SO_4 from a sunflower husk ash deposit. Similarly, during the addition to the peanut shell ash, alumina does have a positive impact on reducing solid K_2SO_4 yields, with increasing reductions at increasing loadings. In comparison to the Al-rich coal ash, alumina's progress is modest and appears to be a function of dilution. Nevertheless, the 1.5% and 3% alumina cases appear to present superior behaviour compared to their Al-rich coal ash counterparts.

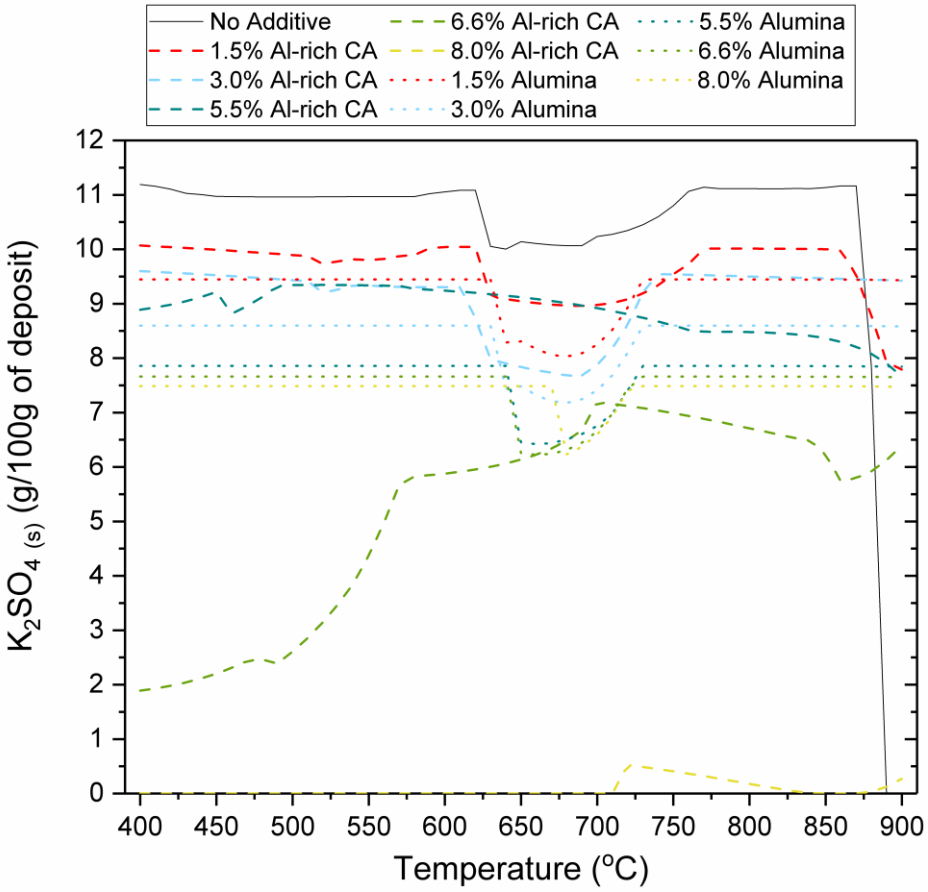

Figure 6.32 – The impact of loading of the Al-rich coal ash and alumina on the yield of solid K_2SO_4 in a sunflower husk ash/flue gas mixture

6.5.3 Miscanthus Husk Ash

Figure 6.33 presents the impact of various loadings of Al-rich coal ash and alumina on the yield of gaseous KCl and $FeCl_2$ from a sunflower husk ash deposit. The addition of the alumina leads to a lower KCl yield at 1.5% and 3% loading than the Al-rich coal ash (as also seen with the peanut shell ash); however, there is no additional improvement when loading is increased further. The Al-rich coal ash only becomes active at a loading of 5.5%, but this performance vastly exceeds the alumina in terms of KCl yield. The addition of alumina creates a much more balanced ash immediately at 1.5% loading, providing far more alumino-silicates to capture potassium than its counterpart at the same loading, hence why it is able to have an immediate impact. However, as the loading of alumina increases, the silica content starts to decrease substantially, hence preventing any further improvement in the capture potential. The potassium content also decreases greatly

between 3% and 8% loading, but this does not have any impact on the KCl yield, showing that the method of dilution is rather fruitless with high potassium ashes. With respect to the Al-rich coal ash, the KCl yield does continue to fall between 5.5% and 8% because the silica content is maintained around 50%; while, it is likely that the reason that the Al-rich coal ash becomes active at 5.5% is a combination of the alumina content having risen sufficiently and, also, the potassium having decreased sufficiently.

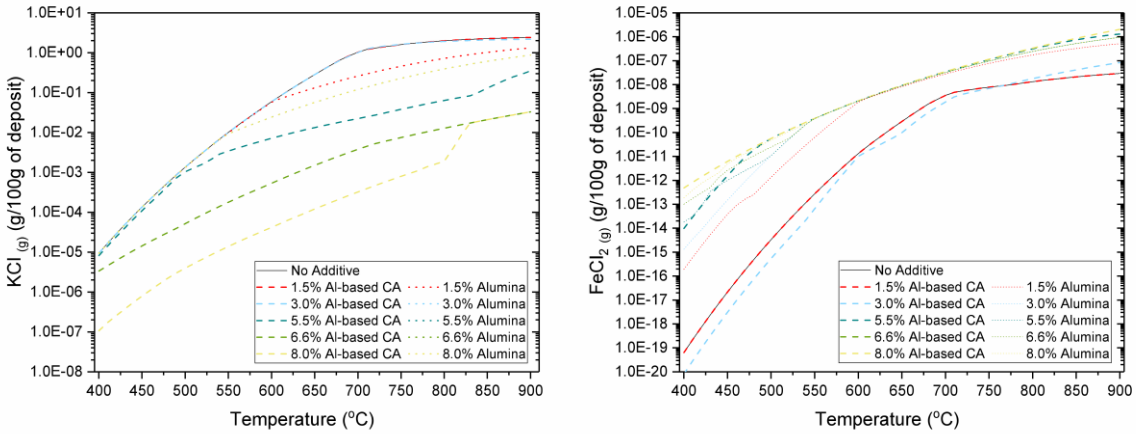

Figure 6.33 – The impact of loading of the Al-rich coal ash and alumina on the yield of KCl and $FeCl_2$ from a miscanthus husk ash/flue gas mixture across the working temperature range

As with the peanut shell ash, the addition of 1.5% alumina prevents the formation of the liquid solution. Both the peanut shell ash and the miscanthus husk ash have substantially adequate native silica contents, so the amplified increase in alumina at 1.5% loading (compared to Al-rich coal ash addition, which leads to a more gradual increase in alumina) is sufficient to immediately prevent the formation of the liquid solution.

Figure 6.34 presents the impact of the Al-rich coal ash and alumina on the yield and formative temperature range of solid KCl from a miscanthus husk ash deposit. Here, the alumina appears to perform similarly as to when it is used with the peanut shell ash. There is an immediate decrease in yield and temperature range when a 1.5% loading is used. The yield and temperature range decrease further when the loading is increased to 3%, but any further increase in loading only reduces yield, with the temperature range staying the same up to 8% alumina addition. The biggest deviation from the peanut shell ash deposit trends is seen with the 8% alumina case, where a greatly reduced but still significant yield is

produced (up to 1.1 g/100 g of deposit). Similar to the other comparisons with the Al-rich coal ash, the lower loadings of alumina, in this case 1.5% and 3%, perform better than their rivals; however, when the Al-rich coal ash becomes active, it vastly outperforms alumina.

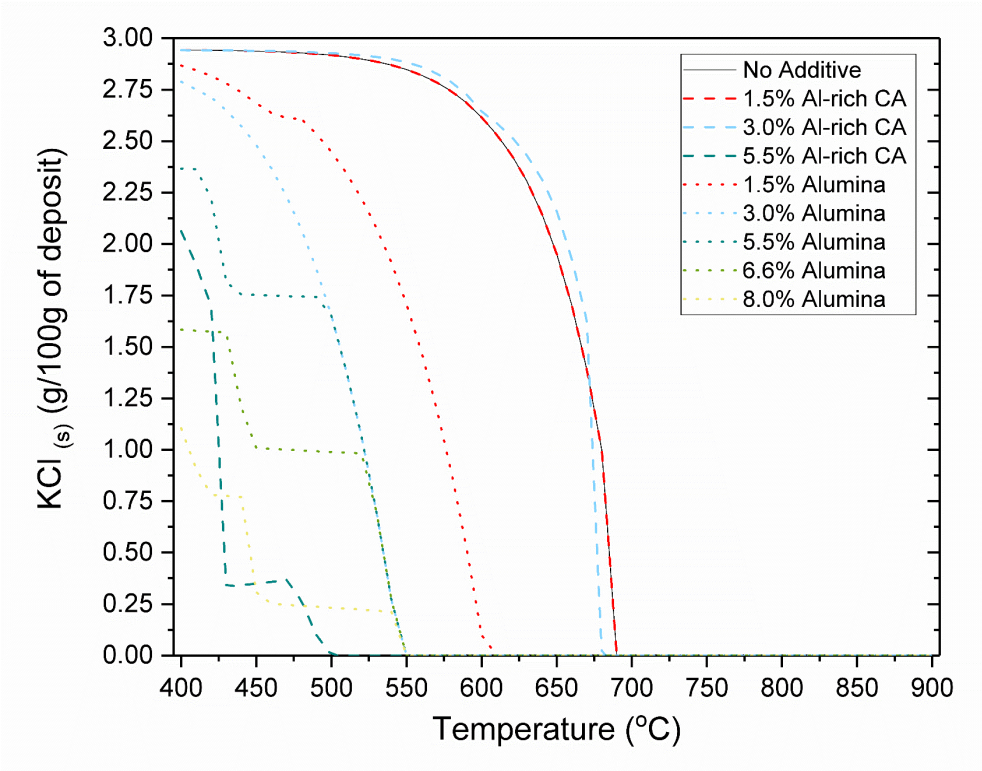

Figure 6.34 – The impact of loading of the Al-rich coal ash and alumina on the yield of solid KCl and the formative temperature range in a miscanthus husk ash/flue gas mixture

Figure 6.35 presents the impact of the Al-rich coal ash and alumina on the yield and formative temperature range of solid K_2SO_4 from a miscanthus husk ash deposit. The addition of alumina appears to have a positive effect on reducing solid K_2SO_4 yield and is the only one to provide a reduction in yield at any loading for the miscanthus husk ash. This is due to the alumina cases being the only series of cases to reduce the SO_3 content in the deposits. Comparable to the KCl trends, the addition of alumina at 1.5% and 3% leads to lower yields than the equivalent Al-rich coal ash cases. Increasing the loading of alumina past 3% does not lead to any significant changes in yield, while the yields post 1.5% loading are only improved when the temperature is above ~750 °C.

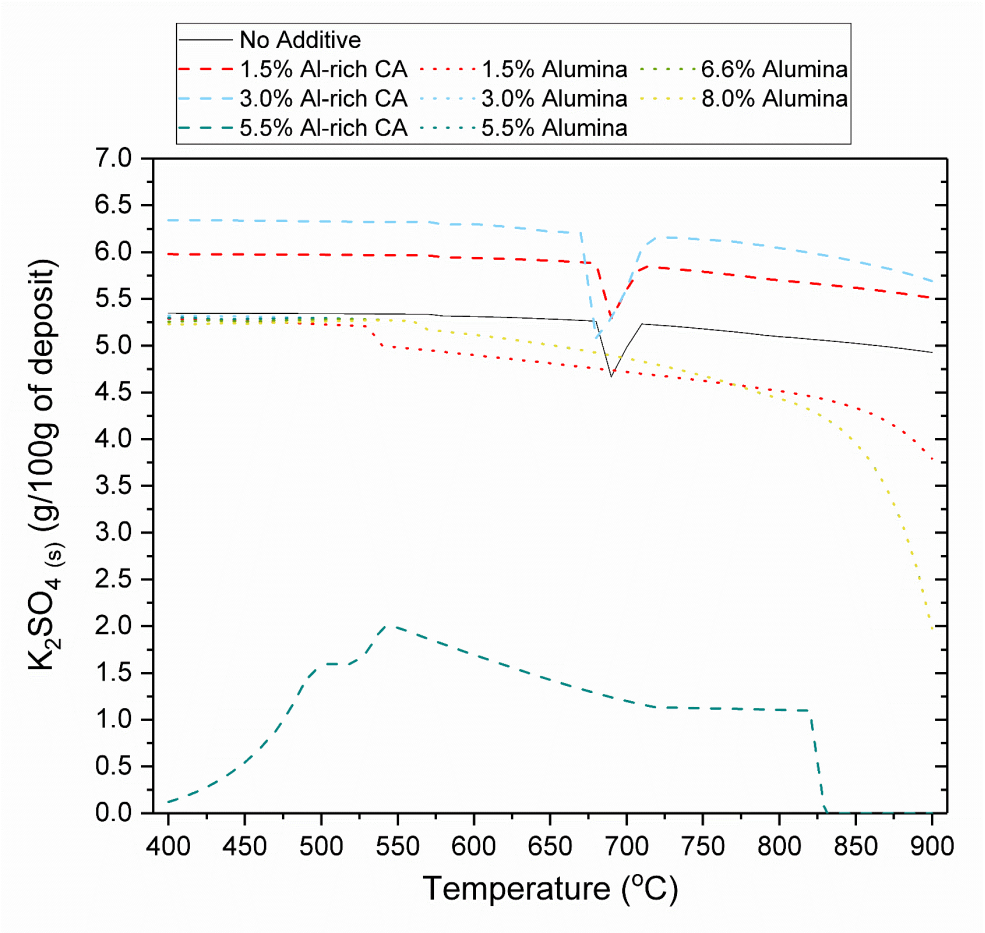

Figure 6.35 – The impact of loading of the Al-rich coal ash and alumina on the yield of solid K_2SO_4 in a miscanthus husk ash/flue gas mixture

6.6 Discussion and Conclusions

This chapter presented a comparison of four additives across four fuels (one coal and three biomass fuels) and a novel method for comparing corrosion inhibiting additives. This was initiated by an attempt to investigate how the Fe-based additive, from chapter 5 and the literature, was able to inhibit corrosion in experimental circumstances. However, FactSage was impractical for these ends due to the limited change in the chemical composition of the deposits with addition of the additive. It was theorised that the benefits reported in the literature were a result of physical processes not taken into account during equilibrium modelling.

In order to properly test the method of utilising FactSage to analyse the benefits of corrosion inhibiting additives and to investigate any chemical benefits of the Fe-based additive, three biomass fuels were sourced from literature and investigated

computationally. In addition, the coal ash (Ca-rich coal ash) previously under investigation was used to contrast with the trends seen from the use of the Fe-based additive, because most coal ashes contain a high proportion of silica and alumina (and, hence, aluminosilicates) and so are suitable economical alternatives for kaolin and other corrosion inhibiting additives. Furthermore, a second coal ash (Al-rich coal ash) was compared with the Ca-rich coal ash in order to highlight the impact of contaminants within the additives. Moreover, alumina was then compared with the Al-rich coal ash to highlight the importance of constituents other than alumina in a corrosion inhibiting additive and to confirm that FactSage would predict a lower activity when solely alumina was used, as shown in the literature.

The impact of the Fe-based additive was found to be different depending on the biomass fuel ash. The Fe-based additive was able to adequately reduce the gaseous KCl yield at every loading when used with the peanut shell ash, but only became active at a loading of 5.5% when used with the miscanthus husk ash and was not effective with this metric when used with the sunflower husk ash. The liquid solution was prevented from forming at 5.5% loading during use with both the peanut shell and miscanthus husk, but could only reduce the temperature range with the sunflower husk ash. Inhibition of the solid phase KCl required 5.5% loading also for the peanut and miscanthus, but could not be achieved for the sunflower husk. The solid phase K_2SO_4 could only be impacted via dilution and this actually caused an increase for the miscanthus husk ash, which has a very low native SO_3 content.

On analysis, the impact of the Fe-based additive was dictated by the original ash composition. The peanut shell ash and miscanthus husk ash both have a sufficiently high silica content but the peanut shell ash also contains 8.25% alumina, compared to 0.45% for the miscanthus husk ash; this results in the Fe-based additive being more beneficial for the peanut shell ash over a wider range of loadings than for the miscanthus husk ash. The sunflower husk ash has a very low silica and alumina content and, hence, the only benefit of using the Fe-based additive is to introduce plenty of inerts and impede liquid formation by contracting the possible temperature range. The information presented here most likely does not warrant the use of the Fe-based additive for the purpose of inhibiting fireside

corrosion alone, but it will most likely have some positive impact on reducing fireside corrosion if used for NO_x abatement at a loading of 5.5% or higher.

The Ca-rich coal ash is evidently more proficient at inhibiting fireside corrosion than the Fe-based additive, as expected. The Ca-rich coal ash performed similarly well with the peanut shell ash and the miscanthus husk ash, requiring a loading of 3% to have a significant impact on most metrics. To be impactful with the sunflower husk ash, a 5.5% loading was required; except for the yield of solid phase K_2SO_4, which was severely aggravated by the addition of any Ca-rich coal ash. This highlights the importance of understanding the impact of any contaminants in the added coal ash. The Ca-rich coal ash had a considerable sulphur content and had a negative impact with each biomass ash when initially added, but tended to improve when the loading was increased and more potassium was captured. For the sunflower husk ash, the potassium content was so considerable that the combination of reduced dilution (compared to other ashes) and introducing more sulphur resulted in the yield of solid phase K_2SO_4 being unable to drop below the baseline values.

The Al-rich coal ash proved far better at reducing yields than the Ca-rich coal ash, but in some cases required a greater loading than the Ca-rich coal ash to start to have an impact. The Al-rich coal ash proved particularly capable at eliminating the solid phase KCl and K_2SO_4 yield when 6.6% loading was used with the peanut shell ash and miscanthus husk ash, and all but eliminating them when 8% loading was used with the sunflower husk ash. The trends presented here should encourage an operator to, if possible, use coal ash with the greatest Si/Al content or, at the very least, encourage an operator that there is value in knowing the composition of an added coal ash.

Alumina was then tested with an understanding that it is reported in literature as being less impactful than kaolin and other additives containing alumino-silicates and, so, deposits loaded with alumina should yield more corrosive compounds in FactSage. This was largely found to be true. Although the addition of alumina was impactful to some extent for reducing the yields of gaseous and solid KCl from the peanut shell and miscanthus husk ashes, it was modest in comparison to the Al-rich coal ash. Furthermore, when sunflower husk ash was investigated, alumina had no impact on these metrics. One behaviour of note was the impact of alumina on liquid yields, eliminating any liquid formation from the

peanut shell and miscanthus husk ashes, and offering steady reduction in the formative temperature range from the sunflower husk ash. This positive impact arose from the fact that the action of loading 'pure' alumina will greatly increase the amount of inerts in the deposit, interfering with liquid formation. The investigation of alumina highlighted the idea that the needs of the ash dictate the composition of the additive; alumina showed some mildly positive behaviour when the ash had a significant native silica content and should only be used with such ashes.

FactSage is a quick and economical alternative to undertaking experimental tests, but without this experimental data, the trends harvested should only be analysed qualitatively. FactSage has demonstrated the ability to show the effects of chemical adsorption, inert loading and dilution, but it is not capable of including the effects of physical absorption in its calculations (Becidan, et al., 2009); this will add some portion of error to any quantitative conclusions, and may cause underestimations about the effectiveness of some additives. Furthermore, some of the trends witnessed are caused by unexplained phenomena and this highlights a weakness in the FactSage program, in that it is not possible to track the progress or journey of elements or compounds. Rather, one is left to study the major differences between the inputted compositions for hints as to the cause of trend variations, when it is entirely possible that subtle changes in the composition may lead to changes in the thermochemistry that opens discreet avenues for reactions only clear to those actively searching for them. For this reason, it would be recommended that, for a comprehensive prediction, equilibrium modelling should be combined not only with experimental tests but also with kinetic modelling.

A weakness in the structure of the model is that the increased ash content in the boiler is not taken into account. Biomass fuels tend to have very low ash content, as low as >1% of the fuel; utilising an additive will greatly increase the mineral content (up to ~10% with an additive loading of 8%) and will impact ash deposition rates and slagging and fouling processes. While the trends presented here show that the coal ashes in particular are capable of absorbing volatile potassium compounds, and this will likely have an impact of reducing ash deposition rates, it is important that the trade-off should be analysed further.

CHAPTER 7 – CONCLUSIONS AND SUGGESTIONS FOR FUTURE WORK

7.1 The Impact of Burner Staging on NO Reduction by Reburning During Oxy-coal Combustion

7.1.1 Conclusions

The 250 kW_{th} combustion test facility at PACT was used to study the impact of burner staging on NO formation and NO reburning during oxy-coal combustion using a scaled-down model of a popular industrial low NO_x burner. The burner configuration was altered during two oxy-coal regimes (OF 27 and OF 30) and a varying amount of NO was included in the synthetic recirculated flue gas, while gas species were monitored in the flue and in-flame. The following observations were made:

- Commissioning tests justified maintaining the proportion of oxidant flowing through the primary register at 20% for all tests and the injection of NO into each stream.
- Commissioning tests also highlighted issues with stability, which were solved by increasing the O_2 in the primary to 21% and decreasing the thermal rating from 200 kW_{th} to 170 kW_{th}.
- During the OF 27 regime, the rate of destruction of recycled NO remained stable across burner environments; this was not the case for the OF 30 regime, as rates dropped when the secondary oxidant proportion was increased.
- This was thought to be due to the decreased density/volumetric flow of the OF 30 flame compromising residence time of recycled NO in the fuel-rich zone.
- Varying the secondary oxidant proportion from 0.00 to 0.57 for the OF 27 regime, the NO_x emission rate rose from 77 to 143 mg/MJ, while the unburned carbon in ash fell around 13%. During the OF 30 regime, increasing the secondary oxidant proportion from 0.36 to 0.50 increased the NO_x emission rate from 72 to 84 mg/MJ. This was believed to be due to the increased flow rate of the secondary stream providing more oxygen to and increasing mixing into the fuel-rich zone.
- NO formation was found to be lower for the two OF 30 flames compared to the two OF 27 flames.

- Radial profiles of key gas species were analysed for a range of NO recycling regimes at two burner configurations (S: 0.36 and S: 0.50) and two oxy-fuel regimes (OF 27 and OF 30). In addition, axial profiles of the same species were analysed for two burner staging environments at OF 30.
- Trends from these profiles implied that burner staging not only controlled NO formation but also the products of NO reburning to prevent reformation of NO.

7.1.2 Suggestions for Future Work

Oxy-fuel combustion allows for the unique opportunity to control the oxygen concentration of any stream; an optimisation of oxygen concentration in certain streams should be carried out with regards to NO formation, NO reburning and combustion efficiency. Particular attention should be paid to the oxygen concentration in the primary stream in order to further promote volatile-N to N_2 pathways. Any impacts of a decreased O_2 concentration in the primary stream on ignition may be crucial and should also be monitored, as this was theorised to cause large standard deviations in the data from the commissioning tests.

Further, an expansion of the range of analysis would be preferable. Some analytical techniques were desired for this study but were not available; these were then also mentioned during feedback at conferences, so there is definitely a desire within academia and industry for this greater detail. These techniques involved mapping the major volatile-N compounds in the flame profiles using in-situ FTIR (Fourier Transform Infra-red Spectroscopy) and mapping local velocity vectors in-flame, using (perhaps) a bidirectional velocity probe. The first technique would confirm the mass transfer assumptions made in the analysis in Chapter 4 regarding volatile-N diffusion across the shear boundary and its subsequent oxidation. The latter technique would confirm the changes in size and shape of recirculation zones within and around the flame. The combination of the techniques already utilised and these new suggestions would build a more accurate and complete picture of nitrogen evolution in staged oxy-coal flames.

7.2 The Impact of an Fe-based Additive on Selective Non-Catalytic Reduction

7.2.1 Conclusions

A 100 kW_{th} combustion test facility was used to investigate the impact of an Fe-based additive on ammonia based selective non-catalytic reduction (SNCR). A variety of Fe-based additive loadings was used at a range of normalised stoichiometric ratios. The following observations were made:

- The presence of the Fe-based additive led to an increase in NO reduction due to SNCR and an increase in ammonia utilisation efficiency.
- This benefit was found to increase with increasing loading of the additive.
- This benefit was explained to be greater than it appeared in the figures. The presence of the Fe-based additive would decrease the initial NO concentration of the theoretical SNCR 'reactor', and this should lead to a lower NO reduction due to SNCR. However, an interaction between the additive and the ammonia leads to an increase instead.
- From literature, it was assumed that the interaction involved ammonia molecules binding to the iron oxide, creating an active site for NO reduction and reducing the reliance on chain initiation and branching reactions.

The interaction witnessed was then subjected to economic analysis and kinetic modelling:

- Utilising the Fe-based additive was shown to be a more economical and environmentally friendly alternative to increasing ammonia usage in order to increase NO reduction.
- Kinetic modelling showed a slight increase in NO reduction with the presence of the Fe-based additive, but more importantly the temperature window was significantly shifted upwards.
- Alternative ammonia injection sites were modelled, but there was no definite evidence that these would lead to a greater performance than using the original site.
- Sensitivities of the Fe-based additive-SNCR hybrid technology to local O_2 and CO concentrations were also discussed.

7.2.2 Suggestions for Future Work

A progression for the Fe-based additive technology should involve investigations into whether the in-flame benefits, witnessed in literature and Chapter 5, are impacted by the use of low-NO_x burners and the increased residence time of Fe and NO within the fuel-rich zone that would accompany this technology. Furthermore, this idea can be expanded to investigate any impact of the Fe-based additive on NO reburning during oxy-coal combustion, marrying Chapters 4, 5 and 6. Future smart combustion systems should rely on multiple technologies being used in combination; this concept requires further promotion and practice.

The kinetic modelling in Chapter 5 utilised kinetic parameters derived from literature. It would be preferable that kinetic data was sourced with the particular Fe-based additive and atmospheres used experimentally. To that end, an in-house laboratory-scale study to determine kinetic parameters of this interaction should be carried out.

Many popular deNO_x catalysts can have the unintended side effect of oxidising SO_2 to SO_3 and sulphur trioxide is far more difficult to remove using conventional flue gas desulphurisation technologies than sulphur dioxide. The studies in this thesis did not investigate sulphur emissions at all, therefore, it is recommended that future work using the Fe-based additive should consider and investigate any impact of the Fe-based additive on SO_2 oxidation.

7.3 The Use of Equilibrium Modelling to Compare Corrosion-Inhibiting Fuel Additives

7.3.1 Conclusions

The equilibrium modelling module of FactSage was used to predict the impact of the Fe-based additive on corrosive processes in ash deposits. A range of fuels (one coal and three biomass) were investigated and the additive was compared with two coal ashes with varying compositions and pure alumina. The following observations were made:

- The studied coal ash deposit was relatively inert and no major changes in the production of KCl or $FeCl_2$ were witnessed with the addition of the Fe-based additive.

- The Fe-based additive showed some ability to reduce formation of corrosive species, but this was heavily dependent on the original ash composition.
- The depicted trends implied that it would not be feasible to use the Fe-based additive solely for the purpose of inhibiting fireside corrosion, but an operator may see improvements with regard to tube life if it were used for other uses in the boiler.
- The Ca-rich coal ash performed far better than the Fe-based additive in reducing the formation of corrosive species, but, due to its contaminating sulphur content, performed worse than the Al-rich coal ash. This highlighted the importance of contaminants and how operators should be selective in their reuse of waste coal ash.
- Alumina was found to have some impact but far less than the Al-rich coal ash, agreeing with trends found in literature. The use of alumina highlighted the idea that the needs of the ash dictate the composition of the additive, as alumina performed perfectly well with the biomass ash that had a significant silica content.
- FactSage was shown to provide quick and economical analysis of the impacts of fuel additives; however, its weaknesses and uncertainties were discussed in detail.

7.3.2 Suggestions for Future Work

Originally, the study presented in Chapter 6 was to include, and be led by, experimental investigations. It is necessary that this work still occur for two reasons. The first is that it is necessary to present more fundamental evidence of corrosion inhibition, than that which has been presented in literature, to confirm the applicability of the Fe-based additive for this role. The second is to compare experimental findings with those from a complimentary equilibrium model, and, hence, determine whether FactSage is accurately predicting changes in the production of corrosive species or phase changes of these species. Furthermore, an analysis can be made as to the extent of which the lack of kinetic considerations and physical interactions causes the predicted trends to differ from observed trends.

REFERENCES

Abas, N., Kalair, A., Khan, N. (2015) Review of fossil fuels and future energy technologies. Futures, 69, 31-49.

Abu-Zahra, M.R.M., Sodiq, A., Feron, P.H.M. (2016) Commercial liquid absorbent-based PCC processes. In: P.H.M. Feron, ed. Absorption-Based Post-Combustion Capture of Carbon Dioxide. Woodhead Publishing. pp. 757-778.

Adanez, J., Abad, A., Mendiara, T., Gayan, P., de Diego, L.F., Garcia-Labiano, F. (2018) Chemical looping combustion of solid fuels. Progress in Energy and Combustion Science, 65, 6-66.

Aho, M., Vainikka, P., Taipale, R., Yrjas, P. (2008) Effective new chemicals to prevent corrosion due to chlorine in power plant superheaters. Fuel, 87, 647-654.

Al-Abbas, A.H. and Naser, J. (2012) Effect of Chemical Reaction Mechanisms and NOx Modeling on AirFired and Oxy-Fuel Combustion of Lignite in a 100-kW Furnace. Energy and Fuels, 26, 3329-3348.

Andersson, K., Normann, F., Johnsson, F., Leckner, B. (2008) NO emission during oxy-fuel combustion of lignite. Industrial & Engineering Chemistry Research, 47(6), 1835-1845.

Antunes, R.A. and de Oliveira, M.C.L. (2013) Corrosion in biomass combustion: A materials selection analysis and its interaction with corrosion mechanisms and mitigation strategies. Corrosion Science, 76, 6-26.

Apostolescu, N., Geiger, B., Hizbullah, K., Jan, M.T., Kureti, S., Reichert, D., et al. (2006) Selective catalytic reduction of nitrogen oxides by ammonia on iron oxide catalysts. Applied Catalysis B: Environmental, 62(1-2), 104-114.

Atkinson, R. (2000) Atmospheric chemistry of VOCs and NOx. Atmospheric Environment, 34(12-14), 2063-2101.

Azuhata, S., Akimoto, H., Hishinuma, Y. (1982) Effect of H2O2 on homogeneous gas phase NO reduction reaction with NH3. AIChE Journal, 28(1), 7-11.

Backreedy, R.I., Jones, J.M., Ma, L., Pourkashanian, M., Williams, A., Arenillas, A., et al. (2005) Prediction of unburned carbon and NOx in a tangentially fired power station using single coals and blends. Fuel, 84, 2196-2203.

Bale, C.W., Belisle, E., Chartrand, P., Decterov, S.A., Eriksson, G., Gheribi, A.E., et al. (2016) FactSage thermochemical software and databases, 2010-2016. CALPHAD: Computer Coupling of Phase Diagrams and Thermochemistry, 54, 35-53.

Baltasar, J., Carvalho, M.G., Coelho, P., Costa, M. (1997) Flue gas recirculation in a gas-fired laboratory furnace: measurements and modelling. Fuel, 76(10), 919-929.

Banna, S.M. and Branch, M.C. (1981) Mixing and reaction of NH3 with NO in combustion products. Combustion and Flame, 42, 173-181.

Bassilakis, R., Zhao, Y., Solomon, P.R., Serio, M.A. (1993) Sulfur and nitrogen evolution in the Argonne coals: experiment and modeling. Energy and Fuels, 7(6), 710-720.

Baxter, L.L., Miles, T.R., Miles, T.R. Jr., Jenkins, B.M., Dayton, D.C., Milne, T.A., et al. (1996) The behavior of inorganic material in biomass-fired power boilers—field and laboratory experiences: vol. II of Alkali deposits found in biomass power plants. National Renewable Energy Laboratory, 1617 Cole Boulevard, Golden, CO.

Beccidan, M., Sorum, L., Frandsen, F., Pedersen, A.J. (2009) Corrosion in waste-fired boilers: A thermodynamic study. Fuel, 88, 595-604.

Becher, V., Goanta, A., Gleis, S., Spliethoff, H. (2007) Controlled staging with non-stoichiometric burners for oxy-fuel processes. The 32nd international technical conference on coal utilization and fuel systems, the power of coal. Clearwater, Florida.

Bosch, H. and Janssen, F. (1988) Control technologies. Catalysis Today, 2(4), 381-401.

Brostrom, M., Kassman, H., Helgesson, A., Berg, M., Andersson, C., Backman, R., et al. (2007) Sulfation of corrosive alkali chlorides by ammonium sulfate in a biomass fired CFB boiler. Fuel Processing Technology, 88, 1171-1177.

Bryers, R.W. (1996) Fireside slagging, fouling, and high temperature corrosion of heat-transfer surface due to impurities in steam-raising fuels. Progress in Energy and Combustion Science, 22(1), 29-120.

Busca, G., Lietti, L., Ramis, G., Berti, F. (1998) Chemical and mechanistic aspects of the selective catalytic reduction of NOx by ammonia over oxide catalysts: A review. Applied Catalysis B: Environmental,18(1-2), 1-36.

Cao, H., Sun, S., Liu, Y., Wall, T.F. (2010) Computational Fluid Dynamics Modeling of NOx Reduction Mechanism in Oxy-Fuel Combustion. Energy and Fuels, 24, 131-135.

Chan, L.K., Sarofim, A.F., Beer, J.M. (1983) Kinetics of the NO-Carbon Reaction at Fluidized Bed Combustor Conditions. Combustion and Flame, 52, 37-45.

Chen, C.Y., Lan, G.S., Tuan, W.H. (2000) Microstructural evolution of mullite during the sintering of kaolin powder compacts. Ceramics International, 26(3), 715-720.

Chen, J.C., Castagnoli, C., Niksa, S. (1992) Coal Devolatilization during Rapid Transient Heating. 2. Secondary Pyrolysis. Energy and Fuels, 6(3), 264-271.

Choi, C.R. and Kim, C.N. (2009) Numerical investigation on the flow, combustion and NOx emission characteristics in a 500 MWe tangentially fired pulverized-coal boiler. Fuel, 88(9), 1720-1731.

Chui, E.H., Douglas, M.A., Tan, Y. (2003) Modeling of oxy-fuel combustion for a western Canadian sub-bituminous coal. Fuel, 82(10), 1201-1210.

Chui, E.H., Majeski, A.J., Douglas, M.A., Tan, Y., Thambimuthu, K.V. (2004) Numerical investigation of oxy-coal combustion to evaluate burner and combustor design concepts. Energy, 29(9-10), 1285-1296.

Clements, A.G., Black, S., Szuhánszki, J., Stęchły, K., Pranzitelli, A., Nimmo, W., Pourkashanian, M. (2015) LES and RANS of air and oxy-coal combustion in a pilot-scale facility: Predictions of radiative heat transfer. Fuel, 151, 146–155.

CMU.edu (2020) Integrated Environmental Control Model. [Online]. [Accessed 04 October 2020]. Available from: https://www.cmu.edu/epp/iecm/

Cochran, J.R., Gregory, M.G., Rummenhohl, V. (1993) 'The Effect of Various Parameters on SCR System Cost', Power-Gen '93, the Fourth International Power Generation Exhibition & Conference, ASME, Dallas, Texas, November 1993.

Coda, B., Aho, M., Berger, R., Hein, K.R.G. (2001) Behavior of Chlorine and Enrichment of Risky Elements in Bubbling Fluidized Bed Combustion of Biomass and Waste Assisted by Additives. Energy & Fuels, 15(3), 680-690.

Correa da Silva, R., Kangwanpongpan, T., Krautz, H.J. (2014) Flame pattern, temperatures and stability limits of pulverized oxy-coal combustion. Fuel, 115, 507-520.

Correa da Silva, R., Krautz, H.J. (2014) Emission performance of type-1 pulverized coal flames operating under oxy-fired conditions. Applied Thermal Engineering, 64, 430-440.

Correa da Silva, R., Krautz, H.J. (2018) Combustion measurements of type-1 pulverized coal flames operating under oxy-fired conditions. Fuel Processing Technology, 171, 232-247.

Creutzig, F., Breyer, C., Hilaire, J., Minx, J., Peters, G.P., Socolow, R. (2019) The mutual dependence of negative emission technologies and energy systems. Energy and Environmental Science, 12, 1805-1817.

Daood, S.S., Javed, M.T., Gibbs, B.M., Nimmo, W. (2013) NOx control in coal combustion by combining biomass co-firing, oxygen enrichment and SNCR. Fuel, 105, 283-292.

Daood, S.S., Ord, G., Wilkinson, T., Nimmo, W. (2014a) Fuel additive technology – NOx reduction, combustion efficiency and fly ash improvement for coal fired power stations. Fuel, 134, 293-306.

Daood, S.S., Ord, G., Wilkinson, T., Nimmo, W. (2014b) Investigation of the influence of metallic fuel improvers on coal combustion/pyrolysis. Energy & Fuels, 28(2), 1515-1523.

Daood, S.S., Ottolini, M., Taylor, S., Ogunyinka, O., Hossain, M.M., Lu, G, et al. (2017) Pollutant and corrosion control technology and efficient coal combustion. Energy & Fuels, 31(5), 5581-5596.

Dayton, D.C., Belle-Oudry, D., Nordin, A. (1999) Effect of Coal Minerals on Chlorine and Alkali Metals Released during Biomass/Coal Cofiring. Energy & Fuels, 13(6), 1203-1211.

DEFRA (2019) Clean Air Strategy 2019. [Online]. [Accessed 27 April 2020]. Available from: https://assets.publishing.service.gov.uk/government/uploads/system/uploads/attachment_data/file/770715/clean-air-strategy-2019.pdf

Directive (EU) 2015/2193 of the European Parliament and of the Council of 25 November 2015 on the limitation of emissions of certain pollutants into the air from medium combustion plants. [Online]. [Accessed 27 April 2020]. Available from: https://eur-lex.europa.eu/legal-content/EN/TXT/?uri=CELEX:32015L2193

Directive 2010/75/EU of the European Parliament and of the Council of 24 November 2010 on industrial emissions (integrated pollution prevention and control). [Online]. [Accessed 27 April 2020]. Available from: https://eur-lex.europa.eu/legal-content/EN/TXT/?uri=CELEX:32010L0075

Doosan Babcock (2015) Burners and Firing Systems for Oxyfuel Combustion. Oxyfuel Combustion Capacity Building Course.

Doosan Babcock (2020) Pulverised fuel burners. [Online]. [Accessed 19 September 2020]. Available from: http://www.doosanbabcock.com/download/pdf/media/brochures/PulverisedFuelBurners.pdf

Drax (2016) Drax to save 20 millionth tonne of carbon through use of sustainable biomass. [Online]. [Accessed 15 April 20]. Available from: https://www.drax.com/press_release/drax-save-20-millionth-tonne-carbon-use-sustainable-biomass/

Drax Power Ltd (2014) Biomass combustion. Inventors: Paul Straker, Jason Shipstone and Adam Nicholson. 20/09/2017. Appl: 31/03/2014. GB Patent GB2525776B.

EPA (2000) U.S. Environmental Protection Agency, Office of Air Quality Planning and Standards. EPA Air Pollution Control Cost Manual Section 4 Chapter 2. [Online]. [Accessed 15 April 20]. Available from: https://www3.epa.gov/ttncatc1/dir1/c_allchs.pdf

EPA (2003) EPA-CICA Fact Sheet: SCR. [Online]. [Accessed 15 April 20]. Available from: https://www3.epa.gov/ttncatc1/dir1/fscr.pdf

EPRI (2001) Cost of Corrosion in the Electric Power Industry. [Online]. [Accessed 30 April 2020]. Available from: https://www.epri.com/#/pages/product/1004662/?lang=en-US

European Commission (1994) The role of fuel additives to control environmental emissions and ash fouling. 7220-EC/846.

European Commission (2017) Sustainable and optimal use of biomass for energy in the EU beyond 2020. [Online]. [Accessed 19 September 2020]. Available from: https://ec.europa.eu/energy/sites/ener/files/documents/biosustain_annexes_final.pdf

Fenimore, C.P. (1971) Formation of nitric oxide in premixed hydrocarbon flames. Symposium (International) on Combustion, 13(1), 373-380.

Fennell, P.S. and Hayhurst, A.N. (2002) The kinetics of the reduction of NO to N2 by reaction with particles of Fe. Proceedings of the Combustion Institute, 29(2), 2179-2185.

Fry, A., Adams, B., Paschedag, A., Kazalski, P., Carney, C., Oryshchyn, D., et al. (2011) Principles for retrofitting coal burners for oxy-combustion. International Journal of Greenhouse Gas Control, S5, S151-S158.

Fu, S., Song, Q., Yao, Q. (2014) Experimental and Kinetic Study on the Influence of Iron Oxide on the Selective Noncatalytic Reduction DeNOx Process. Industrial & Engineering Chemistry Research, 53(14), 5801-5809.

Fu, S., Song, Q., Yao, Q. (2015) Study on the catalysis of CaCO3 in the SNCR deNOx process for cement kilns. Chemical Engineering Journal, 262, 9-17.

Gharebaghi, M., Irons, R.M.A, Ma, L., Pourkashanian, M., Pranzitelli, A. Large eddy simulation of oxy-coal combustion in an industrial combustion test facility. International Journal of Greenhouse Gas Control, S5, S100-S110.

Glarborg, P., Jensen, A.D., Johnsson, J.E. (2003) Fuel nitrogen conversion in solid fuel systems. Progress in Energy and Combustion Science, 29(2), 89-113.

Glarborg, P., Miller, J.A., Kee, R.J. (1986) Kinetic modeling and sensitivity analysis of nitrogen oxide formation in well-stirred reactors. Combustion and Flame, 65(2), 177-202.

Glarborg, P., Miller, J.A., Ruscic, B., Klippenstein, S.J. (2018) Modeling nitrogen chemistry in combustion. Progress in Energy and Combustion Science, 67, 31-68.

Gomez-Garcia, M.A., Pitchon, V., Kiennemann, A. (2005) Pollution by nitrogen oxides: an approach to NOx abatement by using sorbing catalytic materials. Environment International, 31(3), 445-467.

Goodwin, D.G., Speth, R.L., Moffat, H.K., Weber, B.W. (2018) Cantera: An object-oriented software toolkit for chemical kinetics, thermodynamics, and transport processes. https://www.cantera.org. Version 2.4.0. doi:10.5281/zenodo.1174508

Grabke, H.J., Reese, E., Spiegel, M. (1995) The effects of chlorides, hydrogen chloride, and sulphur dioxide in the oxidation of steels below deposits. Corrosion Science, 37(7), 1023-1043.

Grabke, H.J., Spiegel, M., Zahs, A. (2004) Role of alloying elements and carbides in the chlorine-induced corrosion of steels and alloys. Materials Research, 7(1), 89-95.

Gradon, B. and Lasek, J. (2010) Investigations of the reduction of NO to N2 by reaction with Fe. Fuel, 89(11), 3505-3509.

Gullett, B.K., Lin, M.L., Groff, P.W., Chen, J.M. (1994) NOx removal with combined selective catalytic reduction and selective noncatalytic reduction: pilot-scale test results. Journal of Air & Waste Management Association, 44(10), 1188-1194.

Guo, X., Wei, X., Li, S. (2012) Detailed Modeling of the Effects of K/Na Additives on the Thermal DeNOx Process. Energy Fuels, 27, 421-429.

Hallgren, A.L., Engvall, K., Skrifvars, B.J. (1999) Ash-Induced Operational Difficulties in Fluidised Bed Firing of Biofuels and Waste. Biomass Conference of the Americas, 1365-1370.

Hampartsoumian, E., Folayan, O.O., Nimmo, W., Gibbs, B.M. (2003) Optimisation of NOx reduction in advanced coal reburning systems and the effect of coal type. Fuel, 82(4), 373-384.

Han, K., Lu, C. (2007) Kinetic Model and Simulation of Promoted Selective Non-catalytic Reduction by Sodium Carbonate. Chinese Journal of Chemical Engineering, 15(4), 512-519.

Hao, J., Yu, W., Lu, P., Zhang, Y., Zhu, X. (2015) The effects of Na/K additives and flyash on NO reduction in a SNCR process. Chemosphere, 122, 213-218.

Harb, J.N. and Smith, E.E. (1990) Fireside corrosion in PC-fired boilers. Progress in Energy and Combustion Science, 16(3), 169-190.

Hayhurst, A.N. and Lawrence, A.D. (1997) The Reduction of the Nitrogen Oxides NO and N2O to Molecular Nitrogen in the Presence of Iron, Its Oxides, and Carbon Monoxide in a Hot Fluidized Bed. Combustion and Flame, 110, 351-365.

Heck, R.M. (1999) Catalytic abatement of nitrogen oxides-stationary applications. Catalysis Today, 53(4), 519-523.

Hees, J., Zabrodiec, D., Massmeyer, A., Pielsticker, S., Govert, B., Habermehl, M., et al. (2016) Detailed analyzes of pulverized coal swirl flames in oxy-fuel atmospheres. Combustion and Flame, 172, 289-301.

Hendry, A. and Lees, D.J. (1980) Corrosion of austentic steels in molten sulphate deposits. Corrosion Science, 20(3), 383-404.

Hesselmann, G. and Marta, R. (2001) What are the general principles of low NOx burner design for fossil fuel fired utility boilers? IFRF online combustion handbook. Available from: http://www.handbook.ifrf.net/handbook/

Hill, S.C. and Smoot, L.D. (2000) Modeling of nitrogen oxides formation and destruction in combustion systems. Progress in Energy and Combustion Science, 26(4-6), 417-458.

Holcomb, G.R., Covino, B.S., Bullard, S.J., Ziomek-Moroz, M., Alman, D.E. (2005) Oxidation of alloys for advanced steam turbines. DOE/ARC-2005-066. [Online]. [Accessed 19 September 2020]. Available from: https://www.osti.gov/servlets/purl/895403

Holgate, S.T. (2017) 'Every breath we take: the lifelong impact of air pollution' – a call for action. Clinical Medicine, 17(1), 8-12.

Horvath, I.T. (2003) Encyclopedia of Catalysis: Volume 5. Hoboken, New Jersey: John Wiley & Sons Inc.

IEA (2019) Data and statistics. [Online]. [Accessed 28 April 2020]. Available from: https://www.iea.org/data-and-statistics

IEA Bioenergy (2016) The status of large scale biomass firing: The milling and combustion of biomass materials in large pulverised coal boilers. [Online]. [Accessed 15 April 2020]. Available from: http://task32.ieabioenergy.com/wp-content/uploads/2017/03/IEA_Bioenergy_T32_cofiring_2016.pdf

IEA Clean Coal Centre (2015) Emission Standards: China. [Online]. [Accessed 28 April 2020]. Available from: https://www.iea-coal.org/wp-content/uploads/2017/12/China-emission-standards.pdf

IEA Clean Coal Centre (2019a) Emission Standards: India. [Online]. [Accessed 28 April 2020]. Available from: https://www.iea-coal.org/library/emission-standards/

IEA Clean Coal Centre (2019b) Emission Standards: Japan. [Online]. [Accessed 28 April 2020]. Available from: https://www.iea-coal.org/library/emission-standards/

IEA Clean Coal Centre (2019c) Emission Standards: South Korea. [Online]. [Accessed 28 April 2020]. Available from: https://www.iea-coal.org/library/emission-standards/

IEA Clean Coal Centre (2019d) Emission Standards: USA. [Online]. [Accessed 28 April 2020]. Available from: https://www.iea-coal.org/library/emission-standards/

IFRF (2006) IFRF Today, FFRC Liekkipäivä, Åbo Akademi, Turku. [Online]. [Accessed 14 April 2020]. Available from: http://www.ffrc.fi/Liekkipaiva_2006/Liekkipaiva2006_IFRF_Today_HUPA.pdf

Irons, R.M.A., Price, H.J., Squires, R.T. (1991) Tailoring ammonia-based SNCR for installation on power station boilers. Joint EPA/EPRI Symposium on Stationary Combustion NOx Control, 99-118.

Jabaz, I., Jiao, F., Wu, X., Yu, D., Ninomiya, Y., Zhang, L. (2017) Influence of gaseous SO2 and sulphate-bearing ash deposits on the high-temperature corrosion of heat exchanger tube during oxy-fuel combustion. Fuel Processing Technology, 167, 193-204.

Jagustyn, B., Batorek-Giesa, N., Wilk, B. (2011) Evaluation of properties of biomass used for energy purposes. Chemik, 65(6), 557-563.

Javed, M.T., Irfan, N., Gibbs, B.M. (2007) Control of combustion-generated nitrogen oxides by selective non-catalytic reduction. Journal of Environmental Management, 83(3), 251-289.

Jensen, L.S., Jannerup, H.E., Glarborg, P., Jensen, A., Dam-Johansen, K. (2000) Experimental investigation of NO from pulverised char combustion. Proceedings of the Combustion Institute, 28(2), 2271-2278.

Kambara, S., Takarada, T., Yamamoto, Y., Kato, K. (1993) Relation between functional forms of coal nitrogen and formation of NOx precursors during rapid pyrolysis. Energy and Fuels, 7(6), 1013-1020.

Kanagawa, M., Nakata, T. (2008) Assessment of access to electricity and the socio-economic impacts in rural areas of developing countries. Energy Policy, 36(6), 2016-2029.

Khare, S.P., Wall, T.F., Farida, A.Z., Liu, Y., Moghtaderi, B., Gupta, R.P. (2008) Factors influencing the ignition of flames from air-fired swirl pf burners retrofitted to oxy-fuel. Fuel, 87(7), 1042- 1049.

Klippenstein, S.J., Harding, L.B., Glarborg, P. and Miller, J.A. (2011) The role of NNH in NO formation and control. Combustion and Flame, 158(4), 774-789.

Konnov, A.A., Colson, G., de Ruyck, D. (2000) The new route forming NO via NNH. Combustion and Flame, 121(3), 548-550.

Kumar, D. and Kumar, D. (2018) Sustainable Management of Coal Preparation. Woodhead Publishing.

Kung, S.C. Fireside corrosion in coal- and oil-fired boilers. (2006) ASM Handbook, Volume 13C, Corrosion: Environments and Industries, (Cramer, S.D. and Covino, Jr., B.S.), ASM International.

Kurkela, E. (1996) Formation and removal of biomass-derived contaminants in fluidized-bed gasification processes, Technical Research Centre of Finland. [Online]. [Accessed 15 April 2020]. Available from: https://www.osti.gov/etdeweb/servlets/purl/442486

Kyi, S. and Chadwick, B.L. (1999) Screening of potential mineral additives for use as fouling preventatives in Victorian brown coal combustion. Fuel, 78, 845-855.

Lasek, J.A. (2014) Investigations of the reduction of NO to N2 by reaction with Fe under fuel-rich and oxidative atmosphere. Heat Mass Transfer, 50(7), 933-943.

Lee, G.W., Shon, B.H., Yoo, J.G., Jung, J.H., Oh, K.J. (2008) The influence of mixing between NH3 and NO for a de-NOx reaction in the SNCR process. Journal of Industrial and Engineering Chemistry, 14(4), 457-467.

Levy, J.M., Chan, L.K., Sarofim, A.F., Beer, J.M. (1981) NO/Char Reactions at Pulverised Coal Flame Conditions. Symposium (International) on Combustion, 18(1), 111-120.

Li, H., Yan, J., Yan, J., Anheden, M. (2009) Impurity impacts on the purification process in oxy-fuel combustion based CO2 capture and storage system. Applied Energy, 86(2), 202-213.

Li, T., Zhuo, Y., Chen, C., Xu, X. (2010) Effect of CaO on NH3+ NO + O2 reaction system in the absence and presence of high concentration CO2. Asia-Pacific Journal of Chemical Engineering, 5(2), 287-293.

Liao, Y., Cao, Y., Chen, T., Ma, X. (2015) Experiment and simulation study on alkalis transfer characteristic during direct combustion utilization of bagasse. Bioresource Technology, 194, 196-204.

Ling, Z., Kuang, M., Zeng, X., Zhang, G. (2013) Combustion Flexibility of a Large-Scale Down-Fired Furnace with Respect to Boiler Load and Staging Conditions at Partial Loads. Energy and Fuels, 28, 725-734.

Lissianski, V.V., Maly, P.M., Zamansky, V.M., Gardiner, W.C. (2001a) Utilization of iron additives for advanced control of NOx emissions from stationary combustion sources. Industrial & Engineering Chemistry Research, 40(15), 3287-3293.

Lissianski, V.V., Zamansky, V.M., Maly, P.M. (2001b) Effect of metal-containing additives on NOx reduction in combustion and reburning. Combustion and Flame, 125(3), 1118-1127.

Liu, H., Hampartsoumian, E., Gibbs, B.M. (1997) Evaluation of the optimal fuel characteristics for efficient NO reduction by coal reburning. Fuel, 76(11), 985-993.

Liu, H., Zailani, R., Gibbs, B.M. (2005a) Comparisons of pulverised coal combustion in air and in mixtures of O2/CO2. Fuel, 84(7-8), 833-840.

Liu, H., Zailani, R., Gibbs, B.M. (2005b) Pulverized coal combustion in air and in O2/CO2 mixtures with NOx recycle. Fuel, 84(16), 2109-2115.

Liu, Y., Wan, K., He, Y., Wang, Z., Xia, J., Cen, K. (2020) Experimental study of potassium release during biomass-pellet combustion and its interaction with inhibitive additives. Fuel, 260, 116346.

Llorente, M.J.F., Arocas, P.D., Nebot, L.G., Garcia, J.E.C. (2008) The effect of the addition of chemical materials on the sintering of biomass ash. Fuel, 87, 2651-2658.

Lodder, P. and Leders, J.B. (1985) Effect of natural gas, C2H6, and CO on the homogeneous gas phase reduction of NO by NH3. The Chemical Engineering Journal, 30(3), 161-167.

Lyon, R.K. (1975) Method for the reduction of the concentration of NO in combustion effluents using ammonia. U.S. Patent 3,900,554.

Lyon, R.K. and Benn, D. (1979) Kinetics of the NO-NH3-O2 reaction. Symposium (International) on Combustion, 17(1), 601-610.

Lyon, R.K. and Hardy, J.E. (1986) Discovery and development of the thermal deNOx process. Industrial & Engineering Chemistry Fundamentals, 25(1), 19-24.

Lyon, R.K. and Longwell, J.P. (1976) Selective, non-catalytic reduction of NOx by NH3. EPRI NOx Control Technology Seminar.

Ma, H., Zhou, L., Ma, S., Du, H. (2017) Design of porous wall air coupling with air staged furnace for preventing high temperature corrosion and reducing NOx emissions. Applied Thermal Engineering, 124, 865-870.

Mackrory, A.J. and Tree, D.R. (2009) Predictions of NOx in a Laboratory Pulverized Coal Combustor Operating under Air and Oxy-Fuel Conditions. Combustion Science and Technology, 181(11), 1413-1430.

Mackrory, A.J. and Tree, D.R. (2012) Measurement of nitrogen evolution in a staged oxy-combustion coal flame. Fuel, 93, 298-304.

Mackrory, A.J., Lokare, S., Baxter, L.L., Tree, D.R. (2007) 'An investigation of nitrogen evolution in oxy-fuel combustion'. The 32nd international technical conference on coal utilization and fuel systems, the power of coal. Clearwater, Florida.

Malmgren, A. and Riley, G. (2012) Biomass Power Generation. In: A. Sayigh, ed. Comprehensive Renewable Energy Volume 5: Biomass and Biofuel Production. Elsevier. pp. 27-53.

Maly, P.M., Zamansky, V.M., Ho, L., Payne, R. (1999) Alternative fuel reburning. Fuel, 78(3), 327-334.

Manny, E.H., Bartok, W., Crawford, A.R., Hall, R.E., Vatsky, J. (1978) Studies of waterwall corrosion with staged combustion of coal. Ash Deposits and Corrosion Due to Impurities in Combustion Gases, (Bryers, R.W.), Hemisphere Publishing.

McCahey, S., McMullan, J.T., Williams, B.C. (1999) Techno-economic analysis of NOx reduction technologies in p.f. boilers. Fuel, 78(14), 1771-1778.

Meij, R., te Winkel, B. (2005) The emissions and environmental impact of PM10 and trace elements from a modern coal-fired power plant equipped with ESP and wet FGD. Fuel Processing Technology, 85, 641-656.

Mereb, J.B. and Wendt, J.O.L. (1994) Air staging and reburning mechanisms for NO, abatement in a laboratory coal combustor. Fuel, 73(7), 1020-1026.

Miller, J.A. and Bowman, C.T. (1989) Mechanism and Modeling of Nitrogen Chemistry in Combustion. Progress in Energy and Combustion Science, 15, 287-338.

Miller, J.A., Branch, M.C., McLean, W.J., Chandler, D.W., Smooke, M.D., Kee, R.J. (1985) The conversion of HCN to NO and N2 in H2-O2-HCN-Ar flames at low pressure. Symposium (International) on Combustion, 20(1), 673-684.

Minchener, A.J. and McMullan, J.T. (2007) Clean Coal Technology R, D&D. Significant achievements of European Coal and Steel Community R&D programmes in the development of clean coal power generation technology, IEA Coal Research Ltd, 26 February.

Moguel, O.F., Szuhánszki, J., Clements, A.G., Ingham, D.B., Ma, L., Pourkashanian, M. (2018) Oscillating coal and biomass flames: A spectral and digital imaging approach for air and oxyfuel conditions. Fuel Processing Technology, 173, 243–252.

Muzio, L.J. and Quartucy, G.C. (1997) Implementing NOx control: research to application. Progress in Energy and Combustion Science, 23(3), 233-266.

Muzio, L.J., Arand, J.K. and Texeira, D.P. (1977) Gas phase decomposition of nitric oxide in combustion products. Symposium (International) on Combustion, 16(1), 199-208.

Muzio, L.J., Maloney, K.L., Arand, J.K. (1979) Reactions of NH3 with NO in coal-derived combustion products. Symposium (International) on Combustion, 17(1), 89-96.

Nelson, R.K., Franklin, J.D., Scherer, B. (1994) Prediction of NOx Generation in Coal Fired Boilers. Power-Gen Americas ’94.

Nielsen, H.P., Frandsen, F.J., Dam-Johansen, K., Baxter, L.L. (2000) The implications of chlorine-associated corrosion on the operation of biomass-fired boilers. Progress in Energy and Combustion Science, 26(3), 283-298.

Nimmo, W. and Liu, H. (2010) Chapter 4: Developments in NOx emission control by ‘reburning’ pulverised coal combustion. Coal Combustion Research, (Grace, C.T.), Nova Science Publishers, Inc.

Niu, Y., Tan, H., Hui, S. (2016) Ash-related issues during biomass combustion: Alkali-induced slagging, silicate melt-induced slagging (ash fusion), agglomeration, corrosion, ash utilization, and related countermeasures. Progress in Energy and Combustion Science, 52, 1-61.

Niu, Y., Tan, H., Ma, L., Pourkashanian, M., Liu, Z., Liu, Y., et al. (2010) Slagging Characteristics on the Superheaters of a 12 MW Biomass-Fired Boiler. Energy Fuels, 24, 5222-5227.

Nordgren, D., Hedman, H., Padban, N., Bostrom, D., Ohman, M. (2013) Ash transformations in pulverised fuel co-combustion of straw and woody biomass. Fuel Processing Technology, 105, 52-58.

Normann, F., Andersson, K., Leckner, B., Johnsson, F. (2008) High-temperature reduction of nitrogen oxides in oxy-fuel combustion. Fuel, 87(17-18), 3579-3585.

Normann, F., Andersson, K., Leckner, B., Johnsson, F. (2009) Emission control of nitrogen oxides in the oxy-fuel process. Progress in Energy and Combustion Science, 35(5), 385-397.

Ochi, K., Kiyama, K., Yoshizako, H., Okazaki, H., Taniguchi, M. (2009) Latest low-NOx combustion technology for pulverised-coal-fired boilers. Hitachi Review, 58(5), 187-193.

Okazaki, K. and Ando, T. (1997) NOx reduction mechanism in coal combustion with recycled CO2. Energy, 22(2-3), 207-215.

Østberg, M., Dam-Johansen, K., Johnsson, J.E. (1997) Influence of mixing on the SNCR process. Chemical Engineering Science, 52(15), 2511-2525.

Paneru, M., Stein-Brzozowska, G., Maier, J., Scheffknecht, G. (2013) Corrosion Mechanism of Alloy 310 Austenitic Steel beneath NaCl Deposit under Varying SO2 Concentrations in an Oxy-fuel Combustion Atmosphere. Energy and Fuels, 27, 5699-5705.

Parvulescu, V.I., Grange, P., Delmon, B. (1998) Catalytic removal of NO. Catalysis Today, 46(4), 233-316.

Pehnt, M. and Henkel, J. (2009) Life cycle assessment of carbon dioxide capture and storage from lignite power plants. International Journal of Greenhouse Gas Control, 3(1), 49-66.

Perea-Moreno, M.A., Manzano-Agugliaro, F., Hernandez-Escobedo, Q., Perea-Moreno, A.J. (2018) Peanut Shell for Energy: Properties and Its Potential to Respect the Environment. Sustainability, 10(9), 3254.

Pohl, J.H. and Sarofim, A.F. (1977) Devolatilization and oxidation of coal nitrogen. Symposium (International) on Combustion, 16(1), 491-501.

Qi, G. and Yang, R.T. (2005) Ultra-active Fe/ZSM-5 catalyst for selective catalytic reduction of nitric oxide with ammonia. Applied Catalysis B: Environmental, 60(1-2), 13-22.

Reddy, B.V. and Khanna, S.N. (2004) Self-stimulated NO reduction and CO oxidation by iron oxide clusters. Physical Review Letters, 93(6), 068301.

Reid, W.T. (1971) External Corrosion and Deposits: Boiler and Gas Turbines, American Elsevier Publishing.

Reidl, R., Dahl, J., Obernberger, I., Narodoslawsky, M. (1999) Corrosion in fire tube boilers of biomass combustion plants. Proceedings of the China International Corrosion Control Conference ’99.

Rigby, J., Ma, J., Webb, B.W., Fletcher, T.H. (2001) Transformations of Coal-Derived Soot at Elevated Temperature. Energy and Fuels, 15(1), 52-59.

Rizvi, T., Xing, P., Pourkashanian, M., Darvell, L.I., Jones, J.M., Nimmo, W. (2015) Prediction of biomass ash fusion behaviour by the use of detailed characterisation methods coupled with thermodynamic analysis. Fuel, 141, 275-284.

Skalska, K., Miller, J.S., Ledakowicz, S. (2010) Trends in Nox abatement: a review. Science of the Total Environment, 408(19), 3976-3989.

Smart, J., Lu, G., Yan, Y., Riley, G. (2010) Characterisation of an oxy-coal flame through digital imaging. Combustion and Flame, 157(6), 1132-1139.

Smart, J.P. and Morgan, M.E. (1992) The comparison between constant velocity and constant residence time scaling. IFRF Doc No. F 37/y/28.

Smart, J.P., Knill, K.J., Visser, B.M., Weber, R. (1989) Reduction of NOx emissions in a swirled coal flame by particle injection into the internal recirculation zone. Symposium (International) on Combustion, 22(1), 1117-1125.

Sowa, J.M. and Fletcher, T.H. (2011) Investigation of an iron-based additive on coal pyrolysis and char oxidation at high heating rates. Fuel Processing Technology, 92(12), 2211-2218.

Spinti, J.P. and Pershing, D.W. (2003) The fate of char-N at pulverized coal conditions. Combustion and Flame, 135(3), 299-313.

Srivastava, S.C., Godiwalla, K.M., Banerjee, M.K. (1997) Fuel ash corrosion of boiler and superheater tubes. Journal of Materials Science, 32, 835-849.

Stam, A.F. and Brem, G. (2019) Fouling in coal-fired boilers: Biomass co-firing, full conversion and use of additives – A thermodynamic approach. Fuel, 239, 1274-1283.

Stanmore, B.R., Visona, S.P. (2000) Prediction of NO emissions from a number of coal-fired power station boilers. Fuel Processing Technology, 64(1-3), 25-46.

Stone, R. (2002) Counting the Cost of London's Killer Smog. Science, 298(5601), 2106-2107.

Sturgeon, D.W., Rogerson, J.W., Hesselmann, G.J. (2013) Doosan Power Systems OxyCoal™ burner technology development. Energy Procedia, 37, 6481-6488.

Sun, Y., Fan, W., Zhu, T., Hong, X. (2017) Effect of CaO on NOx Reduction by Selective Non-Catalytic Reduction under Variable Gas Compositions in a Simulated Cement Precalciner Atmosphere. International Journal of Environmental Research and Public Health, 14(12), 1474.

Szuhánszki, J., Farias Moguel, O., Finney, K., Akram, M., Pourkashanian, M. (2017) Biomass combustion under oxy-fuel and post combustion capture conditions at the PACT 250 kW

air/oxy-fuel CTF. Supergen Bioenergy Hub Assembly, Hillsborough, Northern Ireland, 25th October 2017.

Szuhánszki, János (2014) Advanced oxy-fuel combustion for carbon capture and sequestration. PhD thesis, University of Leeds.

Tan, Y., Croiset, E., Douglas, M.A., Thambimuthu, K.V. (2006) Combustion characteristics of coal in a mixture of oxygen and recycled flue gas. Fuel, 85(4), 507-512.

Termuehlen, H., Emsperger, W. (2003) Steam Generator Technology. In Clean and Efficient Coal-Fired Power Plants. New York, NY: The American Society of Mechanical Engineers.

ThyssenKrupp Materials International (2011) Material data sheet P22/T22. [Online]. [Accessed 29 April 2019]. Available from: http://www.s-k-h.com/media/de/service/werkstoffblaetter_englisch/kesselrohre_en/10crmo910_p22_t22_engl.pdf

Tillman, D.A. (2018) Coal-Fired Electricity and Emissions Control: Efficiency and Effectiveness. Butterworth-Heinemann.

Tillman, D.A., Duong, D.N.B., Harding, N.S. (2012) Solid Fuel Blending. Butterworth-Heinemann.

Toftegaard, M.B., Brix, J., Jensen, P.A., Glarborg, P., Jensen, A.D. (2010) Oxy-fuel combustion of solid fuels. Progress in Energy and Combustion Science, 36(5), 581-625.

Tomeczek, J. (2007) Corrosion modelling of austenitic steel in molten sulphate deposit. Corrosion Science, 49(4), 1862-1868.

Tomeczek, J. and Wacławiak, K. (2009) Two-dimensional modelling of deposits formation on platen superheaters in pulverized coal boilers. Fuel, 88(8), 1466-1471.

Toporov, D.D. (2014) Combustion of Pulverised Coal in a Mixture of Oxygen and Recycled Flue Gas. London: Elsevier.

Toporov, D., Bocian, P. Heil, P., Kellermann, A., Stadler, H., Tschunko, S., et al. (2008) Detailed investigation of a pulverized fuel swirl flame in CO2/O2 atmosphere. Combustion and Flame, 155(4), 605-618.

Topsøe, N.Y., Dumesic, J.A., Topsøe, H. (1995) Vanadia/titania catalysts for selective catalytic reduction of nitric oxide by ammonia II. Studies of active sites and formulation of catalytic cycles. Journal of Catalysis, 151(1), 241-252.

Tsubouchi, N. and Ohtsuka, Y. (2008) Nitrogen chemistry in coal pyrolysis: Catalytic roles of metal cations in secondary reactions of volatile nitrogen and char nitrogen. Fuel Processing Technology, 89(4), 379-390.

Tully, S. (2006) The Human Right to Access Electricity. The Electricity Journal, 19(3), 30-39.

Uberoi, M., Punjak, W.A., Shadman, F. (1990) The Kinetic and Mechanism of Alkali Removal from Flue Gases by Solid Sorbents. Progress in Energy and Combustion Science, 16, 205-211.

Urbas, J. and Boyle, J.M. (1998) Design, Optimization and Economic Analysis of SNCR/SCR Hybrid on a Utility Boiler in the Ozone Transport Region. 1998 American/Japanese Flame Research Committees International Symposium, 1-14.

USEPA. (1994) Alternative Control Technologies Document - NOx Emissions from Utility Boilers. EPA-453/R-94-023.

van der Lans, R.P., Glarborg, P., Dam-Johansen, K. (1997) Influence of process parameters on nitrogen oxide formation in pulverised coal burners. Progress in Energy and Combustion Science, 23(4), 349-347.

Varagani, R.K., Chatel-Pelage, F., Pranda, P., Rostam-Abadi, M., Lu, Y., Bose, A.C. (2005) Performance Simulation and Cost Assessment of Oxy-Combustion Process for CO2 Capture from Coal-Fired Power Plants. Fourth Annual Conference on Carbon Sequestration.

Vattenfall (2008) Carbon Capture and Storage - Technology, costs and way forward. [Online]. [Accessed 19 September 2020]. Available from: https://group.vattenfall.com/siteassets/corporate/investors/x_investors/2.-investor-presentations/lars-stromberg-ccs-and-renewa.pdf

Wall, T.F. (1992) Mineral matter transformations and ash deposition in pulverised coal combustion. Symposium (International) on Combustion, 24(1), 1119-1126.

Wang, G., Jensen, P.A., Wu, H., Frandsen, F.J., Sander, B., Glarborg, P. (2018a) Potassium Capture by Kaolin, Part 1: KOH. Energy & Fuels, 32(2), 1851-1862.

Wang, G., Jensen, P.A., Wu, H., Frandsen, F.J., Sander, B., Glarborg, P. (2018b) Potassium Capture by Kaolin, Part 2: K2CO3, KCl, and K2SO4. Energy & Fuels, 32(3), 3566-3578.

Wang, L., Hustad, J.E., Skreiberg, O., Skjevrak, G., Gronli, M. (2012) A critical review on additives to reduce ash related operation problems in biomass combustion applications. Energy Procedia, 20, 20-29.

Watanabe, H., Yamamoto, J., Okazaki, K. (2011) NOx formation and reduction mechanisms in staged O2/CO2 combustion. Combustion and Flame, 158, 1255-1263.

Wei, X., Lopez, C., von Puttkamer, T., Schnell, U., Unterberger, S., Hein, K.R.G. (2002) Assessment of Chlorine−Alkali−Mineral Interactions during Co-Combustion of Coal and Straw. Energy & Fuels, 16(5), 1095-1108.

Weitkamp, J. (2000) Zeolites and catalysis. Solid State Ionics, 131(1-2), 175-188.

Wendt, J.O.L., Sternling, C.V., Matovich, M.A. (1973) Reduction of sulphur trioxide and nitrogen oxides by secondary fuel injection. Symposium (International) on Combustion, 14(1), 897-904.

Wendt. J.O.L., Linak, W.P., Groff, P.W., Srivatava, R.K. (2001) Hybrid SNCR-SCR technologies for NOx control: modeling and experiment. AIChE Journal, 47(11), 2603-2617.

Wenli, D., Dam-Johansen, K., Østergaard, K. (1989) The influence of additives on selective non-catalytic reduction of nitric oxide with NH3. ACHEMASIA.

Wenli, D., Dam-Johansen, K., Østergaard, K. (1991) Widening the temperature range of the thermal deNOx process. An experimental investigation. Symposium (International) on Combustion, 23(1), 297-303.

Werther, J., Saenger, M., Hartge, E.U., Ogada, T., Siagi, Z. (2000) Combustion of agricultural residues. Progress in Energy and Combustion Science, 26, 1−27.

Wright, J. (2003) Environmental Chemistry. Routledge, Taylor and Francis Group, London and New York, pp. 240–265.

Wünning, J.A. and Wünning, J.G. (1997) Flameless oxidation to reduce thermal no-formation. Progress in Energy and Combustion Science, 23(1), 81-94.

Yan, X., Che, D., Xu, T. (2005) Effect of rank, temperatures and inherent minerals on nitrogen emissions during coal pyrolysis in a fixed bed reactor. Fuel Processing Technology, 86(7), 739-756.

Zamansky, V.M., Ho, L., Maly, P.M., Seeker, W.R. (1996) Reburning promoted by nitrogen and sodium containing compounds. Symposium (International) on Combustion, 26(2), 2075-2082.

Zamansky, V.M., Lissianski, V.V., Maly, P.M., Ho, L., Rusli, D., Gardiner, W.C. (1999) Reactions of sodium species in the promoted SNCR process. Combustion and Flame, 117(4), 821-831.

Zanganeh, K.E. and Shafeen, A. (2007) A novel process integration, optimization and design approach for large-scale implementation of oxy-fired coal power plants with CO2 capture. International Journal of Greenhouse Gas Control, 1(1), 47-54

Zeldovich, Y.B. (1946) The oxidation of nitrogen in combustion and explosions. Acta Physicochem USSR, 577–628.

Zeng, Y., Li, K., Hughes, R., Luo, J. (2017) Corrosion Mechanisms and Materials Selection for the Construction of Flue Gas Component in Advanced Heat and Power Systems. Industrial & Engineering Chemistry Research, 56, 14141-14154.

Zhang, G., Xu, W., Wang, X., Yang, Y. (2015) Analysis and optimization of a coal-fired power plant under a proposed flue gas recirculation mode. Energy Conversion and Management, 102, 161-168.

Zhang, H. and Fletcher, T.H. (2001) Nitrogen transformations during secondary coal pyrolysis. Energy and Fuels, 15(6), 1512-1522.

Zhang, J., Kelly, K.E., Eddings, E.G., Wendt, J.O.L. (2011) CO2 effects on near field aerodynamic phenomena in 40 kW, co-axial, oxy-coal, turbulent diffusion flames. International Journal of Greenhouse Gas Control, 5S, S47-S57.

Zheng, Y., Jensen, P.A., Jensen, A.D., Sander, B., Junker, H. (2007) Ash transformation during co-firing coal and straw. Fuel, 86, 1008-1020.

Zhou, H., Wang, J., Zhou, B. (2015) Effect of Five Different Additives on the Sintering Behavior of Coal Ash Rich in Sodium under an Oxy-fuel Combustion Atmosphere. Energy and Fuels, 29, 5519-5533.

Zhou, K., Xu, M., Yu, D., Liu, X., Wen, C., Zhan, Z., Yao, H. (2010) Formation and Control of Fine Potassium-Enriched Particulates during Coal Combustion. Energy & Fuels, 24(12), 6266-6274.

APPENDIX 1 – KLIPPENSTEIN_GLARBORG.CTI (Klippenstein, et al., 2011)

```
units(length='cm', time='s', quantity='mol', act_energy='cal/mol')

ideal_gas(name='gas',
       elements="O H C N Ar",
       species="""AR     H     O     OH     H2     O2     HO2    H2O
              H2O2   CO     CO2    NH3    NH2    NH     N      N2H4
              N2H3   N2H2   H2NN   NNH    NO     NO2    NO3    N2O
              HNO    HON    HONO   HNO2   H2NO   NH2OH  HNOH   HONO2
              N2""",
       reactions='all',
       initial_state=state(temperature=300.0, pressure=OneAtm))

#-------------------------------------------------------------------------------
# Species data
#-------------------------------------------------------------------------------

species(name='AR',
      atoms='Ar:1',
      thermo=(NASA([200.00, 1000.00],
               [ 2.50000000E+00,  0.00000000E+00,  0.00000000E+00,
                 0.00000000E+00,  0.00000000E+00, -7.45375000E+02,
                 4.37967490E+00]),
            NASA([1000.00, 6000.00],
               [ 2.50000000E+00,  0.00000000E+00,  0.00000000E+00,
                 0.00000000E+00,  0.00000000E+00, -7.45375000E+02,
                 4.37967490E+00])),
      transport=gas_transport(geom='atom',
                        diam=3.33,
                        well_depth=136.5))

species(name='H',
      atoms='H:1',
      thermo=(NASA([200.00, 1000.00],
               [ 2.50000000E+00,  0.00000000E+00,  0.00000000E+00,
                 0.00000000E+00,  0.00000000E+00,  2.54736600E+04,
                -4.46682850E-01]),
            NASA([1000.00, 6000.00],
               [ 2.50000000E+00,  0.00000000E+00,  0.00000000E+00,
                 0.00000000E+00,  0.00000000E+00,  2.54736600E+04,
                -4.46682850E-01])),
      transport=gas_transport(geom='atom',
                        diam=2.05,
                        well_depth=145.0))

species(name='O',
      atoms='O:1',
      thermo=(NASA([200.00, 1000.00],
```

```
            [ 3.16826710E+00, -3.27931884E-03,  6.64306396E-06,
             -6.12806624E-09,  2.11265971E-12,  2.91222592E+04,
              2.05193346E+00]),
        NASA([1000.00, 6000.00],
            [ 2.54363697E+00, -2.73162486E-05, -4.19029520E-09,
              4.95481845E-12, -4.79553694E-16,  2.92260120E+04,
              4.92229457E+00])),
    transport=gas_transport(geom='atom',
                diam=2.75,
                well_depth=80.0))

species(name='OH',
    atoms='H:1 O:1',
    thermo=(NASA([200.00, 1000.00],
            [ 3.99198424E+00, -2.40106655E-03,  4.61664033E-06,
             -3.87916306E-09,  1.36319502E-12,  3.37165248E+03,
             -1.03814059E-01]),
        NASA([1000.00, 6000.00],
            [ 2.83853033E+00,  1.10741289E-03, -2.94000209E-07,
              4.20698729E-11, -2.42289890E-15,  3.70056220E+03,
              5.84513094E+00])),
    transport=gas_transport(geom='linear',
                diam=2.75,
                well_depth=80.0))

species(name='H2',
    atoms='H:2',
    thermo=(NASA([200.00, 1000.00],
            [ 2.34430290E+00,  7.98042480E-03, -1.94779170E-05,
              2.01569670E-08, -7.37602890E-12, -9.17924130E+02,
              6.83002180E-01]),
        NASA([1000.00, 6000.00],
            [ 2.93283050E+00,  8.26598020E-04, -1.46400570E-07,
              1.54098510E-11, -6.88796150E-16, -8.13055820E+02,
             -1.02431640E+00])),
    transport=gas_transport(geom='linear',
                diam=2.92,
                well_depth=38.0,
                polar=0.79,
                rot_relax=280.0))

species(name='O2',
    atoms='O:2',
    thermo=(NASA([200.00, 1000.00],
            [ 3.78245636E+00, -2.99673415E-03,  9.84730200E-06,
             -9.68129508E-09,  3.24372836E-12, -1.06394356E+03,
              3.65767573E+00]),
        NASA([1000.00, 6000.00],
            [ 3.66096083E+00,  6.56365523E-04, -1.41149485E-07,
              2.05797658E-11, -1.29913248E-15, -1.21597725E+03,
              3.41536184E+00])),
```

```
      transport=gas_transport(geom='linear',
                              diam=3.458,
                              well_depth=107.4,
                              polar=1.6,
                              rot_relax=3.8))

species(name='HO2',
      atoms='H:1 O:2',
      thermo=(NASA([200.00, 1000.00],
               [ 4.30178800E+00, -4.74902010E-03,  2.11579530E-05,
                -2.42759610E-08,  9.29206700E-12,  2.63190983E+02,
                 3.71587740E+00]),
            NASA([1000.00, 6000.00],
               [ 4.17226590E+00,  1.88120980E-03, -3.46292970E-07,
                 1.94685160E-11,  1.76091530E-16,  3.02010736E+01,
                 2.95697380E+00])),
      transport=gas_transport(geom='nonlinear',
                              diam=3.458,
                              well_depth=107.4,
                              rot_relax=1.0))

species(name='H2O',
      atoms='H:2 O:1',
      thermo=(NASA([200.00, 1000.00],
               [ 4.19863520E+00, -2.03640170E-03,  6.52034160E-06,
                -5.48792690E-09,  1.77196800E-12, -3.02937260E+04,
                -8.49009010E-01]),
            NASA([1000.00, 6000.00],
               [ 2.67703890E+00,  2.97318160E-03, -7.73768890E-07,
                 9.44335140E-11, -4.26899910E-15, -2.98858940E+04,
                 6.88255000E+00])),
      transport=gas_transport(geom='nonlinear',
                              diam=2.605,
                              well_depth=572.4,
                              dipole=1.844,
                              rot_relax=4.0))

species(name='H2O2',
      atoms='H:2 O:2',
      thermo=(NASA([200.00, 1000.00],
               [ 4.31515149E+00, -8.47390622E-04,  1.76404323E-05,
                -2.26762944E-08,  9.08950158E-12, -1.76843601E+04,
                 3.27373216E+00]),
            NASA([1000.00, 6000.00],
               [ 4.57977305E+00,  4.05326003E-03, -1.29844730E-06,
                 1.98211400E-10, -1.13968792E-14, -1.79847939E+04,
                 6.64969660E-01])),
      transport=gas_transport(geom='nonlinear',
                              diam=3.458,
                              well_depth=107.4,
                              rot_relax=3.8))
```

```
species(name='CO',
      atoms='C:1 O:1',
      thermo=(NASA([200.00, 1000.00],
               [ 2.71518561E+00,  2.06252743E-03, -9.98825771E-07,
                 2.30053008E-10, -2.03647716E-14, -1.41518724E+04,
                 7.81868772E+00]),
            NASA([1000.00, 3500.00],
               [ 3.57953347E+00, -6.10353680E-04,  1.01681433E-06,
                 9.07005884E-10, -9.04424499E-13, -1.43440860E+04,
                 3.50840928E+00])),
      transport=gas_transport(geom='linear',
                        diam=3.65,
                        well_depth=98.1,
                        polar=1.95,
                        rot_relax=1.8))

species(name='CO2',
      atoms='C:1 O:2',
      thermo=(NASA([200.00, 1000.00],
               [ 3.85746029E+00,  4.41437026E-03, -2.21481404E-06,
                 5.23490188E-10, -4.72084164E-14, -4.87591660E+04,
                 2.27163806E+00]),
            NASA([1000.00, 3500.00],
               [ 2.35677352E+00,  8.98459677E-03, -7.12356269E-06,
                 2.45919022E-09, -1.43699548E-13, -4.83719697E+04,
                 9.90105222E+00])),
      transport=gas_transport(geom='linear',
                        diam=3.763,
                        well_depth=244.0,
                        polar=2.65,
                        rot_relax=2.1))

species(name='NH3',
      atoms='H:3 N:1',
      thermo=(NASA([300.00, 1000.00],
               [ 2.20435200E+00,  1.01147600E-02, -1.46526500E-05,
                 1.44723500E-08, -5.32850900E-12, -6.52548800E+03,
                 8.12713800E+00]),
            NASA([1000.00, 5000.00],
               [ 2.46190400E+00,  6.05916600E-03, -2.00497700E-06,
                 3.13600300E-10, -1.93831700E-14, -6.49327000E+03,
                 7.47209700E+00])),
      transport=gas_transport(geom='nonlinear',
                        diam=2.92,
                        well_depth=481.0,
                        dipole=1.47,
                        rot_relax=10.0))

species(name='NH2',
      atoms='H:2 N:1',
```

```
    thermo=(NASA([300.00, 1000.00],
            [ 3.43249300E+00,  3.29954000E-03, -6.61360000E-06,
              8.59094700E-09, -3.57204700E-12,  2.17722800E+04,
              3.09011100E+00]),
         NASA([1000.00, 5000.00],
            [ 2.96131100E+00,  2.93269900E-03, -9.06360000E-07,
              1.61725700E-10, -1.20420000E-14,  2.19197700E+04,
              5.77787800E+00])),
    transport=gas_transport(geom='nonlinear',
                    diam=2.65,
                    well_depth=80.0,
                    polar=2.26,
                    rot_relax=4.0))

species(name='NH',
    atoms='H:1 N:1',
    thermo=(NASA([200.00, 1000.00],
            [ 3.49290840E+00,  3.11791970E-04, -1.48904840E-06,
              2.48164420E-09, -1.03569670E-12,  4.18942940E+04,
              1.84832770E+00]),
         NASA([1000.00, 6000.00],
            [ 2.78369290E+00,  1.32984290E-03, -4.24780470E-07,
              7.83485040E-11, -5.50444700E-15,  4.21345140E+04,
              5.74077980E+00])),
    transport=gas_transport(geom='linear',
                    diam=2.65,
                    well_depth=80.0,
                    rot_relax=4.0))

species(name='N',
    atoms='N:1',
    thermo=(NASA([300.00, 1000.00],
            [ 2.50307100E+00, -2.18001800E-05,  5.42052900E-08,
             -5.64756000E-11,  2.09990400E-14,  5.60989000E+04,
              4.16756600E+00]),
         NASA([1000.00, 5000.00],
            [ 2.45026800E+00,  1.06614600E-04, -7.46533700E-08,
              1.87965200E-11, -1.02598400E-15,  5.61160400E+04,
              4.44875800E+00])),
    transport=gas_transport(geom='atom',
                    diam=3.298,
                    well_depth=71.4))

species(name='N2H4',
    atoms='H:4 N:2',
    thermo=(NASA([300.00, 1000.00],
            [ 6.44260600E-02,  2.74973000E-02, -2.89945100E-05,
              1.74524000E-08, -4.42228200E-12,  1.04519200E+04,
              2.12778900E+01]),
         NASA([1000.00, 5000.00],
            [ 4.97731700E+00,  9.59551900E-03, -3.54763900E-06,
```

```
                6.12429900E-10, -4.02979500E-14,  9.34121900E+03,
               -2.96299000E+00])),
      transport=gas_transport(geom='nonlinear',
                        diam=4.23,
                        well_depth=205.0,
                        polar=4.26,
                        rot_relax=1.5))

species(name='N2H3',
      atoms='H:3 N:2',
      thermo=(NASA([300.00, 1000.00],
               [ 3.17420400E+00,  4.71590700E-03,  1.33486700E-05,
                -1.91968500E-08,  7.48756400E-12,  1.72727000E+04,
                 7.55722400E+00]),
            NASA([1000.00, 5000.00],
               [ 4.44184600E+00,  7.21427100E-03, -2.49568400E-06,
                 3.92056500E-10, -2.29895000E-14,  1.66422100E+04,
                -4.27520500E-01])),
      transport=gas_transport(geom='nonlinear',
                        diam=3.9,
                        well_depth=200.0,
                        rot_relax=1.0))

species(name='N2H2',
      atoms='H:2 N:2',
      thermo=(NASA([300.00, 1000.00],
               [ 1.61799900E+00,  1.30631200E-02, -1.71571200E-05,
                 1.60560800E-08, -6.09363900E-12,  2.46752600E+04,
                 1.37946700E+01]),
            NASA([1000.00, 5000.00],
               [ 3.37118500E+00,  6.03996800E-03, -2.30385400E-06,
                 4.06278900E-10, -2.71314400E-14,  2.41817200E+04,
                 4.98058500E+00])),
      transport=gas_transport(geom='nonlinear',
                        diam=3.798,
                        well_depth=71.4,
                        rot_relax=1.0))

species(name='H2NN',
      atoms='H:2 N:2',
      thermo=(NASA([300.00, 1695.00],
               [ 2.88544262E+00,  4.69495999E-03,  7.01983230E-07,
                -1.53359038E-09,  3.79345858E-13,  3.36030690E+04,
                 8.95096779E+00]),
            NASA([1695.00, 5000.00],
               [ 3.13531032E+00,  5.68632569E-03, -1.93983467E-06,
                 3.01290501E-10, -1.74978144E-14,  3.33678346E+04,
                 7.04815840E+00])),
      transport=gas_transport(geom='nonlinear',
                        diam=3.798,
                        well_depth=71.4,
```

```
                    rot_relax=1.0))

species(name='NNH',
      atoms='H:1 N:2',
      thermo=(NASA([200.00, 1000.00],
              [ 4.25474632E+00, -3.45098298E-03,  1.37788699E-05,
               -1.33263744E-08,  4.41023397E-12,  2.88323793E+04,
                3.28551762E+00]),
            NASA([1000.00, 6000.00],
              [ 3.42744423E+00,  3.23295234E-03, -1.17296299E-06,
                1.90508356E-10, -1.14491506E-14,  2.88067740E+04,
                6.39209233E+00])),
      transport=gas_transport(geom='nonlinear',
                    diam=3.798,
                    well_depth=71.4,
                    rot_relax=1.0))

species(name='NO',
      atoms='N:1 O:1',
      thermo=(NASA([200.00, 1000.00],
              [ 4.21859896E+00, -4.63988124E-03,  1.10443049E-05,
               -9.34055507E-09,  2.80554874E-12,  9.81823786E+03,
                2.28060952E+00]),
            NASA([1000.00, 6000.00],
              [ 3.26071234E+00,  1.19101135E-03, -4.29122646E-07,
                6.94481463E-11, -4.03295681E-15,  9.89456954E+03,
                6.36900469E+00])),
      transport=gas_transport(geom='linear',
                    diam=3.621,
                    well_depth=97.53,
                    polar=1.76,
                    rot_relax=4.0))

species(name='NO2',
      atoms='N:1 O:2',
      thermo=(NASA([200.00, 1000.00],
              [ 3.94403120E+00, -1.58542900E-03,  1.66578120E-05,
               -2.04754260E-08,  7.83505640E-12,  2.87409757E+03,
                6.31199190E+00]),
            NASA([1000.00, 6000.00],
              [ 4.88475400E+00,  2.17239550E-03, -8.28069090E-07,
                1.57475100E-10, -1.05108950E-14,  2.29397777E+03,
               -1.17416951E-01])),
      transport=gas_transport(geom='nonlinear',
                    diam=3.5,
                    well_depth=200.0,
                    rot_relax=1.0))

species(name='NO3',
      atoms='N:1 O:3',
      thermo=(NASA([200.00, 1000.00],
```

```
            [ 2.17359330E+00,  1.04902685E-02,  1.10472669E-05,
             -2.81561867E-08,  1.36583960E-11,  7.81290905E+03,
              1.46022090E+01]),
        NASA([1000.00, 6000.00],
            [ 7.48347702E+00,  2.57772064E-03, -1.00945831E-06,
              1.72314063E-10, -1.07154008E-14,  6.12990474E+03,
             -1.41618136E+01])),
    transport=gas_transport(geom='nonlinear',
                diam=4.175,
                well_depth=378.4,
                rot_relax=1.0))

species(name='N2O',
    atoms='N:2 O:1',
    thermo=(NASA([300.00, 1000.00],
            [ 2.54305800E+00,  9.49219300E-03, -9.79277500E-06,
              6.26384500E-09, -1.90182600E-12,  8.76510000E+03,
              9.51122200E+00]),
        NASA([1000.00, 5000.00],
            [ 4.71897700E+00,  2.87371400E-03, -1.19749600E-06,
              2.25055200E-10, -1.57533700E-14,  8.16581100E+03,
             -1.65725000E+00])),
    transport=gas_transport(geom='linear',
                diam=3.828,
                well_depth=232.4,
                rot_relax=1.0))

species(name='HNO',
    atoms='H:1 N:1 O:1',
    thermo=(NASA([200.00, 1000.00],
            [ 4.53525574E+00, -5.68543377E-03,  1.85198540E-05,
             -1.71881225E-08,  5.55818157E-12,  1.16110981E+04,
              1.74318356E+00]),
        NASA([1000.00, 6000.00],
            [ 3.16598124E+00,  2.99958892E-03, -3.94376786E-07,
             -3.85344089E-11,  7.07602668E-15,  1.17654289E+04,
              7.64513642E+00])),
    transport=gas_transport(geom='nonlinear',
                diam=3.492,
                well_depth=116.7,
                rot_relax=1.0))

species(name='HON',
    atoms='H:1 N:1 O:1',
    thermo=(NASA([300.00, 1671.00],
            [ 3.33656431E+00,  2.67682939E-03,  5.61801303E-07,
             -1.11362279E-09,  2.84076438E-13,  2.95979751E+04,
              5.96343188E+00]),
        NASA([1671.00, 5000.00],
            [ 3.78577430E+00,  2.86062728E-03, -1.02423922E-06,
              1.64463139E-10, -9.77943616E-15,  2.93319701E+04,
```

```
                3.12193293E+00])),
      transport=gas_transport(geom='nonlinear',
                        diam=3.492,
                        well_depth=116.7,
                        rot_relax=1.0))

species(name='HONO',
      atoms='H:1 N:1 O:2',
      thermo=(NASA([200.00, 1000.00],
               [ 3.21417090E+00,  8.12768690E-03,  1.66025590E-06,
                -9.52851820E-09,  4.87150580E-12, -1.07532370E+04,
                 9.82195040E+00]),
            NASA([1000.00, 6000.00],
               [ 5.79190180E+00,  3.65152120E-03, -1.29289360E-06,
                 2.06887160E-10, -1.23152540E-14, -1.15655890E+04,
                -4.05582330E+00])),
      transport=gas_transport(geom='nonlinear',
                        diam=3.828,
                        well_depth=232.4,
                        rot_relax=1.0))

species(name='HNO2',
      atoms='H:1 N:1 O:2',
      thermo=(NASA([300.00, 1500.00],
               [ 1.93483800E+00,  1.01003600E-02, -4.96461600E-06,
                 8.70112000E-10, -2.32413500E-15, -5.91571591E+03,
                 1.47282082E+01]),
            NASA([1500.00, 4000.00],
               [ 6.47963000E+00,  1.99527400E-03, -1.74038700E-07,
                -9.69587200E-11,  1.70148000E-14, -7.80950291E+03,
                -1.06771518E+01])))

species(name='H2NO',
      atoms='H:2 N:1 O:1',
      thermo=(NASA([300.00, 1500.00],
               [ 2.53059000E+00,  8.59603500E-03, -5.47103000E-06,
                 2.27624900E-09, -4.64807300E-13,  6.86803000E+03,
                 1.12665100E+01]),
            NASA([1500.00, 4000.00],
               [ 5.67334600E+00,  2.29883700E-03, -1.77444600E-07,
                -1.10348200E-10,  1.85976200E-14,  5.56932500E+03,
                -6.15354000E+00])),
      transport=gas_transport(geom='nonlinear',
                        diam=3.492,
                        well_depth=116.7,
                        rot_relax=1.0))

species(name='NH2OH',
      atoms='H:3 N:1 O:1',
      thermo=(NASA([300.00, 1412.00],
               [ 1.59842441E+00,  1.54722273E-02, -1.24132635E-05,
```

```
                5.50996715E-09, -1.00114333E-12, -6.34935610E+03,
                1.50585859E+01]),
            NASA([1412.00, 5000.00],
               [ 5.12276969E+00,  5.73428233E-03, -1.86277359E-06,
                2.78938290E-10, -1.57685159E-14, -7.42648110E+03,
               -3.34064363E+00])),
        transport=gas_transport(geom='nonlinear',
                        diam=3.492,
                        well_depth=116.7,
                        rot_relax=1.0))

species(name='HNOH',
        atoms='H:2 N:1 O:1',
        thermo=(NASA([300.00, 1500.00],
                [ 2.12527400E+00,  1.06628180E-02, -7.60258800E-06,
                 3.08164100E-09, -5.72649800E-13,  9.55354400E+03,
                 1.30967180E+01]),
            NASA([1500.00, 4000.00],
               [ 6.39613400E+00,  1.82106700E-03, -1.87089100E-07,
                -7.84447100E-11,  1.44485550E-14,  7.85961500E+03,
                -1.04047850E+01])),
        transport=gas_transport(geom='nonlinear',
                        diam=3.492,
                        well_depth=116.7,
                        rot_relax=1.0))

species(name='HONO2',
        atoms='H:1 N:1 O:3',
        thermo=(NASA([200.00, 1000.00],
                [ 1.69329154E+00,  1.90167702E-02, -8.25176697E-06,
                 -6.06113827E-09,  4.65236978E-12, -1.73882411E+04,
                 1.71839655E+01]),
            NASA([1000.00, 6000.00],
               [ 8.03098942E+00,  4.46958589E-03, -1.72459491E-06,
                 2.91556153E-10, -1.80102702E-14, -1.92821685E+04,
                -1.62616720E+01]))))

species(name='N2',
        atoms='N:2',
        thermo=(NASA([200.00, 1000.00],
                [ 3.53100528E+00, -1.23660988E-04, -5.02999433E-07,
                  2.43530612E-09, -1.40881235E-12, -1.04697628E+03,
                  2.96747038E+00]),
            NASA([1000.00, 6000.00],
               [ 2.95257637E+00,  1.39690040E-03, -4.92631603E-07,
                 7.86010195E-11, -4.60755204E-15, -9.23948688E+02,
                 5.87188762E+00])),
        transport=gas_transport(geom='linear',
                        diam=3.621,
                        well_depth=97.53,
                        polar=1.76,
```

```
                    rot_relax=4.0))

#-----------------------------------------------------------------------
# Reaction data
#-----------------------------------------------------------------------
#  ***************************************************************************
#  H2/O2 subset *
#  ***************************************************************************

# Reaction 1
reaction('H + O2 <=> O + OH', [3.600000e+15, -0.41, 16600.0])
#  RAS/GLA08a HES98

# Reaction 2
three_body_reaction('H + H + M <=> H2 + M', [7.000000e+17, -1.0, 0.0],
            efficiencies='H2:0.0 H2O:0.0 N2:0.0')
#  RAS/GLA08a COH/WES83

# Reaction 3
reaction('H + H + N2 <=> H2 + N2', [5.400000e+18, -1.3, 0.0])
#  RAS/GLA08a COH/WES83

# Reaction 4
reaction('H + H + H2 <=> H2 + H2', [1.000000e+17, -0.6, 0.0])
#  RAS/GLA08a COH/WES83

# Reaction 5
reaction('H + H + H2O <=> H2 + H2O', [1.000000e+19, -1.0, 0.0])
#  RAS/GLA08a COH/WES83

# Reaction 6
three_body_reaction('H + O + M <=> OH + M', [6.200000e+16, -0.6, 0.0],
            efficiencies='H2O:5.0')
#  RAS/GLA08a MIL/BOW89

# Reaction 7
falloff_reaction('H + O2 (+ M) <=> HO2 (+ M)',
            kf=[1.500000e+12, 0.6, 0.0],
            kf0=[6.370000e+20, -1.72, 520.0],
            efficiencies='H2:2.0 H2O:11.0 N2:1.0 O2:0.78',
            falloff=Troe(A=0.8, T3=1e-30, T1=1e+30))
#  RAS/GLA08a LI/DRY04

# Reaction 8
three_body_reaction('O + O + M <=> O2 + M', [1.900000e+13, 0.0, -1788.0],
            efficiencies='H2O:10.0 N2:1.5 O2:1.5')
#  RAS/GLA08a NBS86

# Reaction 9
reaction('O + H2 <=> OH + H', [3.800000e+12, 0.0, 7948.0],
       options='duplicate')
```

```
#  RAS/GLA08a CEC05

# Reaction 10
reaction('O + H2 <=> OH + H', [8.800000e+14, 0.0, 19175.0],
       options='duplicate')
#  RAS/GLA08a CEC05

# Reaction 11
reaction('OH + OH <=> O + H2O', [4.300000e+03, 2.7, -1822.0])
#  RAS/GLA08a SRI/MIC06

# Reaction 12
three_body_reaction('OH + H + M <=> H2O + M', [4.500000e+22, -2.0, 0.0],
              efficiencies='AR:0.38 H2:0.73 H2O:12.0')
#  RAS/GLA08a CON/WES04

# Reaction 13
reaction('OH + H2 <=> H + H2O', [2.100000e+08, 1.52, 3449.0])
#  RAS/GLA08a MIC92

# Reaction 14
reaction('H2 + O2 <=> HO2 + H', [7.400000e+05, 2.433, 53502.0])
#  RAS/GLA08a MIC/WAG00

# Reaction 15
reaction('HO2 + H <=> OH + OH', [8.400000e+13, 0.0, 400.0])
#  RAS/GLA08a RAS/GLA08a

# Reaction 16
reaction('HO2 + H <=> H2O + O', [1.400000e+12, 0.0, 0.0])
#  RAS/GLA08a CEC05

# Reaction 17
reaction('HO2 + O <=> OH + O2', [1.600000e+13, 0.0, -445.0])
#  RAS/GLA08a CEC05

# Reaction 18
reaction('HO2 + OH <=> H2O + O2', [3.600000e+21, -2.1, 9000.0],
       options='duplicate')
#  RAS/GLA08a RAS/GLA08a

# Reaction 19
reaction('HO2 + OH <=> H2O + O2', [2.000000e+15, -0.6, 0.0],
       options='duplicate')

# Reaction 20
reaction('HO2 + OH <=> H2O + O2', [-2.200000e+96, -24.0, 49000.0],
       options=['negative_A', 'duplicate'])

# Reaction 21
reaction('HO2 + HO2 <=> H2O2 + O2', [1.900000e+11, 0.0, -1408.0],
```

```
       options='duplicate')
#  RAS/GLA08a KAP/TROE02

# Reaction 22
reaction('HO2 + HO2 <=> H2O2 + O2', [1.000000e+14, 0.0, 11034.0],
       options='duplicate')

# Reaction 23
falloff_reaction('H2O2 (+ M) <=> OH + OH (+ M)',
            kf=[4.000000e+11, 0.0, 37137.0],
            kf0=[2.291000e+16, 0.0, 43638.0],
            efficiencies='AR:0.64 H2:2.5 H2O:12.0',
            falloff=Troe(A=0.5, T3=1e-30, T1=1e+30, T2=1e+30))
#  RAS/GLA08a KAP/TRO02
#  (Fc=0.5)

# Reaction 24
reaction('H2O2 + H <=> H2O + OH', [1.000000e+13, 0.0, 3580.0])
#  RAS/GLA08a CEC05

# Reaction 25
reaction('H2O2 + H <=> HO2 + H2', [1.700000e+12, 0.0, 3760.0])
#  RAS/GLA08a CEC05

# Reaction 26
reaction('H2O2 + O <=> HO2 + OH', [9.600000e+06, 2.0, 3970.0])
#  RAS/GLA08a NBS86,MAR99,LI/DRY04

# Reaction 27
reaction('H2O2 + OH <=> H2O + HO2', [1.900000e+12, 0.0, 427.0],
       options='duplicate')
#  RAS/GLA08a HIP/TRO95

# Reaction 28
reaction('H2O2 + OH <=> H2O + HO2', [1.600000e+18, 0.0, 29410.0],
       options='duplicate')
#  RAS/GLA08a HIP/TRO95
#  ********************************************************************************
#  CO/CO2 subset *
#  ********************************************************************************

# Reaction 29
falloff_reaction('CO + O (+ M) <=> CO2 (+ M)',
            kf=[1.800000e+10, 0.0, 2384.0],
            kf0=[1.350000e+24, -2.79, 4191.0],
            efficiencies='CO:1.9 CO2:3.8 H2:2.5 H2O:12.0',
            falloff=Troe(A=1.0, T3=1e-30, T1=1e+30, T2=1e+30))
#  RAS/GLA08a MUL/DRY99

# Reaction 30
reaction('CO + O2 <=> CO2 + O', [4.700000e+12, 0.0, 60500.0])
```

```
#  RAS/GLA08a BAC/MAC05

# Reaction 31
reaction('CO + HO2 <=> CO2 + OH', [1.600000e+05, 2.18, 17943.0])
#  RAS/GLA08a YOU/KLI07

# Reaction 32
reaction('CO + OH <=> CO2 + H', [8.000000e+10, 0.0, 0.0],
       options='duplicate')
#  RAS/GLA08a (1 bar, 300<T<2000K)

# Reaction 33
reaction('CO + OH <=> CO2 + H', [8.800000e+05, 1.77, 954.0],
       options='duplicate')
#  RAS/GLA08a (1 bar, 300<T<2000K)
#  ************************************************************************
#  H/N/O subset
#  ************************************************************************

# Reaction 34
three_body_reaction('NH3 + M <=> NH2 + H + M', [2.200000e+16, 0.0, 93470.0])
#  SKR/GLA04 DAV/HAN90

# Reaction 35
reaction('NH3 + H <=> NH2 + H2', [6.400000e+05, 2.39, 10171.0])
#  SKR/GLA04 MIC/SUT86

# Reaction 36
reaction('NH3 + O <=> NH2 + OH', [2.800000e+02, 3.29, 4471.0])
#  KLIMIC09

# Reaction 37
reaction('NH3 + OH <=> NH2 + H2O', [2.000000e+06, 2.04, 566.0])
#  SKR/GLA04 SAL/HAN84

# Reaction 38
reaction('NH3 + HO2 <=> NH2 + H2O2', [3.000000e+11, 0.0, 22000.0])
#  SKR/GLA04 JAM est

# Reaction 39
reaction('NH2 + H <=> NH + H2', [7.200000e+05, 2.32, 799.0])
#  SKR/GLA04 LIN/PAG95

# Reaction 40
reaction('NH2 + O <=> HNO + H', [6.600000e+13, 0.0, 0.0])
#  TIA/QI09 DRA/WAG84,ADA/PHI94

# Reaction 41
reaction('NH2 + O <=> NH + OH', [7.000000e+12, 0.0, 0.0],
       options='duplicate')
#  TIA/QI09 INO/WAS99,DRA/WAG84,ADA/PHI94
```

```
# Reaction 42
reaction('NH2 + O <=> NH + OH', [8.600000e-01, 4.01, 1673.0],
       options='duplicate')

# Reaction 43
reaction('NH2 + OH <=> NH + H2O', [3.300000e+06, 1.949, -217.0])
#  KLIMIC09,adj

# Reaction 44
reaction('NH2 + HO2 <=> H2NO + OH', [5.000000e+13, 0.0, 0.0])
#  SKR/GLA04 JAM est

# Reaction 45
reaction('NH2 + HO2 <=> NH3 + O2', [9.200000e+05, 1.94, -1152.0])
#  SKR/GLA04 DEA/BOZ00

# Reaction 46
reaction('NH2 + O2 <=> H2NO + O', [2.600000e+11, 0.4872, 29050.0])
#  pw

# Reaction 47
reaction('NH2 + O2 <=> HNO + OH', [2.900000e-02, 3.764, 18185.0])
#  pw

# Reaction 48
reaction('NH2 + NH2 <=> NH3 + NH', [5.600000e+00, 3.53, 552.0])
#  KLIMIC09

# Reaction 49
reaction('NH2 + NH <=> NH3 + N', [9.600000e+03, 2.46, 107.0])
#  KLIMIC09

# Reaction 50
reaction('NH2 + N <=> N2 + H + H', [7.000000e+13, 0.0, 0.0])
#  SKR/GLA04 WHY/PHI83

# Reaction 51
reaction('NH2 + HNO <=> NH3 + NO', [3.600000e+06, 1.63, -1250.0])
#  SKR/GLA04 LIN96

# Reaction 52
reaction('NH2 + NO <=> N2 + H2O', [1.300000e+16, -1.25, 0.0],
       options='duplicate')
#  MILKLI00,fit

# Reaction 53
reaction('NH2 + NO <=> N2 + H2O', [-3.100000e+13, -0.48, 1180.0],
       options=['negative_A', 'duplicate'])

# Reaction 54
```

```
reaction('NH2 + NO <=> NNH + OH', [3.100000e+13, -0.48, 1180.0])
#  MILKLI00,fit

# Reaction 55
reaction('NH2 + NO2 <=> N2O + H2O', [3.000000e+14, -0.77, 242.0])
#  SONG

# Reaction 56
reaction('NH2 + NO2 <=> H2NO + NO', [1.300000e+15, -0.77, 242.0])
#  SONG

# Reaction 57
reaction('NH2 + HONO <=> NH3 + NO2', [7.100000e+01, 3.02, -4940.0])
#  SKR/GLA04 LIN96

# Reaction 58
reaction('NH + H <=> N + H2', [3.000000e+13, 0.0, 0.0])
#  SKR/GLA04 DAV/HAN90,rv

# Reaction 59
reaction('NH + O <=> NO + H', [9.200000e+13, 0.0, 0.0])
#  SKR/GLA04 CEC94

# Reaction 60
reaction('NH + OH <=> HNO + H', [3.200000e+14, -0.376, -46.0])
#  KLIMIC09

# Reaction 61
reaction('NH + OH <=> N + H2O', [1.600000e+07, 1.733, -576.0])
#  KLIMIC09

# Reaction 62
reaction('NH + O2 <=> HNO + O', [4.600000e+05, 2.0, 6500.0])
#  SKR/GLA04 MIL/MEL92

# Reaction 63
reaction('NH + O2 <=> NO + OH', [1.300000e+06, 1.5, 100.0])
#  SKR/GLA04 MIL/MEL92

# Reaction 64
reaction('NH + NH <=> NH2 + N', [5.700000e-01, 3.88, 342.0])
#  KLIMIC09

# Reaction 65
reaction('NH + N <=> N2 + H', [3.000000e+13, 0.0, 0.0])
#  SKR/GLA04 JAM est

# Reaction 66
reaction('NH + NO <=> N2O + H', [1.800000e+14, -0.351, -244.0])
#  pw
```

```
# Reaction 67
reaction('NH + NO <=> N2 + OH', [2.700000e+12, -0.0721, -512.0])
#  pw

# Reaction 68
reaction('NH + HONO <=> NH2 + NO2', [1.000000e+13, 0.0, 0.0])
#  SKR/GLA04 JAM est

# Reaction 69
reaction('NH + NO2 <=> N2O + OH', [4.100000e+12, 0.0, 0.0])
#  HAR/PHI86

# Reaction 70
reaction('NH + NO2 <=> HNO + NO', [5.900000e+12, 0.0, 0.0])
#  HAR/PHI86

# Reaction 71
reaction('N + OH <=> NO + H', [3.800000e+13, 0.0, 0.0])
#  SKR/GLA04 FLO/HAN77,HOW/SMI80

# Reaction 72
reaction('N + O2 <=> NO + O', [6.400000e+09, 1.0, 6280.0])
#  SKR/GLA04 BAU/DRY73

# Reaction 73
reaction('N + NO <=> N2 + O', [2.100000e+13, 0.0, 0.0])
#  TIA/QI09 CEC05

# Reaction 74
reaction('NNH <=> N2 + H', [1.000000e+09, 0.0, 0.0])
#  pw

# Reaction 75
reaction('NNH + H <=> N2 + H2', [1.000000e+14, 0.0, 0.0])
#  SKR/GLA04 JAM est

# Reaction 76
reaction('NNH + O <=> N2O + H', [1.900000e+14, -0.274, -22.0])
#  pw

# Reaction 77
reaction('NNH + O <=> N2 + OH', [1.200000e+13, 0.145, -217.0])
#  pw

# Reaction 78
reaction('NNH + O <=> NH + NO', [5.200000e+11, 0.381, -409.0])
#  pw

# Reaction 79
reaction('NNH + OH <=> N2 + H2O', [5.000000e+13, 0.0, 0.0])
#  SKR/GLA04 JAM est
```

```
# Reaction 80
reaction('NNH + O2 <=> N2 + HO2', [5.600000e+14, -0.385, -13.0])
#  pw

# Reaction 81
reaction('NNH + NH <=> N2 + NH2', [5.000000e+13, 0.0, 0.0])
#  SKR/GLA04 JAM est

# Reaction 82
reaction('NNH + NH2 <=> N2 + NH3', [5.000000e+13, 0.0, 0.0])
#  SKR/GLA04 JAM est

# Reaction 83
reaction('NNH + NO <=> N2 + HNO', [5.000000e+13, 0.0, 0.0])
#  SKR/GLA04 JAM est

# Reaction 84
falloff_reaction('NH2 + NH2 (+ M) <=> N2H4 (+ M)',
            kf=[5.600000e+14, -0.414, 66.0],
            kf0=[1.600000e+34, -5.49, 1987.0],
            falloff=Troe(A=0.31, T3=1e-30, T1=1e+30, T2=1e+30))
#  KLIMIC09
#  (Fc=0.31) ??

# Reaction 85
reaction('N2H4 + H <=> N2H3 + H2', [7.000000e+12, 0.0, 2500.0])
#  SKR/GLA04 VAG95

# Reaction 86
reaction('N2H4 + O <=> N2H2 + H2O', [4.400000e+11, 0.0, -1270.0])
#  SKR/GLA04 VAG96

# Reaction 87
reaction('N2H4 + O <=> N2H3 + OH', [6.700000e+08, 1.5, 2851.0])
#  SKR/GLA04 DEA/BOZ00

# Reaction 88
reaction('N2H4 + OH <=> N2H3 + H2O', [4.000000e+13, 0.0, 0.0])
#  SKR/GLA04 HAR/ATK79

# Reaction 89
reaction('N2H4 + NH2 <=> N2H3 + NH3', [3.900000e+12, 0.0, 1500.0])
#  SKR/GLA04 GEH/WAG71,JAM est

# Reaction 90
reaction('N2H3 <=> N2H2 + H', [3.600000e+47, -10.38, 69009.0])
#  SKR/GLA04 DEA/BOZ00 1ATM N2 600-2500K

# Reaction 91
reaction('NH2 + NH2 <=> N2H3 + H', [1.200000e+12, -0.03, 10084.0])
```

```
#  SKR/GLA04 DEA/BOZ00 1 ATM N2 !

# Reaction 92
reaction('N2H3 + H <=> N2H2 + H2', [2.400000e+08, 1.5, -10.0])
#  SKR/GLA04 DEA/BOZ00

# Reaction 93
reaction('N2H3 + O <=> N2H2 + OH', [1.700000e+08, 1.5, -646.0])
#  SKR/GLA04 DEA/BOZ00

# Reaction 94
reaction('N2H3 + O <=> NH2 + HNO', [3.000000e+13, 0.0, 0.0])
#  SKR/GLA04 DEA/BOZ00

# Reaction 95
reaction('N2H3 + O => NH2 + NO + H', [3.000000e+13, 0.0, 0.0])
#  SKR/GLA04 DEA/BOZ00

# Reaction 96
reaction('N2H3 + OH <=> N2H2 + H2O', [1.200000e+06, 2.0, -1192.0])
#  SKR/GLA04 DEA/BOZ00

# Reaction 97
reaction('N2H3 + OH <=> H2NN + H2O', [3.000000e+13, 0.0, 0.0])
#  SKR/GLA04 DEA/BOZ00

# Reaction 98
reaction('N2H3 + OH <=> NH3 + HNO', [1.000000e+12, 0.0, 15000.0])
#  SKR/GLA04 JAM est

# Reaction 99
reaction('N2H3 + HO2 <=> N2H2 + H2O2', [1.400000e+04, 2.69, -1600.0])
#  SKR/GLA04 DEA/BOZ00

# Reaction 100
reaction('N2H3 + HO2 <=> N2H4 + O2', [9.200000e+05, 1.94, 2126.0])
#  SKR/GLA04 DEA/BOZ00

# Reaction 101
reaction('N2H3 + NH2 <=> N2H2 + NH3', [9.200000e+05, 1.94, -1152.0])
#  SKR/GLA04 DEA/BOZ00

# Reaction 102
reaction('N2H3 + NH2 <=> H2NN + NH3', [3.000000e+13, 0.0, 0.0])
#  SKR/GLA04 DEA/BOZ00

# Reaction 103
reaction('N2H3 + NH <=> N2H2 + NH2', [2.000000e+13, 0.0, 0.0])
#  SKR/GLA04 JAM est

# Reaction 104
```

```
reaction('NH2 + NH <=> N2H2 + H', [4.300000e+14, -0.272, -77.0])
#  KLIMIC09

# Reaction 105
reaction('NH2 + NH2 <=> N2H2 + H2', [1.700000e+08, 1.62, 11783.0])
#  KLIMIC09

# Reaction 106
three_body_reaction('N2H2 + M <=> NNH + H + M', [1.900000e+27, -3.05, 66107.0],
                    efficiencies='H2O:7.0')
#  SKR/GLA04 DEA/BOZ00 M=N2

# Reaction 107
reaction('N2H2 + H <=> NNH + H2', [8.500000e+04, 2.63, 230.0])
#  SKR/GLA04 LIN/PAG96

# Reaction 108
reaction('N2H2 + O <=> NNH + OH', [3.300000e+08, 1.5, 497.0])
#  SKR/GLA04 DEA/BOZ00

# Reaction 109
reaction('N2H2 + O <=> NH2 + NO', [1.000000e+13, 0.0, 0.0])
#  SKR/GLA04 JAM est

# Reaction 110
reaction('N2H2 + OH <=> NNH + H2O', [5.900000e+01, 3.4, 1360.0])
#  SKR/GLA04 LIN/PAG96

# Reaction 111
reaction('N2H2 + NH2 <=> NNH + NH3', [8.800000e-02, 4.05, 1610.0])
#  SKR/GLA04 LIN/PAG96

# Reaction 112
reaction('N2H2 + NH <=> NNH + NH2', [2.400000e+06, 2.0, -1192.0])
#  SKR/GLA04 DEA/BOZ00

# Reaction 113
reaction('N2H2 + NO <=> N2O + NH2', [4.000000e+12, 0.0, 11922.0])
#  SKR/GLA04 DEA/BOZ00

# Reaction 114
reaction('NH2 + NH2 <=> H2NN + H2', [7.200000e+04, 1.88, 8802.0])
#  KLIMIC09

# Reaction 115
reaction('H2NN <=> NNH + H', [3.400000e+26, -4.83, 46228.0])
#  SKR/GLA04 DEA/BOZ00 1 ATM

# Reaction 116
reaction('H2NN + H <=> NNH + H2', [4.800000e+08, 1.5, -894.0])
#  SKR/GLA04 DEA/BOZ00
```

```
# Reaction 117
reaction('H2NN + H <=> N2H2 + H', [7.000000e+13, 0.0, 0.0])
#  SKR/GLA04 DEA/BOZ00

# Reaction 118
reaction('H2NN + O <=> NNH + OH', [3.300000e+08, 1.5, -894.0])
#  SKR/GLA04 DEA/BOZ00

# Reaction 119
reaction('H2NN + O <=> NH2 + NO', [7.000000e+13, 0.0, 0.0])
#  SKR/GLA04 DEA/BOZ00

# Reaction 120
reaction('H2NN + OH <=> NNH + H2O', [2.400000e+06, 2.0, -1192.0])
#  SKR/GLA04 DEA/BOZ00

# Reaction 121
reaction('H2NN + OH => NH2 + NO + H', [2.000000e+12, 0.0, 0.0])
#  SKR/GLA04 DEA/BOZ00

# Reaction 122
reaction('H2NN + HO2 => NH2 + NO + OH', [9.000000e+12, 0.0, 0.0])
#  SKR/GLA04 DEA/BOZ00

# Reaction 123
reaction('H2NN + HO2 <=> NNH + H2O2', [2.900000e+04, 2.69, -1600.0])
#  SKR/GLA04 DEA/BOZ00

# Reaction 124
reaction('H2NN + O2 <=> NH2 + NO2', [1.500000e+12, 0.0, 5961.0])
#  SKR/GLA04 DEA/BOZ00

# Reaction 125
reaction('H2NN + NH2 <=> NNH + NH3', [1.800000e+06, 1.94, -1152.0])
#  SKR/GLA04 DEA/BOZ00

# Reaction 126
three_body_reaction('H2NO + M <=> HNO + H + M', [2.800000e+24, -2.83, 64915.0],
                    efficiencies='H2O:10.0')
#  SKR/GLA04 DEA/BOZ00

# Reaction 127
three_body_reaction('H2NO + M <=> HNOH + M', [1.100000e+29, -4.0, 44000.0],
                    efficiencies='H2O:10.0')
#  SKR/GLA04 DEA/BOZ00

# Reaction 128
reaction('H2NO + H <=> HNO + H2', [3.000000e+07, 2.0, 2000.0])
#  SKR/GLA04 JAM est
```

```
# Reaction 129
reaction('H2NO + H <=> NH2 + OH', [5.000000e+13, 0.0, 0.0])
#  SKR/GLA04 JAM est

# Reaction 130
reaction('H2NO + O <=> HNO + OH', [3.000000e+07, 2.0, 2000.0])
#  SKR/GLA04 JAM est

# Reaction 131
reaction('H2NO + OH <=> HNO + H2O', [2.000000e+07, 2.0, 1000.0])
#  SKR/GLA04 JAM est

# Reaction 132
reaction('H2NO + HO2 <=> HNO + H2O2', [2.900000e+04, 2.69, -1600.0])
#  SKR/GLA04 DEA/BOZ00

# Reaction 133
reaction('H2NO + O2 <=> HNO + HO2', [3.000000e+12, 0.0, 25000.0])
#  SKR/GLA04 JAM est

# Reaction 134
reaction('H2NO + NH2 <=> HNO + NH3', [3.000000e+12, 0.0, 1000.0])
#  SKR/GLA04 JAM est

# Reaction 135
reaction('H2NO + NO <=> HNO + HNO', [2.000000e+04, 2.0, 13000.0])
#  SKR/GLA04 JAM est

# Reaction 136
reaction('H2NO + NO2 <=> HONO + HNO', [6.000000e+11, 0.0, 2000.0])
#  SKR/GLA04 JAM est

# Reaction 137
falloff_reaction('NH2OH (+ M) <=> NH2 + OH (+ M)',
            kf=[1.400000e+20, -1.31, 64080.0],
            kf0=[5.400000e+37, -5.96, 66783.0],
            falloff=Troe(A=0.31, T3=1e-30, T1=1e+30, T2=1e+30))
#  KLIMIC09

# Reaction 138
reaction('NH2OH + H <=> HNOH + H2', [4.800000e+08, 1.5, 6249.0])
#  DB HTRANS

# Reaction 139
reaction('NH2OH + H <=> H2NO + H2', [2.400000e+08, 1.5, 5067.0])
#  DB HTRANS

# Reaction 140
reaction('NH2OH + O <=> HNOH + OH', [3.300000e+08, 1.5, 3865.0])
#  DB HTRANS
```

```
# Reaction 141
reaction('NH2OH + O <=> H2NO + OH', [1.700000e+08, 1.5, 3010.0])
#  DB HTRANS

# Reaction 142
reaction('NH2OH + OH <=> HNOH + H2O', [1.500000e+04, 2.61, -3537.0])
#  KLIMIC09

# Reaction 143
reaction('NH2OH + OH <=> H2NO + H2O', [1.500000e+05, 2.28, -1296.0])
#  KLIMIC09

# Reaction 144
reaction('NH2OH + NH2 <=> HNOH + NH3', [1.100000e-01, 4.0, -97.0])
#  KLIMIC09

# Reaction 145
reaction('NH2OH + NH2 <=> H2NO + NH3', [9.500000e+00, 3.42, -1013.0])
#  KLIMIC09

# Reaction 146
reaction('NH2OH + NH <=> HNOH + NH2', [2.900000e-03, 4.4, 1564.0])
#  KLIMIC09

# Reaction 147
reaction('NH2OH + NH <=> H2NO + NH2', [1.500000e-03, 4.6, 2424.0])
#  KLIMIC09

# Reaction 148
reaction('NH2OH + HO2 <=> HNOH + H2O2', [2.900000e+04, 2.69, 9557.0])
#  DB HTRANS

# Reaction 149
reaction('NH2OH + HO2 <=> H2NO + H2O2', [1.400000e+04, 2.69, 6418.0])
#  DB HTRANS

# Reaction 150
three_body_reaction('HNOH + M <=> HNO + H + M', [2.000000e+24, -2.84, 58934.0],
                    efficiencies='H2O:10.0')
#  SKR/GLA04 DEA/BOZ00

# Reaction 151
reaction('HNOH + H <=> NH2 + OH', [4.000000e+13, 0.0, 0.0])
#  SKR/GLA04 DEA/BOZ00

# Reaction 152
reaction('HNOH + H <=> HNO + H2', [4.800000e+08, 1.5, 378.0])
#  SKR/GLA04 DEA/BOZ00

# Reaction 153
reaction('HNOH + O <=> HNO + OH', [7.000000e+13, 0.0, 0.0],
```

```
       options='duplicate')
#  SKR/GLA04 DEA/BOZ00

# Reaction 154
reaction('HNOH + O <=> HNO + OH', [3.300000e+08, 1.5, -358.0],
       options='duplicate')
#  SKR/GLA04 DEA/BOZ00

# Reaction 155
reaction('HNOH + OH <=> HNO + H2O', [2.400000e+06, 2.0, -1192.0])
#  SKR/GLA04 DEA/BOZ00

# Reaction 156
reaction('HNOH + HO2 <=> HNO + H2O2', [2.900000e+04, 2.69, -1600.0])
#  SKR/GLA04 DEA/BOZ00
# HNOH+HO2=NH2OH+O2            2.9E04  2.690   -1600 ! SKR/GLA04 DEA/BOZ00

# Reaction 157
reaction('HNOH + O2 <=> HNO + HO2', [3.000000e+12, 0.0, 25000.0])
#  SKR/GLA04 JAM est

# Reaction 158
reaction('HNOH + NH2 <=> N2H3 + OH', [1.000000e+01, 3.46, -467.0])
#  SKR/GLA04 DEA/BOZ00

# Reaction 159
reaction('HNOH + NH2 <=> H2NN + H2O', [8.800000e+16, -1.08, 1113.0])
#  SKR/GLA04 DEA/BOZ00

# Reaction 160
reaction('HNOH + NH2 <=> NH3 + HNO', [1.800000e+06, 1.94, -1152.0])
#  SKR/GLA04 DEA/BOZ00

# Reaction 161
reaction('HNOH + NO2 <=> HONO + HNO', [6.000000e+11, 0.0, 2000.0])
#  SKR/GLA04 JAM est

# Reaction 162
reaction('HNO + H <=> NO + H2', [4.400000e+11, 0.72, 650.0])
#  SKR/GLA04 SOT/PAG92

# Reaction 163
reaction('HNO + O <=> NO + OH', [2.300000e+13, 0.0, 0.0])
#  SKR/GLA04 INO/WAS99

# Reaction 164
reaction('HNO + OH <=> NO + H2O', [3.600000e+13, 0.0, 0.0])
#  SKR/GLA04 BAU73

# Reaction 165
reaction('HNO + O2 <=> HO2 + NO', [2.000000e+13, 0.0, 16000.0])
```

```
#  SKR/GLA04 DEA/BOZ00

# Reaction 166
reaction('HNO + HNO <=> N2O + H2O', [9.000000e+08, 0.0, 3100.0])
#  SKR/GLA04 NBS91

# Reaction 167
reaction('HNO + NO2 <=> HONO + NO', [4.400000e+04, 2.64, 4040.0])
#  RAS/GLA08 MEB/LIN98

# Reaction 168
falloff_reaction('NO + H (+ M) <=> HNO (+ M)',
            kf=[1.500000e+15, -0.41, 0.0],
            kf0=[2.400000e+14, 0.206, -1550.0],
            efficiencies='N2:1.6',
            falloff=Troe(A=0.82, T3=1e-30, T1=1e+30, T2=1e+30))
#  RAS/GLA08 NBS91
#  RAS/GLA08 RIL/FON03
#  RAS/GLA08 Fc=0.82 (NBS91)
#  RAS/GLA08 RIL/FON03

# Reaction 169
falloff_reaction('NO + O (+ M) <=> NO2 (+ M)',
            kf=[1.300000e+15, -0.75, 0.0],
            kf0=[4.720000e+24, -2.87, 1550.0],
            efficiencies='AR:0.0',
            falloff=Troe(A=0.88, T3=1000.0, T1=10000.0, T2=1e+30))
#  RAS/GLA08 ALL/DRY97,NBS91
#  RAS/GLA08 ALL/DRY97 (Fc=0.95-1E-04*T)
#  RAS/GLA08a

# Reaction 170
falloff_reaction('NO + O (+ AR) <=> NO2 (+ AR)',
            kf=[1.300000e+15, -0.75, 0.0],
            kf0=[7.560000e+19, -1.41, 0.0],
            falloff=Troe(A=0.75, T3=1000.0, T1=100000.0, T2=1e+30))
#  RAS/GLA08aLL/DRY97,NBS91
#  RAS/GLA08 YAR/SUT91 (Fc=0.95-1E-04*T)
#  RAS/GLA08a

# Reaction 171
falloff_reaction('NO + OH (+ M) <=> HONO (+ M)',
            kf=[1.100000e+14, -0.3, 0.0],
            kf0=[3.392000e+23, -2.5, 0.0],
            falloff=Troe(A=0.75, T3=1e-30, T1=1e+30, T2=1e+30))
#  RAS/GLA08 FUL/TRO98
#  RAS/GLA08 FUL/TRO98 [M=He,T=400K]

# Reaction 172
reaction('NO + HO2 <=> NO2 + OH', [2.100000e+12, 0.0, -497.0])
#  RAS/GLA08 CEC05
```

```
# Reaction 173
reaction('NO2 + H <=> NO + OH', [1.300000e+14, 0.0, 362.0])
#  RAS/GLA08 KO/FON91

# Reaction 174
reaction('NO2 + O <=> NO + O2', [1.100000e+14, -0.52, 0.0])
#  RAS/GLA08 BEM/CLY74

# Reaction 175
falloff_reaction('NO2 + O (+ M) <=> NO3 (+ M)',
            kf=[3.500000e+12, 0.24, 0.0],
            kf0=[2.500000e+20, -1.5, 0.0],
            falloff=Troe(A=0.71, T3=1e-30, T1=1700.0, T2=1e+30))
#  RAS/GLA08 HAH/TRO00
#  RAS/GLA08 (M=N2)
#  RAS/GLA08 Fc=0.71*exp(-T/1700)

# Reaction 176
falloff_reaction('NO2 + OH (+ M) <=> HONO2 (+ M)',
            kf=[3.000000e+13, 0.0, 0.0],
            kf0=[2.938000e+25, -3.0, 0.0],
            falloff=Troe(A=0.4, T3=1e-30, T1=1e+30, T2=1e+30))
#  RAS/GLA08 TRO01
#  RAS/GLA08 Fc=0.4

# Reaction 177
reaction('NO2 + HO2 <=> HONO + O2', [1.900000e+00, 3.32, 3044.0])
#  RAS/GLA08a

# Reaction 178
reaction('NO2 + HO2 <=> HNO2 + O2', [1.900000e+01, 3.26, 4983.0])
#  RAS/GLA08a

# Reaction 179
reaction('NO2 + H2 <=> HONO + H', [1.300000e+04, 2.76, 29770.0])
#  RAS/GLA08 PAR/LIN98

# Reaction 180
reaction('NO2 + H2 <=> HNO2 + H', [2.400000e+00, 3.73, 32400.0])
#  RAS/GLA08a

# Reaction 181
reaction('NO2 + NO2 <=> NO + NO + O2', [4.500000e+12, 0.0, 27599.0])
#  RAS/GLA08 PAR/LIN98

# Reaction 182
reaction('NO2 + NO2 <=> NO3 + NO', [9.600000e+09, 0.73, 20900.0])
#  GLA/MIL98 NBS91

# Reaction 183
```

```
reaction('HONO + H <=> HNO + OH', [5.600000e+10, 0.86, 5000.0])
#  SKR/GLA04 HSU/MEL97

# Reaction 184
reaction('HONO + H <=> NO + H2O', [8.100000e+06, 1.89, 3850.0])
#  SKR/GLA04 HSU/MEL97

# Reaction 185
reaction('HONO + O <=> NO2 + OH', [1.200000e+13, 0.0, 5960.0])
#  SKR/GLA04 NBS91

# Reaction 186
reaction('HONO + OH <=> NO2 + H2O', [1.700000e+12, 0.0, -520.0])
#  RAS/GLA08 BUR/RAV92

# Reaction 187
reaction('HONO + NO2 <=> HONO2 + NO', [2.000000e+11, 0.0, 32700.0])
#  RAS/GLA08 PAR/LIN98

# Reaction 188
reaction('HONO + HONO <=> NO + NO2 + H2O', [3.500000e-01, 3.64, 12140.0])
#  RAS/GLA08 MEB/MEL98

# Reaction 189
falloff_reaction('HNO2 (+ M) <=> HONO (+ M)',
            kf=[2.500000e+14, 0.0, 32300.0],
            kf0=[3.100000e+18, 0.0, 31500.0],
            falloff=Troe(A=1.149, T3=1e-30, T1=3125.0, T2=1e+30))
#  RAS/GLA08a

# Reaction 190
reaction('HNO2 + O <=> NO2 + OH', [1.700000e+08, 1.5, 2000.0])
#  RAS/GLA08 DEA/BOZ00

# Reaction 191
reaction('HNO2 + OH <=> NO2 + H2O', [4.000000e+13, 0.0, 0.0])
#  RAS/GLA08a

# Reaction 192
reaction('NO3 + H <=> NO2 + OH', [6.000000e+13, 0.0, 0.0])
#  GLA/MIL98 BEC/SCH92

# Reaction 193
reaction('NO3 + O <=> NO2 + O2', [1.000000e+13, 0.0, 0.0])
#  GLA/MIL98 ATK/TRO92

# Reaction 194
reaction('NO3 + OH <=> NO2 + HO2', [1.400000e+13, 0.0, 0.0])
#  GLA/MIL98 ATK/TRO92

# Reaction 195
```

```
reaction('NO3 + HO2 <=> NO2 + O2 + OH', [1.500000e+12, 0.0, 0.0])
#  GLA/MIL98 BEC/SCH92

# Reaction 196
reaction('NO3 + NO2 <=> NO + NO2 + O2', [5.000000e+10, 0.0, 2940.0])
#  GLA/MIL98 DEM/RAV90

# Reaction 197
reaction('HONO2 + H <=> H2 + NO3', [5.600000e+08, 1.5, 16400.0])
#  RAS/GLA08 BOU/LIN97

# Reaction 198
reaction('HONO2 + H <=> H2O + NO2', [6.100000e+01, 3.3, 6285.0])
#  RAS/GLA08 BOU/LIN97

# Reaction 199
reaction('HONO2 + H <=> OH + HONO', [3.800000e+05, 2.3, 6976.0])
#  RAS/GLA08 BOU/LIN97

# Reaction 200
reaction('HONO2 + OH <=> H2O + NO3', [1.000000e+10, 0.0, -1240.0])
#  RAS/GLA08 LAM/BEN84

# Reaction 201
falloff_reaction('N2O (+ M) <=> N2 + O (+ M)',
                 kf=[1.300000e+12, 0.0, 62570.0],
                 kf0=[4.000000e+14, 0.0, 56600.0],
                 efficiencies='CO2:3.0 H2O:12.0 N2:1.7 O2:1.4')
#  SKR/GLA04 JOH/GLA92,ROH/HAN96

# Reaction 202
reaction('N2O + H <=> N2 + OH', [6.400000e+07, 1.835, 13492.0])
#  pw

# Reaction 203
reaction('N2O + O <=> NO + NO', [9.200000e+13, 0.0, 27679.0])
#  SKR/GLA04 MEA/AND00

# Reaction 204
reaction('N2O + O <=> N2 + O2', [3.700000e+12, 0.0, 15936.0])
#  SKR/GLA04 MEA/AND00

# Reaction 205
reaction('N2O + OH <=> N2 + HO2', [1.300000e-02, 4.72, 36560.0])
#  SKR/GLA04 MEB/LIN96

# Reaction 206
reaction('N2O + OH <=> HNO + NO', [1.200000e-04, 4.33, 25080.0])
#  SKR/GLA04 MEB/LIN96

# Reaction 207
```

```
reaction('N2O + NO <=> NO2 + N2', [5.300000e+05, 2.23, 46280.0])
#  SKR/GLA04 MEB/LIN96!
```

APPENDIX 2 – CSTR Model Script: FE-SNCR CSTR.PY

```
# -*- coding: utf-8 -*-
"""
Created on Wed Aug  7 13:34:55 2019

@author: Thomas
"""
import os
import sys
import cantera as ct
import cantera.ctml_writer

all_species = ct.Species.listFromFile('Klippenstein_Glarborg.cti')
species = []

for S in all_species:
    comp = S.composition
    species.append(S)

fe=ct.Species('Fe','Fe:1')
fe.thermo=ct.NasaPoly2(200.00, 6000.00, 100000.00, [1000.00, 3.26197970E+00,
                                    -1.05582533E-03, 5.92906998E-07, -1.07189455E-10,
                                    7.48064402E-15, 4.90969873E+04, 3.52443894E+00,
                                    1.70744428E+00, 1.06339224E-02, -2.76118171E-05,
                                    2.80917854E-08, -1.01219824E-11, 4.91843725E+04,
                                    9.80811099E+00])
species.append(fe)

fenh2=ct.Species('FeNH2','Fe:1, N:1, H:2')
fenh2.thermo=ct.NasaPoly2(200.00, 6000.00, 100000.00, [1000.00, 3.26197970E+00,
                                    -1.05582533E-03, 5.92906998E-07, -1.07189455E-10,
                                    7.48064402E-15, 4.90969873E+04, 3.52443894E+00,
                                    1.70744428E+00, 1.06339224E-02, -2.76118171E-05,
                                    2.80917854E-08, -1.01219824E-11, 4.91843725E+04,
                                    9.80811099E+00])
species.append(fenh2)


species_names = {S.name for S in species}
#print('Species: {0}'.format(', '.join(S.name for S in species)))

all_reactions = ct.Reaction.listFromFile('Glarborg_Klippenstein_ck.cti')
reactions = []

#print('\nReactions:')
for R in all_reactions:
    if not all(reactant in species_names for reactant in R.reactants):
        continue

    if not all(product in species_names for product in R.products):
```

```
      continue
   reactions.append(R)

#Fe-based additive reactions
   ra1=ct.Reaction.fromCti('''reaction('NH3 + O + Fe <=> Fe + NH2 + OH',
                    [(1.87, 'm/s'), 0, (88336, 'J/mol')])''')
   reactions.append(ra1)

   ra2=ct.Reaction.fromCti('''reaction('Fe + NH2 + O2 <=> NO + H2O + Fe',
                    [(3.43E9, 'mol/m2/s'), 0, (0, 'J/mol')])''')
   reactions.append(ra2)

   ra3=ct.Reaction.fromCti('''reaction('Fe + NH2 + NO  <=> N2 + H2O + Fe',
                    [(2.77E15, 'm/s'), 0, (109928, 'J/mol')])''')
   reactions.append(ra3)


#    print(R.equation)

gas=ct.Solution(thermo='IdealGas', kinetics='GasKinetics',
            species=species, reactions=reactions)

p=100000
T=1800
gas.TPX=T,p,'''NO:500, NH3:250, N2:766000, O2:97000, CO2:92000,
          H2O:44000, CO:500, Fe:4500'''


upstream = ct.Reservoir(gas)

cstr = ct.IdealGasReactor(gas)

cstr.volume = 0.1256

env = ct.Reservoir(gas)

w = ct.Wall(cstr, env, A=1.256, U=0.02)

sccm = 1.54e6
vdot = sccm * 1.0e-6/60.0 * ((ct.one_atm / gas.P) * ( gas.T / 273.15)) # m^3/s
mdot = gas.density * vdot
mfc = ct.MassFlowController(upstream, cstr, mdot=mdot)

downstream = ct.Reservoir(gas)

v = ct.Valve(cstr, downstream, K=1000)

network = ct.ReactorNet([cstr])

t = 0.0
dt   = 1.0e-4
```

```
states = ct.SolutionArray(gas, extra=['t'])
while t < 10.0e-0:
   t += dt
   network.advance(t)
   states.append(cstr.thermo.state, t=t)

if __name__ == '__main__':
   print(__doc__)
   try:
      import matplotlib.pyplot as plt
      plt.figure(1)
      plt.plot(states.t, states('NO','NH3').X)
      plt.legend(('NO','NH3'))
      plt.title('Mole Fractions')
      plt.show()
#       plt.figure(2)
#       plt.plot(states.t, states('NH2').X)
#       plt.legend(('NH2'))
#       plt.title('Mole Fraction of NH2')
#       plt.show()
#       plt.figure(3)
      plt.figure(4)
      plt.plot(states.t, ((0.0005-states('NO').X)/0.0005))
      plt.title('NO Reduction')
      plt.show()
#       plt.figure(7)
#       plt.plot(states.t, states('NNH', 'NH').X)
#       plt.legend(('NNH', 'NH'))
#       plt.title('Mole Fractions')
#       plt.show()
      plt.figure(9)
      plt.plot(states.t, states.T)
      plt.title('Temperature')
      plt.show()
   except ImportError:
      print('Matplotlib not found. Unable to plot results.')

#element = 'N'

#diagram = ct.ReactionPathDiagram(gas, element)
#diagram.title = 'Reaction path diagram following {0}'.format(element)
#diagram.label_threshold = 0.0000000000000001
#diagram.threshold = 1e-10
#diagram.show_details=True
#diagram.scale = 1

#dot_file = 'rxnpath.dot'
#img_file = 'rxnpath.png'
#img_path = os.path.join(os.getcwd(), img_file)
```

```
#diagram.write_dot(dot_file)
#print(diagram.get_data())

#print("Wrote graphviz input file to '{0}'.".format(os.path.join(os.getcwd(), dot_file)))

#os.system('dot {0} -Tpng -o{1} -Gdpi=200'.format(dot_file, img_file))
#print("Wrote graphviz output file to '{0}'.".format(img_path))

#if "-view" in sys.argv:
#    import webbrowser
#    webbrowser.open('file:///' + img_path)

print('NO red=', (100*(0.0005-states('NO').X)/0.0005))
```